

The role of pore pressure diffusion in a reservoir-induced
seismicity site in NE Brazil

Aderson F. do Nascimento



A thesis submitted in fulfillment of the requirements
for the degree of Doctor of Philosophy
to the
University of Edinburgh
2002




ABSTRACT

The Açú Dam (Barragem Eng. Armando Ribeiro Gonçalves) is a 34m high earth-filled dam, which is $2.4 \times 10^9 m^3$ in volume, and is located near the city of N. São Rafael, in NE Brazil. This is an area of the Precambrian shield composed of a paragneiss, biotite gneiss, gneiss-migmatic complex of Archean formation and biotite granite of Neoproterozoic age. Seismic monitoring, around this water reservoir, began in 1987, two years after impoundment. The largest magnitude earthquake so far (magnitude $2.8m_b$) occurred in August 1994. Previous workers have shown, using a smoked-drum seismograph network operated during two field campaigns (1989 and 1990/91), that the seismic activity occurred preferentially with strike-slip dextral focal mechanisms on NE oriented faults. Their work concluded that the seismicity was a typical case of pore pressure triggering of seismic events in NE oriented faults under regional E-W compression. From August 1994 until May 1997, a network of 8 three-component digital seismographs operated at the Açú reservoir. A detailed analysis of this data forms the first part of this thesis. The earthquake locations revealed remarkably well-defined NE trending fault structures beneath the reservoir due to the simple seismic-wave velocity structure of the area. This digital data is shown here to be very suitable for focal mechanism determination and also to investigate seismic anisotropy in the area. This is possible due to the low attenuation of the seismic waves and good signal-to-noise ratio in the seismograms provided by the crystalline rocks of the area. The focal mechanism determination and the shear-wave study of this seismicity confirm that the area is in E-W compression and also that the shear-wave splitting is controlled by the seismic anisotropy associated with the Precambrian foliation. Moreover, this study shows that the seismicity migrates between different faults and within individual faults over different time periods. To investigate this behaviour and relate it to changing water levels in the reservoir and the resulting groundwater flow beneath, a fully three-dimensional groundwater flow code (PARADIGM) is used. PARADIGM is employed to simulate the pressure field in both the rock matrix and an idealised fault geometry. This flow modelling forms the second major component of this thesis. The significance of my approach is that I explicitly consider the physical meaning of hydraulic conductivity and storativity and their impact on fluid flow. In this model, both realistic information on the hydrogeological regime of the area and measurements of real fault zone hydraulic properties are included. The combination of the spatio-temporal analysis of the seismic activity and the numerical simulations carried out in PARADIGM provide new insights into the mechanism that causes the migratory behaviour. The integrated investigation present in this thesis (numerical simulations plus the spatio-temporal analysis of earthquake locations) shows that the timing and location of the seismic events are controlled by a small number of highly permeable, heterogeneous fault structures. This means that an homogeneous equivalent medium cannot be derived to explain the seismicity in this area. I also show that the migratory behaviour is a natural consequence of the heterogeneity fault hydraulic properties. The pressure variations necessary to trigger seismicity are minute (0.01 bar) and corroborates the idea that the tectonic stress conditions must be close to the critical value for failure.

DECLARATION

This thesis has been composed solely by myself. The work presented is my own except where otherwise acknowledged.



ACKNOWLEDGEMENTS

I'm very certain that this part is the only part of the thesis where I can express myself in a non-scientific way: here I can express my emotions, use slangs, contractions etc. I'll certainly make use of this directive, mates!

I am very fortunate to be given the opportunity to be supervised by Patience Cowie and Rebecca Lunn. My first 'THANK YOU!' will go to both of them. Their patience to correct my misspellings and to support me when I seemed pretty much lost throughout the development of this thesis, are very much appreciated. Thank you also for believing that I could make it. I have a lot of respect and admiration for both of them. I am also grateful to Bob Pearce for setting up the PDAS seismic network, his support for my scholarship applications and for the useful discussions regarding the PDAS data at the early stages of the project, general seismology and for welcoming me in Edinburgh! Thanks, Bob!

My acknowledgements also go to Mario Takeya and Marcelo Assumpção who gave my first lectures in seismology. I am also very grateful for their support in hard moments of this thesis. Thank you, Mario and Marcelo for also believing I could make it. Thanks also to Joaquim Ferreira for his many advices in the seismological aspects and for his great support. My big 'THANK YOU' goes also to you, Joaquim. My thanks also go to all the staff of the 'Laboratório de Sismologia', in Natal. I also want to extend my gratitude to José A. M. Moreira and Walter Medeiros for their entertaining (and thoughtful?) advices and support. I am also very fortunate to have support from a friend such as Cláudio Melo. Valeu, Sócio! Your friendship and unconditional support are very important to me. I also got support from other friends from Brazil: José Dias, Marcio Magini and George Sand. Valeu, Feras! I wish to say big thanks to Fabio Zulbati for his friendship and for being such a real human being - you're great, man! *Ave Carbonara!* Thanks also to Matthew Purcell for being such a great flatmate and 'winemate' as well. My words of gratitude go also to Peter Hanssen—someone I know since I first arrived in Edinburgh. The 'Cabrones Utd' posse is also acknowledged here for the 'Meadows Football Circus' every Saturday and for company accompanied by good food and wine. In special to: Rafael, Demian, Christos, Emiliano and Ana. I also wish to thanks Sara Pellegrini for her cheerful smile and support. My words of gratitude also go to the Huc-Niño family, Victor and Olga.

Following on a personal note, I want to say my 'THANK YOU' to my parents, my brother and my sister for their love, affection and support along these years.

My financial support came from CNPq (Conselho Nacional de Desenvolvimento Científico e Tecnológico) and from The Overseas Research Students Award Scheme, for which I am grateful.

LIST OF SYMBOLS

A list of the symbols in alphabetical order, first in the Latin, then the Greek alphabets. The point of first appearance is given in parenthesis, which refers to an equation unless otherwise indicated. Sometimes the same symbol is used for different meanings, and vice-versa, as indicated, however the meaning is clear within the context used.

Symbol	Description	Dimension
A	Percentage anisotropy [3.1]	-
	Area of the cross section of sandy formation [Figure 5.2]	L^2
b^{-1}	Correlation length [8.11]	L
b_h	Hydraulic aperture [7.10]	L
B	Skempton's coefficient 2.10	-
$C()$	Covariance function [8.4]	-
D	Hydraulic diffusivity [2.11]	L^2T^{-1}
D_f	Fault diffusivity [7.14]	L^2T^{-1}
D_{homog}	Hydraulic diffusivity of the equivalent homogeneous media [7.3]	L^2T^{-1}
e	Fault aperture [5.14]	L
$E[]$	Expectation operator [8.3]	-
f_{dec}	Sampling/decimation frequency [Sec. 3.2]	<i>samples per second</i>
G	Shear modulus [2.7]	Pa
\mathbf{h}	Length vector [8.7]	L
h	Piezometric head [5.5]	L
	Length [8.9]	L
h_f	Piezometric head in fault node [7.13]	L
h_m	Piezometric head in matrix node [7.13]	L
$H(t)$	Heavide unit step function [2.17]	ML^2T^{-2}
k	Permeability [5.10]	L^2
$\underline{\underline{K}}$	Hydraulic conductivity tensor [7.1]	LT^{-1}

K	Hydraulic conductivity [5.6]	LT^{-1}
K_0	Hydraulic conductivity at no applied stress [5.16]	LT^{-1}
\mathbf{K}_F	Fault hydraulic conductivity tensor in the x-y plane [7.7]	LT^{-1}
K_{homog}	Hydraulic conductivity of the equivalent homogeneous media [7.3]	LT^{-1}
K_f	Bulk modulus of the fluid [7.4]	$ML^{-1}T^{-2}$
K_g	Bulk modulus of the solid that constitutes the porous media [7.4]	$ML^{-1}T^{-2}$
K_d	Bulk modulus of the dry porous media [7.4]	$ML^{-1}T^{-2}$
L	Matrix-to-fault link [7.12]	L
l	Thickness of the sandy formation [5.6]	L
m	Fluid mass content per unit volume [2.9] mean [8.5]	ML^{-3} -
m_0	Fluid mass content per unit volume measure with respect to a reference state [2.9]	ML^{-3}
$m(x)$	Mean of x [8.3]	-
M	Mass in the system [5.3]	M
N	Poroelastic modulus [7.3]	ML^2T^{-2}
p	Pressure [2.6]	$ML^{-1}T^{-2}$
p_0	surface pressure at $t = 0$ [2.13]	$ML^{-1}T^{-2}$
p_d	Drained pore pressure [2.11]	$ML^{-1}T^{-2}$
q	Flux [5.7]	L
$q_{m \rightarrow f}$	Leakage between the matrix and the fault	LT^{-1}
q_x, q_y, q_z	Flow per unit area [5.1]	LT^{-1}
Q	Flux through a porous media [5.6]	L^3/T
r	Distance between two points [8.11]	L
S	Strength [2.5]	ML^2T^{-2}
S	Specific storativity, storativity [5.5]	M^{-1}
S_f	Fault Storativity [7.11]	-
S_{homog}	Storativity of the equivalent homogeneous media [7.3]	L^{-1}
\mathcal{T}	Time interval [Sec. 3.2]	T
t	Time [refeq:drained]	T
t_{fast}	Arrival time of the fast S [3.1]	T
t_{slow}	Arrival time of the slow S [3.1]	T
t_O	Earthquake origin time [Sec. 3.4]	T
t_P	P-wave time arrival [Sec. 3.4]	T
t_S	S-wave time arrival [Sec. 3.4]	T
T_f	Fault transmissivity [7.10]	L^2T^{-1}
V	Total Volume [5.2]	-
V_{pore}	Pore volume [5.2]	L^3

V_P	P-wave velocity [Sec. 3.4]	L^2T^{-1}
V_S	S-wave velocity [Sec. 3.4]	L^2T^{-1}
x, y	Horizontal space coordinates	L
z	Elevation head [5.8]	L
z	Vertical space coordinates	L
$Z(x)$	Random function of x [8.3]	-
α	Angle between failure and σ_1	rad
	Rate of Hydraulic cond. decay with depth/effective stress [8.1]	-
β_f	Coefficient of compressibility of the fluid [5.17]	$M^{-1}LT^2$
β_s	Coefficient of compressibility of the solid that constitutes the porous media [5.17]	$M^{-1}LT^2$
β_p	Coefficient of compressibility of the porous media [5.17]	$M^{-1}LT^2$
$\gamma(\cdot)$	Variogram function [8.8]	-
$\gamma^*(\cdot)$	Experimental variogram function [8.8]	-
δ_{ij}	Kronecker delta [2.7]	-
ΔV	Saturated soil element [2.13]	L^3
$\Delta x, \Delta x, \Delta x$	soil elements dimensions	L
ϵ_{ij}	Strain tensor [2.7]	-
η	Fluid viscosity [5.10]	$ML^{-1}T^{-1}$
Λ	Distance from the station to earthquake	L
μ_f	Coefficient of internal friction [2.6]	-
ν	Drained Poisson's ratio	-
ν_u	Undrained Poisson's ratio	-
ρ	Fluid density [2.9]	ML^{-3}
ρ_0	Fluid density measured with respect to a reference state [2.9]	ML^{-3}
σ^2	Variance [Sec. 8.3.2]	-
σ	Effective stress [5.16]	$ML^{-1}T^{-2}$
	Standard deviation [Sec. 8.4]	-
σ_1, σ_3	Principal stresses [2.1]	$ML^{-1}T^{-2}$
σ_{ij}	Stress tensor [2.7]	Pa
σ_n	Normal stress [2.1]	$ML^{-1}T^{-2}$
τ	Shear stress [2.1]	$ML^{-1}T^{-2}$
τ_0	Cohesion [2.3]	$ML^{-1}T^{-2}$
ϕ	Angle of internal friction [2.3]	rad
	Porosity [5.2]	-
ϕ^*	Porosity of a rock in which the only void space is due to the presence of parallel planes [5.14]	-
ω	Characterist frequency of a lake level variation [2.13]	T^{-1}

LIST OF FIGURES

1.1	General location map	2
2.1	Schematic fracturing test	5
2.2	Mohr diagram	6
2.3	Coulomb law of failure	6
2.4	Pore pressure and shear failure	7
2.5	Mohr circle representing the elastic effect of reservoir loading	8
2.6	Schematic figure of the the change in stability of a fault plane relative to the position of the reservoir.	8
2.7	Mohr circle representing the fluid pressure effect on the strength of the rock.	9
2.8	Plot of equation 2.12	12
3.1	Network configuration C	17
3.2	Examples of seismograms recorded at 200 Hz before and after removing the precursors to P-wave.	18
3.3	Example of seismogram recorded at 500 samples per second.	19
3.4	Wadati diagram for the 58 selected events	20
3.5	Hypocentral maps	21
3.6	Hypocentral parameters	21
3.7	Focal mechanisms solution of earthquakes in 1994 and 1994	22
3.8	Examples of shear-wave splitting for station BASQ	26

3.9	Rose diagrams and polarisation measurements against angle of emergence and back azimuth angle for station BACP	27
3.10	Rose diagrams and polarisation measurements against angle of emergence and back azimuth for station BASQ	28
3.11	Geological map and polarisation measurements	30
3.12	Schematic illustration of relative amplitude measurements.	32
4.1	Monthly seismicity vs. water level	36
4.2	Epicentral map showing the active clusters in 1989, 1990/91 and 1994-97	37
4.3	Hypocentral map showing different clusters	38
4.4	Spatio-temporal evolution of the seismicity recorded by the digital seismic network	39
4.5	Earthquake monthly activity versus water level	41
4.6	Distribution of $(t_S - t_P)$ arrival times as recorded by BA1	42
4.7	Epicentral map showing the active clusters in 1989, 1990/91 and 1994-97	44
5.1	Flow through a saturated soil element	47
5.2	Darcy's experiment	49
5.3	Fluid flow through porous media. Example of rapid and slow flow.	51
5.4	Parallel plate model	52
6.1	Map showing topography, main rivers and Açú reservoir in NE Brazil	56
6.2	Map showing isohyets of annual precipitation (mm)	57
6.3	Figure showing the potential evapotranspiration in the study area.	58
6.4	SFER and STAC flow measurements	59
6.5	Unconfined valley aquifer in semi-arid region.	60
6.6	Daily water fluctuation at the Açú reservoir	61
6.7	Locations of the well and topographic points used for water table height constraints	62
6.8	Borborema Province	63
7.1	Schematic diagram showing a schematic diagram of the 3D mesh defined in PARADIGM	66

7.2	Regional model	67
7.3	Gridded lakes	68
7.4	Gridded lakes and rivers	69
7.5	Example of lake level input	70
7.6	Piezometric head predictions from the sections indicated in Figure 7.2. $K=8.5 \times 10^{-7}$ m/day and $S=10^{-6} m^{-1}$	71
7.7	Piezometric head predictions from layers at 100, 1,000 and 3,000 m. $K=8.5 \times 10^{-7}$ m/day and $S=10^{-6} m^{-1}$	72
7.8	Node transformation	73
7.9	Refined model	74
7.10	Example of piezometric head predictions for the refined model. $K=8.5 \times 10^{-7}$ m/day and $S=10^{-6} m^{-1}$	76
7.11	Time varying output for nodes in the centre of the refined model at depths of 50, 150, 250 and 350 m.	77
7.12	Fluxogram of the general procedure to find the matching K and S	78
7.13	Node at depth reaching oscillatory steady-state regime	79
7.14	Idealised water level and predicted head values for the homogeneous model	79
7.15	Schematic diagram showing fault orientation in PARADIGM	81
7.16	Flow in a fault	82
7.17	Refined model with fault	84
7.18	Sensitivity analysis for T_f and S_f	86
7.19	Flow circulating within a fault	87
7.20	Time varying outputs for numerical runs with different matrix-to-fault link	88
7.21	Piezometric heads in the faults for different values of L	89
7.22	Effect of L in the numerical runs	90
7.23	Idealised water level and predicted head values for the homogeneous fault model	92
7.24	Examples of piezometric head predictions in the fault shown in Figure 7.17	94
7.25	Time varying output for nodes at 1,050, 2,050 and 3,050 m	95

8.1	Conceptual model of fault zone	97
8.2	Conceptual scheme of fault-related fluid flow	98
8.3	Example of exposure of brittle fault in Pre-Cambrian rocks	99
8.4	Fits of Equation 8.1	100
8.5	Example of piezometric head prediction in the seismogenic fault.	101
8.6	Variation of K and T_f over depth	103
8.7	Covariance and variogram	106
8.8	Examples of two-dimensional realisations of stationary fields generated by the turning bands method.	108
8.9	Examples of correlated fields with decrease of transmissivity with increasing depth. . .	110
8.10	How the time delay and the amplitude variations are performed	112
8.11	Contour plot for the time delay and amplitude variation	113
8.12	Histogram of the number of events as a function of the time delay	115
8.13	Output from a non-uniform fault without a random transmissivity field	118
8.14	Output from a fault with a random transmissivity field and $\sigma^2=0.25$	119
8.15	Output from a fault with a random transmissivity field and $\sigma^2=0.50$	120
8.16	Histogram percentage of triggered nodes for an ensemble of five different correlated random fields. For these fields, $b^{-1} = 166.67m$ and $\sigma^2=0.25$	123
8.17	Single realisation of a random correlated field with $b^{-1} = 166.67m$ and $\sigma^2=0.25$	124
8.18	Histogram of percentage of triggered nodes from an ensemble of five different correlated random fields. For these fields, $b^{-1} = 166.67m$ and $\sigma^2=0.50$	126
8.19	Single realisation of a random correlated field with $b^{-1} = 166.67m$ and $\sigma^2=0.50$	127
8.20	Histogram of percentage of triggered nodes for an ensemble of five different correlated random fields. For these fields, $b^{-1} = 500m$ and $\sigma^2=0.25$	129
8.21	Single realisation of a random correlated field with $b^{-1} = 500m$ and $\sigma^2=0.25$	130
8.22	Histogram percentage of triggered nodes for an ensemble of five different correlated random fields. For these fields, $b^{-1} = 500m$ and $\sigma^2=0.50$	132
8.23	Single realisation of a random correlated field with $b^{-1} = 500m$ and $\sigma^2=0.50$	133

B.1	Network configuration A	152
B.2	Network configuration B	153
B.3	Network configuration C	154
B.4	Network configuration D	155
B.5	Network configuration E	156
D.1	Vectorplot for displaying focal mechanisms	163
D.2	Solution for FM1	164
D.3	Solution for FM2	164
D.4	Solution for FM3	165
D.5	Solution for FM4	165
D.6	Solution for FM5	166
D.7	Solution for FM6	166
D.8	Solution for FM7	167
D.9	Solution for FM8	167
D.10	Solution for FM9	168
D.11	Solution for FM10	168
E.1	Single realisation of a random correlated field with $b^{-1} = 166.67m$ and $\sigma^2=0.25$	170
E.2	Single realisation of a random correlated field with $b^{-1} = 166.67m$ and $\sigma^2=0.25$	171
E.3	Single realisation of a random correlated field with $b^{-1} = 166.67m$ and $\sigma^2=0.25$	172
E.4	Single realisation of a random correlated field with $b^{-1} = 166.67m$ and $\sigma^2=0.25$	173
E.5	Single realisation of a random correlated field with $b^{-1} = 166.67m$ and $\sigma^2=0.25$	174
E.6	Single realisation of a random correlated field with $b^{-1} = 166.67m$ and $\sigma^2=0.50$	176
E.7	Single realisation of a random correlated field with $b^{-1} = 166.67m$ and $\sigma^2=0.50$	177
E.8	Single realisation of a random correlated field with $b^{-1} = 166.67m$ and $\sigma^2=0.50$	178
E.9	Single realisation of a random correlated field with $b^{-1} = 166.67m$ and $\sigma^2=0.50$	179
E.10	Single realisation of a random correlated field with $b^{-1} = 166.67m$ and $\sigma^2=0.50$	180

E.11	Single realisation of a random correlated field with $b^{-1} = 500m$ and $\sigma^2=0.25$	182
E.12	Single realisation of a random correlated field with $b^{-1} = 500m$ and $\sigma^2=0.25$	183
E.13	Single realisation of a random correlated field with $b^{-1} = 500m$ and $\sigma^2=0.25$	184
E.14	Single realisation of a random correlated field with $b^{-1} = 500m$ and $\sigma^2=0.25$	185
E.15	Single realisation of a random correlated field with $b^{-1} = 500m$ and $\sigma^2=0.25$	186
E.16	Single realisation of a random correlated field with $b^{-1} = 500m$ and $\sigma^2=0.50$	188
E.17	Single realisation of a random correlated field with $b^{-1} = 500m$ and $\sigma^2=0.50$	189
E.18	Single realisation of a random correlated field with $b^{-1} = 500m$ and $\sigma^2=0.50$	190
E.19	Single realisation of a random correlated field with $b^{-1} = 500m$ and $\sigma^2=0.50$	191
E.20	Single realisation of a random correlated field with $b^{-1} = 500m$ and $\sigma^2=0.50$	192

LIST OF TABLES

2.1	RIS models and their main features	14
3.1	Table with composite focal mechanisms of events from 1994 until 1997	23
3.2	Basic statistics of the polarisation alignments of the stations	25
3.3	Details of focal mechanisms for the 10 selected events.	33
4.1	Activation period of events recorded by the digital seismic network	45
4.2	Water level increase associated with cluster activation	45
5.1	Typical values of hydraulic conductivity	52
5.2	Typical specific storage values	53
6.1	River flow measurements at SAC and SFER	59
6.2	Summary of data used in groundwater modelling	64
7.1	Boundary conditions and model data for the regional model	68
7.2	Model parameters for the regional model in Figure 7.10.	75
7.3	Model parameter data for the numerical experiment output in Figure 7.23	92
8.1	Fault zone architectural styles and its corresponding hydraulic conductivity structures	99
8.2	Model parameter data for the new fault grid	101
8.3	Summary statistics of events with time delay greater than 32 days occurring at depth range of 1800 to 2200m	114
8.4	Transmissivity fields parameters	116

8.5	Activation period of events	134
A.1	Splitting measurements for 40 event-station raypaths within the shear-wave window. .	150
B.1	Deployment periods of the networks	151
B.2	Stations locations	151
C.1	Solution quality of hypocentre determination.	158
C.2	List of earthquakes	162

CONTENTS

Abstract	i
Declaration	ii
Acknowledgements	iii
1 Introduction	1
2 Background on reservoir-induced seismicity	4
2.1 Fracturing macroscopic criteria	4
2.1.1 Stress relations, Mohr diagram and the Coulomb law.	4
2.2 Models of RIS	7
2.2.1 Simple elastic response	7
2.2.2 Pore pressure effects	9
2.3 RIS modelling approaches	13
3 Data analysis of the PDAS network in Açu	16
3.1 Description of the network	16
3.2 Working with digital data	16
3.3 Phase picking	18
3.4 Event location	19
3.5 Focal Mechanism	20

3.6	Anisotropy	23
3.6.1	Definition and causes	23
3.6.2	Seismic anisotropy from the Açú data set	24
3.6.3	Interpretation of the shear-wave observations	29
3.7	Focal mechanisms in the presence of anisotropy	31
3.7.1	Application of the RAMP method to the Açú earthquakes	32
3.8	Summary	34
4	Spatio-temporal evolution of the seismicity at Açú reservoir	35
4.1	The relationship between the water level and the seismicity (1994-1997)	35
4.1.1	Spatio-temporal analysis from the permanent station BA1	40
4.2	Summary	45
5	Ground Water Theory	47
5.1	Mass balance equation - flow in saturated porous media	47
5.2	Darcy's Law	48
5.3	Permeability and hydraulic conductivity definitions and the groundwater flow equation	50
5.4	Hydraulic properties of basement rock	51
5.4.1	Hydraulic conductivity	51
5.4.2	Specific storage coefficient	53
5.4.3	Hydraulic diffusivity	53
5.5	Summary	54
6	Background to the site	55
6.1	The hydrological regime	55
6.1.1	Water input: rainfall	57
6.1.2	Outputs: river discharges and evapotranspiration	58
6.1.3	Storage	60
6.1.4	Groundwater storage	61

6.2	Basement geology and hydrological properties	61
6.3	Summary	63
7	Groundwater modelling - homogeneous model	65
7.1	Numerical modelling with PARADIGM	65
7.2	Regional and refined local models in the Açu reservoir	66
7.2.1	Regional model	66
7.2.2	Simulation results from the regional model	67
7.2.3	Refined local model	73
7.2.4	Simulation results from the refined local model	73
7.3	Finding the time lag with the matrix model	75
7.4	The matrix and fault model	81
7.4.1	Placing the seismogenic fault in the numerical model	83
7.5	Sensitivity Analysis	83
7.6	The matrix-to-fault link	88
7.7	Finding the time lag with the matrix and fault model	91
7.8	Summary	93
8	Groundwater modelling - heterogeneous model	96
8.1	Evidence for the heterogeneous hydraulic structure of faults	97
8.2	Including the depth vs. hydraulic conductivity dependence	98
8.2.1	Matrix only model with dependence of K over depth	102
8.2.2	Matrix and fault model with dependence of K and T_f over depth	102
8.3	Including heterogeneous hydraulic properties in the fault	104
8.3.1	Review of the properties of a stationary random function	104
8.3.2	Spatial statistics	105
8.3.3	Simulation of the spatially correlated random fields	107
8.4	Pore pressure diffusion in a non-uniform transmissivity field	109

8.5	Numerical simulation with non-uniform and random transmissivity fields	116
8.6	Numerical simulations with random correlated transmissivity fields	121
8.6.1	Correlation length of 166.67m and variance of 0.25	121
8.6.2	Correlation length of 166.67m and variance of 0.50	125
8.6.3	Correlation length of 500m and variance of 0.25	128
8.6.4	Correlation length of 500m and variance of 0.50	131
8.7	Interpretation of the numerical simulations	131
8.8	Summary	134
9	Summary and discussions	136
10	Synthesis and Conclusions	140
10.1	Conclusions	140
10.2	Future work	141
	Bibliography	148
A	Polarisation measurements	149
B	Network configurations	151
C	Earthquake locations	157
D	Vectorplots and seismograms	163
E	Heterogeneous fault transmissivity fields	169
E.1	Correlation length of 166.67m and variance of 0.25	169
E.2	Correlation length of 166.67m and variance of 0.50	175
E.3	Correlation length of 500m and variance of 0.25	181
E.4	Correlation length of 500m and variance of 0.50	187
F	Preprint of do Nascimento <i>et al.</i> (2001)	193

1 INTRODUCTION

In this thesis I investigate the seismicity associated with the construction of the Armando Ribeiro Gonçalves Dam, often called Açú dam, or Açú reservoir, located in NE Brazil (Figure 1.1). The term “Reservoir-Induced Seismicity” (RIS) is applied to the seismicity that is associated with the construction and subsequent filling of water reservoirs. Nevertheless, the increase or appearance of seismicity in the crust is sometimes also associated with other man-made activities such as injection of fluids in boreholes and mining exploration (Carder, 1945; Healy *et al.*, 1968; Raleigh *et al.*, 1976; Talwani and Acree, 1984/85; Gupta, 1992).

The construction of water dams in particular, has received special attention from engineers and geoscientists because induced seismicity has a great potential to destroy these constructions, leading to human and material losses. Following damaging reservoir-induced earthquakes in the 1960s at Koyna, India; Hsingfengkiang, China; Kariba, Zimbabwe and Kremasta, Greece (Gupta, 1992), a great improvement in seismic monitoring occurred, and local seismographic station networks were deployed to monitor several reservoirs in the 1970s (Talwani, 1976; Beck, 1976; Gough, 1969; Gough and Gough, 1970). These led to lower detection thresholds and improved hypocentral locations of seismic events. Complementary field studies identified the factors that are likely to control the observed RIS: ambient stress field conditions, fracture occurrence, hydromechanical properties of the rocks beneath the reservoir, geology of the area, dimensions of the reservoir and lake-level fluctuations (Zoback and Hickman, 1982; Talwani, 1997). Observational and theoretical models (Bell and Nur, 1978; Roeloffs, 1988; Talwani, 1997) attest to the existence of two effects when a water reservoir is filled: 1 - the change in ambient stress condition due to the weight of the water, which may lead to failure; 2 - the increase of interstitial pore pressure in the rock matrix, fractures and faults beneath the reservoir. This second effect can be due to fluid diffusion, or due to compaction of the water saturated rock due to the weight of the reservoir, or both. Therefore, the analysis of reservoir induced-seismicity potentially provides an excellent opportunity to investigate mechanical and/or hydraulic properties of the crust (Bell and Nur, 1978; Talwani and Acree, 1984/85; Roeloffs, 1988; Talwani, 1997).

The observational investigations of RIS are often jeopardised by the lack of accurate hypocentral locations. This is caused by the complexity of the velocity structure in the area investigated or by the lack of appropriate seismic surveillance: i.e. the number, or the arrangement of seismic stations. Accurate hypocentral location and continuous seismic monitoring are important because they give information on important aspects of the RIS like migration of seismicity with time. The numerical models used to investigate RIS worldwide rely on simplified assumptions in lake geometry and physical properties of the reservoir subsurface rocks. Two of the common simplifications made in numerical models are: 2D geometry of the rocks beneath the reservoir (Bell and Nur, 1978; Roeloffs, 1988; Simpson and Narasimhan, 1992) and/or the use of models in which the hydraulic properties of the rock are uniform (Bell and Nur, 1978; Simpson and Narasimhan, 1992; Lee and Wolf, 1998; Kalpna, 2000). Moreover,

published models of RIS so far lack *in situ* hydrogeological information to justify the choices of the model parameters used in the numerical simulations. Another common problem in RIS studies and also in related fluid-induced seismicity literature is the misuse and misinterpretation of hydrogeological rock properties (Shapiro *et al.*, 1997, 1999; Shapiro, 2000). In other words, the literature dealing with induced seismicity lacks hydrogeological insight so that wrong assumptions and interpretations are often made as a consequence.

This thesis presents a three-dimensional study of RIS using high quality seismological observations and realistic hydrogeological rock properties and correct interpretation of the meaning of these properties. To investigate the relationship between surface water levels in the reservoir and induced seismicity, I use a fully three-dimensional groundwater flow code (PARADIGM). The area of interest lies in NE Brazil (Figure 1.1). The reason for using this area is that the errors associated with earthquake location here are very small ($\sim 100\text{m}$). The Açú reservoir lies on a stable cratonic area, so the association between water level fluctuation and the seismicity is easily observed. Here, I bring together seismo-

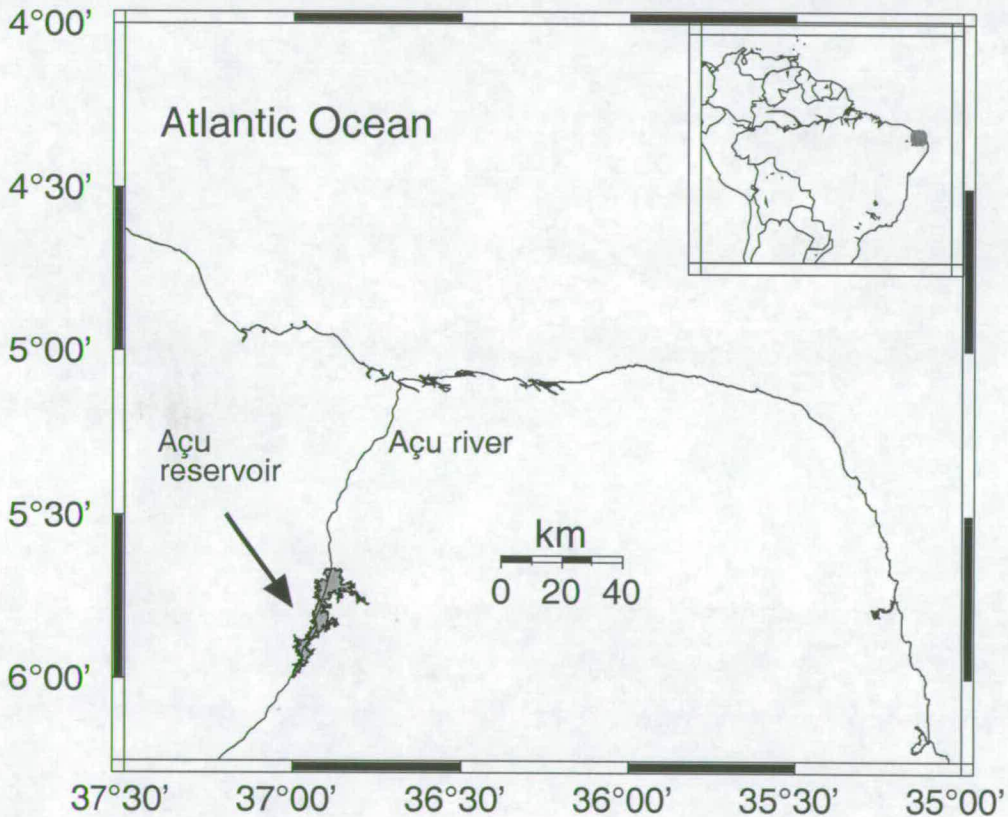


Figure 1.1: Map showing the location of the Açú reservoir in northeastern Brazil.

logical and hydrogeological aspects which were neglected by other authors in RIS such as: precise earthquake information to observe earthquake migration; realistic information on the hydrogeological regime of the area considered and the effect of fault zone heterogeneity in the diffusion of the pressure under the Açú reservoir as predicted by PARADIGM. The latter model, incorporates conceptual models of faults derived from field and laboratory observations. The combination of seismology and flow modelling presented in this thesis provides a robust way to address interpretations of hydrogeological

properties in rocks such as the validity of characterising of rock volume by an equivalent homogeneous media. Another important point to be addressed in this area is what causes the seismicity to migrate between different faults and within individual faults over different time periods. The combination of numerical simulations of fluid flow and the spatio-temporal seismicity data provides insights into the mechanisms that cause this migratory behaviour.

In **Chapter 2** a brief literature review of RIS is given. The main ideas, theories and models concerning induced seismicity are presented and discussed here. **Chapter 3** presents the earthquake data analysis from a digital network deployed in the area from August 1994 until July 1997: events location, focal mechanism determination and seismic anisotropy investigations are presented. In **Chapter 4**, I present the spatio-temporal analysis of the seismic activity in the Açú reservoir and its correlation with the water level fluctuation in the reservoir. This spatio-temporal analysis is obtained by combining the data acquired by the digital network deployed in the area from August 1994 until July 1997 and by an analogue seismic station in operation since August 1987. An outline of the ground water theory that is necessary to understand the following Chapters is presented in **Chapter 5**. In **Chapter 6** the relevant hydrological, hydrogeological and geological data in the Açú area to be incorporated into the numerical model, are presented. In **Chapter 7** a 3D regional ground water model is build within PARADIGM to investigate pore pressure diffusion in the seismically active area of the reservoir. An outline of the numerical scheme used by PARADIGM and the procedure adopted to built the groundwater model and sensitivity analyses are also presented here. The modelling shows that the diffusion of pore pressure is controlled by a high permeability fault and that the standard assumption of an equivalent homogeneous media invokes physically unrealistic rock properties. In **Chapter 8**, heterogeneity is added to the fault. This addition is based on field observation and laboratory data. With this added complexity in the fault, the migration and spatio-temporal distribution of pore pressure fluctuations is investigated and compared with the real data provided from the spatio-temporal analysis of seismicity in this area (see **Chapter 4**). The results of this thesis are summarised and discussed in **Chapter 9**. The conclusions from this thesis are presented in **Chapter 10** and suggestions for useful further work are also made.

The original contribution of this thesis is to combined both seismological and hydrogeological analysis to investigate the RIS associated with the Açú reservoir in NE Brazil. This combination provided a unique approach to the study of RIS. Also, for the first time, a 3D numerical groundwater model incorporating hydrogeological information to study the role of pressure diffusion in a RIS area was carried out.

2 BACKGROUND ON RESERVOIR-INDUCED SEISMICITY

An increase of seismic activity in some areas of the earth has been linked with impoundment of artificial water reservoirs and the injection of fluids into the crust (Gupta, 1992; Cornet and Yin, 1992; Shapiro *et al.*, 1997; Tadokoro and Ando, 2000). Seismicity associated with impoundment of reservoirs is termed Reservoir-Induced Seismicity (RIS). In this chapter, a brief literature review on RIS is given. The main ideas/theories and models about induced seismicity are presented and discussed here.

Since the first identification of a correlation between seismicity and lake impoundment in the early 1940s (Carder, 1945), the literature on RIS has increased and aroused scientific interest (Talwani and Acree, 1984/85; Simpson *et al.*, 1988; Gupta, 1992; Rajendran and Talwani, 1992). Following damaging reservoir-induced earthquakes during the 1960s at: Koyna (India); Hsingfengkiang (China); Kariba (Zimbabwe) and Kremasta (Greece), there was great improvement in seismic monitoring using local networks to study these areas (Talwani, 1997). According to Gupta (1992), there are approximately 70 reported cases of RIS. Most of these cases documented in the literature come from the United States and Europe. However, there may be more cases where RIS is present but was never reported, mainly because of the lack of appropriate seismic surveillance. The most conclusive cases of RIS come from examples where the seismic monitoring began before the impoundment and therefore it was possible to observe the increase of seismic activity after the reservoir filling. There are also cases, however, in which reports of felt events by the local population are enough to establish the relation between seismicity and the reservoir impoundment. To study the RIS phenomenon, it is necessary to understand the basics of the rock fracturing mechanism. Thus, in the next section, the basic theory of rock fracturing is presented.

2.1 Fracturing macroscopic criteria

2.1.1 Stress relations, Mohr diagram and the Coulomb law.

Consider a two-dimensional stress field as shown in Figure 2.1 applied to a cylindrical specimen of rock. In this diagram, σ_n and τ , the normal and shear stresses components are taken as the axes of abscissa and ordinate, respectively. On a plane perpendicular to the $\sigma_1\sigma_3$ -plane and making an angle α with the σ_1 -axis, σ_n and τ are then given by;

$$\tau = \frac{\sigma_1 - \sigma_3}{2} \sin 2\alpha \quad (2.1)$$

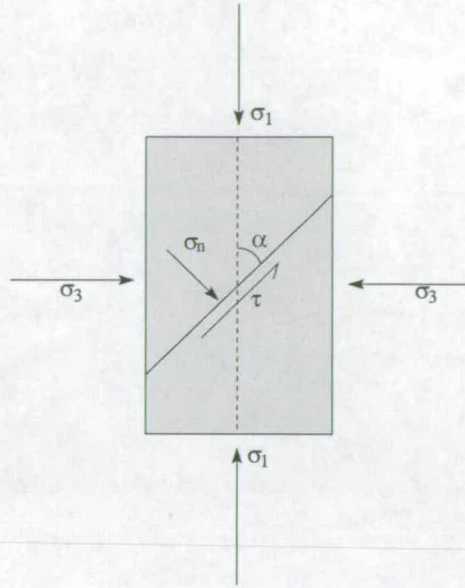


Figure 2.1: Schematic figure showing the stress field in a homogeneous and isotropic rock.

and

$$\sigma_n = \frac{\sigma_1 + \sigma_3}{2} - \frac{\sigma_1 - \sigma_3}{2} \cos 2\alpha \quad (2.2)$$

The graphical representation of τ and σ_n using the principal stresses, σ_1 and σ_3 , is given in Figure 2.2. This representation is called Mohr's diagram.

In a triaxial test, each pair of values of σ_1 and σ_3 for which failure occurs allows a particular Mohr circle to be constructed. When failure tests with increasing values of σ_1 and σ_3 are carried out, a family of such circles is obtained, whose centres lie at successively greater distances out on the σ_n -axis. When a series of such tests is made, an envelope of the successive overlapping Mohr circles may be plotted (Figure 2.3). The Mohr failure envelope defines the combination of τ and σ_n for which failure is reached. The Mohr failure envelope can be approximated by the equation:

$$\tau = \tau_0 + \sigma_n \tan \phi \quad (2.3)$$

and is widely referred to as Coulomb's law of failure. τ_0 is the intercept of the σ_n -axis and represents, in physical terms, the initial shear strength of the rock when the normal stress is zero i.e., the cohesion. The slope of the Mohr envelope, $\tan \phi$ is called the coefficient of internal friction μ_f and ϕ is a rock constant called the angle of internal friction.

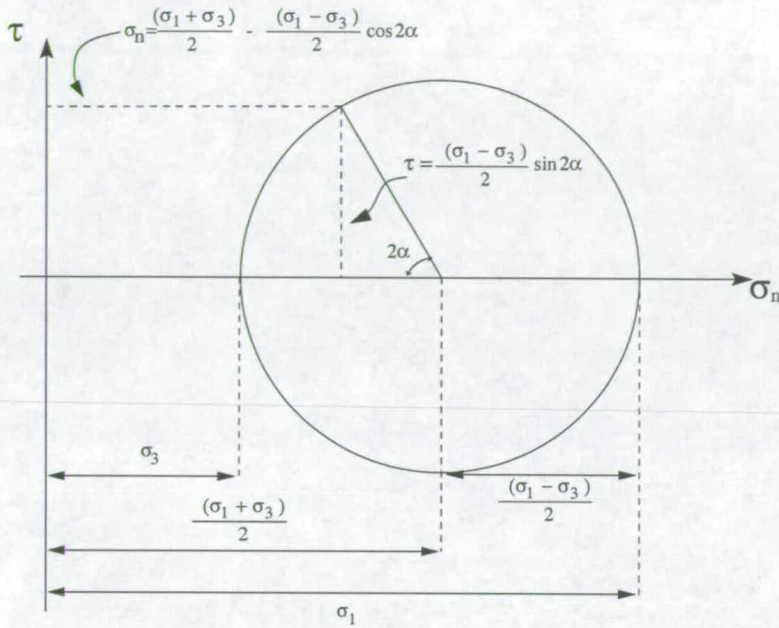


Figure 2.2: Mohr diagram for normal shear stresses produced by the principal stresses (modified from Hubbert and Rubey (1959)).

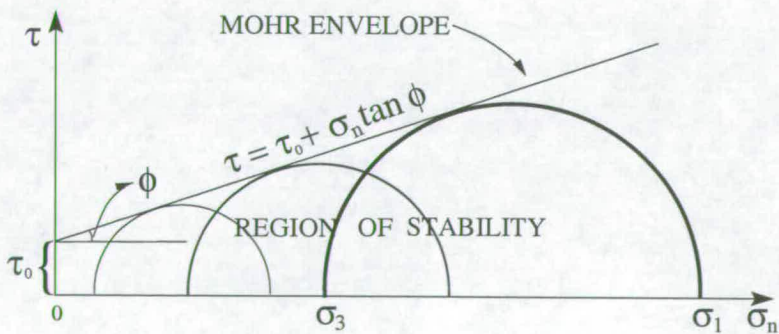


Figure 2.3: Mohr envelope of stress circles for a series of tests showing failure according to Coulomb's law of failure (modified from Hubbert and Rubey (1959)).

2.2 Models of RIS

RIS is caused by shear failure on a pre-existing fault plane. The change in shear stress, $\Delta\tau$, on this fault plane before and after the lake impoundment is:

$$\Delta\tau = \mu_f \Delta\sigma_n \quad (2.4)$$

The change in fault strength ΔS is defined as:

$$\Delta S = \mu_f \Delta\sigma_n - \Delta\tau \quad (2.5)$$

where $\Delta\tau$ is the changes in shear stress on the fault (in the direction of slip) and $\Delta\sigma_n$ is the change in compressive normal stress across the fault. μ_f is the coefficient of friction. If pore pressure is present, 2.5 becomes:

$$\Delta S = \mu_f (\Delta\sigma_n - p) - \Delta\tau \quad (2.6)$$

Negative values of ΔS signify fault weakening while positive values imply fault strengthening. From equation 2.6, a decrease in ΔS can be caused by a decrease in $\Delta\sigma_n$ or an increase in $\Delta\tau$. An increase in pore pressure Δp , as shown in Figure 2.4 always decreases ΔS .

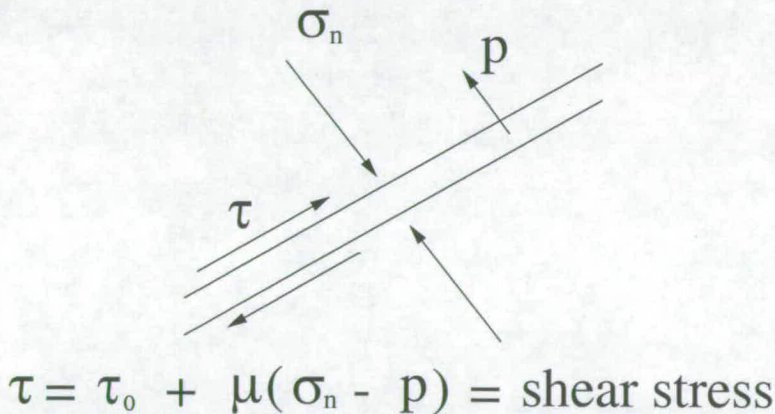


Figure 2.4: Pore pressure and shear failure. After Simpson and Narasimhan (1992).

The importance of the results of the above theory is the acknowledgement that the critical state of stress in a rock may be reached both by the purely elastic effect changing the radius of the Mohr circle towards failure (i.e. changing σ_n or τ), and via the increment of an interstitial pressure (i.e. changing p).

2.2.1 Simple elastic response

The elastic response of the subsurface to loading causes changes in normal and shear stress on the fault plane. The changes in stress may be calculated using elasticity theory (Gough, 1969; Gough and Gough, 1970). The effect of the elastic response is to change the differential stresses. Hence, the

radius of the Mohr circle changes. Figure 2.5 shows the Mohr circle representing the elastic effect of reservoir loading on the strength of the rock underneath. In the case of Figure 2.5, the reservoir lies on the hanging wall of a normal fault. Therefore, σ_1 is increased with the impoundment of the reservoir. The $\Delta\tau$ term is either added or subtracted from ΔS depending on the sense of the in situ shear stress.

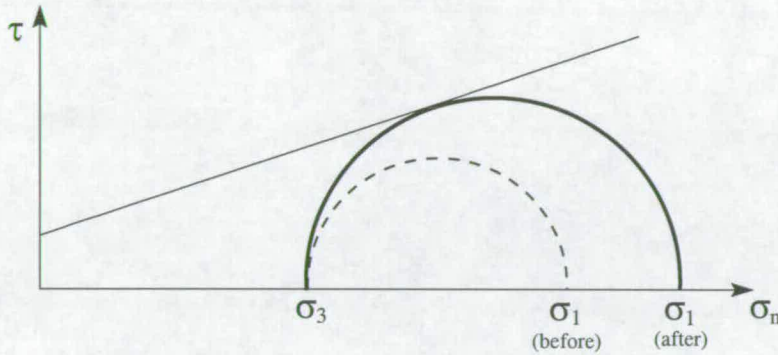


Figure 2.5: Mohr circle representing the elastic effect of reservoir loading on the strength of the rock underneath. The dashed circle is before and the full circle is after loading.

Figure 2.6 shows a series of simplified sketches showing the change in stability of a fault plane relative to the position of the reservoir. In the case of a strike-slip fault, there is no change in $\Delta\tau$, therefore, one would not expect RIS in areas prone to strike-slip faulting if this were the controlling mechanism. If

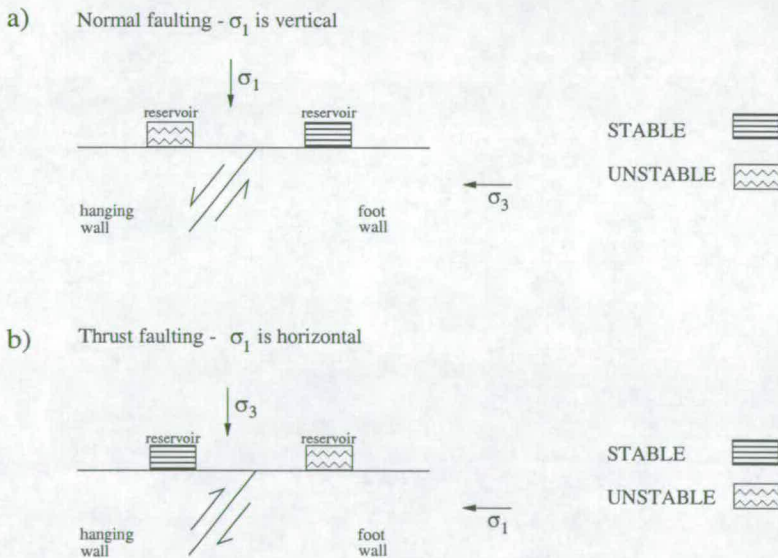


Figure 2.6: Schematic figure of the the change in stability of a fault plane relative to the position of the reservoir.

the elastic effect was the dominant mechanism of RIS, then as the weight of the reservoir ΔS changes instantly, and seismicity would be triggered quickly after the impoundment. However, there are cases of ongoing seismicity decades after the initial impoundment (Roeloffs, 1988; Simpson *et al.*, 1988; Ferreira *et al.*, 1995; Talwani, 1995, 1997).

2.2.2 Pore pressure effects

To explain this long-lasting seismicity the decrease of the effective normal stress due to the increase in pore pressure in the rockmass began to be investigated by many authors (Healy *et al.*, 1968; Nur and Booker, 1972; Raleigh *et al.*, 1976; Bell and Nur, 1978). The effect of the pore pressure, seen in Figure 2.7 is to reduce the effective normal stress and push the Mohr circle towards failure.

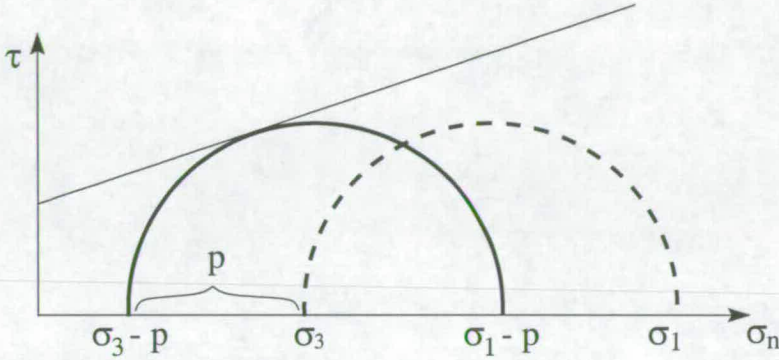


Figure 2.7: Mohr circle representing the fluid pressure effect on the strength of the rock. The dashed circle is before fluid is injected and the full circle is after the fluid pressure is applied.

Models of RIS (Bell and Nur, 1978; Roeloffs, 1988) started to incorporate the formulation of Rice and Cleary (1976). In this formulation, the existence of a fluid phase implies that there are two different deformation regimes to be considered - the drained regime and the undrained regime (Detournay and Cheng, 1993; Guéguen and Palciauskas, 1994). These two regimes are proposed to be responsible for the ongoing seismicity in cases of RIS (as opposed to the simple elastic response). *Drained* and *undrained* conditions receive their names because of laboratory tests that duplicate these respective conditions.

Before presenting the Rice and Cleary (1976) formulation, it is useful to present the classical stress-strain (or constitutive) relations for an isotropic, linearly elastic solid (Landau and Lifshitz, 1959):

$$2G\epsilon_{ij} = \sigma_{ij} - \frac{\nu}{1+\nu}\sigma_{kk}\delta_{ij} \quad (2.7)$$

where ν is the Poisson's ratio measured under drained condition. σ_{ij} , ϵ_{ij} and G are the stress, strain tensors and the shear modulus respectively.

The Rice and Cleary (1976) formulation augmented equation 2.7 by the addition of pore pressure as a variable on the stress side of the equation.

$$2G\epsilon_{ij} = \sigma_{ij} - \frac{\nu}{1+\nu}\sigma_{kk}\delta_{ij} + \frac{3(\nu_u - \nu)}{B(1+\nu)(1+\nu_u)}p\delta_{ij} \quad (2.8)$$

The fluid mass content per unit volume m is described by:

$$m - m_0 = \frac{3\rho_0(\nu_u - \nu)}{2GB(1 + \nu)(1 + \nu_u)} \left(\sigma_{kk} + \frac{3}{B}p \right) \quad (2.9)$$

where ν_u is Poisson's ratio measured under undrained conditions. ρ is density. m_0 and ρ_0 are the mass per unit volume and fluid density measured with respect to the same reference state as that used for the stress and strain tensors. For instance, without the pore pressure p , equation 2.8 degenerates to the classical elastic equation. Equations 2.8 and 2.9 state that the stress field and the pore pressure are coupled.

Pore pressure changes due to elastic compression - Undrained response

Under undrained conditions, the rock mass is subject to a change in confining pressure and pore fluid is prevented from escaping or entering. The undrained response refers to the increase in pore pressure Δp_u in the rock mass driven by the confining pressure. In reality, the stress change $\Delta\sigma_{ij}$ occurs over a time scale too short to allow the loss or gain of pore fluid in a element by diffusive transport to or from neighbouring elements, i.e., $\Delta m = 0$. Leading to:

$$\Delta p_u = B \frac{\sigma_{kk}}{3} \quad (2.10)$$

where B is Skempton's coefficient (Rice and Cleary, 1976), $0 \leq B \leq 1$, and σ_{kk} is the mean stress. Skempton's coefficient measures how the pore pressure increases when a confining stress is applied under undrained conditions. In the context of RIS, there will be an instantaneous increase in the pore pressure in the substratum due to the additional loading at the surface. So, with the increase in pore pressure due to the undrained response, ΔS decreases and failure may occur. If this mechanism is dominant, one should not observe much delay between the peak water level and the maximum seismic activity. However, like the elastic response, this only explains any initial seismicity associated with impoundment.

Pore pressure changes due to diffusion - Drained response

Here, the term drained response refers to conditions in which the fluid has time to move through the rockmass. The change in pore pressure Δp_d is governed by the diffusion equation:

$$D\nabla^2 p_d = \frac{\partial p_d}{\partial t} \quad (2.11)$$

where D is called the hydraulic diffusivity.

In this type of response, the pressure increase at depth on the fault following impoundment is delayed; the time lag depending upon the value of D and the distance. If a pressure $p(z = 0, t = 0)$ is imposed

at the surface and retained for $t > 0$ and D is a constant, equation 2.11 has the solution:

$$\frac{p_d(z, t)}{p(0, 0)} = 1 - \operatorname{erf} \frac{z}{2\sqrt{Dt}} \quad (2.12)$$

From equation 2.12, a set of curves may be plotted. Figure 2.8a shows the values that equation 2.12 assumes when $D = 10^6 \text{ m}^2 \text{ day}^{-1}$ and the distance z is set to vary from 2.0 km to 5.0 km. The pressure front arrives first at the shallower depths. So, in the context of RIS, one would expect triggered seismicity to start at shallow depths and then migrate to deeper parts of the subsurface. Figure 2.8b illustrates the effect of D on the solution given by equation 2.12. As D decreases, the time taken for the pressure front to reach the same depth increases (here the depth was 2.0 km). As D increases, the time lag between the initial pressure perturbation and the pressure at a certain depth decreases.

Talwani (1976) used this concept of pressure diffusion to account for the observed time lag between lake level rise and the onset of seismicity in the Clark Hill reservoir, South Carolina, USA. More recently, Rajendran and Talwani (1992), using data from Lake Jocassee and Monticello reservoirs in South Carolina, USA and comparing their data with worldwide data, also suggested that pore pressure diffusion was the dominant mechanism for stress perturbation at hypocentral depths. Their argument for the preference of this mechanism is based on the growth of the epicentral area with time. They assumed that the increase in epicentral area is directly caused by diffusion of pressure to hypocentral depths, then a 'seismic' hydraulic diffusivity was estimated from the epicentral growth rate.

In Rajendran and Talwani (1992), the effect on the pore pressure at depths caused by seasonal lake-level variations in artificial lake may be mimicked by another solution of equation 2.11. If the pressure on the surface is given by a harmonic function:

$$p(0, t) = p_0 \cos \omega t \quad (2.13)$$

where $\omega = 2\pi(\text{year})^{-1}$ is the characteristic frequency of a lake level fluctuation, for instance, and p_0 is the amplitude of the lake-level increase. The solution of 2.11 subjected to 2.13 is:

$$p_d(z, t) = p_0 e^{-\sqrt{\frac{\omega}{2D}}z} \cos\left(\sqrt{\frac{\omega}{2D}}z - \omega t\right) \quad (2.14)$$

Some interesting aspects of solution 2.14 are highlighted:

- The amplitude of the pore pressure decays with increasing depth.
- There is a time lag δ between the input pore pressure at the surface and the response at depths given by:

$$\delta = \sqrt{\frac{1}{2\omega D}}z \quad (2.15)$$

- Equation 2.15 shows that the extent of the pore pressure perturbation at depth depends on the oscillation period of the input at the surface. The higher the frequency oscillation of this input, the smaller is the extent of this perturbation at increasing depths. This skin depth effect is given

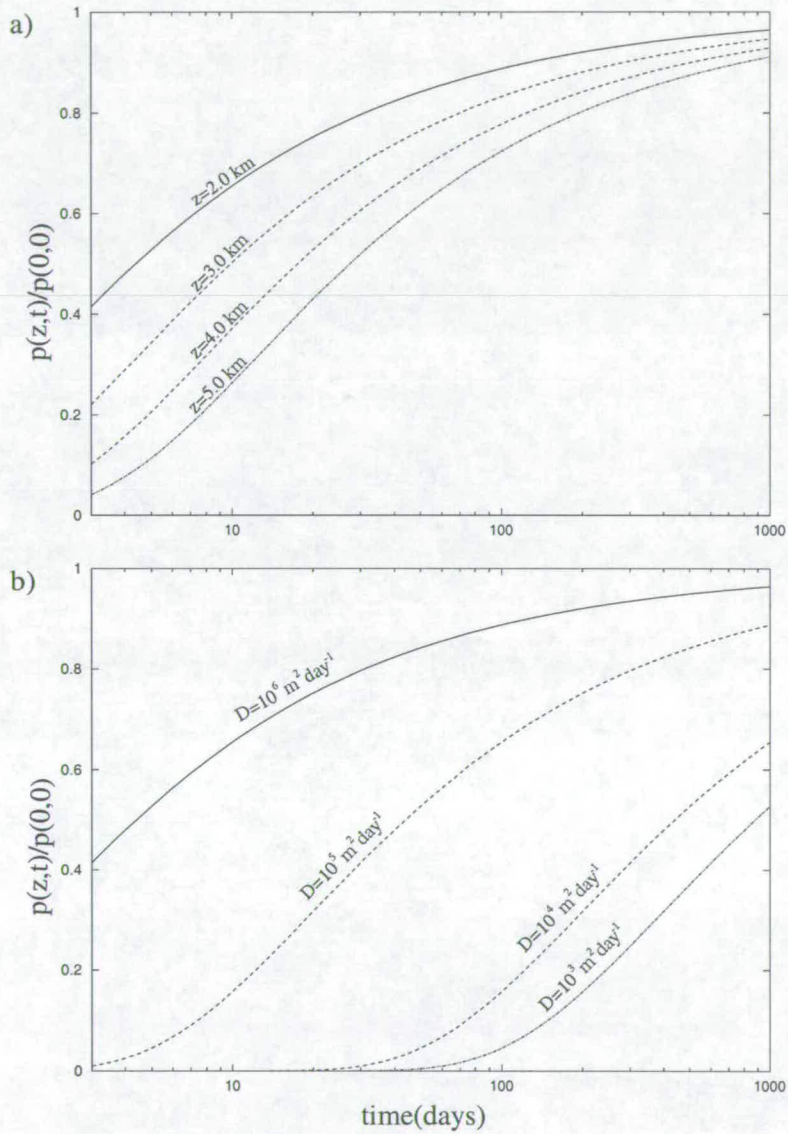


Figure 2.8: a shows the values of equation 2.12 for different values of z and t and $D = 10^6 \text{ m}^2 \text{ day}^{-1}$. b shows the values of equation 2.12 for different values of D and t and $z = 2.0 \text{ km}$.

by the equation:

$$\frac{p_d(z, t)}{p_0} = e^{-\sqrt{\frac{\omega}{2D}}z} \quad (2.16)$$

Talwani (1997), analysing cases of RIS in the USA (Monticello Reservoir), identified the role played by the undrained and drained responses in RIS. According to Talwani (1997), the initial seismicity is due to the increase in pore pressure due to the undrained response. This occurs because of an instantaneous increase in pore pressure in closed pores (e.g. fault gouge/clay) causing seismicity shortly after the impoundment began. As time passes, the change in pore pressure caused by this undrained response diffuses away and little seismicity is observed. The second phase of seismicity is caused by the later arrival of the diffusive pore pressure front.

2.3 RIS modelling approaches

In this section previous RIS modelling studies are reviewed. The purpose of this is to highlight the achievements and limitations of previous approaches to the understanding of RIS. For reasons of clarity, the order of discussions of the RIS models will be, when possible, chronological.

Fluid pressure increase as a mechanism for the triggering of seismic events was first identified by Healy *et al.* (1968) from earthquake activity that followed injection of waste fluid into a deep well. According to Healy *et al.* (1968), the increase in fluid pressure reduced the effective normal stress along the fault planes, as explained by Hubbert and Rubey (1959). This reduction on the effective normal stress led to failure. The role of pressure increase in triggering seismic activity was also later recognised by other authors (Nur and Booker, 1972; Ohtake, 1974; Raleigh *et al.*, 1976). The recognition of the importance of fluid pressures in triggering earthquakes and also the theoretical tools developed by Rice and Cleary (1976) have led to numerical simulations of reservoir-induced seismic activity. These theories relate the stress field to the pore pressure in a saturated porous elastic media. This is an idealised representation of water-permeated rocks under a reservoir. Bell and Nur (1978) and Roeloffs (1988), used the following formulation of Rice and Cleary (1976) for numerical simulations related to induced seismic activity in artificial lakes.

Roeloffs (1988) identified and separated the poroelastic approximations into three types: **coupled**, (the elastic stresses influence pore pressure and vice-versa); **uncoupled**, in which the elastic stresses and pore pressure are independent; **decoupled**, the elastic stresses influence pore pressure but not vice-versa. She concluded that 2D uncoupled and coupled steady-state pore pressure solutions were close for a large range of (but not for all) medium properties. In addition, decoupled and coupled pressure solutions were quite close for all medium properties.

Many authors (Bell and Nur, 1978; Roeloffs, 1988; Simpson and Narasimhan, 1992; Lee and Wolf, 1998; Kalpna, 2000) have proposed different models to explain the cause of initial and ongoing seismicity in different sites of RIS. These model approaches consist of using the Rice and Cleary (1976) formulation, or its simplifications with different media properties (Table 2.1). Most models (Bell and Nur, 1978; Roeloffs, 1988; Simpson and Narasimhan, 1992; Lee and Wolf, 1998) use the formulation

of Rice and Cleary (1976) (or its particular cases) in 2D media. Kalpna (2000) is the only author that applies the Rice and Cleary (1976) formulation in its decoupled formulation in a 3D idealised medium.

Model	response investigated	media properties	geometry
Bell and Nur (1978)	decoupled	homogeneous rock matrix, homogeneous fault	2D
Roeloffs (1988)	coupled, uncoupled and decoupled	homogeneous rock matrix	2D
Kalpna (2000)	decoupled	homogeneous rock matrix	3D
Simpson and Narasimhan (1992)	coupled	homogeneous rock matrix, homogeneous fault	2D
Lee and Wolf (1998)	uncoupled	heterogeneous rock matrix, homogeneous fault	2D

Table 2.1: RIS models and their main features.

Table 2.1 summarises the main features of the RIS models discussed in this section. Faults incorporated in these models have uniform hydraulic properties and are 1D features imbedded in 2D half spaces. So far, no investigation of RIS using a more realistic representation of the permeability structure of faults has been made.

Bell and Nur (1978) found that the elastic effect of water load alone is an unlikely mechanism for explaining the RIS in Lake Oroville, California. On the other hand, using 2D modelling where the elastic stress influences pore pressure, but not vice-versa (decoupled approximation) as more successful. Bell and Nur (1978) concluded that models including the pore pressure effects play an important role in the triggering of seismicity under artificial lakes.

Roeloffs (1988) addressed the problem of induced seismicity by analysing the fault stability due to cyclic changes in reservoir water level in 2D models. Roeloffs (1988) also modified the diffusion equation (equation 2.11) to include the pore pressure increase in the subsurface caused by the undrained response. She used a unit step increase in pore pressure at surface, $p(0, t) = H(t)$, to calculate the pore pressure $p(z, t)$, at a depth z and after a time t . For the unidimensional case, she found:

$$p(z, t) = (1 - \alpha) \operatorname{erfc} \frac{z}{2\sqrt{Dt}} + \alpha H(t) \quad (2.17)$$

$H(t)$ is the Heaviside unit step function and $\alpha = B \frac{1+\nu_u}{3(1-\nu)}$.

Thus the coupled response may be dominated by the undrained response immediately on impoundment and be primarily due to diffusion later.

More recently, Kalpna (2000) developed an algorithm for simulation of stresses and pore pressure using a Green's function method. This method differs from both the Bell and Nur (1978) and the Roeloffs (1988) methods for solving the decoupled case. His major achievement was to find the

solution of equations 2.8 and 2.9 for the decoupled case. In his computations, the actual lake level changes of the reservoir load are used. However, his model does not take into account local geological heterogeneities, such as fractures, that may be present in the subsurface.

✦ Some RIS modelling studies have taken limited account of inhomogeneities in rock properties. Simpson and Narasimhan (1992) coupled elastic deformation and time-dependent fluid flow to model the influence of surface loading on the pore pressure response in a homogeneous rock matrix in which a homogeneous fault is present. With this 2D model, they were able to explain qualitatively both the occurrence of RIS after a relatively short time following reservoir filling and the occurrence after a noticeable elapse of time following the reservoir filling. According to them, the combination of undrained loading and local diffusion near the fault produces a transient increase in pore pressure after the increase in reservoir load. The short time seismic activity after reservoir loading is explained as follows: if the decay of this transient increase is quick compared to the rate of loading, large increases in pore pressure are prevented. If the rate of loading is rapid compared to the transient decay, increases in pore pressure will occur and failure will take place. When the short term effect has almost vanished, the diffusion becomes the dominant effect.

Lee and Wolf (1998) present 2D numerical results of pore pressure diffusion only - the drained response. In their analysis, the pore pressure diffusion in a heterogeneous 2D matrix and also in a homogeneous matrix with a homogeneous fault were investigated. They used these models to analyse the periodic seismicity observed in southeastern Alaska. They show that geologic heterogeneity can strongly influence the extent to which the hydraulic disturbance can be transmitted through the earth's crust. They also conclude that if a high degree of vertical interconnectivity exists, the hypocentral depths of the events in that area can be of the order of several kilometres.

Despite the recognition that fractures play an important role in RIS, the models of Simpson and Narasimhan (1992) and Lee and Wolf (1998) are still simplistic 2D models. They lack *in situ* physical values such as the depth of the water table, which leads to unrealistic boundary conditions for their models. Also, they do not consider in their analysis the magnitude of pressure change that may be required to initiate failure in a pre-stressed crust. So, a quantitative assessment of the magnitude of pressure change required to trigger seismicity is not yet possible.

The work of this thesis is to build an RIS model incorporating *in situ* physical values such as the depth of the water table and the rock hydraulic properties to identify the mechanisms involved in the triggering of earthquakes beneath the Açu area.

3 DATA ANALYSIS OF THE PDAS NETWORK IN AÇU

This chapter deals with the description of the seismic network used to locate the seismic events in the Açu area. Here, the digital signal processing of the data, hypocentral location, focal mechanisms and seismic anisotropy studies are presented. In reality this chapter can be seen as a separate entity of this thesis. Nevertheless, the work carried out with these earthquake data adds important aspects to the discussion on the nature of both the seismicity and the seismic anisotropy in the region.

3.1 Description of the network

From August 1994 until July 1997, a network of 8 three-components digital seismographs operated in the Açu area. This seismograph network continuously monitored events that occurred in the dam region. The total number of events that it was possible to locate (i.e. events recorded at three stations or more) was 286. The total number of events recorded by this network was 376. The remaining 90 events refer to teleseismic events, events from another regions in northeastern Brazil, or local events recorded in only one or two stations. Each seismograph station was composed of three S-13 seismometers and a PDAS-100 recorder from Teledyne Geotech. The natural frequency of the seismometers is 1 Hz and their sensitivity is $629 \text{ V m}^{-1} \text{ s}^{-1}$. The PDAS recorder digitises the signal at 16 bit, allowing up to 96 dB of dynamic range. During the years this network was installed, the location of the seismic stations changed five times. The reason for these changes was to improve hypocentral locations, improve the coverage of the focal sphere, and to have stations within the shear-wave window. Figures B.1, B.2, B.3, B.4 and B.5 (located in Appendix B) show these different configurations. The deployment period of each network configuration is displayed in Table B.1. Figure 3.1 shows one of the network configurations. This configuration was deployed from 20/10/1995 to 17/10/1996. The triangles represent the location of the stations around the lake and the circles are the events that were detected using this configuration. The two letters below each triangle represent the station codes. This figure shows a detail of the Açu reservoir shown in Figure 1.1.

3.2 Working with digital data

As mentioned in the previous section, the data were acquired in digital format. The digital format is easy to work with producing good quality data - for instance, spurious effects can be filtered out, - and it allows data manipulation not available with analogue format (smoked drum records, for example), such as rotation of components, power spectra analysis and accurate phase picking. Nevertheless, it must be borne in mind that when the signal is being digitised, one is modelling in a discrete form a continuous process. The decimation of this continuous process can be seen as the modulation of a sequence of

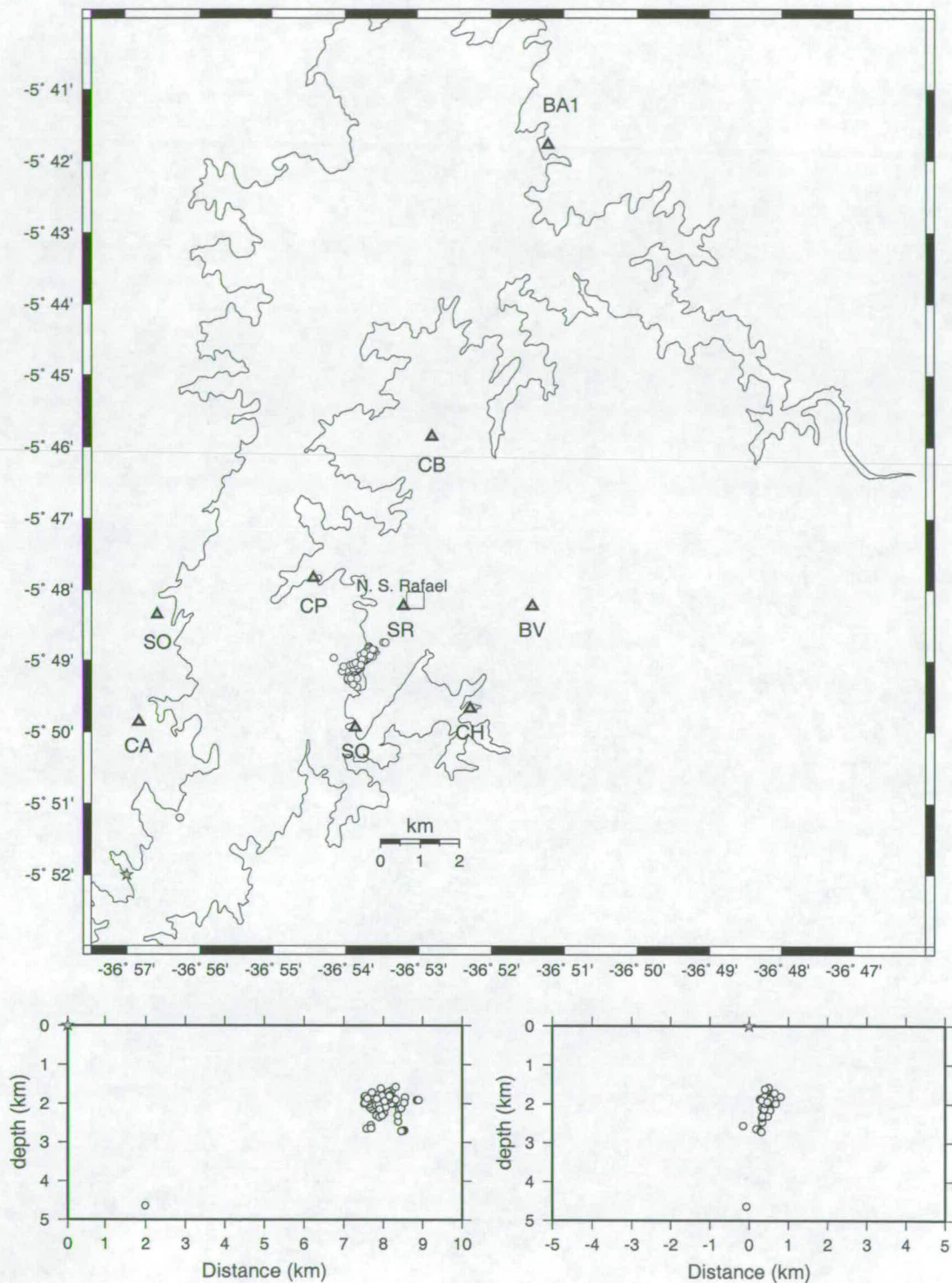


Figure 3.1: Network configuration C. Deployed from 20/10/1995 to 17/01/1996. The triangles represent the location of the stations around the lake and the circles are the events that were detected using this configuration. The two letters below each triangle represent the station codes.

delta functions which are separated by a time interval \mathcal{T} and f_{dec} is the sampling/decimation frequency. The data employed in this research were decimated at 200 samples per second, and later (January 1996 until August 1997) at 500 samples per second. According to the sampling theorem ((Scherbaum, 1996)), for a signal to be uniquely represented by a sampling rate of f_{dec} it shall not contain any energy greater than or equal to $f_{dec}/2$, where $f_{dec}/2$ is called the Nyquist frequency. If the original signal contains energy in the frequency range greater than or equal to $f_{dec}/2$, these frequencies will produce an aliasing effect. In our recording system (PDAS-100), the sampling frequency is 1000 samples per second, but due to storage limits in the field, it was decided that this signal should be decimated and recorded at 200 samples per second. For that, the reason PDAS-100 uses a built-in anti-alias filter. An example of such a record is shown in Figure 3.2a. The presence of some spurious precursors to the P-wave arrival can be clearly noticed. In order to remove this spurious precursors, the effect of the built in anti-alias filter from the PDAS-100 for the 200 samples per second sampling frequency is calculated - the Finite Impulse Response (FIR). Then, the FIR is convolved with the signal to be processed to achieve the corrected signal. Figure 3.2b shows an example of a seismogram after this processing. As mentioned before, from January 1996 the sampling rate used was 500 samples per second. With this sampling rate the spurious effects of the built-in anti-alias filter do not appear. Figure 3.3 shows a seismogram recorded at 500 samples per second. The precursors are no longer present in this record and no further processing was necessary.

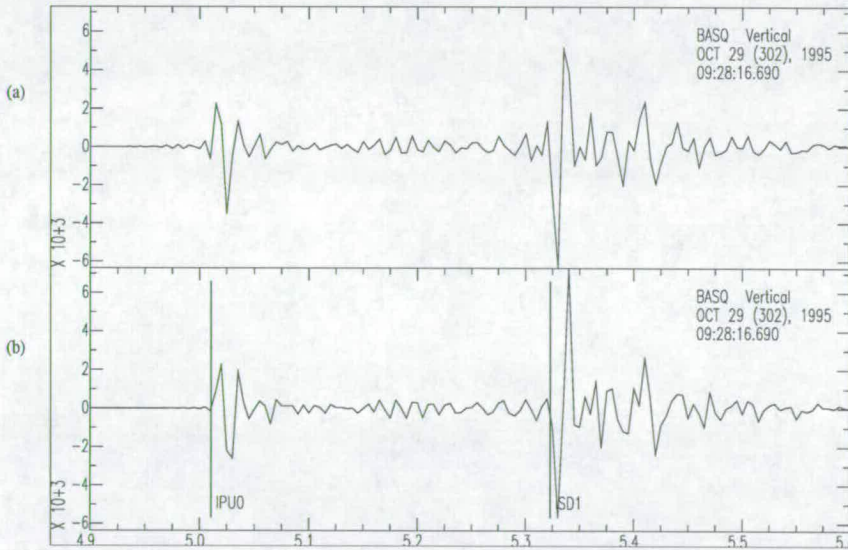


Figure 3.2: (a) Example of a seismogram recorded at 200 samples per second. Note that due to the built-in anti-alias filter of the recording equipment, there are some precursors to the P-wave arrival. (b) Seismogram after removing the precursors to the P-wave.

3.3 Phase picking

After correcting the data for this acausal effect, the Seismic Analysis Code (SAC) (Tapley and Tull, 1991) was used to pick the P and S wave arrivals. In general, the error in the P-wave arrival was ± 0.01 s. For S-waves the error was ± 0.02 since the arrival of these latter waves are preceded by P-wave

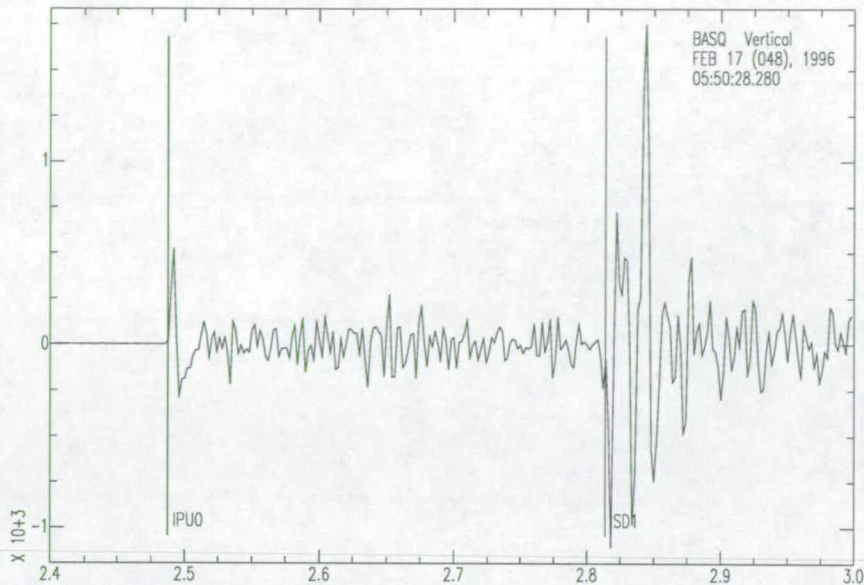


Figure 3.3: Example of a seismogram recorded at 500 samples per seconds. Note that in this case the P-wave arrival is not disturbed by the acausal precursors. No correction was applied to such records.

coda, which could lead to misidentification. SAC allows the phase picking to be output in the format used by the hypocentral location code HYPO71 by Lee and Lahr (1975). For that, each picked arrival time had a quality factor assigned to it ranging from 0 (excellent) to 4 (very poor) as suggested by Lee and Lahr (1975). It was decided to give quality 0 (full weight) for estimated reading errors ≤ 0.01 s and quality 1 (weight=0.75) for estimated reading errors between 0.01 s and 0.02 s. For reading errors estimated between 0.02 s and 0.04 s, a quality factor 3 was given (weight=0.25). Quality factors of 4 (weight=0) were given for readings with estimated reading errors greater than 0.04 s. For most events, the assigned quality value for P-waves was 0 and for S-waves was 1.

3.4 Event location

After picking all the P and S phases from the 286 local events, they were located using HYPO71. The location list of these events is found in Appendix C. The velocity model used in this work was the same as that used by do Nascimento (1997), which assumes an isotropic, homogeneous, infinite half-space. The choice of this quite simple velocity model was made because the study region lies on a Pre-Cambrian crystalline basement. Rocks of this type exhibit high consolidation, high rigidity and very low attenuation. These properties are demonstrated by the seismograms recorded. Most of them show very simple waveform and an impulsive arrival.

do Nascimento (1997) presented this half-space model with $V_P=6.00$ km/s and $V_S=3.51$ km/s. He chose 58 events that were recorded in at least five stations with absolute timing for the P and S waves arrival and calculated the values of V_P/V_S via the Wadati diagram. In this diagram, the temporal separation of the P and S waves ($t_S - t_P$) is plotted against the time of the P-arrival minus the time of origin ($t_P - t_O$). The angular coefficient of this plot is the $V_P/V_S - 1$ (Kisslinger and Engdahl, 1973). In his study, do Nascimento (1997) found V_P/V_S to be equal to 1.71, as shown in Figure 3.4.

These 58 events had their hypocentres located by HYPO71 (Lee and Lahr, 1975) using different values of V_P/V_S and V_P . The model that produced the smallest values of rms error in the epicentral location and error in the depth estimate was the one in which $V_P/V_S = 1.71$ and $V_P = 6.00 \text{ km/s}$. The choice of $V_P/V_S = 1.71$ is the same as the one suggested by the Wadati diagram (Figure 3.4). These

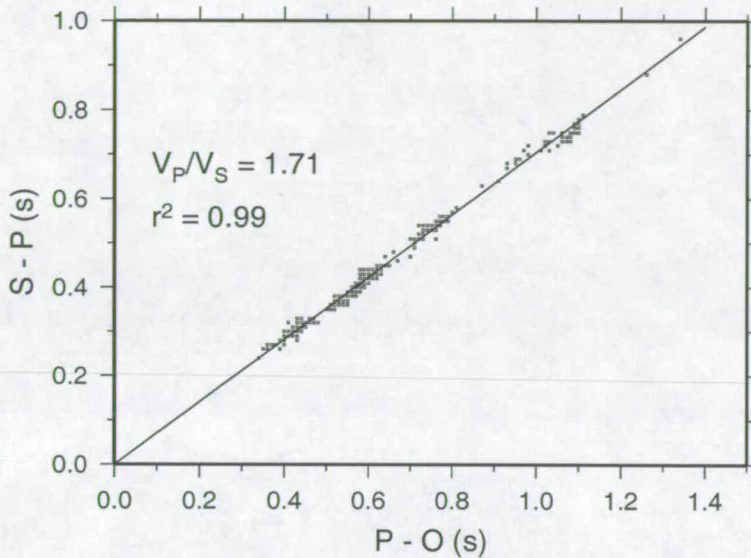


Figure 3.4: The angular coefficient of the points is 0.71, which corresponds to $V_P/V_S = 1.71$. After do Nascimento (1997).

values for V_P and V_S are the same as those found by Ferreira *et al.* (1995) for the Açú area. Such values of V_P and V_P/V_S are consistent with laboratory measurements compiled by Schön (1996) for the types of rocks in the area, i.e. the different rock types on Figure 3.11 have similar velocities. The homogeneity of the elastic properties in the subsurface of the Açú reservoir is attested by the straight slope of the Wadati diagram in Figure 3.4

The location of the 247 events in which the errors in both the vertical and horizontal dimensions are $\leq 0.3 \text{ km}$ are shown in Figure 3.5. The hypocentral locations shown in Figure 3.5 indicate three separated clusters of events. The actual existence of three spatially separated clusters is attested by the fact that the error locations are smaller than the actual separation of each of the clusters. Figure 3.6 shows the associated HYPO71 errors and location parameters. It can be seen from 3.6a, b, c that most of the events have vertical and horizontal errors $\leq 0.1 \text{ km}$ and a $rms \leq 0.02 \text{ s}$. The minimum number of readings (P and S) is 4 (Figure 3.6d), which indicates that the event was recorded in at least three stations. From Figure 3.6e we see that the maximum azimuthal gap between a located epicentre and any two stations is 180° or less for most events. Figure 3.6f shows that the majority of events have a hypocentral depth between 1.4 and 3 *km*.

3.5 Focal Mechanism

The focal mechanism of previous seismicity in this region has been analysed by Ferreira *et al.* (1995). They studied three clusters of induced seismicity events in 1989, 1990 and 1991. They found that the

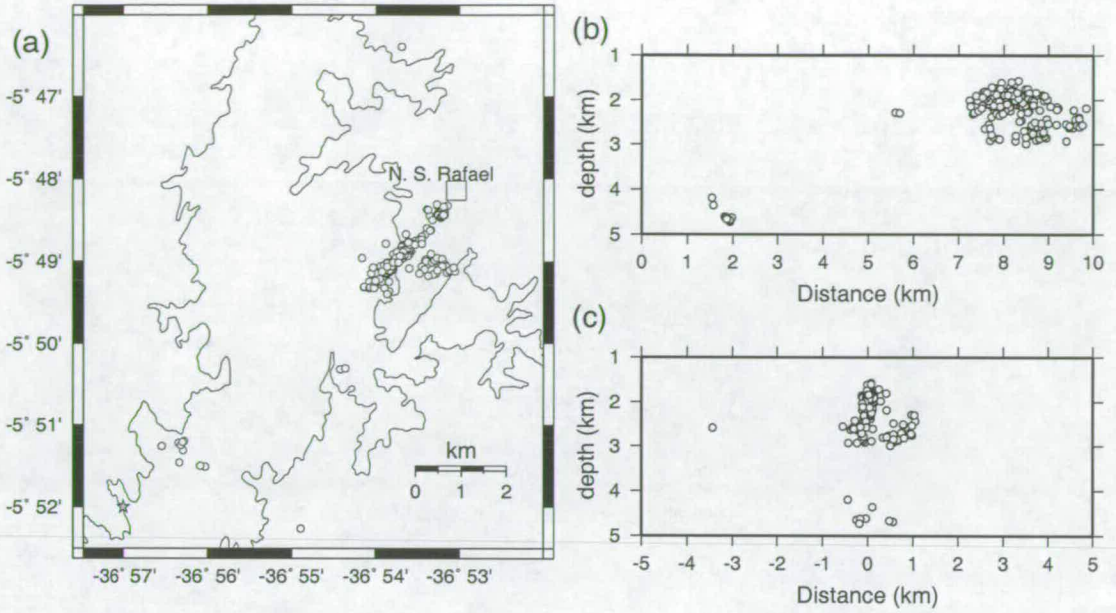


Figure 3.5: Hypocentral map showing the 247 events with at least 0.3km errors in both vertical and horizontal determination. **a** shows the epicentres plotted on the horizontal plane. **b** shows the projection of the hypocentres in a plane striking 47° from north. **c** is a projection of the same hypocentres in a plane perpendicular to the one shown in **b**. The starting point of both projections is indicated by the star in the left hand corner of Figure **a**.

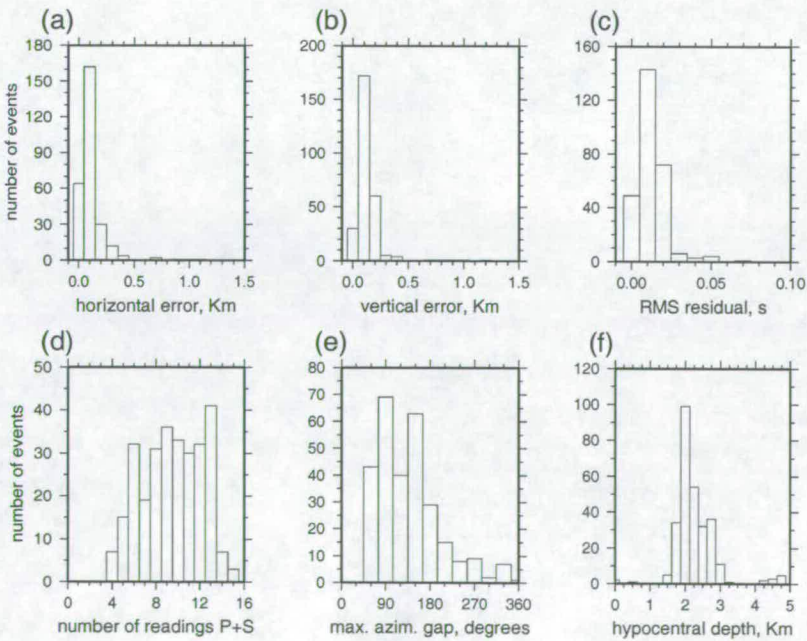


Figure 3.6: **a** to **f** shows hypocentre parameters from HYPO71 (Lee and Lahr, 1975) output.

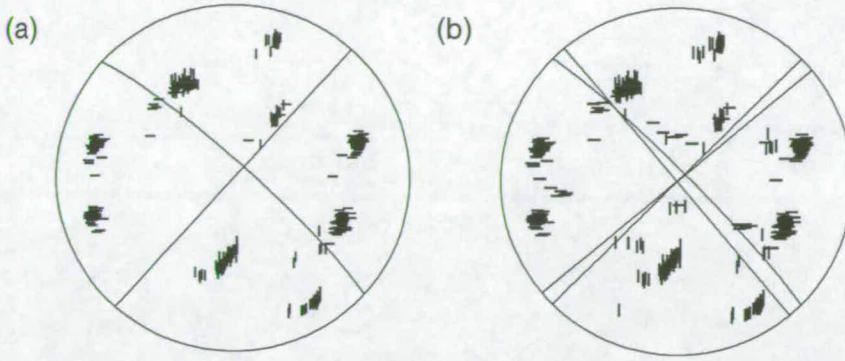


Figure 3.7: a Composite P-wave first-motion polarity data shown on equal-area plots of the lower focal hemisphere; compressional (positive) and dilatational (negative) first motions are indicated by vertical and horizontal bars respectively, to show conflicting polarities more clearly. b Composite focal mechanism from the events between 1994 and 1997. Most of the mismatches are near the nodal plane.

activity in the Açú reservoir occurs mainly by right-lateral strike-slip faulting in SW-NE oriented faults, with an E-W P axis and N-S T axis. Later, do Nascimento (1997) studied the induced seismicity at the Açú reservoir for the period 1994 and 1995. He concluded that this activity was also associated with a NE-SW oriented fault with P and T axes similar to those found by Ferreira *et al.* (1995). In both the above mentioned works, the authors used a code called FPFIT by Reasenberg and Oppenheimer (1985) to compute the composite focal mechanism of their selected events. This code finds a pair of planes that minimises the discrepancies between a set of generated double-couple models and the observed P-wave polarities in each of the stations. The method finds a “unique” solution to the focal plane, since solutions closer to the nodal planes have a smaller weight in the computation of the function to be minimised. In particular, the activity between 1994 and 1995 showed in Figure 3.7a indicates a nearly pure right-lateral strike-slip fault (do Nascimento, 1997).

In the present study, the 1996 and 1997 seismic activity data were included in the determination of the focal mechanism. The inclusion of these data is of paramount importance since at this time the network had a greater number of stations close to the epicentral area, to ensure that the focal mechanisms could be better constrained. To analyse these data, a different programme, called RAMP by Pearce (1977, 1980); Pearce and Rogers (1989) was used. This programme searches for double-couple point source mechanisms compatible with input P-wave polarities. The programme searches over a specified grid e.g 5° steps for the strike, dip and rake (the convention of Aki and Richards (1980)), which gives 93,312 possible solutions. In this method all the solutions fitted are considered equally compatible with the data. So, it is expected that the method will not provide a single best solution, but a set of compatible solutions. In order to have a good determination of the azimuth and incident angle on the focal sphere, events (regardless of the cluster they belong to) were selected that had at least 12 readings (P and S readings) and vertical and horizontal errors ≤ 0.1 km. The criteria used to select events for focal mechanism determination are very critical. An error in the depth determination of 0.2km in an event 2.0km deep can cause a 3° error in the incident angle. Moreover, an error of 0.2km in the horizontal determination of an event distant by 2.0km can lead to a 5° error in the azimuth determination. Figure 3.7b contains 23 polarity mismatches (the total number of polarities is 532). A visual comparison of Figures 3.7a and 3.7b demonstrates that this focal mechanism is very similar to that obtained by the

FPFIT method. The RAMP method found 6 solutions with only 23 mismatches (4.32% of the total number of polarities observed). These solution are shown in Table 3.1. The solutions calculated using

Strike (°) of fault plane	Dip (°) of fault plane	Slip (°) of fault plane
50	90	0
230(50)	90	0
45	90	5
140(50)	90	180
320(50)	90	180
135(45)	95	180

Table 3.1: Table showing the values of the strike, dip and slip of the fault plane (according to Aki and Richards (1980) conventions) with smallest mismatches. All solutions show a near-pure strike-slip fault.

both approaches give essentially the same focal mechanism during the three years (from 1994 until 1997) that the digital seismograph network operated in the area. These focal mechanism solutions also agree with research carried out by Ferreira *et al.* (1995) during 1989, 1990/91. In general, the solutions of focal mechanisms in this region and in other regions in northeast Brazil are consistent with compression stresses with an E-W orientation and extension with a N-S orientation (Assumpção, 1992; Ferreira *et al.*, 1998). According to these authors, the compressional stress is generated regionally and would be related to the ridge push of the mid-Atlantic ridge against the South-American continent. The regional extension could be due to two reasons: lateral density variations along the continental northeastern shore and sediment load in the continental shelf (Assumpção, 1992; Ferreira *et al.*, 1998).

3.6 Anisotropy

3.6.1 Definition and causes

Seismic anisotropy is the variation in the seismic wave velocity dependent on its propagation direction. On entering an anisotropic rockmass, the S-wave will split into two *quasi*S-waves, with different polarisations and velocities that are fixed for a particular propagation direction. This phenomenon is known as *shear-wave splitting* and is analogous to optical birefringence.

With the advent of digital recording of seismic events, seismic anisotropy has been widely observed (Crampin and Lovell (1991)). The cause of this anisotropy is the subject of much scientific investigation. Current theories are: direct stress-induced anisotropy, minerals alignment, lithologic anisotropy, thin-layer anisotropy and Extensive Dilatancy Anisotropy - EDA (Crampin, 1978, 1981; Crampin *et al.*, 1984a). This last cause of anisotropy is of particular interest to seismologists because it suggests that cracks, fractures and pore spaces will preferentially align with the current stress field. The distribution of such aligned cracks and fractures will produce a hexagonal symmetry with a horizontal symmetry axis. Therefore, if the anisotropy measured is caused by EDA, it provides a method to investigate the current stress field. The two most used parameters for investigating shear-wave splitting in earthquake data are: (1) the polarisation of the first S-wave, and (2) the time delay between the split

S-waves. In terms of travel times, the percentage anisotropy (A), is defined as:

$$A = \frac{t_{slow} - t_{fast}}{t_{fast}} \times 100 \quad (3.1)$$

where $t_{slow} - t_{fast}$ is the maximum difference in arrival times of the two *quasi*S-waves.

Whilst real earthquake data do provide sources of shear-waves, they have some potential drawbacks which, as reviewed by (Rowlands, 1995) are:

- the earthquake hypocentre is unknown or imprecise;
- surface records may suffer distortions due to conversions near the recording station;
- most earthquakes occur in areas where the local geology scatters the direct arrivals;
- a good range of azimuths, incident angles and path lengths is required to determine fully the degree and extent of anisotropy.

Nevertheless, shear-wave splitting has been analysed in many tectonic regions over the past two decades (Crampin and Lovell (1991)), although the combination of issues itemised above has made it difficult to deduce the cause unambiguously (Rowlands (1995)).

3.6.2 Seismic anisotropy from the Açu data set

The Açu data set provides an unique opportunity to investigate S-wave anisotropy in an intraplate area. The low-attenuation and the near uniform velocity field in such Pre-Cambrian shield provides high signal-to-noise ratio and very good S-wave observations. With such a high quality dataset, is possible to eliminate the first three drawbacks itemised in section 3.6.1. In order to carry out the analysis of S-wave splitting the Açu data, events were selected according to the following criteria:

- recorded seismograms had incident angles $\leq 45^\circ$;
- the observed splitting was ≥ 2 samples.

It is widely known that shear-waves can suffer from interference and conversions at the free surface, especially beyond the critical angle, $i_c = \sin^{-1}(V_S/V_P)$ (Nuttli, 1961; Evans, 1984). Such conversions may lead to a misinterpretation of an S to P conversion as being the first pair of split shear-waves (Evans, 1984). In this dataset, it was decided to include observations with an incident angle of $\leq 45^\circ$ as predicted using the above half-space model. This forms the basis of identifying the waveforms from each seismogram that are emerging at an angle subcritical to reflected P. This results in the emergent angle being somewhat less than that predicted by the half-space model, due to a velocity gradient near the surface.

For the shear-wave splitting analysis, visual inspection was chosen to be the best method for identification of the splitting. To do this, the original seismograms were rotated to an angle at which the faster

shear-wave split had a clear arrival. Using this method it was possible to identify 39 seismograms from six different stations with very clear splitting. Figure 3.8 shows two typical examples of shear-wave recorded in the dataset.

For clarity reasons, the ‘BA’ was omitted from the name of the stations when plotted on the maps. Therefore, stations SQ, CP etc on Figures 3.1 and B.1-B.5 are in fact BASQ, BACP etc. All the splitting for the Açu dataset are given in Appendix A. A summary of these results is given in Table 3.2. For stations with more than five polarisation measurements (namely BASQ and BACP) the mean polarisation and standard deviation are also given in this Table. For stations BASQ and BACP, I have plotted the orientations as rose diagram: Figures 3.9a and 3.10a. Figures 3.9b and 3.10b show the polarisation angles versus the emergent angle. Figures 3.9c and 3.10c show the polarisation diagram versus the back azimuth angle. It should be noted that the stations individually do not cover the entire range of back azimuth and emergence angle. This is mainly due to the fact that many localities were inaccessible, or the site did not provide good outcrops to install the seismic stations. It also turned out that station BAPO (Figure B.4), for instance, was almost directly above the seismic activity, but most of its records showed an non-linear ringing on the recorded horizontal components. Nevertheless, polarisation from different stations shows a consistent orientation of around 45° . Since the magnitude of the time delay depends upon the length of the propagation path in the anisotropic medium, the measured delay time delay between the two split shear waves has been normalised to a path length of 1 km in Table 3.2. The values of normalised delay time, show variations between 1.1 ms/km (BARV) and 28.6 ms/km (BASR), which correspond to percentage anisotropies, as calculated by equation 3.1, ranging from 0.3 and 8.9%. For stations BASQ and BACP, the maximum percentage anisotropies were 5% for both these stations. The interpretation of both the polarisations and normalised delay measurements are considered in the next section.

Here, it is convenient to discuss the effect of anisotropy on the earthquake location. The typical observed time delay between the two split shear waves is of 0.01 s (see Table A.1), which is smaller than the error I assumed when picking the arrival of the S-wave (see Section 3.3). Therefore, I conclude that for the hypocentral location resolution I have, the anisotropy is unlikely to affect my hypocentral locations.

Station	Mean Pol. ($^\circ$)	pol. std. ($^\circ$)	Mean normalised delay time (ms/km)	normalised delay time std. (ms/km)	N
BASQ	53	38	7.3	2.3	20
BACP	37	9	9.3	3.7	11
BASR	(145, 155, 30,40)	-	(9.4, 13.6, 20.0, 28.6)	-	4
BARV	(35, 30, 46)	-	(1.1, 6.0, 3.0)	-	3
BAPO	(45)	-	(2.1)	-	1
BACA	(45)	-	(9.3)	-	1

Table 3.2: Statistical calculations are based on a spherical distribution. Hyphens indicate that the standard deviation was not calculated, since there were less than 5 polarisation/time delay measurements available. The measured delay time delay between the two split shear waves has been normalised to a path length of 1 km. N denotes the number of measurements available. Bracketed values are individual values as opposed to the calculated mean polarisation.

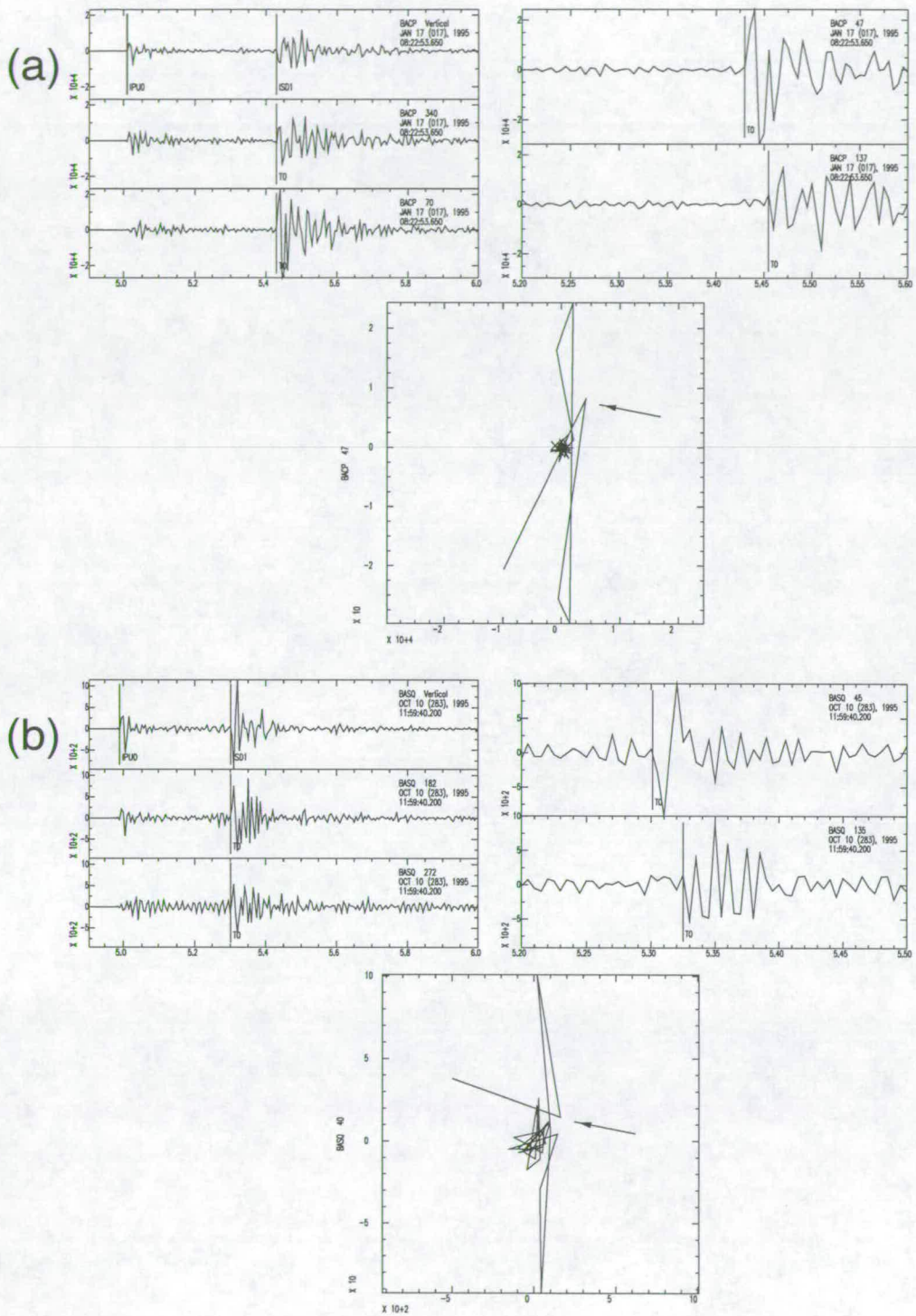


Figure 3.8: The seismogram on the left side shows, from top to bottom, the vertical, radial and transversal components. The seismogram on the right shows in more detail the arrival of the faster and the slower shear-wave, which are marked on the seismogram by **T0**. The polarisation diagram below shows the arrival of the slower shear-wave clearly indicated by a abrupt change in direction indicated by the arrow.

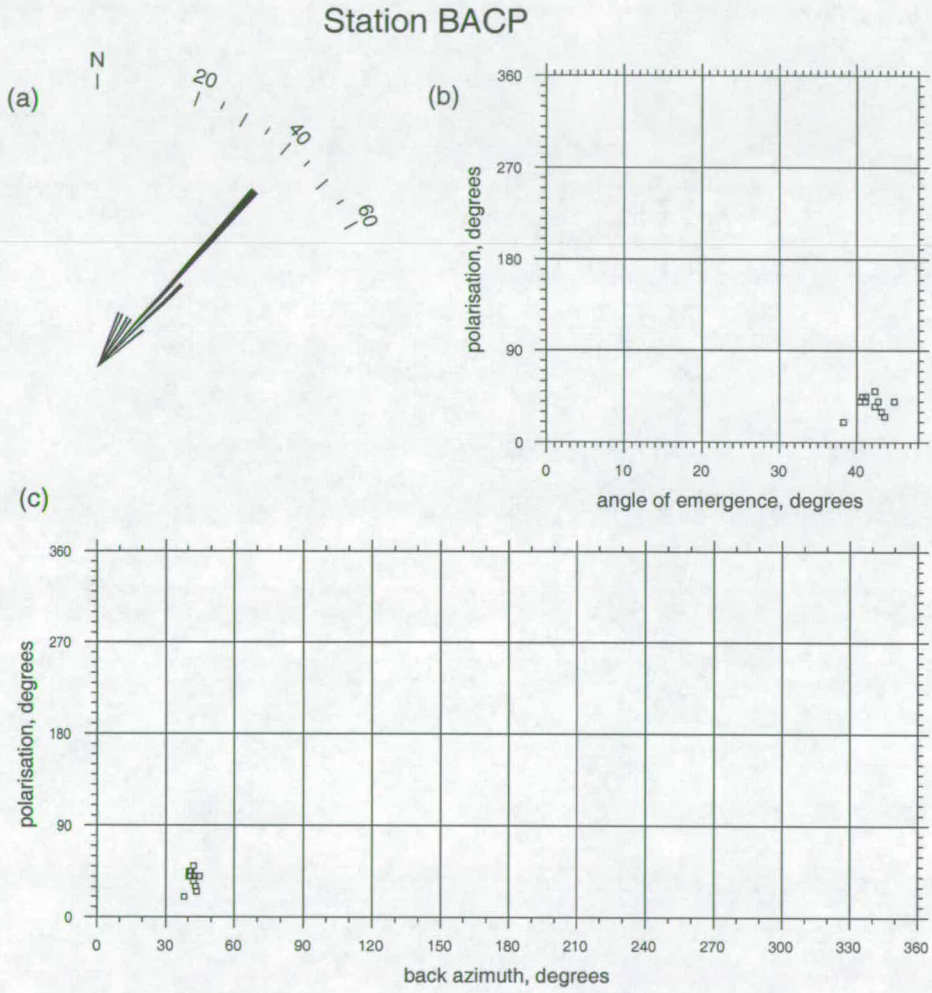


Figure 3.9: **a** Rosette digram showing the distribution of the polarisation direction for station BACP, demonstrating consistent polarisation of the fast shear-wave splitting. **b** and **c** show these measurements plotted against angle of emergence and back azimuth respectively.

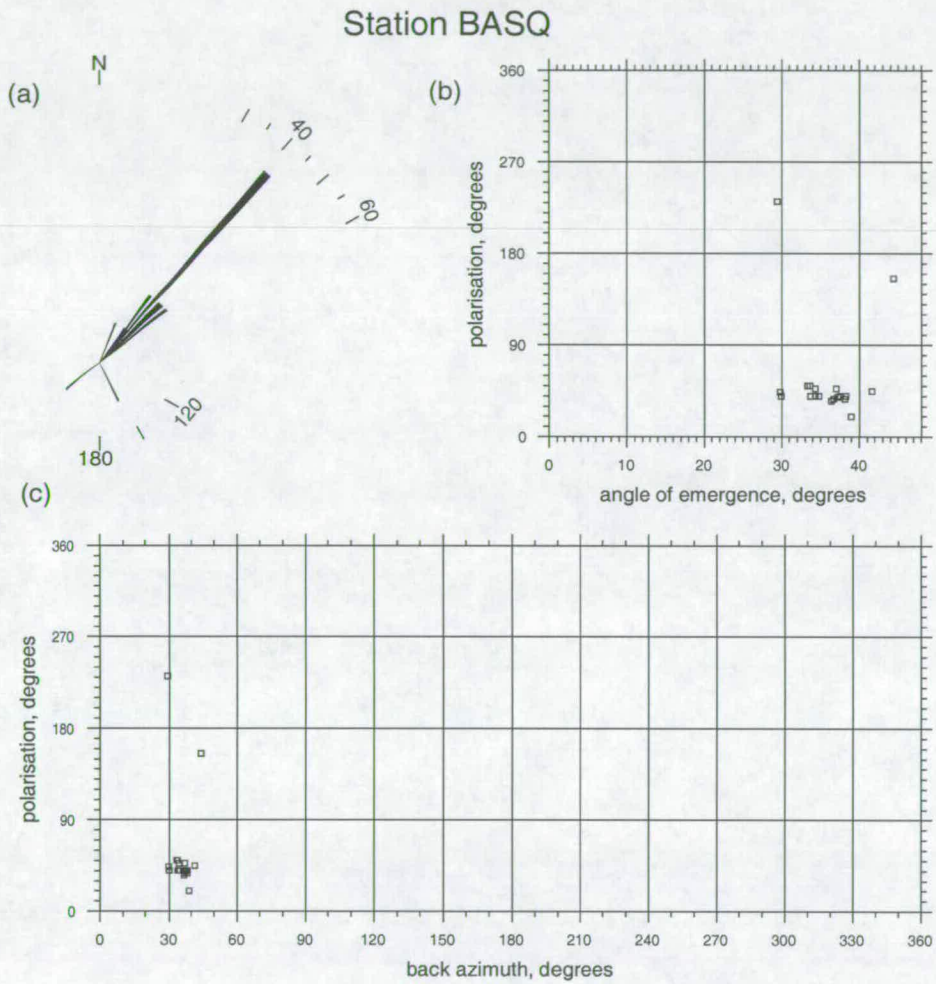


Figure 3.10: Same as Figure 3.9, for station BASQ. This station shows one polarisation direction of the faster shear-wave polarisation which is nearly perpendicular to the main alignment given by the other measurements.

3.6.3 Interpretation of the shear-wave observations

Clear shear-wave splitting is observed in this dataset. Figure 3.11 shows the orientations of the splitting measurements made by stations BASQ, BACP, BASR, BARV, BAPO and BACA. The polarisation direction of the first split shear-wave is consistent for a number of the seismic stations that are located at different azimuths and incident angles (BAPO, BARV, BACA and BASR). This shear-wave splitting is indicative of anisotropy along the ray path, and the consistent polarisation alignments are characteristic of hexagonal symmetry with a horizontal symmetry axis (Shearer, 1999). Such anisotropy has been widely attributed to the presence of stress aligned fluid-filled cracks (Extensive Dilatancy Anisotropy or EDA) on the earth's crust (Crampin, 1987; Crampin and Lovell, 1991; Vavryčuk, 1993; Cassidy and Bostock, 1996). However, in this region, there is convincing evidence that the stress field is dominated by east-west compression (Ferreira *et al.*, 1995; Assumpção, 1992; Ferreira, 1997; do Nascimento, 1997). Based upon this east-west stress orientation, we would expect EDA cracks to result in fast shear-waves polarised close to east-west. This is in maximum conflict with the overwhelming majority of orientations observed (Figures 3.9 and 3.10). Apart from a single orientation measurements at BASQ and two measurements at BASR, that show a preferred orientation in the NW-SE direction, all the remaining 36 orientations show a preferred orientation in the SW-NE direction.

In fact, the dataset suggests that for most of the measurements the shear-wave splitting is controlled by the Precambrian foliation present in the area. The majority of the S-wave splitting follows the orientation of the Precambrian basement foliation as shown in Figure 3.11 (DNPM *et al.*, 1998). This result confirms several other observations of shear-wave splitting from other authors (Gledhill, 1991; Brocher and Christensen, 1990; Zhang and Schwartz, 1994; Menke *et al.*, 1994). This implies also that the EDA the hypothesis of Crampin *et al.* (1984b) cannot explain all examples of crustal anisotropy and other mechanisms should be invoked to explain the observed polarisation direction. In this dataset, the direction of the faster shear-wave splitting is parallel to the observed foliations on the Precambrian basement, indicating that these foliations are indeed controlling the anisotropy in the region, as first suggested by Brocher and Christensen (1990).

My interpretation is also supported by Barruol and Mainprice (1993) who modelled the effect of crust on the splitting measurements of teleseismic SKS waves. They showed that there is a strong correlation between the foliation orientation in the lower and middle crustal rocks and the observed delay. They concluded that a maximum delay time is systematically observed for waves propagating parallel to the foliation and the polarisation of the fast shear-wave is parallel to the lineation. The splitting is small when the waves propagate normal to the foliation. They estimated the amplitude of the delay due to mineral foliation in the lower and middle crust to be between 10 - 20 ms/km.

It is very difficult to see in this dataset a correlation between the geometrical orientation of the foliation and a variation on the measured time delays, as the full geometry of the foliation in the field is not available. So, a correlation between these two factors with the present dataset was not made. However, most of our normalised delay values, as shown in Table 3.2, are inside the range proposed by Barruol and Mainprice (1993). These values of normalised time delays lead us to accept that in an area such as that of the present study, where the gneissic fabric of shallow rocks are controlling the anisotropy, the results of Barruol and Mainprice (1993) may be applied to the upper regions of the crust (as shallow

as 5 km).

Metamorphic foliation as a control on the anisotropy observed in earthquake data in Northeastern Brazil has already been attested by do Nascimento *et al.* (2002). In this work, it was shown that shear-wave observations, in an area 75 km west of the Açú reservoir are controlled by the anisotropy associated with the Precambrian foliation. Hence, the shear-wave observations bear the signature of the palaeo-stress field i.e. Precambrian. The manuscript of do Nascimento *et al.* (2002) is found in Appendix F.

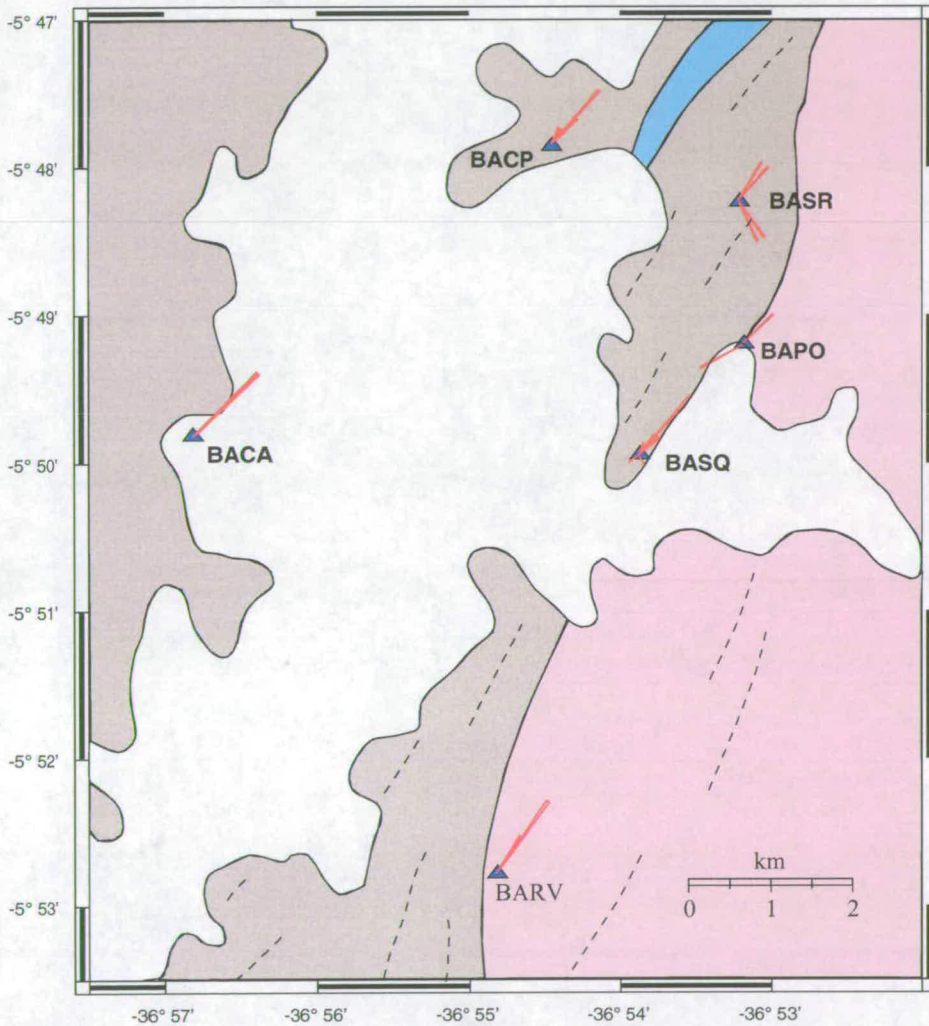


Figure 3.11: Figure showing the geological features in the study area. Brown region indicates Jucurutu Formation, composed of paragneiss and biotite gneiss. Pink region denotes a gneiss-migmatic complex of Archean age. Blue region is a biotite granite of Neoproterozoic age. The dashed lines are photolineations (DNPM *et al.*, 1998). In red, this figure also shows the rosette diagram for each station where shear-wave splitting was available. Most of the faster wave polarisation directions are subparallel to the direction of the metamorphic foliation. The blue triangles represent the stations.

In the next section, a method developed by Karnasopoulou *et al.* (1996) is used to verify if the observed splitting is due to anisotropy along the ray paths, or is due to polarisation at the source.

3.7 Focal mechanisms in the presence of anisotropy

In section 3.6.3, it was claimed that the splitting observed in the seismograms is due to anisotropy along the ray path and not due to the polarisation of the source. To verify the presence of this anisotropy, I used a method for determining focal mechanism solutions using shear-wave polarisations introduced by Karnasopoulou *et al.* (1996). This method consists of processing the data using two different interpretations, or assumptions. In each case, the P-wave input is identical, only the S-wave measurements are different. In the first case it is assumed that shear-wave splitting is present (**interpretation 1**). In this interpretation, the measured polarisation is assumed to represent the first split shear-wave. The second interpretation (**interpretation 2**) assumes that there is no anisotropy. The fast direction of the previous interpretation is assumed to represent an unsplit shear-wave, related directly to the polarisation at the source. Any later arrivals are assumed not to be direct shear-waves and are ignored (Karnasopoulou *et al.*, 1996).

When the measurements at different stations are made to calculate the focal mechanism, their compatibility with a double-couple source can be used as evidence that the second assumption (no anisotropy present) may be correct. If solutions are found, even if they are “better constrained” (i.e. smaller number of acceptable solutions), then it can be said that the second assumption is consistent with the data, although not to the exclusion of the other assumptions. If no solutions are obtained using the second assumption, then either this assumption is not valid for this earthquake, or the earthquake is not a double couple source. If, on the other hand, “better constrained” solutions, or only solutions using the first assumption are found (anisotropy is present), then the presence of anisotropy is confirmed.

To calculate the focal mechanism the Relative Amplitude Moment Tensor Program, (RAMP) was used (Pearce, 1977, 1980; Pearce and Rogers, 1989). RAMP was primarily conceived for comparing the relative amplitude of teleseismic P and pP phases, but it has been modified for local earthquakes (Murdie *et al.*, 1993; Rowlands, 1995; Karnasopoulou *et al.*, 1996). RAMP seeks double-couple point source mechanisms compatible with the input P-wave polarities and the three-component S-wave polarisations. For each seismogram, polarity and amplitude measurements are taken from the three component S-waves. Polarity, can be assigned + for positive polarities, - for negative and U for unknown polarity. If the polarity is unknown, but can be specified with confidence relative to the polarity of another component, then “the same as” (S), or “opposite to” (O) can be specified for the other component. A schematic example for the procedure to measure polarity and amplitude bounds is shown in fig. 3.12.

The events selected for this study were earthquakes that had at least 5 P-wave polarities and good shear-wave forms with an incident angle up to 35° , according to the half-space model used. Ten events passed this selection criterion and their focal mechanisms were determined using both interpretations as described above. In the first case the components were rotated into fast and slow directions and assigned the minimum and maximum amplitude bounds as shown schematically in Figure 3.12, without regard to their arrival time.

In the second case, the measured polarisation represents an unsplit shear-wave, and is related directly to the polarisation at the source. So, the polarity of the faster component (the *X* component) is usually known and is much larger than that of the slower component (the *Y* component).

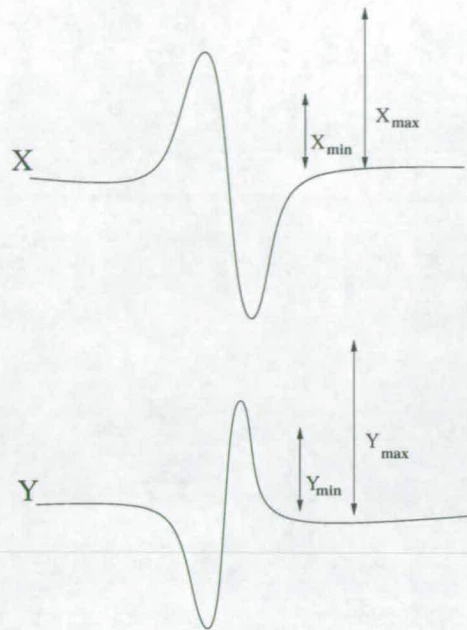


Figure 3.12: Schematic illustration of relative amplitude measurements. Relative amplitude bounds are measured on the horizontal components. X is taken as the faster component, with minimum and maximum amplitude bounds X_{min} and X_{max} , respectively. Y is the slower component, with minimum and maximum amplitude bounds Y_{min} and Y_{max} , respectively.

One of the assumptions of this RAMP method for determining focal mechanism is that the instruments are identically calibrated for amplitude measurement. If that is not possible, this method can still be used with the polarities constraint only.

3.7.1 Application of the RAMP method to the Açu earthquakes

In this section, ten events were selected for calculating their focal mechanisms using RAMP. Appendix D shows the seismograms, amplitude bounds and S waveforms of the ten selected events. In Table 3.3 I show the details of the focal mechanism determination of these selected events. In order to avoid listing all the compatible solutions, I give the percentage of the solution space (number of compatible solutions as a percentage of 93,312 possible solutions), which fits the data for three different grid searches: P-waves only; **interpretation 1** and **interpretation 2**. In both interpretations, the P-wave polarity is also incorporated. Generally, the smaller the number of compatible solutions, the better constrained the solutions.

From Table 3.3 it should be noticed that the results are divided into three categories:

- those focal mechanism solutions in which interpretation 1 gave a smaller number of compatible solutions: FM1, FM6 and FM10.
- those focal mechanism solutions in which interpretation 2 has a smaller number of solutions than assumption 1: FM2, FM3, FM5, FM7, FM8 and FM9. Although, as discussed above this does not rule out the possibility that interpretation 1 is also valid.

Event (date and time)	Station name	Rot. (°)	No. stns.	Shear-waves amplitudes and polarities for Interpretation 1			% solutions space with compatible solutions		
				Min.	Max.	Pol.	P only	Interpretation 1	Interpretation 2
FM1 951010 1159	BASQ	40	7	X 9 Y 4	22 14	- -	1.65	0.004	0.008
FM2 951013 0526	BASQ	40	8	X 10 Y 5	25 16	- +	1.34	0.03	0.002
FM3 951013 0538	BASQ	47	8	X 10 Y 5	25 16	- +	1.18	0.02	0.002
FM4 951029 2058	BASQ	50	8	X 8 Y 4	20 11	- -	0.55	0.02	n/a
FM5 951115 1653	BASQ	231	6	X 9 Y 3	19 9	- -	7.02	3.04	0.60
FM6 951212 0530	BASQ	40	5	X 2 Y 10	7 21	- +	6.43	0.45	1.64
FM7 951215 1354	BASQ	50	5	X 10 Y 8	21 20	- +	5.71	0.88	0.47
FM8 960106 1748	BASQ	44	7	X 8 Y 8	18 20	- +	1.08	0.62	0.02
FM9 960217 0550	BASR	155	8	X 5 Y 3	18 10	- -	0.68	0.21	0.02
FM10 960424 0414	BASR	30	5	X 3 Y 3	9 10	- -	3.17	0.29	1.72

Table 3.3: Rot. is the direction from North; No. stns. is the number of stations used to locate the events; n/a stands for *not available*.

- focal mechanisms for which only interpretation 1 provided compatible solutions: FM4.

It is important to point out that in this last group, interpretation 2 (no anisotropy present) was **not valid**, since no solutions compatible with a double-couple source were found. In none of the examples showed in Table 3.3, were double couple solutions found with interpretation 2 only. This is an independent confirmation that the split observed in the seismogram is indeed due to anisotropy along the ray path, and not due to the polarisation at the source.

3.8 Summary

The use of a network of 8 three-components digital seismographs in an area with a very simple velocity structure, like the one around Açu reservoir, led to excellent location of earthquakes and determination of focal mechanisms. Well-located events are of paramount importance in RIS studies because one can use these data to obtain a picture of the spatio-temporal evolution of the area. Moreover, with the data acquired by this network, it was possible to carry out seismic anisotropy studies. From the analysis and interpretation of these data, it can be concluded that:

- Three spatially distinct earthquake clusters were active from 1994 until 1997. Therefore their migration may be correlated to water level fluctuation of the Açu reservoir;
- the focal mechanism of the earthquakes located (regardless of the cluster to which they belong) indicates nearly pure right-lateral strike-slip faulting. The solution of focal mechanisms in this region is consistent with compressional stresses with an E-W orientation and extension with a N-S orientation (Assumpção, 1992; Ferreira *et al.*, 1998);
- the seismic anisotropy is consistent with the metamorphic fabric of the region, and not with anisotropy of stress-aligned fluid-filled cracks.

4 SPATIO-TEMPORAL EVOLUTION OF THE SEISMICITY AT AÇU RESERVOIR

In this Chapter, the spatio-temporal evolution of the seismicity at the Açú reservoir is described. The correlation between water level and earthquake activity is also shown. The earthquake data used to make this analysis come from the digital network (Chapter 3) and also from the permanent analog station BA1 (see Figure 4.2 and Appendix B). The combination of these two data sets is used to obtain a picture of the seismicity from 1987 to 1997, which is as complete as possible.

From 1987 to 1989 only the number of seismic events was recorded using a single station. Over the next eight years two field campaigns using smoked-drum records were carried out during October to December 1989 and November 1990 to March 1991 (Ferreira *et al.*, 1995). During the intervening periods only the total number of events was again recorded. However, due to the nearly continuous seismic monitoring using the digital PDAS network over almost three years (1994-1997) the seismicity in Açú is now one of the best documented cases of reservoir-induced seismicity in the world. Figure 4.1 shows the monthly variation of water depth and seismic activity, as recorded by the permanent station BA1 (shown in Figure 4.2). The horizontal two-headed arrows near the time axis indicate the duration of the field campaigns carried out by Ferreira *et al.* (1995) and by the present research. From 1987 to 1989, both the water level and the seismic activity had a quasi periodic behaviour. In these first three years of monitoring, the seismicity had a maximum correlation coefficient of 0.55 with the water level, with a delay of 3 months (Ferreira *et al.*, 1995). This clear correlation of the seismic activity with the water level strongly indicates the induced nature of the seismicity in the Açú reservoir. From 1990 until 1994, the water did not have its normal cyclic behaviour (due to a drought) and the seismicity no longer showed a clear correlation with the water depth. Ferreira *et al.* (1995) argue that the probable cause of a significant correlation in the first three years and the lack of correlation from 1990 until 1994 may be related to a migration of the active seismic area. In 1995 and 1996, the correlation is not so clear as in the first three years of monitoring. The reasons for this will be discussed in this Chapter. Figure 4.2 shows a summary of the event locations over the entire time interval of seismic monitoring (1987-1997). In this Chapter, I am primary focus on the digital data for the time period from 1994 to 1997.

4.1 The relationship between the water level and the seismicity (1994-1997)

With such well located events provided by the digital monitoring (Chapter 3), it is possible to examine the relationship between the migration of events and the water level variations (Figures 4.3 and 4.4). It

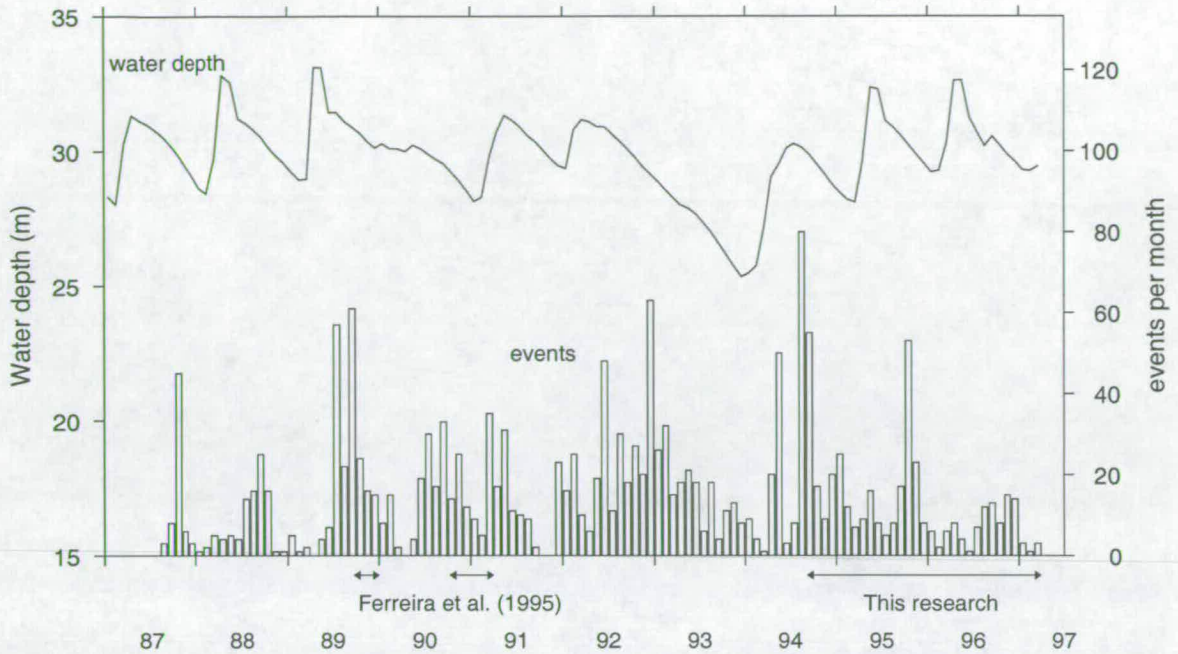


Figure 4.1: Monthly variation of reservoir water depth (top line) and monthly seismic activity (histograms) as recorded by station BA1 (shown in Figure 4.2). The horizontal two-headed arrows near the time axis indicate the duration of the field campaigns carried out by Ferreira *et al.* (1995) and the present research. Water level data are from DNOCS - Depto. Nacional de Obras Contra a Seca, Brazil.

can be noticed from Figure 4.3 that the seismicity between 1994 and 1997 is not clustered in a single spatial region, but clustered in three different regions. Figure 4.3 shows these three identifiable clusters. In this figure, clusters **a**, **b** and **c** are separated spatially (since the maximum location errors associated with each individual cluster is 300 *m* - smaller than the separation between the clusters). For those years of digital seismic monitoring, Figure 4.4i shows the monthly number of events recorded plotted together with the daily water-level change in the reservoir. Figures 4.4ii, iii, iv show respectively the depth of each event (4.4ii), distance along a NW-SE line (4.4ii) and distance along a SW-NE line (4.4iii) versus time (in years). In each of these figures, different symbols are used to plot the different clusters, so it is possible to see how the different clusters are activated in relation to the lake water level, shown in Figure 4.4i. Three months in each year are labelled on the histogram to facilitate reading Figure 4.4i. The letters S, O, N and D are, respectively September, October, November and December. The NW-SE line has its origin at the crossing point with the SW-NE line. The origin of the SW-NE line is indicated by an asterisk at the SW end of the line (Figure 4.3).

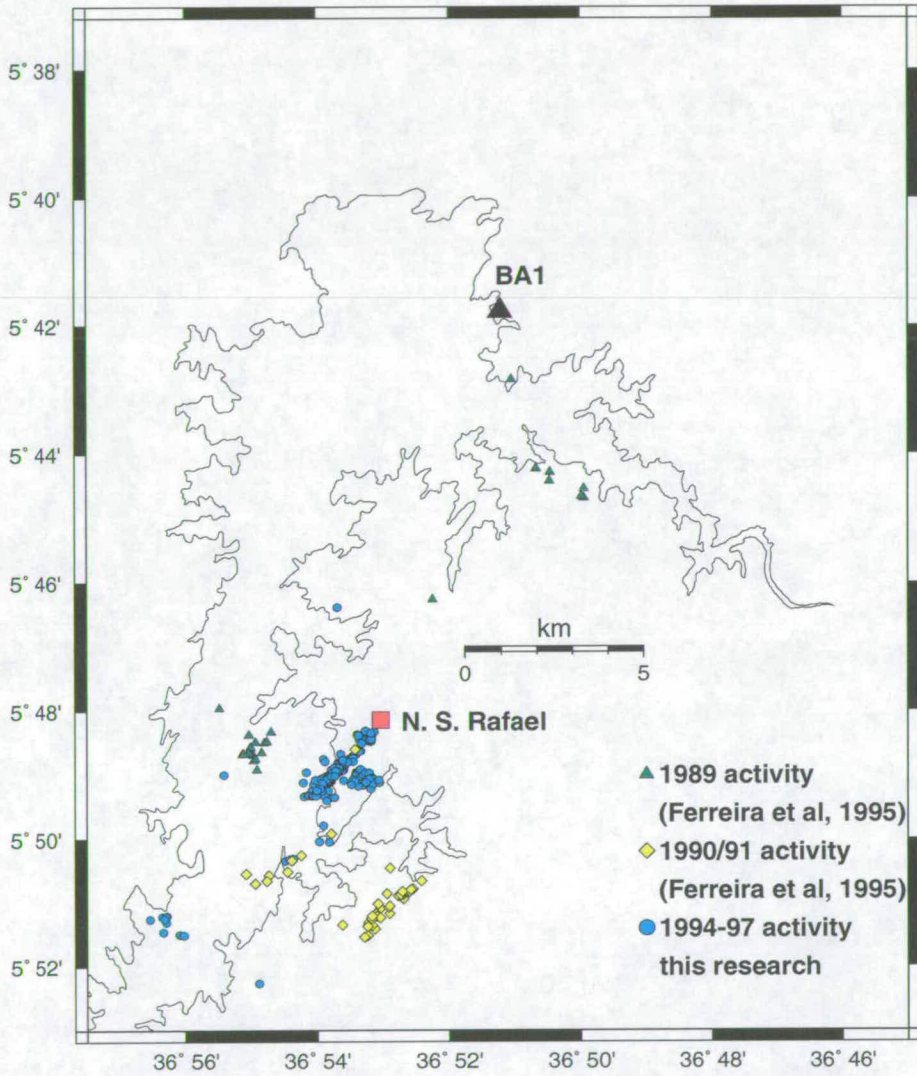


Figure 4.2: Figure showing the clusters located in the Açu reservoir by Ferreira *et al.* (1995) and clustered events located by the digital seismic network from 1994 until 1997. Green triangles represent the 1989 epicentres, yellow diamonds are the 1990/91 events (Ferreira *et al.*, 1995). Blue circles are the epicentres determined with the digital seismic network.

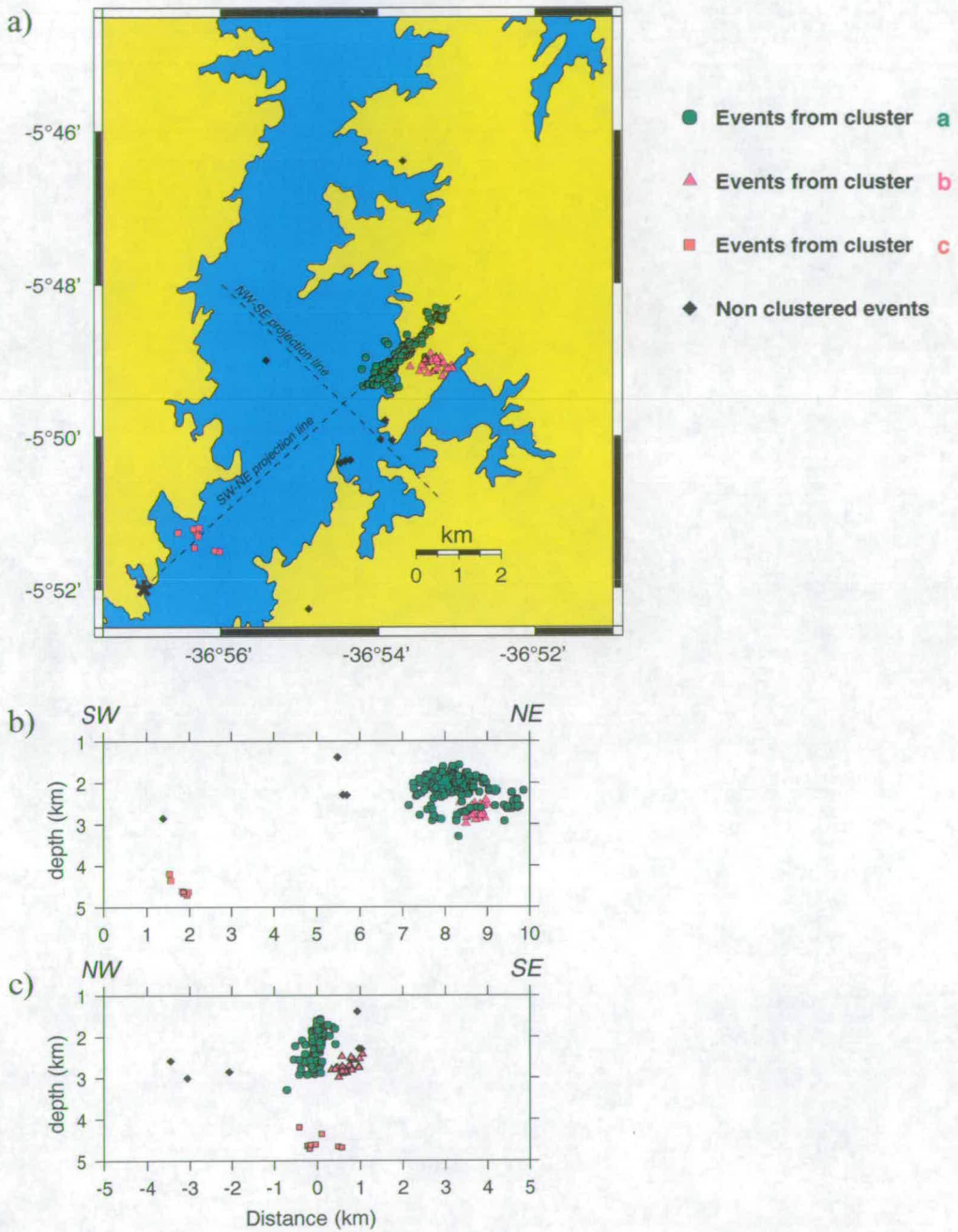


Figure 4.3: (a) Show the epicenters on a horizontal plane (b) projection of the hypocenters on the SW-NE line (c) projection of the hypocenters on the NW-SE line. The different symbols/colour scheme are indicated in the figure itself. The asterisk marks the beginning of the projection along the SW-NE plane. The NW-SE projection is at the crossing point with the SW-NE projection line.

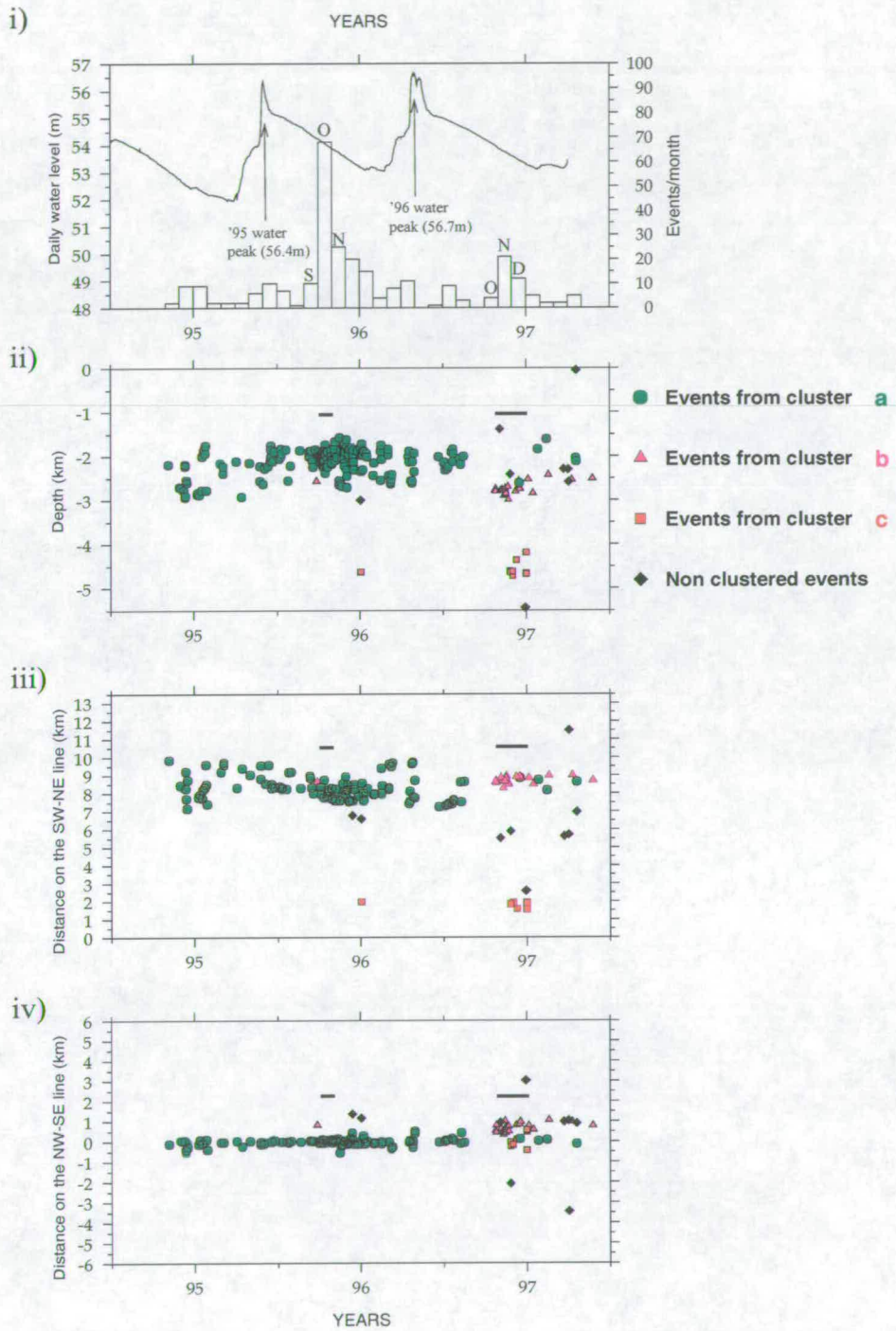


Figure 4.4: See caption on page 40.

Figure 4.4: Spatio-temporal evolution of the seismicity from November 1994 until April 1997. **i** Shows the daily water level variation at the Açu reservoir (top lines) and the monthly histogram of events (bottom) as recorded by the digital seismic network. Arrows indicate the annual maximum water level: 31/05/1995 and 27/04/1996, respectively. A few months of binned seismic activity are labelled to facilitate understanding: S, O, N and D are September, October, November and December, respectively. **ii** Shows the temporal evolution of event depths. A different symbol was used for each cluster as defined in Figure 4.3. The horizontal bars are to mark the months where there is a peak in the seismicity. **iii** and **iv** Show the evolution of seismicity along SW-NE and NW-SE projection lines, as used in Figure 4.3. The symbols which are used to plot the events are the same as those used throughout Figure 4.3 and here. See caption to Figure 4.3 for location of the the origin of the projections.

On the 31st May 1995, a peak in water level (56.4 m, as indicated by the left vertical arrow in Figure 4.4i) was followed by a increase in seismicity between the 7th and the 20th October 1995. The time delay, therefore, was between 131 and 144 days, which is approximately 4.5 months. The seismic activity during October 1995 is the greatest in the entire three years (around 70 events in 3-4 weeks). During this month, the seismicity was also concentrated in a small portion within cluster **a**. The horizontal bar representing this month on Figures 4.4ii, iii, and iv shows a depth range for the majority of these events between 1.8 km and 2.3 km and, in the SW-NE line, those events occur in a region approximately 1.5 km long and along the same fault line, within a zone < 500 m wide, as can be observed in Figure 4.4iv.

On the 27th April 1996, the water level in the Açu reservoir reached another maximum (56.7 m, as indicated by the vertical arrow on the right, in Figure 4.4i). In that year, the pronounced seismic activity started on the 21st of October 1996 in cluster **b**. Therefore, the delay was 177 days, which is approximately 6.0 months. And, later on, on the 25th November 1996, cluster **c** was activated, hence a time delay of 212 days, or approximately 7 months can be inferred. After the 25th of November 1996, clusters **b** and **c** are active concomitantly but activity in **a** virtually ceased. Clusters **b** and **c** are at depths of 2.8 to 3.0 km and 4.0 to 4.7 km, respectively. November and December 1996 are also marked on Figures 4.4ii, iii, and iv as horizontal bars. The observation of longer time delays between the maximum in water level and an increase in seismic activity at greater depths suggests that the triggering of the seismicity is governed by diffusion of hydrostatic pressure from the lake to hypocentral depths.

4.1.1 Spatio-temporal analysis from the permanent station BA1

The employment of all the available data in a RIS site is very important for determining the spatio-temporal pattern of the seismicity as accurately as possible. Interesting effects such as seismicity migration and reactivation of seismicity in certain areas can be masked if only one seismological catalogue is used. Here, the seismic catalogue from the digital network as well as the catalogue from the permanent station BA1 is used.

Figure 4.5 shows the histogram of monthly earthquake activity recorded by the permanent station BA1 and the histogram of monthly earthquake activity located by the digital seismic network. These data cover the time period of January 1994 until April 1997. In general terms, the histograms look very similar. The data collected by BA1 mimic the two peaks of earthquake activity in 1995 and 1996 described above. Therefore, the time delays of 4.5 and 6 months for 1995 and 1996 respectively

are essentially the same. However, there are some differences in these two histograms due to finite detection thresholds. Events with a very small magnitude occurring near BA1 are unlikely to be detected by the digital network and small events very close to the digital network are unlikely to be detected by the permanent station BA1. The possibility of instrumental failure can be discarded as a main contribution to the difference between the two histograms in Figure 4.5. During the period from Nov. 1994 - Jul. 1997 BA1 and the digital network are known to have been operating.

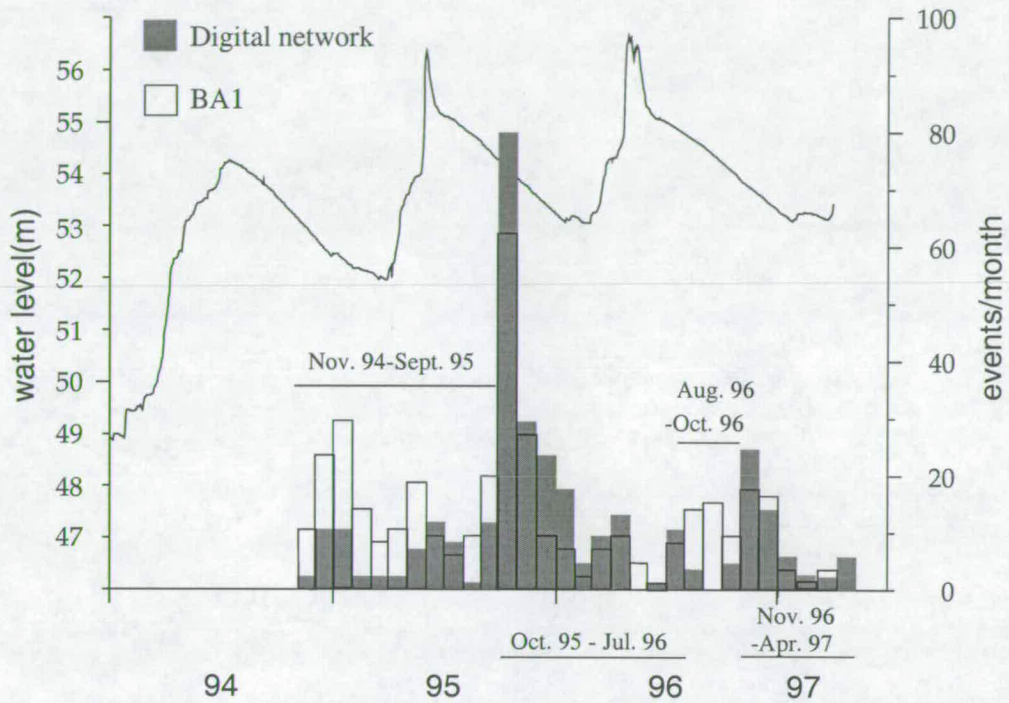


Figure 4.5: Earthquake monthly activity versus water level. The dark-filled bars represent the histogram of the number of events detected by the digital seismic network. The non-filled bars are the histogram of the number of events detected by the permanent station BA1 located in Figure 4.2. The continuous line represents the variation of the water level. From November 1994 until September 1995, the number of earthquakes recorded by the digital seismic network is systematically lower than the amount recorded by BA1. From October 1995 until July 1996, BA1 records systematically more events than the digital seismic network. In this figure the horizontal bars are to indicate the time period in which the permanent station BA1 records systematically more events than the digital seismic network (see text for discussion).

From November 1994 until September 1995, the number of earthquakes recorded by the digital seismic network is systematically lower than the number recorded by BA1. Conversely, from October 1995 until July 1996, BA1 records systematically fewer events than the digital seismic network. In particular, during the months of August, September and October 1996, considerable seismicity (more than ten events per month) was recorded by BA1 (open bar histograms) whilst very low seismicity was recorded by the digital seismic network. From November 1996 until April 1997, the digital network is systematically recording more events than BA1. This can be explained by examining Figure 4.6a and b. Figure 4.6a shows the values of the time delay between the P and S wave arrival times for all the events recorded at BA1 - hereafter ($t_S - t_P$) arrival times - for the period August 1994 until April 1997. Figure 4.6b shows the distribution of $S - P$ arrival times at this station within this period. In these figures, it is noted that there are two main peaks in the distribution of ($t_S - t_P$) arrival at BA1, one around 0.9 s and another at 1.6s. Although with one single-component station one cannot determine a

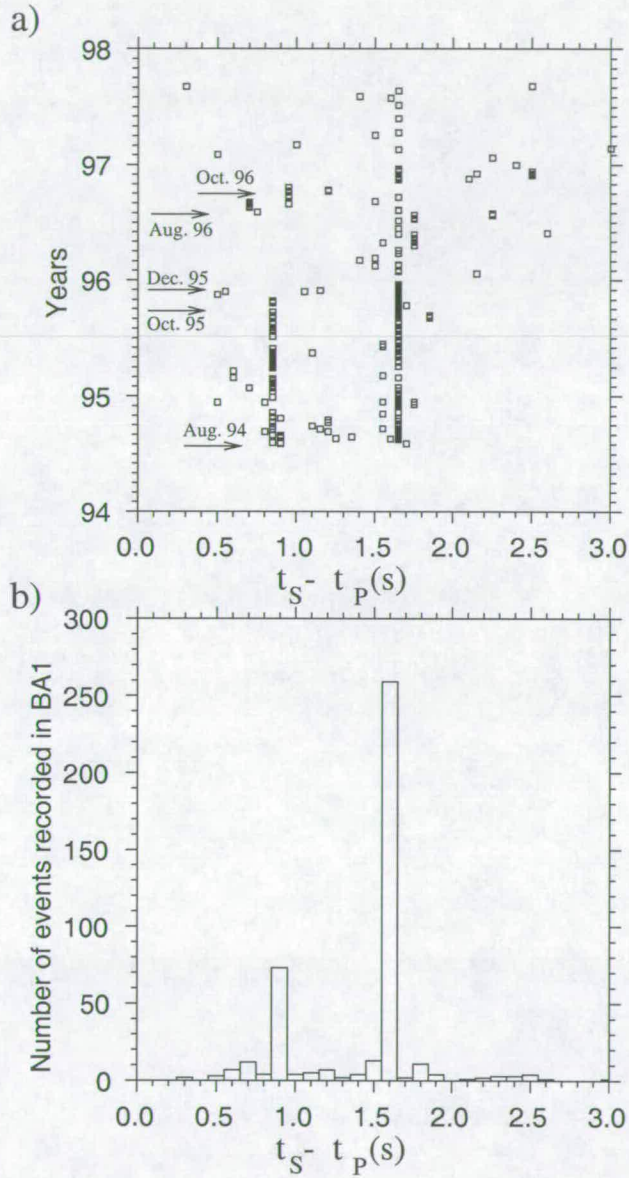


Figure 4.6: Distribution of $(t_S - t_P)$ arrival times as recorded by BA1. **a** Shows the values of $(t_S - t_P)$ arrival times versus time. Arrows indicate the beginning of a month/year, in which the seismicity was in more than one seismic area of the reservoir, or it migrated. **b** Shows the histogram of the distribution of $(t_S - t_P)$ arrival times of the events as recorded by BA1.

hypocentre, it is possible to use S-P arrival time values to calculate the distance of those events from the station. If a homogeneous half-space is used, where values of $V_P/V_S = 1.71$ and $V_P = 6.00$ km/s are valid for the entire region (Chapter 3), it is possible to write that $\Lambda = 8.45(t_S - t_P)$, Λ being the distance from the station to the event in km. Using the values of $(t_S - t_P)$ of the two main peaks (at 0.9 s and 1.6 s), it is found that such events are occurring at two discrete distances of approximately 7.6 km and 13.5 km.

This simple analysis shows that from August 1994 until December 1995, as indicated by arrows on Figure 4.6a, the seismicity was mainly in two areas, one at 7.6 km and another 13.5 km away from BA1. The seismicity at 13.5 km from BA1 is also recorded by the digital seismic network (clusters a and b). However, this analysis suggests that a third cluster, 7.6 km away from BA1 was not detected by the digital seismic network. That is why the number of events recorded by the seismic network in this period (Aug. 1994 to Oct. 1995) is smaller than the one recorded by the permanent station BA1. In Figure 4.7 a smaller circle is used to denote the epicentral locations of events with S-P arrival times of 0.9 s, assuming a hypocentral depth of 5.0 km. The larger circle is to mark epicentral locations with S-P arrival times of 0.9 s, but with a hypocentral depth of 1.0 km. Therefore, it can be concluded that from August 1994 until December 1995 two areas were active in the lake: one near Nova São Rafael (i.e. clusters a and possibly b) and another one 7.6 km from BA1. Since only the $(t_S - t_P)$ arrival times are available, it is not possible to constrain the epicentral location of these events. However, in 1989, Ferreira *et al.* (1995) located a few events in epicentral regions approximately 5 – 6 km south of BA1 shown in Figure 4.7, therefore, these may be reactivating.

There is other evidence for spatial migration shown in Figure 4.5. Overall, from October 1995 until August 1996, mainly the areas southwest of Nova São Rafael were active (clusters a, b and c). Some of the seismicity occurring near BA1 from October 1995 to December 1995 was incompletely recorded by the digital network. However, more seismicity is recorded by the digital network than is by BA1 in this time interval. Figure 4.6a also shows that from August 1996 until the end of October 1996, as indicated by the arrows on this figure and the histogram in Figure 4.6, some seismicity near BA1 was also simultaneously occurring near Nova São Rafael. Again, this seismicity near BA1 was not detected by the digital seismic network and therefore, the number of events recorded by the digital seismic network is smaller than the seismicity recorded by station BA1 (Figure 4.6). From November 1996 onwards, Figure 4.6 shows that the $(t_S - t_P)$ values have a peak around 1.6 s. So, areas near BA1 are quiescent. Consequently, the digital network records systematically more events than BA1 (Figure 4.5). These features indicate a repeated shift of activity in the area.

A detailed spatio-temporal analysis is important to interpret the relationship between the peak in water level and the maximum in seismic activity. In many cases of RIS as with those reported by, for example, Gupta (1992) this care is not always taken and only the number of events recorded by a single station is employed. Hence, it could be that in many cases, a clear correlation of water level with increased seismicity is masked out by the lack of control on the epicentral location of the seismicity. At the Açú reservoir Ferreira *et al.* (1995) argued that in the years where there was an apparent lack of correlation between seismicity and water level, it may be related to migration of the epicentral area. In the present research, data from 1995-1997 have shown this to be the case and, hence this is a credible explanation for lack of correlation in earlier years.

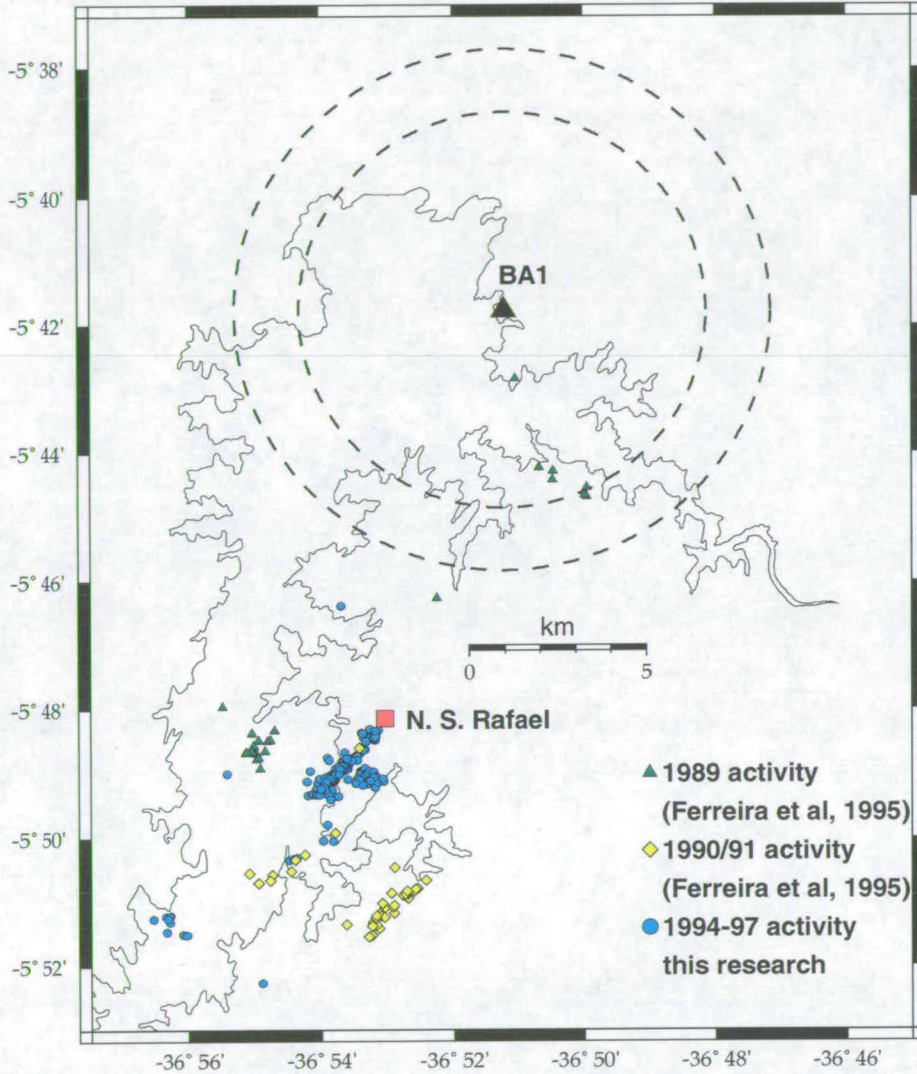


Figure 4.7: Figure showing the clusters located in the Açú reservoir by Ferreira *et al.* (1995) and clustered events located by the digital seismic network from 1994 until 1997. Green triangles represent the 1989 epicentres, yellow diamonds are the 1990/91 events (Ferreira *et al.*, 1995). Blue circles are the epicentres determined with the digital seismic network. The smaller dashed circle around station BA1 is to mark the epicentral locations of events with S-P arrival times of 0.9 s, assuming a hypocentral depth of 5.0 km. The larger circle marks epicentres with S-P arrival times of 0.9 s, but with a hypocentral depth of 1.0 km.

An improvement on relative location of the events can be obtained from a joint hypocentral determination. The horizontal and vertical errors shown in Figures 3.6a and b could be even more reduced—to tenths of metres. With such resolution, one could investigate earthquake migration within a particular cluster with a higher degree of detail.

4.2 Summary

The results of the spatio-temporal analysis can be summarised in two Tables. Table 4.1, can be constructed summarising the spatio-temporal evolution of events located by the digital network, as for these events it was possible to know accurately their hypocentres and times of activation. Moreover,

Period of activation	Active seismic cluster
Nov. 1994 - 15/Aug./1996	a
15/Aug./1996 - 21/Oct./1996	a
21/Oct./1996 - 22/Nov./1996	b
25/Nov./1996 - 30/Dec/1996	c, b
30/Dec./1997 - May/1997	a, b

Table 4.1: Activation period of events recorded by the digital seismic network. With precise hypocentre determination, it is possible to observe migration of seismic events between different faults and within individual faults over different time periods. This table summarises the migration pattern of the seismicity located the digital network.

for the events that were detected by the digital network, it is possible to associate the activation of each cluster to the delayed effect of an increase in water level in the reservoir, as a result of the diffusion of pore pressure into the rockmass. Table 4.2 shows the values of the delays and the depths at which the seismic clusters located by the digital network were activated. As expected, if the diffusion of pressure

Active seismic cluster	Depth range km	percentage of events in this depth range	Time delay (months)
a	1.8 - 2.3	74%	4.5
b	2.7 - 3.0	77%	6.0
c	4.0 - 4.7	89%	7.0

Table 4.2: Summary table showing the depth range and the percentage of of events that occur at this depth range of each cluster shown in Figure 4.3. The time delay corresponds the time interval between the peak in water level variation and the activation of a particular cluster.

is the dominant mechanism for triggering events in the Açu reservoir, the time delays between the maximum in water level and the subsequent increase or activation of seismic events also increased.

Summarising, the seismicity in Açu reservoir mostly occurs in well defined seismic zones. The seismicity is observed to migrate between these zones and within individual zones over different periods of time. Not all the events fit this simple picture but the majority do. Here, it was shown that when hypocentral data were available, the activation of clusters is consistent with the diffusion of pressure throughout the rockmass. In the next Chapter, a review on the theory of groundwater is presented. In Chapter 6 the relevant hydrogeological and geological parameters for the modelling of the groundwater pressure at Açu reservoir are presented. Later on, in Chapter 7, a groundwater model is set up to inves-

investigate in more detail the relationship between groundwater pressure changes and the spatio-temporal distribution of seismic events. The issues that will be tested with the modelling are:

- the relationship between groundwater pressure changes and the spatio-temporal distribution of seismic events;
- the possibility of explaining the spatio-temporal distribution of seismic events using an homogeneous model (with respect to its hydraulic properties);
- the use of a high permeability fault to explain the spatio-temporal distribution of seismic events;
- the inclusion of heterogeneity (with respect to its hydraulic properties) in the fault to explain the spatio-temporal distribution of seismic events;
- the magnitude of threshold pressure change values responsible for the triggering of seismic events beneath the Açu reservoir.

5 GROUND WATER THEORY

5.1 Mass balance equation - flow in saturated porous media

Figure 5.1 defines a volume in a saturated medium with no free surface. The fluxes at the centre of the unit volume are q_x , q_y and q_z in the three orthogonal coordinate directions. The net flux across a plane perpendicular to the x direction is given by the application of Taylor's series expansion of flux for a small volume (Bear and Verruijt, 1987):

$$\left[\left(\rho q_x - \frac{1}{2} \frac{\partial}{\partial x} (\rho q_x) \Delta x \right) - \left[\rho q_x + \frac{1}{2} \frac{\partial}{\partial x} (\rho q_x) \Delta y \Delta z \right] \right] = - \frac{\partial}{\partial x} (\rho q_x) \Delta V \quad (5.1)$$

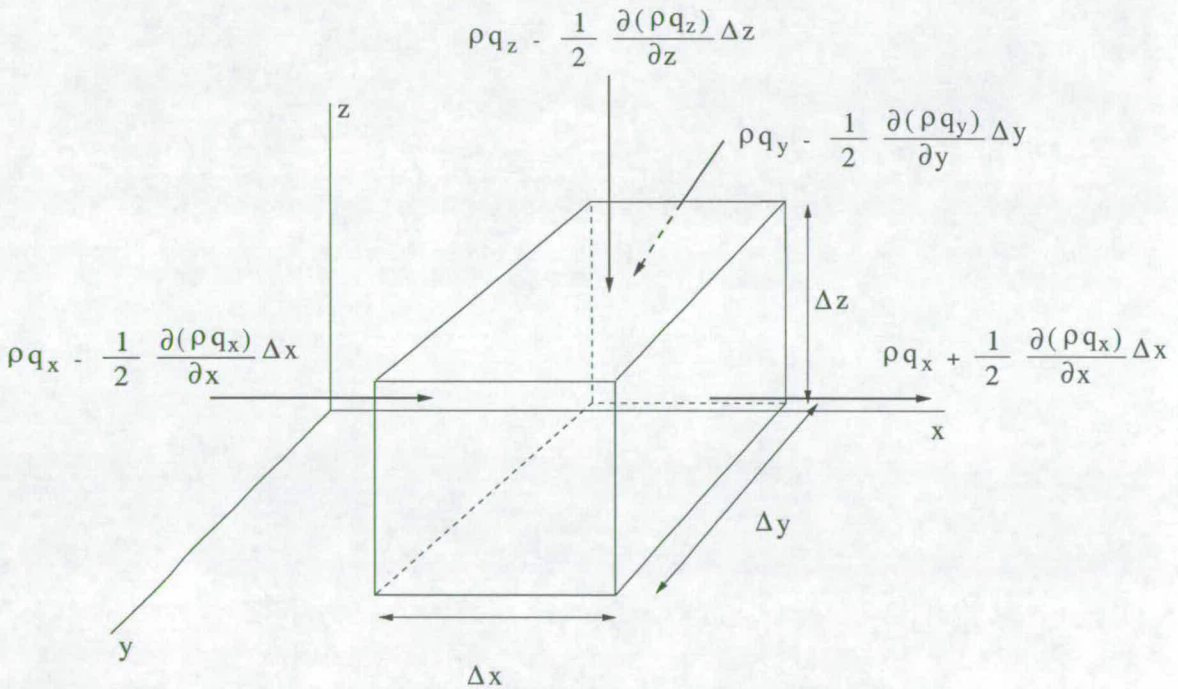


Figure 5.1: Flow through a saturated soil element (after Bear and Verruijt (1987)).

where ρ is the density of water, $\Delta V = \Delta x \Delta y \Delta z$ and q_x is the flow per unit area perpendicular to the face $\Delta y \Delta z$. The other directions yield similar results. When added, all these flow contributions must be equal to the change of fluid mass in the system, $\frac{\partial M}{\partial t}$.

The volume of water in the control volume is equal to $\phi dx dy dz$, where ϕ is the porosity. Porosity is a

measure of the pore volume in a rockmass and is indicated as the fraction of rock that is not occupied by solid matter. Mathematically, porosity is written as:

$$\phi = \frac{V_{pore}}{V} = \frac{Pore\ volume}{Total\ volume} \quad (5.2)$$

Values of porosity will be presented in section 5.4.1.

Using the concept of porosity, one can write:

$$\frac{\partial M}{\partial t} = \frac{\partial}{\partial t}(\rho\phi\ dx\ dy\ dz) \quad (5.3)$$

and hence

$$-\left(\frac{\partial}{\partial x}(\rho q_x) + \frac{\partial}{\partial y}(\rho q_y) + \frac{\partial}{\partial z}(\rho q_z)\right) \Delta V = \frac{\partial}{\partial t}(\rho\phi\Delta V) \quad (5.4)$$

Under saturated conditions, the change in fluid mass can only be attributed to water density or porosity changes. Changes in water density can be neglected when compared to changes in porosity caused by compression of the soil-rock matrix in the vertical direction. Here, it is convenient to define a coefficient of specific storativity S as the the volume of water released from storage per unit volume of aquifer per unit change in piezometric head. Then, using the hydrostatic pressure assumption, $p = \rho g(h - z)$, where h is the piezometric head and z is measured from an arbitrary datum, equation 5.4 becomes:

$$-\left(\frac{\partial q_x}{\partial x} + \frac{\partial q_y}{\partial y} + \frac{\partial q_z}{\partial z}\right) = \frac{S}{\rho g} \frac{\partial p}{\partial t} = S \frac{\partial h}{\partial t} \quad (5.5)$$

S is a property of the rockmass and has unit of inverse distance. Later, on section 5.4.2, values of S for different types of rocks will be discussed/presented. Equation 5.5 is the fundamental equation governing fluid flow in a porous media.

In order to relate equation 5.5 to the pressure diffusion equation described earlier in Chapter 2 (Equation 2.11) it is now necessary to introduce the relationship between the flux, q , and the pressure p .

5.2 Darcy's Law

In 1856, Henri Darcy empirically established using the experiment shown in Figure 5.2 that the flux of water Q through a porous media (a sandy formation, for instance) is:

$$Q = KA \frac{\Delta h}{L} \quad (5.6)$$

where A is the area of the cross-section of the sandy formation, Δh is the water level measured from the bottom of the sandy formation, K is a constant of proportionality and l is the thickness of the sandy formation.

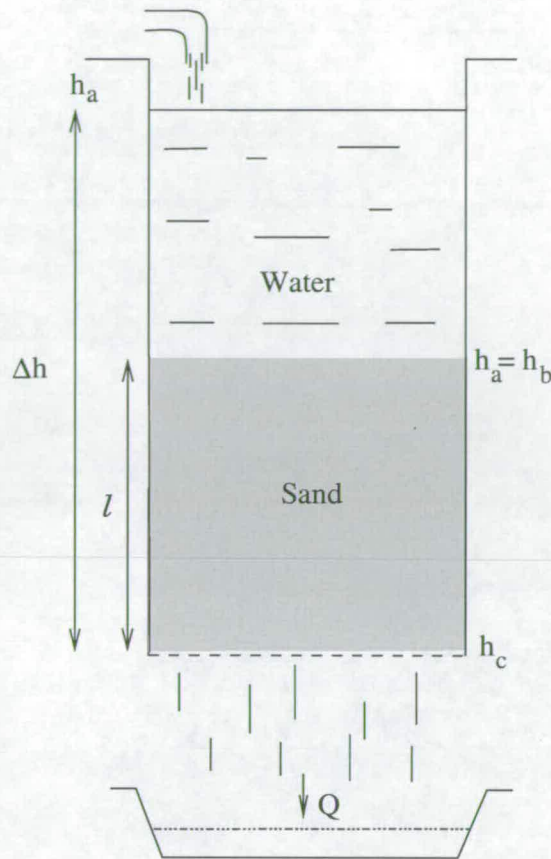


Figure 5.2: Darcy's experiment.

Dividing both sides by A , one obtains the flow per unit area, q (also called the flux), given by:

$$q = \frac{Q}{A} \quad (5.7)$$

In the limit as $l \rightarrow 0$ this becomes

$$q = -K \frac{\partial h}{\partial z} \quad (5.8)$$

or

$$q = -K \frac{\partial}{\partial z} \left(\frac{p}{\rho g} + z \right) \quad (5.9)$$

since $h = \frac{p}{\rho g} + z$. Equation 5.8 is called Darcy's Law.

5.3 Permeability and hydraulic conductivity definitions and the groundwater flow equation

The constant K defined in Section 5.2, is termed hydraulic conductivity and is a function of both the porous media and the fluid flowing through it. In reality, it varies proportionally to the density of the fluid, ρ and is inversely proportional to the viscosity, η . Thus, in order to describe a property of the rock only, the variable k , rock permeability is introduced as:

$$K = \frac{k\rho g}{\eta} \quad (5.10)$$

Permeability, k , is a measure of how easily a fluid flows through a porous medium, regardless of the characteristic of this fluid. Its dimension is $[length^2]$. Often the unit *Darcy* is used to measure permeability. $k = 1 \text{ Darcy}$ ($1 D$) when $Q = 1 \text{ cm s}^{-1}$, for a gradient of $|\nabla P| = 1 \text{ atm cm}^{-1}$, for a fluid viscosity of 10^{-2} poise . Hence, $1 \text{ Darcy} = 0.97 \cdot 10^{-12} \text{ m}^2$. k has been introduced for completeness here, since many authors discuss values of permeability in the literature. However, in this thesis the usage of K (hydraulic conductivity) will be preferred to the usage of k (permeability). That is because the fluid treated in this entire thesis is water. Moreover, the relationship between K and k is very straightforward (equation 5.10).

The dimension of K is $[length \ time^{-1}]$. When equation 5.8 is written, it is implicitly assumed that K (or k) is an isotropic property, i.e., its value is independent of the orientation in space. However, the fluid in a porous medium has a tendency to flow following the direction in space of the highest hydraulic conductivity. For example, in sedimentary layers due to stratification, a horizontal hydraulic conductivity can be much higher (say, two orders of magnitude) than the vertical one. This tendency leads to K (and k) having tensorial properties. Hence, Darcy's law becomes $q = -\underline{K} \cdot \nabla h$. \underline{K} is the hydraulic conductivity tensor.

If Darcy's law (equation 5.8) is then combined with equation 5.5, the following equation is obtained:

$$\nabla \cdot (\underline{K} \cdot \nabla h) = S \frac{\partial h}{\partial t} \quad (5.11)$$

Equation 5.11 is the partial differential equation governing a non-steady flow in a rock mass. If the rock mass is homogeneous and isotropic with respect to the hydraulic conductivity, 5.11 is reduced to:

$$\nabla^2 h = \frac{S}{K} \frac{\partial h}{\partial t} \quad (5.12)$$

This equation is similar to the pore pressure diffusion equation, equation 2.11, as seen in chapter 2.

In chapter 2 it was shown that pore pressure changes can induce seismic activity by reducing the effective normal stress across a fault plane. One way to increase pore pressure change is by the diffusion to depth of a pore pressure increase at the ground surface (equation 2.11). D in equation 2.11 is called hydraulic diffusivity and for a homogeneous isotropic porous media can be related to the equations of

groundwater flow (equation 5.12) by:

$$D = \frac{K}{S} \quad (5.13)$$

Because equations 2.11 and 5.12 are analogous, one way to simulate the pore pressure changes caused by artificial lake filling or fluid injections in the crust is to simulate the change in piezometric head and vice-versa.

5.4 Hydraulic properties of basement rock

5.4.1 Hydraulic conductivity

The hydraulic conductivity is a measure of how easily water flows through a rock. In fractured rocks, flow occurs due to two different types of porosity depending on the origin of the void space: porosity which is formed with the rock matrix; and porosity which evolves subsequently due to weathering or fracturing. Because of these two types of porosity, a distinction can be made between the flow in a fracture (rapid fracture flow) and in intergranular material (slow matrix flow). Figure 5.3 illustrates these two flows. Fractures form the main mechanism for the flow of water in crystalline basement

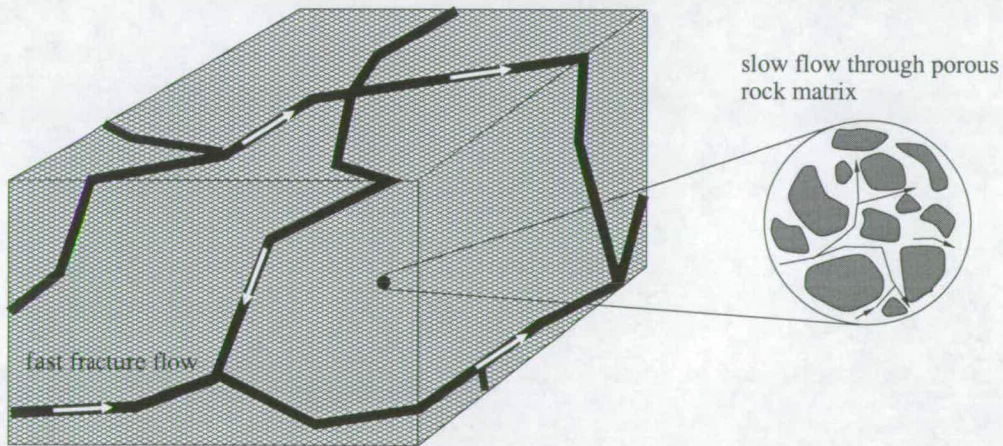


Figure 5.3: Fluid flow through porous media. Example of rapid and slow flow.

rocks. Hence, the hydraulic conductivity mainly depends on the fracture availability, fracture aperture and infilling, and stress (de Marsily, 1986; Singhal and Gupta, 1999).

If fractures are assumed to be planar features which extend indefinitely in the horizontal (x-y) plane (Figure 5.4) with their aperture e oriented along z , then the flow q , within the parallel planes is (after Zimmerman and Bodvarsson (1996)):

$$q = \frac{\rho g \phi^* e^3}{12\eta} |\nabla h| \quad (5.14)$$



Thus,

$$K = \frac{\rho g \phi^* e^3}{12\eta} \quad (5.15)$$

The porosity ϕ^* is the porosity of a rock in which the only void space is due to the presence of this parallel plate. $|\nabla h|$ is the piezometric head gradient and η is the fluid viscosity.

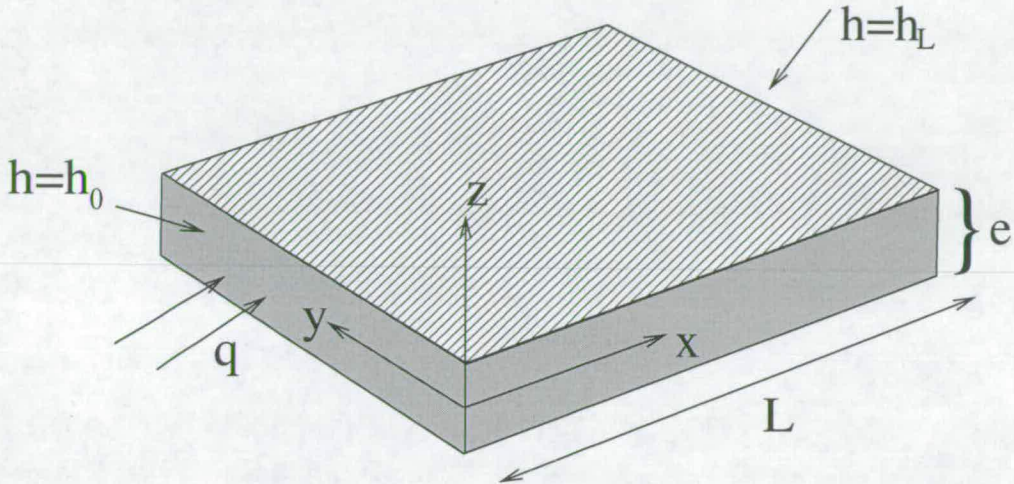


Figure 5.4: Parallel-plate fracture of aperture e , with uniform pressure gradient (after Zimmerman and Bodvarsson (1996)).

Table 5.1 gives the value ranges of hydraulic conductivity and porosity in fractured and intact crystalline rocks found in the literature. A difference of several orders of magnitude is apparent.

Geological medium	K (m/day)	ϕ
Massive crystalline rock	$10^{-8} - 10^{-3}$	0 - 0.05
Fractured & weathered crystalline rock	$10^{-3} - 10$	0.05 - .40

Table 5.1: Value ranges of hydraulic conductivity in fractured and unfractured rocks (compiled from de Marsily (1986); Singhal and Gupta (1999)).

In fractured rock the fluid flow may be dominated by a few highly conductive fractures. Thus, the way to characterise fractured rocks is to characterise the fractures themselves. The primary control on fracture aperture is the orientation and magnitude of compressive stress. In general, the relationship between effective normal stress and hydraulic conductivity can be expressed by an empirical equation (Singhal and Gupta, 1999):

$$K = K_0 \sigma^{-\alpha} \quad (5.16)$$

where K_0 is the value of the hydraulic conductivity when no stress is applied and α is a constant that measures how the hydraulic conductivity decays with depth. σ is the effective normal stress. Values of K_0 and α can be derived from linear regression of field hydraulic conductivity data derived from

hydraulic testing of boreholes over depth. (de Marsily, 1986; Lunn and Mackay, 1997; Singhal and Gupta, 1999). The (observed) decrease in K with depth is explained by the general compression and reduction of hydraulic aperture with increasing stress at depth (Rutqvist *et al.*, 1998).

5.4.2 Specific storage coefficient

When considering water movement in a rock mass, a description of the storage capacity of the medium is necessary. The specific storage, S is defined as the volume of water that can be released from the rock when the hydraulic head is reduced by one unity. S has units of $[length^{-1}]$ and is closely related to the porosity and compressibility factors of the rock by the relationship (de Marsily, 1986):

$$S = \rho\phi g \left(\beta_l - \beta_s + \frac{\beta_p}{\phi} \right) \quad (5.17)$$

where β_l is the coefficient of compressibility of the liquid that travels through the porous medium and β_s is the coefficient of compressibility of the solid that constitutes the medium. β_p is the coefficient of compressibility of the porous medium. S , in reality, is a measure of how much water one can squeeze out from a rock. Hence, its closer relation to the mechanical properties of the rock.

Geological medium	$S (m^{-1})$
Dense rock	$10^{-7} - 10^{-5}$
Fissured and jointed rock	$10^{-5} - 10^{-4}$

Table 5.2: Typical specific storage values for intact and weathered crystalline rocks (after Singhal and Gupta (1999)).

Table 5.2 shows some typical values for S . The highest values of S ($10^{-5} - 10^{-4}$) are associated with granite formations with a high degree of fracturing, in which fluid flow in the formation is dominated by fractures. The low values of S are found in granite with low a degree of fracturing (dense rock) where S is between 10^{-7} and 10^{-5} . So, the lower values of S correspond to dense rock, while the higher values of S correspond to fissured rock. Hence, the fractures in the system tend to increase the capacity of the rock to release water. So, it would be expected that a granite formation with a high degree of fracturing would have a high values of both K and S and vice versa. This is not strictly true because both these properties also depend on the material filling the fractures and their connectivity, not only on the aperture. It is expected that as stress increases, S will decrease, as the rock will have less and less void space in which to store water. A systematic compilation of S with depth has yet to be conducted. However, Kessels and Kuck (1995) reported a reduced specific storage with depth for measurements down to 6,000 m. The explanation for the dearth of field measurements of S versus depth is the high cost and the difficulty involved in performing such measurements.

5.4.3 Hydraulic diffusivity

The hydraulic diffusivity, D , is a single formation characteristic that couples the hydraulic conductivity K and the storage property S . In RIS literature (Talwani and Acree, 1984/85; Talwani, 1997; Shapiro *et al.*, 1997) the term D appears more frequently than the explicit use of $\frac{K}{S}$. Combining Equations

5.10 and 5.17 with 5.13:

$$D = \frac{k}{\eta\phi(\beta_l - \beta_s + \frac{\beta_p}{\phi})} \quad (5.18)$$

However, in this thesis the explicit use of K/S is generally preferred. This is because the transmission and storage properties of a medium are fundamental properties and more importantly, because the relationship $D = K/S$ only holds for a homogeneous, isotropic media.

5.5 Summary

The pore pressure diffusion equation, normally used in RIS literature (Talwani and Acree, 1984/85; Talwani, 1997; Shapiro *et al.*, 1997) is equivalent to the the groundwater equation normally used in hydrological literature (de Marsily, 1986). Therefore, modelling pore pressure diffusion is equivalent to modelling the diffusion for a homogeneous, isotropic medium of the piezometric head.

Values of hydraulic conductivity and storativity in fractured rock can vary over several orders of magnitude. This is because these hydraulic properties depend upon the quantity, orientation, aperture and infilling of fractures. The hydraulic diffusivity D is a physical property that couples the hydraulic conductivity and the storativity. In the RIS literature, D is more frequently used, whereas in the hydrological literature, K and S are preferred. In this research, K and S will be referred to explicitly, as these two quantities are the fundamental properties that govern fluid flow in rocks and importantly, they are not directly proportional to each other and may vary spatially in a semi-independently manner.

6 BACKGROUND TO THE SITE

One of the main objectives of this research is to model the pore pressure diffusion in the subsurface rock in Açu reservoir. In any groundwater modelling study, it is essential that values such as water table conditions and hydraulic rock properties are estimated, since they are used as input parameters to the model. The purpose of this chapter is to present the relevant hydrological and geological data that justify the choice of parameters for the model used in chapters 7 and 8.

6.1 The hydrological regime

In this section the water balance of the catchment in which the Açu reservoir is located is discussed. A fully detailed water balance estimate of the catchment is beyond the scope of this research. However, it is useful to present a rough idea of the annual water budget and the overall hydrological catchment behaviour.

The water balance of a given catchment area is the balance between the water output, input and catchment storage changes. The main components of the water balance are:

- outputs: river discharge to the ocean and evapotranspiration;
- input: rainfall;
- storage: water bodies (e.g. reservoirs) and groundwater.

Firstly, a general description of the catchment is given and after that each of the above components are discussed in turn.

Figure 6.1 shows the Açu reservoir, the rivers in the area and the Borborema Plateaux (hereafter, BP). The BP is the most distinguished morphologic feature in the entire area shown in Figure 6.1. The BP is defined as the set of topographic heights above 200m that extends approximately from the -8°S to -6°S. The Açu reservoir is situated on the Açu river, annotated as **Aç**, in Figure 6.1.

The Açu river basin is defined as the area of land which drains topographically into the Açu river, the boundary is denoted on Figure 6.1 by a thick dashed line (the watershed). The basin comprises an area of approximately 38,000 km^2 (Costa, 1986) and is formed by the Açu river and its tributaries. The location of this river is indicated by **Aç**, in Figure 6.1. The region where the reservoir is located is fairly flat - typically below 100m. The BP also shown on the figure, is characterised by a set of elevations reaching up to 1,100 m near the 7°S. This plateau extends northwards, decreasing to 300 - 400 m in altitude. This morphologic feature performs an important role in the climate and hydrography of

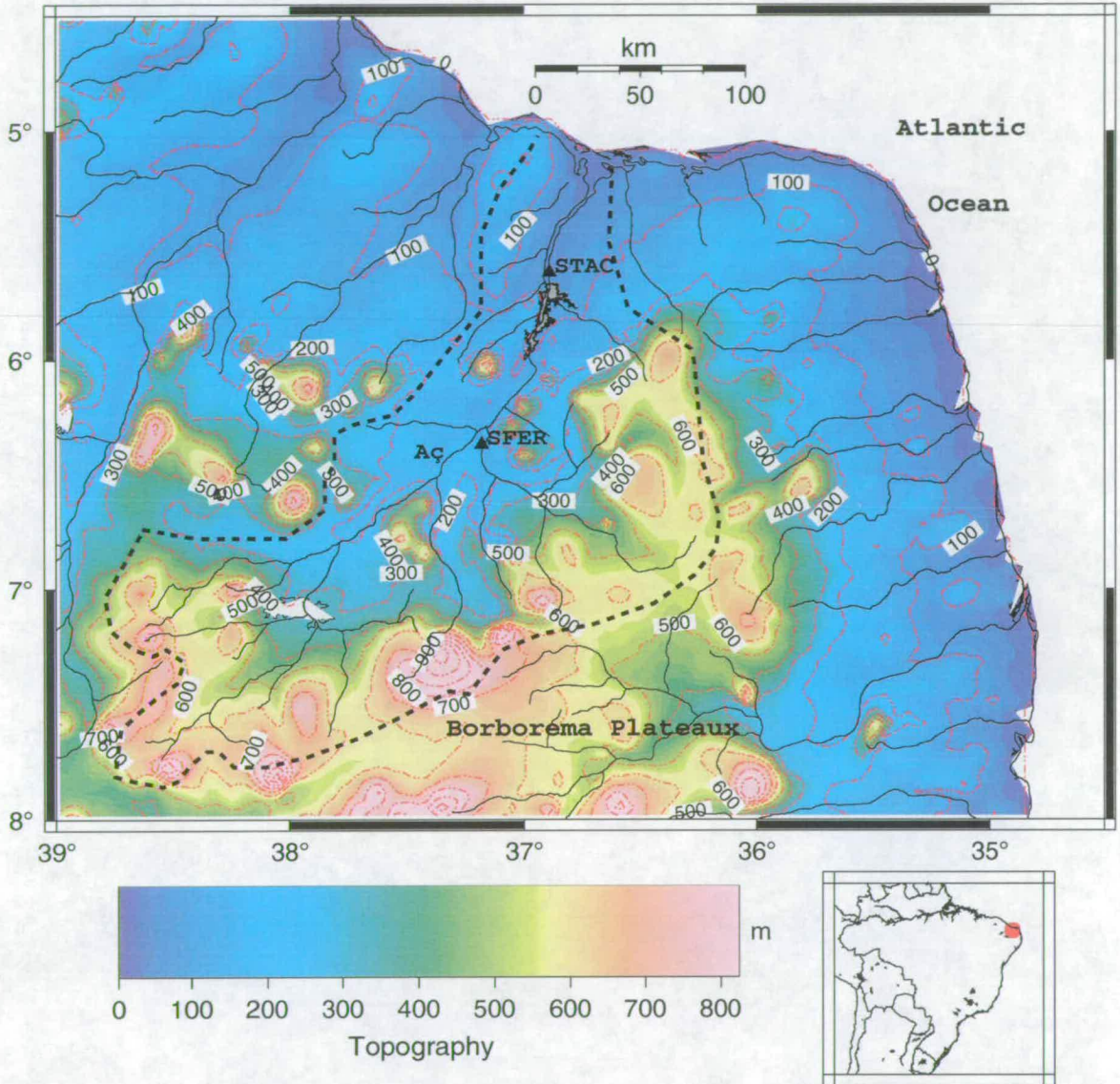


Figure 6.1: Map showing digital the elevation model (USGS, 2001) and the hydrography in NE Brazil. This figure also shows the lake contour of the Açu reservoir and the Borborema Plateaux. The label Açu indicates the Açu river and its basin boundary is denoted by a thick dashed line. River flow measurements are available at two locations: SFER and STAC.

the region. In terms of climate it is important because it is a barrier for atmospheric circulation of the SE winds that reach the East coast of NE Brazil. In terms of hydrography, it is important because the rivers in the Açu basin originate from the BP and ultimately drain into the Açu river channel.

6.1.1 Water input: rainfall

Groundwater originates from the infiltration of rainfall to the water table. The rainfall in the area where the Açu reservoir is located is controlled by winds from the SE. When those winds hit the coastal area of the eastern part of NE Brazil, an instability of this air mass is generated, allowing condensation and precipitation.

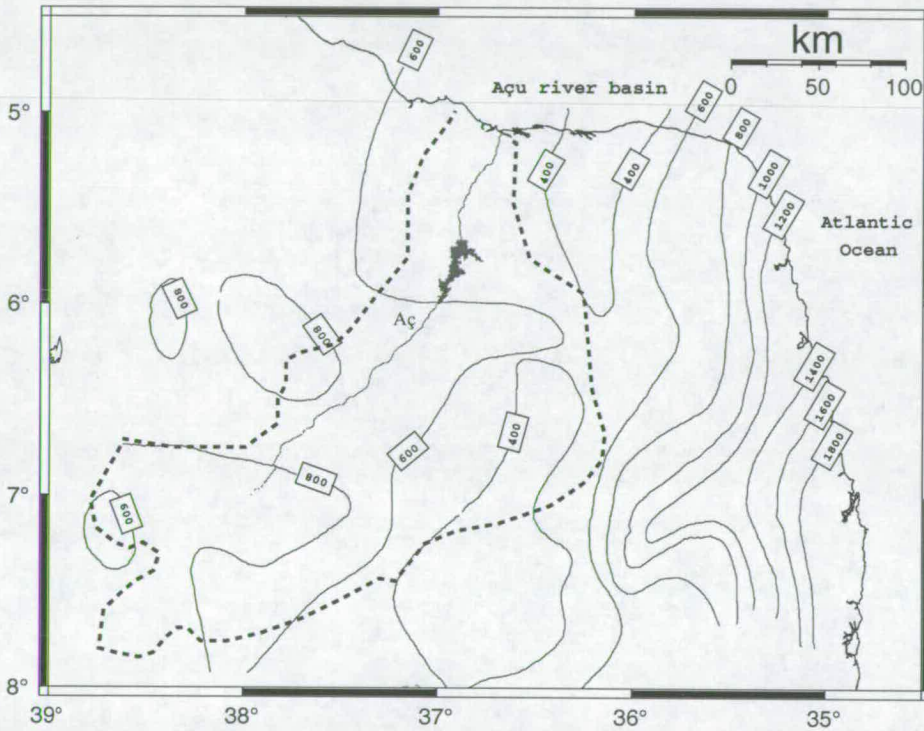


Figure 6.2: Map showing isohyets of annual precipitation (mm). The figure also shows the location of the Açu reservoir and the Açu river. The dashed lines indicated the limits of the Açu catchment area. Source: DNPM (1983).

The spatial distribution of annual rainfall in the northern part of NE Brazil is shown in Figure 6.2. It reveals a remarkable heterogeneity, from 1,800 mm/year in the east coast, down to 400 mm/year near the north coast. For the catchment area itself, the distribution of annual rainfall is less heterogeneous. In the upper reaches of the Açu river the rainfall is greatest - around 800 mm/year - due to orographic influences. Downstream, the annual rainfall reaches around 400 mm/year. In the region where the Açu reservoir is located, the precipitation is around 600 mm/year. A substantial rainfall in the catchment area (~ 300 mm) comes from the narrow rainy season (0 up to 4 months - typically from late March to end of July). At the height of the dry season (October), the precipitation is only 5 mm/month (Costa, 1986).

6.1.2 Outputs: river discharges and evapotranspiration

A map of evapotranspiration is shown in Figure 6.3. When a visual comparison is made between Figures 6.3 and 6.2, it is clear that the annual potential evapotranspiration exceeds the annual rainfall in the region where the Açú reservoir is located.

The vegetation in the area is characterised by xerophilous vegetation, which is typical of (semi-) arid areas like those in NE Brazil. One of the characteristics of these plants is the scarcity of leaves during the 'dry' season and the capacity to grow leaves and turn them green with small amount of water. A typical phenomena happens during the so called 'Green Drought': enough rain has fallen during the winter to turn the vegetation green, but not enough to generate flow in the rivers. This vegetation also has the ability to grow in soils poor in organic matter, which are typical in many parts of northeastern Brazil.

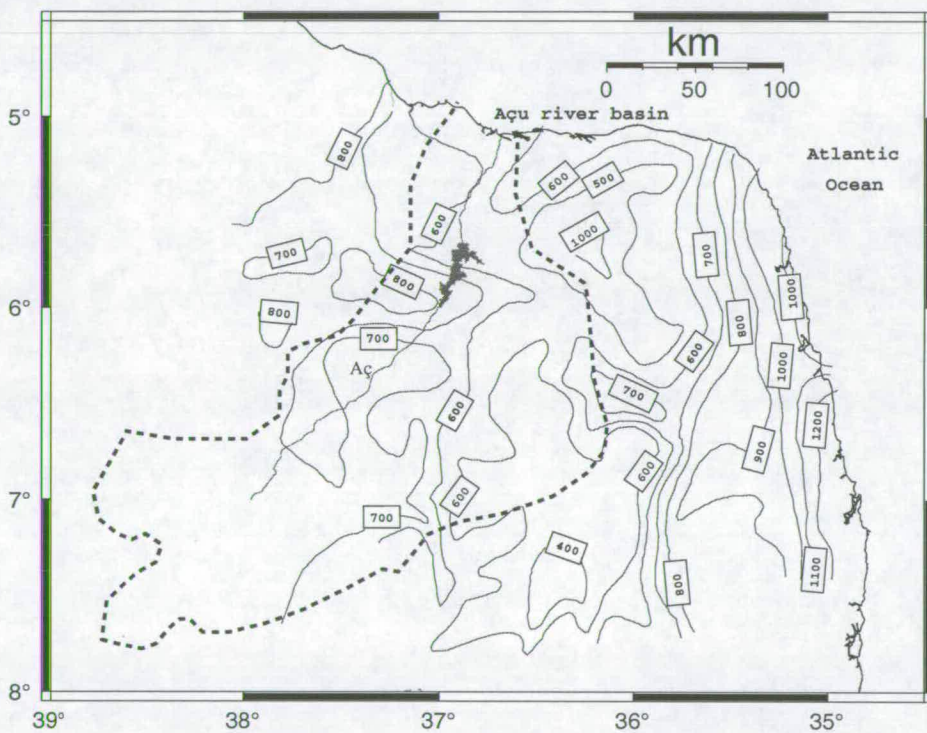


Figure 6.3: Figure showing the potential evapotranspiration in the study area (mm). The figure also shows the location of the Açú reservoir and the Açú river. The dashed lines indicated the limits of the Açú river catchment area. Source: DNPM (1983).

According to Costa (1986) the Açú river has an annual discharge of $2.55 \times 10^9 m^3/year$. Açú river used to be an intermittent river, but is now regulated by the construction of the Açú reservoir. Figure 6.1 shows the locations of two flowmeters. Marked as STAC (below dam) and SFER (above dam). SFER records the flow at one of the Açú rivers tributaries upstream of the Açú reservoir. STAC measures the flow downstream of the Açú reservoir on the Açú river itself. The total flow volume of the measurements from these two flowmeters during 1997 is shown in Table 6.1.

Figure 6.4 shows the daily flow measurements at stations SFER and STAC. The flows at SFER com-

Flowmeter	$\Sigma flow$ in 1997 (m^3)
SFER	3.5×10^7
STAC	3.2×10^8

Table 6.1: River flow measurements at SAC and SFER shown in figure 6.1, from 01/Jan/1997 to 31/12/1997. River flow data from the Agência Nacional de Energia Elétrica (ANEEL, 2001).

prise only a small percentage of the inflow to the reservoir due to the relatively low rainfall (see Figure 6.2) in this part of the catchment. No flow measurements are available on the Açu river itself upstream of the reservoir. Due to the presence of the Açu reservoir, and man-made regulated flows, the Açu river flow downstream of the reservoir shows very little flow variation during the year, being maintained at around $9m^3/s$

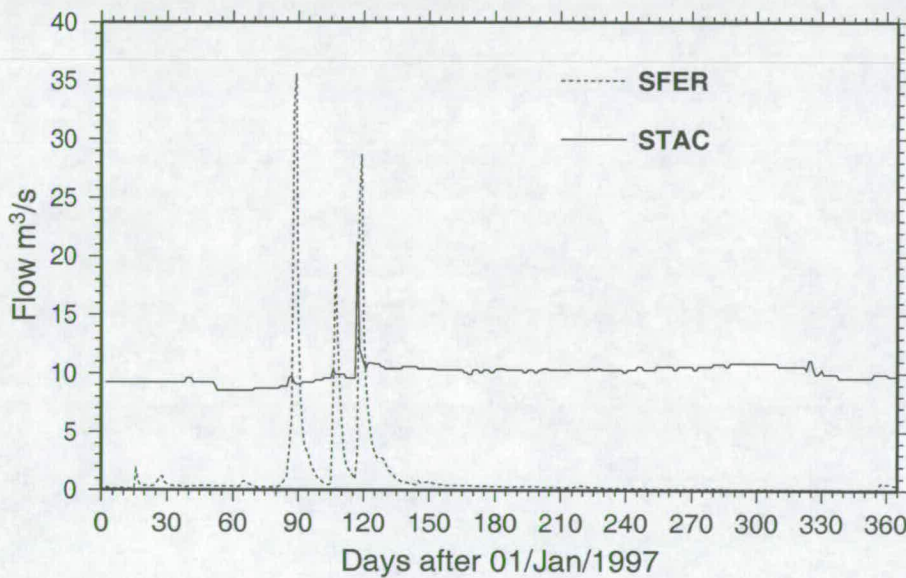


Figure 6.4: Daily flow measurements for the year of 1997 at SFER and STAC (see Figure 6.1). The dashed line refer to flow measurements at station SFER and the continuous line refers to flow measurements at station STAC. River flow data are from ANEEL (2001).

The intermittent behaviour of the Açu river tributaries upstream of the Açu reservoir is evidenced by observing the river flow at station SFER, shown in Figure 6.4. The flow regime is marked by isolated episodes of high flow in that tributary. After these episodes, the flow in the river is very low; typically less than $0.4m^3/s$ between September and January. In semi-arid areas, such as the Açu river basin system, where potential evaporation losses exceed precipitation, direct recharge to groundwater from widespread infiltration is of limited importance. Because the soil is very dry, the moisture does not spread fast enough for the falling rain to be absorbed. Thus, a film of water ponds at the surface and moves away following the surface topography. This mechanism for overland flow is called infiltration excess (de Marsily, 1986). The hydrograph for SFER shown in Figure 6.4 is typical of a hydrological regime driven by infiltration excess: the vast majority of flow occurs due to high intensity rainfall on dry soils producing flash flooding in the rainy season. Outside this period most rainfall is lost to evapotranspiration, the water table is below the river bed and river flows are extremely low, sometimes

falling to zero.

The main form of recharge (to groundwater) in these semi-arid hydrological systems is infiltration through river beds - together with localised ponding in depressions during the high-intensity flash-floods de Marsily (1986). According to Ward and Robinson (1990), the few perennial, or semi-perennial streams that do exist lose water by flow from these streams to the ground, Figure 6.5 shows a schematic illustration of such a groundwater recharge system.

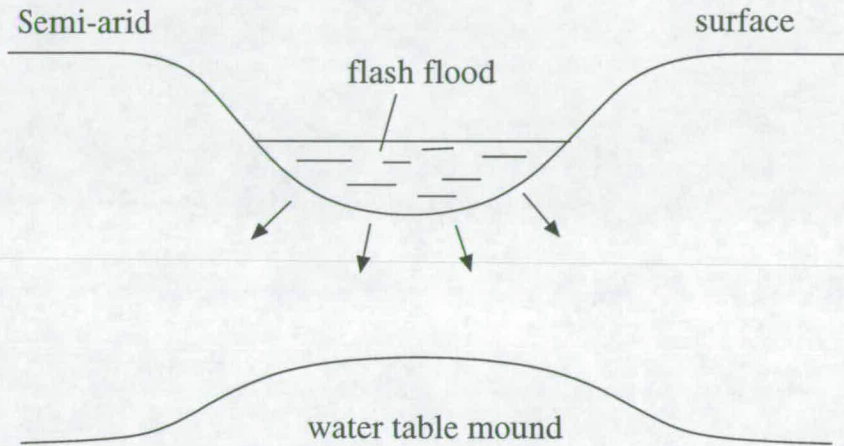


Figure 6.5: the relationship between groundwater and surface water. Schematic illustration of a groundwater recharge system in a semi-arid region. After de Marsily (1986)

Therefore, in the light of what is known about the relationship between groundwater and surface water in semi-arid regions and the intermittent nature of the river system in the upper reaches of the Açu river basin, it can be concluded that the recharge in the river basin is mostly beneath surface water features as any distributed infiltration is likely to be very small. In addition, the extremely low flows from September to December indicate that the water table is at or below the river bed upstream of the reservoir. Another important conclusion is that because the Açu reservoir constitutes the main surface water body in this semi-arid region, it is constantly leaking out water and feeding the regional water table. These assertions are supported by the observations of the regional vegetation being typical of semi-arid dry soils with flash flooding.

6.1.3 Storage

The Açu reservoir has a theoretical capacity of $2.4 \times 10^9 \text{ m}^3$ and had a maximum water depth of 34 m at the time of its construction, in 1983. Figure 6.6 shows the daily variation of the water level in the Açu reservoir from August 1987 to March 1997. The typical annual lake level fluctuations do not exceed 6 meters. Inflow data to the reservoir are not available. Outflows from the reservoir will comprise river discharge (Figure 6.4), surface evaporation, abstractions for domestic, agricultural and industrial use, and leakages to groundwater.

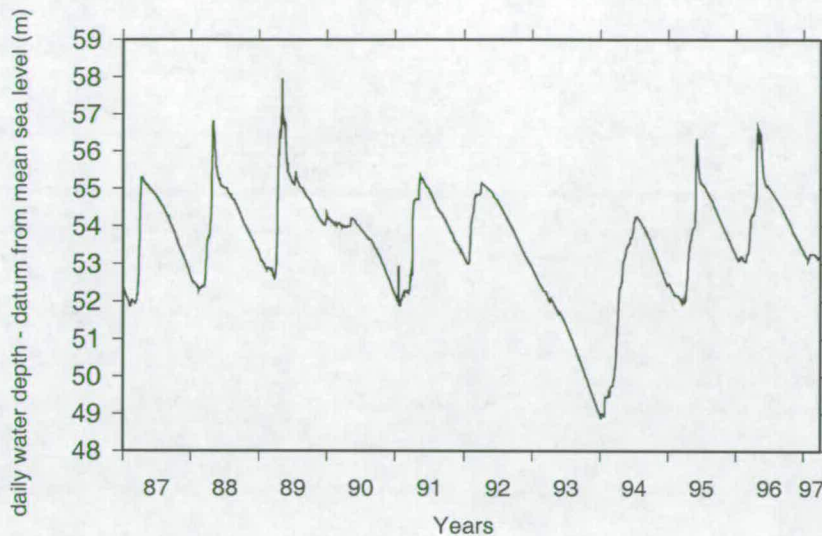


Figure 6.6: Daily water fluctuation at the Açú reservoir. Data level data from DNOCS - Depto. Nacional de Obras Contra a Seca, Brazil.

6.1.4 Groundwater storage

The regional depth of the water table in the area is very difficult to assess because the region lies on a crystalline basement and the population mostly rely on surface water for farming and human usage. This implies that there are very few wells in the region and those water level data that are available may reflect local rather than groundwater levels. Nevertheless, one water table depth constraint is available. Figure 6.7 shows the location of this well. The height of the water measured by this well was 30m above the sea level (data from CPRM (1999)). This height represents a single time point and may not represent the actual height of the water table in a regional scale.

Upstream, no wells are available to assess the depth of the water table, however, as discussed in section 6.1.2 the river hydrograph confirms the water table to be at or below the beds of the inflowing rivers. According to the topographic data from SUDENE (1970), the river bed is at 50m above sea level. Figure 6.7 shows the location of this topographic height at the river bed toward the south end of the reservoir. No well data are available for the east and west sides of the reservoir. However, it is reasonable to assume that groundwater flow follows the regional topography and is flowing from the source area of the BP toward the ocean. Hence, the east and west boundary domain will thereafter be assumed to be streamlines and hence, be no flow boundaries in Chapters 7 and 8.

6.2 Basement geology and hydrological properties

The crystalline basement where the Açú reservoir was built is composed of a paragneiss, biotite gneiss, gneiss-migmatic complex of Archean formation and biotite granite of Neoproterozoic age. Due to this igneous nature, the water absorption and infiltration is very low, when compared to sedimentary rocks, for instance. Consequently, in the modelling of the pore pressure diffusion in the area, the hydraulic

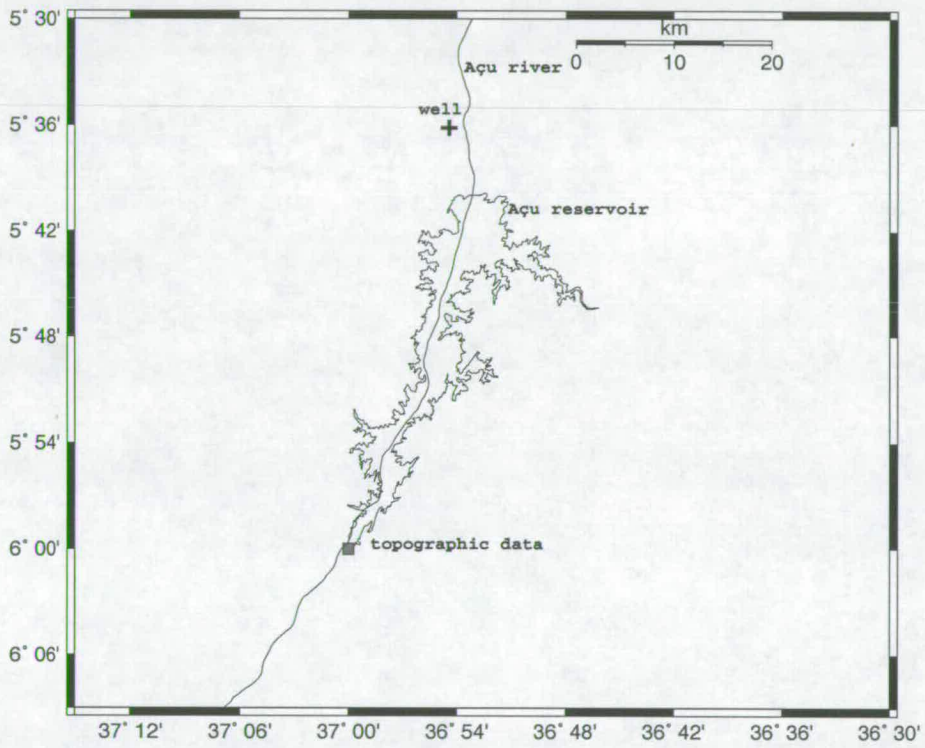


Figure 6.7: Locations of the well and topographic points used for water table height constraints. Well data and its location are from CPRM CPRM (1999).

properties values assigned for the matrix are those reported for basement rocks in the literature.

For basement rock such as that in the area where the Açú reservoir is located, the average values selected from the literature derived from borehole measurements of K and S are $8.5 \times 10^{-5} \text{ m/day}$ and $1.0 \times 10^{-6} \text{ m}^{-1}$. Consequently, these values will be applied as initial estimates of K and S in the modelling study.

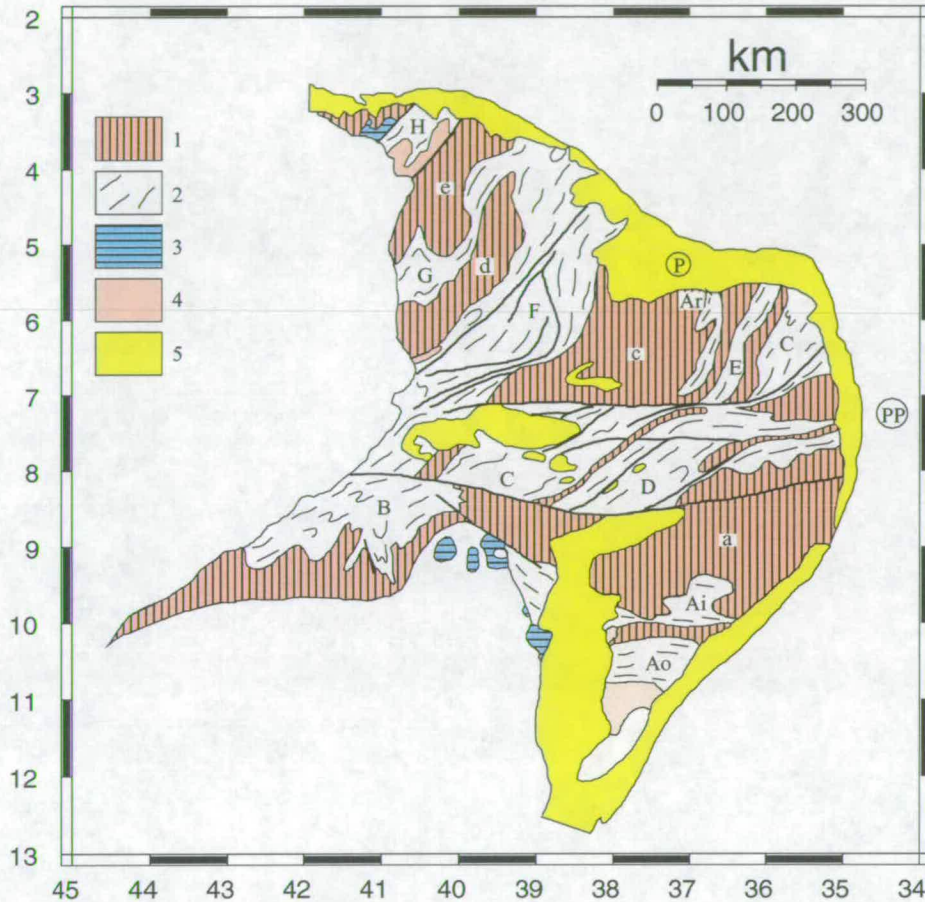


Figure 6.8: Borborema Province. Legend: **1** = Older basement reworked during the Upper Precambrian (a = Pernambuco Alagoas Massif, b = Teixeira Massif, c = Rio Piranhas Massif, d = Tróia Massif, e = Santa Quitéria Massif); **2** = Brasiliano fold belts (A = Sergipán belt, with o = outer zone and i = inner zone, B = Riacho do Pontal belt, C = Piancó-Alto Brígida belt, D = Pajeú-Paraíba belt, E = Serdó belt, F = Jaguaribe belt, G = Curu-Independência belt, H = Médio Coreaú belt); **3** = sedimentary covers correlative of the Brasiliano belts; **4** = molasse deposits; **5** = Phanerozoic sedimentary covers. Heavy lines represent major faults. After de Almeida *et al.* (1981). **P** = Potiguar basin; **PP** = Pernambuco-Paraíba basin. Here, the locatin of the Açú reservoir is plotted (over the Rio Piranhas Massif) labelled as *Ar*.

6.3 Summary

From the hydrological regime of the catchment area and the hydrological properties of the area, the following table of data has been compiled that will be used as model parameters for the groundwater modelling in Chapters 7 and 8.

Data	value
Height of water table north of the dam	30m
Height of water table south of the dam	50m
Boundary conditions to the east and west of the reservoir	no flow
Initial estimate of hydraulic conductivity of the crystalline basement	$8.5 \times 10^{-5} \text{m/day}$
Initial estimate of hydraulic storativity of the crystalline basement	$1.0 \times 10^{-6} m^{-1}$

Table 6.2: Summary of data used in groundwater modelling.

7 GROUNDWATER MODELLING - HOMOGENEOUS MODEL

As discussed in Chapter 2, the relationship between water level variations and seismicity in artificial lakes is well established (Bell and Nur, 1978; Roeloffs, 1988; Gupta, 1992; Rajendran and Talwani, 1992; Talwani, 1997). At Açu, the induced nature of the seismicity has been recognised by Ferreira *et al.* (1995), do Nascimento (1997) and also in Chapter 4. According to these authors, the dominant mechanism of RIS is the diffusion of pore pressure through the rockmass beneath the Açu reservoir.

As reviewed in Chapter 2, the models so far developed to investigate reservoir-induced seismicity are either 2D homogeneous models (Roeloffs, 1998; Talwani, 1997), or 2D homogeneous models containing a 1D linear fault with permeability different from that of the homogeneous matrix (Bell and Nur, 1978). These modellers investigated the role of the drained and undrained response of the crust beneath the reservoir, and the effect of inhomogeneities in rock properties in reservoir induced seismicity. Simpson and Narasimhan (1992) concentrated their approach on the effects of inhomogeneities due to the presence of a high permeability fault. Simpson and Narasimhan (1992) separated the elastic and pore pressure effects into two steps in their 2D model simulation. Other authors (Lee and Wolf, 1998) studied the effect of a highly permeable fault in a homogeneous 2D matrix media. Lee and Wolf (1998) also studied the effect of media heterogeneity in the propagation of fluids in a 2D rock matrix. The only 3D model, by Kalpna (2000), does not take into account the presence of highly permeable faults in the 3D matrix media.

In this Chapter, a numerical model is used to investigate the pressure field beneath the Açu reservoir. The additional features of this model are:

- inclusion of a 3D geometry;
- incorporation of realistic boundary conditions to investigate the fluid flow in the area;
- inclusion of a 2D structural inhomogeneity (fault);

In this Chapter, the modelling approach presented concentrates on the diffusion process (drained response), since it is the dominant mechanism of RIS at Açu.

7.1 Numerical modelling with PARADIGM

As stated earlier, the diffusion of pore pressure is the predominant mechanism controlling the seismicity in the region. To model this process, a three-dimensional groundwater flow code, PARADIGM

(Lunn and Mackay, 1997) is used. The flow equations in PARADIGM are solved using an implicit finite difference solution on a 3D mesh. The 3D mesh is formed by nodes in each of the spatial directions which can be variably spaced. Figure 7.1 shows a schematic diagram of a 3D mesh.

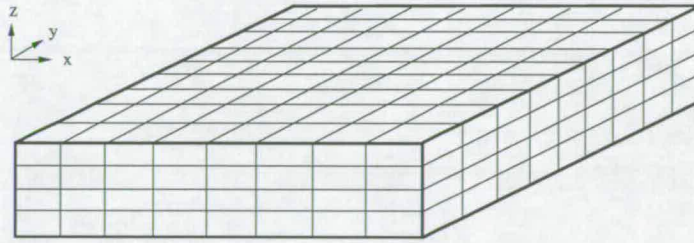


Figure 7.1: Schematic diagram showing a schematic diagram of a regular 3D mesh defined in PARADIGM.

The governing flow equation for the matrix is that for unsteady flow in a porous media:

$$\nabla \cdot (\underline{\mathbf{K}} \cdot \nabla h) = S_s \frac{\partial h}{\partial t} \quad (7.1)$$

Well, groundwater recharge, and surface water features are incorporated as fixed head boundaries or source/sink terms for groundwater flow. Hydraulic properties within PARADIGM can be defined as fully heterogeneous by specification on a nodal basis. PARADIGM also allows for the inclusion of faults in the modelling; this will be discussed later in section 7.4.

7.2 Regional and refined local models in the Açú reservoir

7.2.1 Regional model

In order to model the pressure diffusion beneath the Açú reservoir, a regional groundwater model was derived comprising the regions between $-6^{\circ}00'S$ to $-5^{\circ}38'S$ and $-37^{\circ}04'W$ to $-36^{\circ}45'W$ and 8km depth (33.7x41.1x8.0 km). This model was built in PARADIGM with a grid resolution of 91x111x80 elements as shown in Figure 7.2.

A constant head boundary condition was applied to all the southern and northern boundary nodes. The values of the head were 50m for the southern nodes and 30m (downstream for the dam) for the northern nodes. The 30m value for the north boundary conditions were taken from a well on the Potiguar basin as discussed in Chapter 6, a few kilometres north of the dam (CPRM, 1999). A 50 m constant head boundary condition was assigned to the southern boundary assuming that the regional water table is at or below the bed of the inflowing rivers (Chapter 6). For the west and east nodes, a no-flow boundary condition was assigned; this is consistent with the regional groundwater flowing in a northerly direction toward the sea.

Because of the seasonal variation of the water level in the lake, the model has been designed to take into account the effect of the change in lake level shape due to annual flooding of different low-lying areas by the lake. To model this effect, a time-varying boundary condition on the top of the

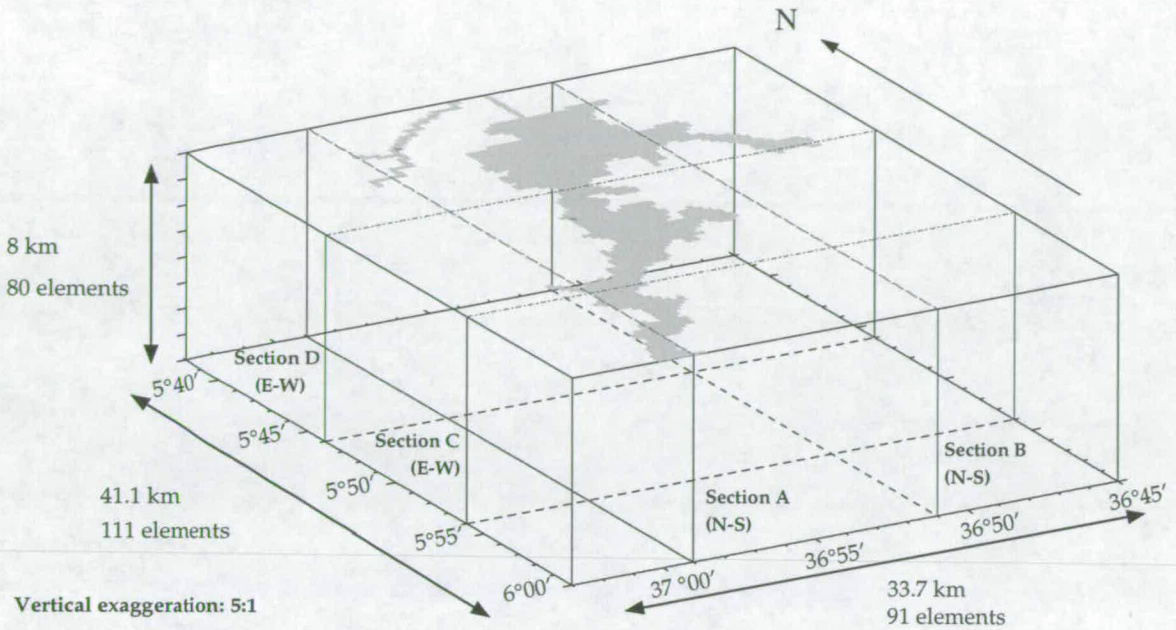


Figure 7.2: Regional model. The reservoir is shown in grey.

3D grid is employed. These time-varying boundary conditions are calculated from the topographic data and comprise the different shapes that the reservoir covers for different depths of water level in the reservoir. To produce the lake shapes, topographic maps at the scale 1:100,000 from SUDENE (Superintendência do Desenvolvimento do Nordeste) were interpolated using GMT (Wessel and Smith, 1998) and used to provide different lake level contours. After this interpolation, the lakes were gridded in order to match the grid resolution used in the regional model. The result of these operations is shown in Figure 7.3.

Because the topographic coverage is not completely accurate, some nodes of the lake are assigned as being part of the lake, that are in reality, dry. To overcome this problem, the lake boundary nodes shown in Figure 7.3 were manually edited wherever field evidence indicated that regions were not flooded. Figure 7.4 shows the final result. In this figure, rivers Paraú and Açu (the river that the Açu reservoir regulates) were added to the regional flow model. These rivers are defined as nodes of constant head at the ground surface in PARADIGM, with a value taken from the topographic maps of 32m above sea level.

A summary of boundary conditions and the model parameter data is shown in Table 7.1 for the regional model.

7.2.2 Simulation results from the regional model

In the first instance, PARADIGM has been run for the regional model assigning a constant value of hydraulic conductivity of $K=8.5 \times 10^{-7}$ m/day and a storativity of $S=10^{-6}$ for the entire rock matrix. These values of K and S were chosen because they represent typical values for basement rock, as shown in Chapter 5. The seasonal lake variation used in the simulations is a simple repetitive sinusoidal



Figure 7.3: Figure showing the lake nodes for different lake levels above ordinance datum (a. o. d.).

Fixed head boundary condition to the south	50 m
Fixed head boundary condition to the north	30 m
Boundary condition in west and east sides	no flow
Fixed head boundary condition for the tributaries	32 m
Discretisation in the x and y directions	370.65 m
Discretisation in the z direction	100 m
Number of nodes in the x direction	91
Number of nodes in the y direction	111
Number of nodes in the z direction	80
Number of time steps	45
Time step length	8 days
Matrix hydraulic conductivity	8.5×10^{-7} m/day
Matrix storativity	$10^{-6} m^{-1}$

Table 7.1: Boundary conditions and model data for the regional model.



Figure 7.4: Figure showing the lake nodes for different lake levels. Here, some nodes were removed/added based on field data to correct some unrealistic effects of the interpolation and to add rivers Paraú and Açú (see text).

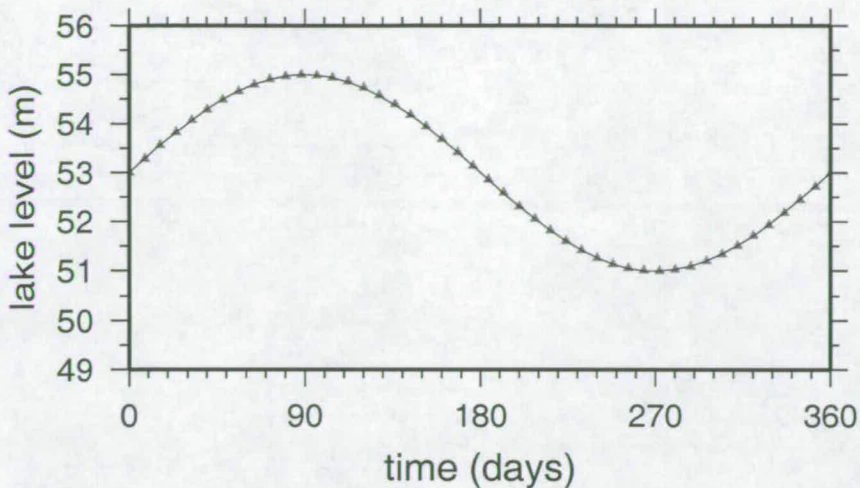


Figure 7.5: Figure showing the lake level input used in the simulations.

oscillation, as shown in Figure 7.5. Each year comprises 45 time steps and each time step has a length of 8 days; so, a complete cycle has 360 days. These assumptions simplify the simulation, reducing the computational expense, whilst making a negligible difference to the resulting head predictions.

The model uses as an initial condition the piezometric head predictions of the steady-state simulation of equation 7.1 for a 53m lake level at the surface. In other words, equation 7.1 is solved with the time varying term and the term on the right-hand side of the equation set to zero to provide initial conditions for the time-varying simulation; i.e.

$$\nabla \cdot (\underline{\mathbf{K}} \cdot \nabla h) = 0 \quad (7.2)$$

The results shown in Figure 7.6 are piezometric head predictions after 360 days for cross-sections A, B, C and D marked on Figure 7.2. The length of the arrow indicates the magnitude of the predicted piezometric head gradient ∇h , and the direction of flow is given by the direction of the arrow.

In **section A** of Figure 7.6, the locations of the reservoir and the Paraú river (marked as “tributary” in Figure 7.6) are indicated, and their effects on the head predictions are clearly apparent; the lake is a groundwater source and the river behaves as a groundwater sink. The regional flow is in a predominantly south to north direction as expected. In the south, the piezometric head gradient is low, as shown by the separation of the isovalues of heads and the size of the flow arrows. Close to the reservoir small N-S flows are predicted since the groundwater outflows from the reservoir are locally overriding the regional groundwater flow. Towards the north, a strong gradient due to the presence of the dam is predicted.

In **section B**, one can see the effect of both the reservoir and the dam wall. Towards the southern end, the head in the reservoir is close in value to the regional water level assigned at the southern boundary. Hence, the flow rate is very low. As one approaches the north end, due to the presence of the reservoir and the dam, the piezometric head gradient becomes stronger, hence the density of isovalues of predicted piezometric head and the size of the flow arrows increases.

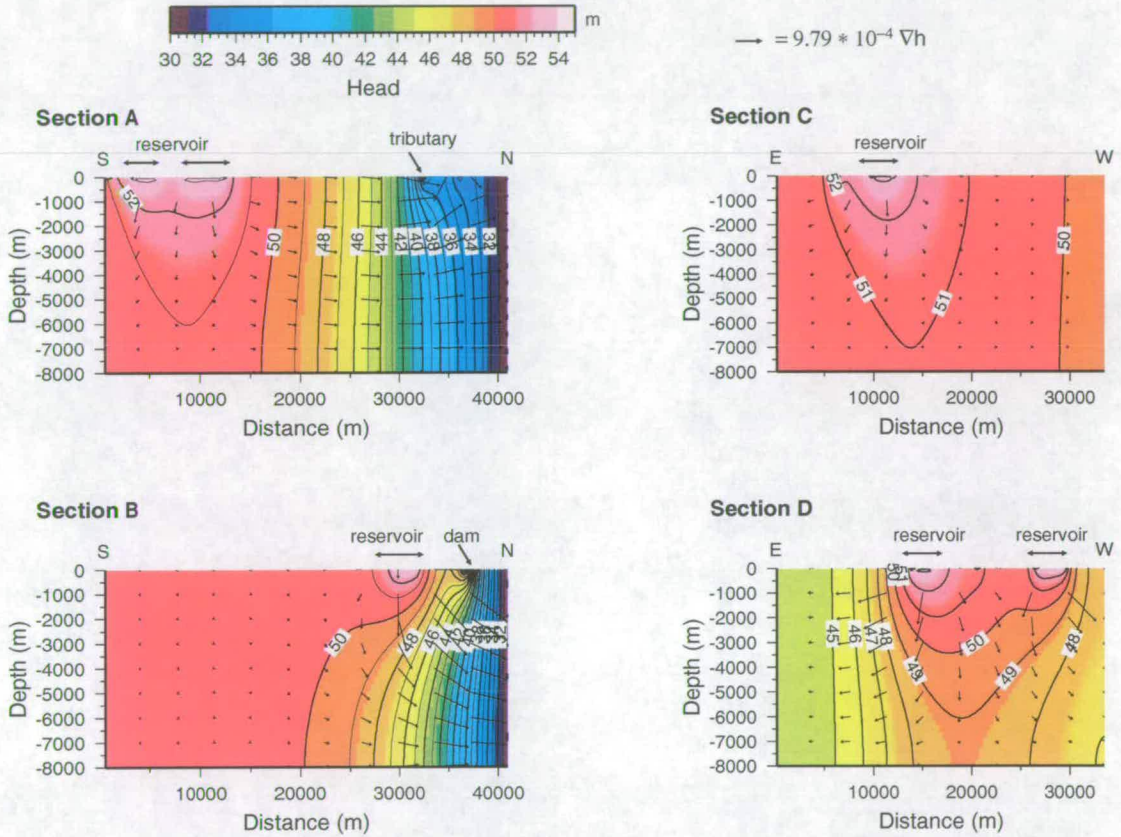


Figure 7.6: Piezometric head predictions from the sections indicated in Figure 7.2, $K=8.5 \times 10^{-7} \text{ m}^2/\text{day}$ and $S=10^{-6} \text{ m}^{-1}$. The arrows indicate direction and magnitude of the piezometric head gradient. Double headed arrows indicate the presence of the reservoir/tributaries.

Sections C and D show respectively E-W cross-sections towards the southern and northern ends of the regional model, shown in Figure 7.2. In both cases, the no-flow boundary conditions ensure that there is very little lateral flow and that regional groundwater moves predominantly in a S-N direction towards the ocean.

Figure 7.7 shows piezometric head predictions of the same model simulation for 3 different layers at depths of 50, 950 and 2,950 m.

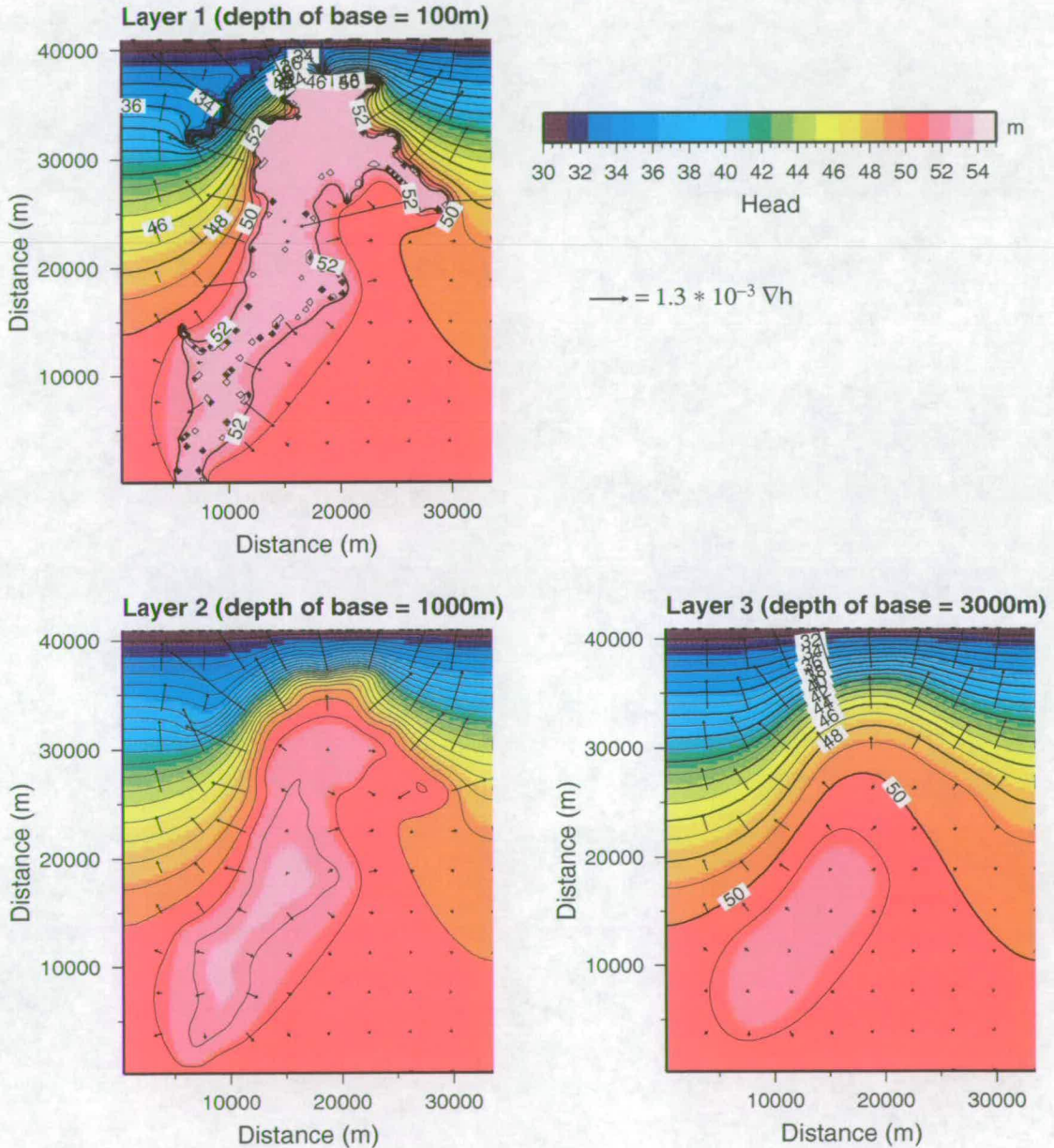


Figure 7.7: Piezometric head predictions after 360 days from layers at depths of 50, 950 and 2,950 m. $K=8.5 \times 10^{-7}$ m/day and $S=10^{-6}$ m^{-1} . The arrows indicate direction and magnitude of the piezometric head gradient.

Layer 1 shows an outward flow pattern from the lake, demonstrating it to be a regional groundwater source. At this depth, the effects of the interactions of the tributaries with the lake and the irregular

lake shape are stronger than, for instance, at deeper layers. The strong S-N gradients at the northern part of the model are evident from the density of piezometric head isovalues, and by the size of the flow arrows. This reflects the strong head gradient across the dam. In the south, the piezometric head gradients are smaller, and at shallow depths the regional groundwater flow is masked by the outward leakage of water from the lake.

Layers 2 and 3, which are at depths of 950 and 2,950 m, show less complex flow patterns. The effects on groundwater of the tributaries and the irregular lake shape become weaker as depth increases. By 3,000 m whilst a recharge mound is still visible beneath the lake, the groundwater flows are less strong and away from the lake flows are influenced by the S-N regional gradient. This decrease in influence of the reservoir continues as one investigates layers at even greater depths.

The predicted piezometric head cross-sections shown in Figure 7.6 are used as lateral boundary conditions for a more detailed model of the seismic area: this is described in the next section.

7.2.3 Refined local model

In order to obtain a more detailed flow model of the area of seismic activity, the predicted heads from cross-sections A, B, C and D (Figure 7.6) from the regional model were used as lateral boundary conditions for a refined local model.

For the refined model, the resolution was doubled (i.e. one node in the x and y directions from the regional model becomes 4 nodes in the refined model). The vertical resolution remains the same. Figure 7.8 illustrates this procedure. The refined model, shown in Figure 7.9, is 14,826x14,826x8,000

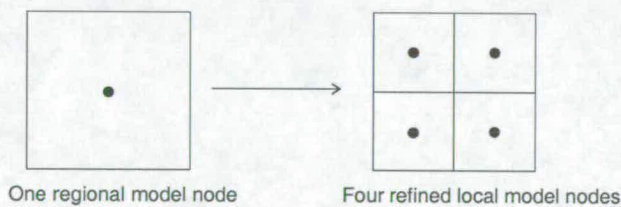


Figure 7.8: Transformation employed to every regional node represented in the refined model.

m with 80x80x80 grid elements and is centred around the area of maximum seismic activity. Figures 7.9a and 7.9b show perspective and plan views of the refined model respectively.

7.2.4 Simulation results from the refined local model

For the results of the simulation with the refined model, a similar approach to that taken in the regional model is now used again. The initial conditions are again determined by solving equation 7.2 using, as fixed boundary conditions, the outputs from the regional model and the 53m lake level at the surface.

The parameter values are the same as those of the regional model: only the grid resolution has changed. Table 7.2 shows the model parameters for the regional model. Figure 7.10 shows piezometric head pre-

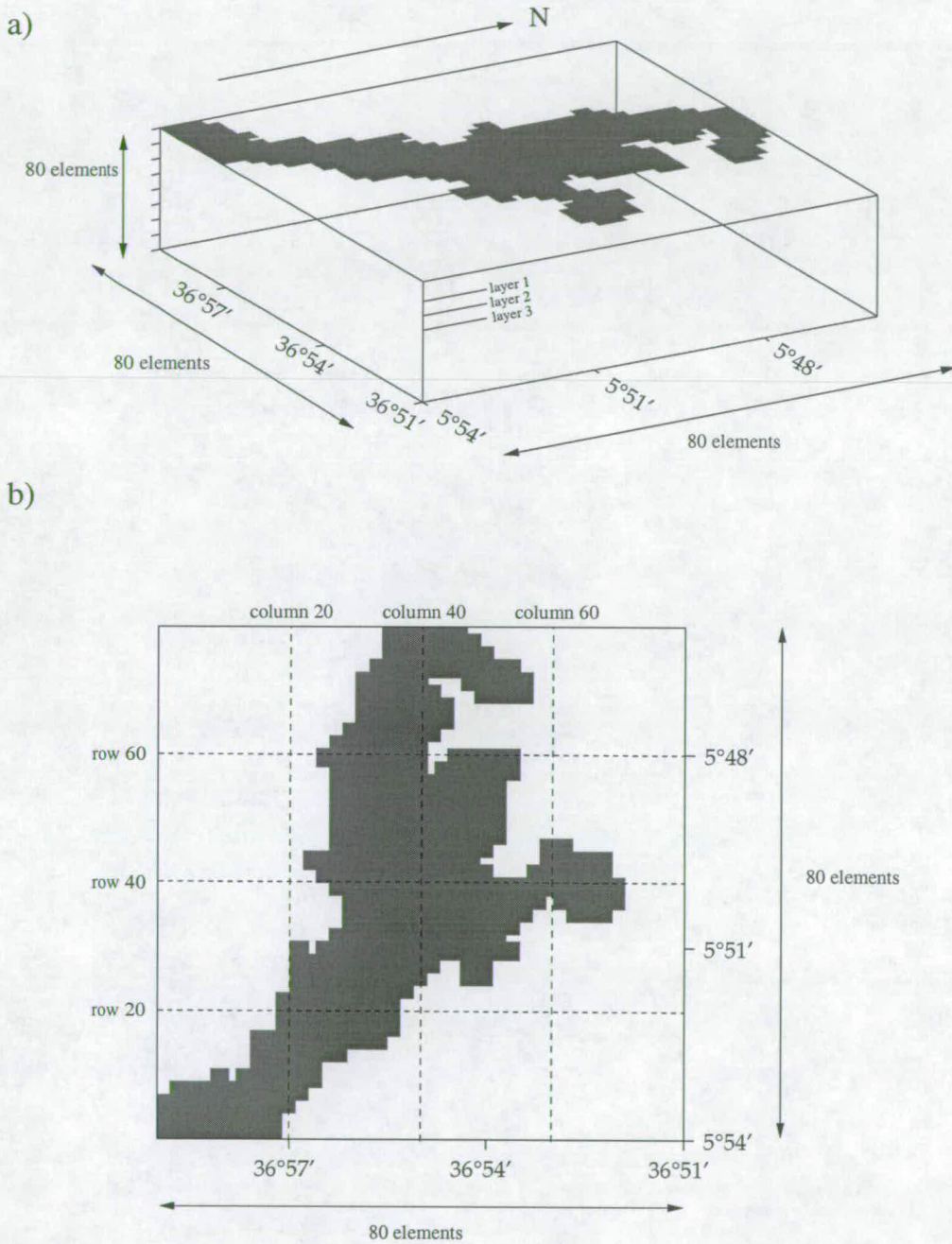


Figure 7.9: Refined groundwater model of the Açu. The output from sections A, B, C and D (Figure 7.3) from the regional model were used as lateral boundary conditions for this refined local model. The locations of some rows, columns and layers are marked for future reference.

Discretisation in the x and y directions	185.325 m
Discretisation in the z direction	100 m
Number of nodes in the x and y directions	80
Number of nodes in the z direction	80
Matrix hydraulic conductivity	8.5×10^{-7} m/day
Matrix storativity	$10^{-6} m^{-1}$
Number of time steps	45
Time step length	8 days

Table 7.2: Model parameters for the refined model in Figure 7.10.

dictions from the refined model for rows, columns and layers marked on Figure 7.9. All the piezometric heads presented here in this subsection are results from of the time-varying simulation after 360 days. The bottom panel of Figure 7.10 shows three E-W cross sections for rows 20, 40 and 60, the positions of which are indicated in Figure 7.9b. The flow lines indicate that, as expected, flow is outwards from the lake and the magnitude of these outflows increases as one moves from row 20 to row 60 (towards the dam). The flow is also pulled more strongly towards the east due to the presence of the Paraú river in the regional model. The middle panel of Figure 7.10 shows the piezometric head predictions for three S-N cross sections at columns 20, 40 and 60. It can be seen that they all reflect the regional south-to-north flow, and show groundwater recharge occurring from the reservoir, as indicated by the directions of the flow lines. The upper panel of Figure 7.10 shows piezometric head predictions for layers at depths of 50, 950, and 2,950 m. The flow lines indicate flow outwards from the lake. As with the regional model, as one moves deeper, the effect of the lake is less noticeable.

All of the PARADIGM results described so far are for a single point in time. It is now useful to analyse the time varying response at individual nodes in the refined model. Figure 7.11a shows the sinusoidal idealised lake level variation. Figure 7.11b shows the head values for nodes within the matrix at different depths. These nodes are at $x=40$ and $y=40$ in the centre of the refined model at depths of 50, 150, 250 and 350 m. For the literature derived values of K and S (8.5×10^{-7} m/day and $10^{-6} m^{-1}$) shown here, only the top node directly beneath the reservoir exhibits the annual head variation. Beyond this, the damping of the pressure wave is so rapid that any oscillation is negligible. Obviously, such rapid damping can not be the case if pressure changes at approximately 2km depth are the cause of the ongoing seismicity. It is therefore necessary to investigate further the values of K and S in the light of the seismicity data.

7.3 Finding the time lag with the matrix model

In this section, the induced seismicity in the Açú reservoir will be investigated by analysing the piezometric water head diffusion (or analogously, the pressure diffusion) using the refined local model. Different values of hydraulic properties will be explored to simulate the observed delay between the peak water level in the reservoir and the maximum seismic activity.

The flow diagram in Figure 7.12 describes the general procedure adopted for deriving hydraulic properties from the seismological data.

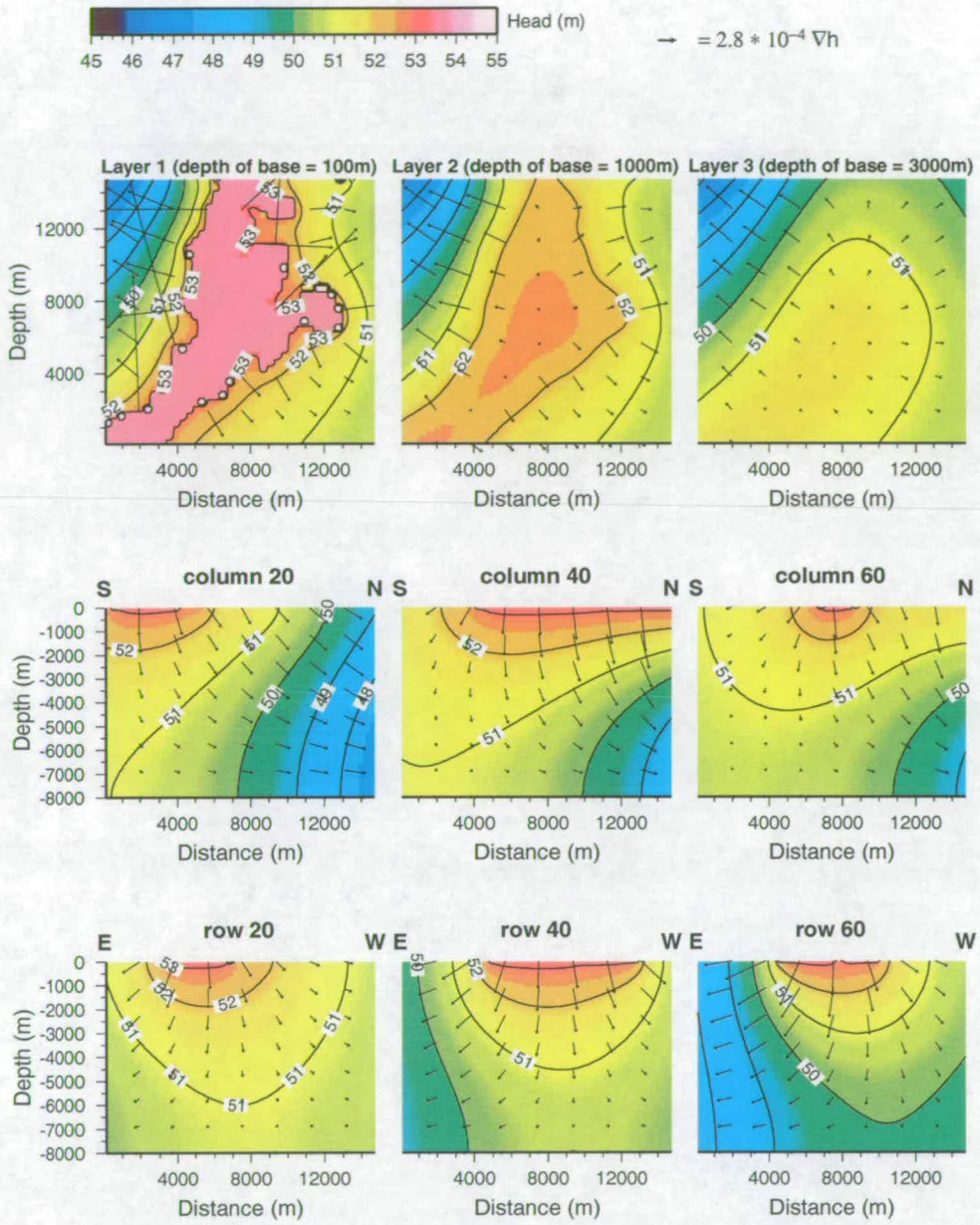


Figure 7.10: Example of piezometric head predictions after 360 days for the refined model. The bottom panel shows the output from rows 20, 40 and 60. The middle panel shows output from columns 20, 40 and 60. The upper panel shows outputs for layers at depths of 50, 950, and 2,950 m. In this run, $K=8.5 \times 10^{-7}$ m/day and $S=10^{-6} m^{-1}$. The arrows indicate the direction and magnitude of the piezometric head gradient.

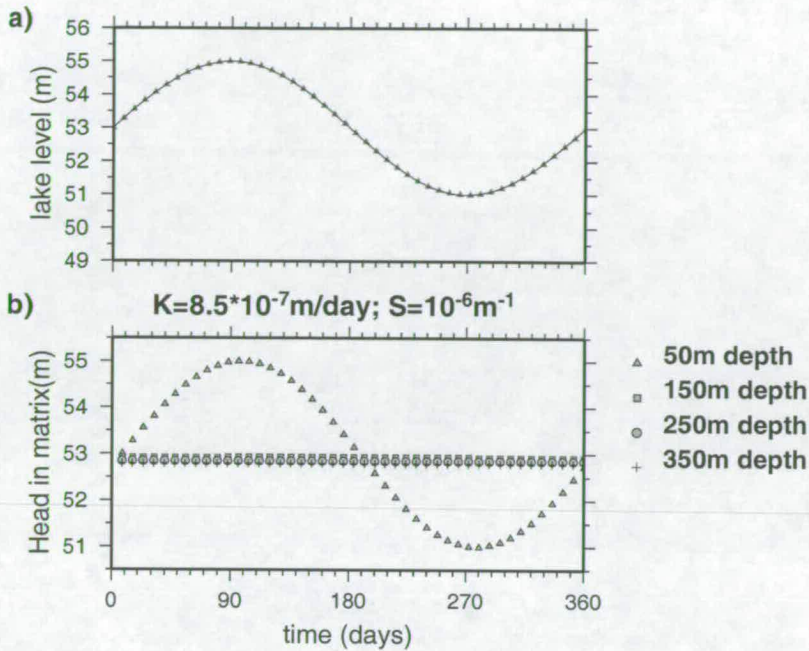


Figure 7.11: Time varying output for nodes in the centre of the refined model at depths of 50, 150, 250 and 350 m.

In **stage 1**, for a given pair of K and S values i.e values of hydraulic diffusivity, D , a steady-state solution is derived for the regional model. This steady-state solution uses, as fixed boundary conditions, the values shown in Table 7.1 and the 53m lake lake shape shown in Figure 7.4. Then, a regional time varying simulation is run (**stage 2**) until the head predictions reach what is described here as an oscillating steady-state. This is achieved when at each node in the grid, the head varies in an annual repetitive cycle. An example of the head variation for a single matrix node at 1050m depth is shown in Figure 7.13. Here, five years have been simulated, the final two years of which are the same, so an oscillating steady-state has been reached. This approach ensures that any errors implicit in the choice of initial conditions have been removed. In **stage 3**, the piezometric head predictions of sections A, B, C and D (shown in Figure 7.2) are output from the regional model. Those boundary conditions are used for the next stage. In **stage 4**, a steady-state solution is derived for the refined model. Then, in **stage 5**, a time varying simulation with the refined model is run until the head predictions reach an oscillating steady-state, as in stage 2. In **stage 6**, the time delay between the peak in water level input and the peak in the piezometric head prediction at 2,050m depth is compared with the time delay between the peak in lake level and the maximum seismic activity at 2.0km depth. The time delay that is to be achieved is the one observed for cluster a, in 1995. The time delay from the seismological data is ≈ 4.5 months (between 131 to 144 days), as shown in Table 4.2. Each time step has a length of 8 days and the synthetic lake level input has the peak at the 10th time step (88th day after the beginning of the year). So, the time delay found in our procedure has to be a multiple of 8 days. Given the time delay from the seismological observations, a delay of 136 days is therefore the time delay to be calibrated using the refined model. On **stage 7**, depending whether the delay was larger than 136 days, or smaller than 136 days, a new value of D is chosen and the procedure starts again from stage 1. If the time delay is 136 days, D is accepted (**stage 8**).

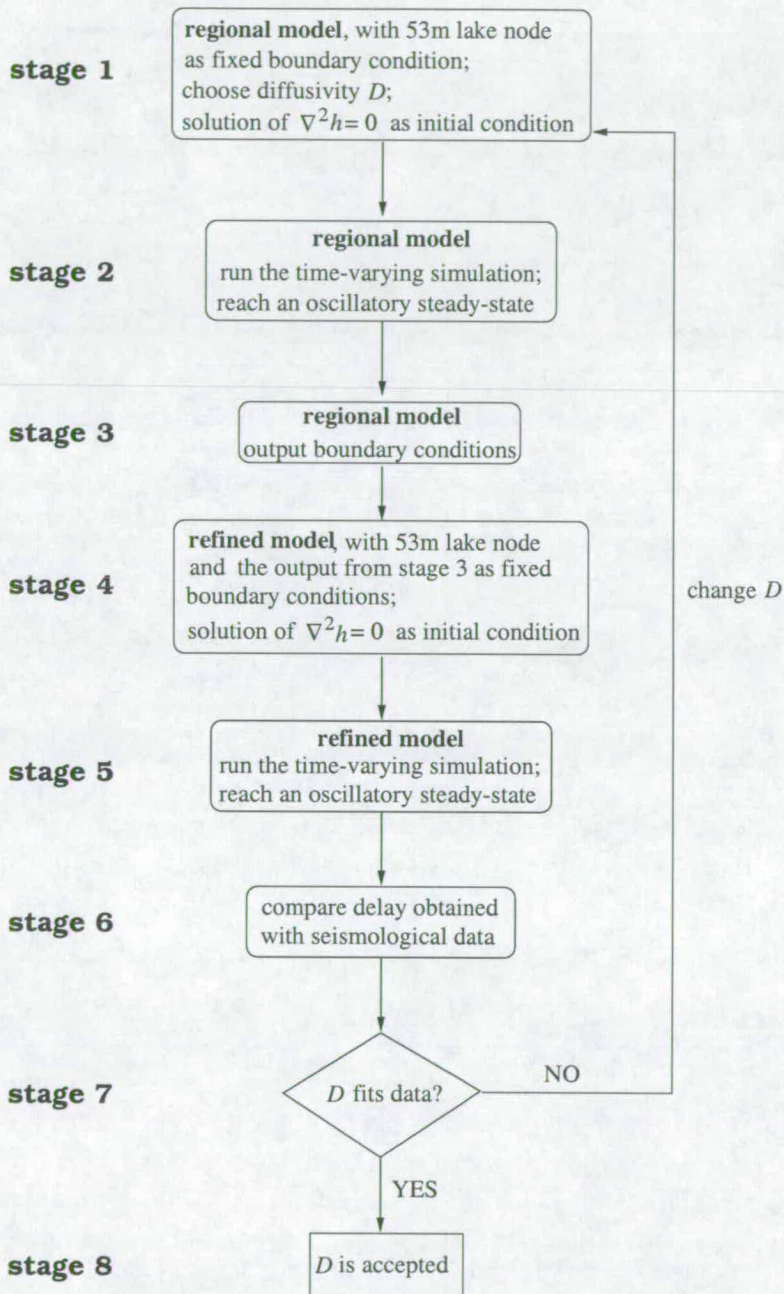


Figure 7.12: Flow diagram showing the general procedure adopted to match the observed delay between the peak in water level in the reservoir and the maximum seismic activity.

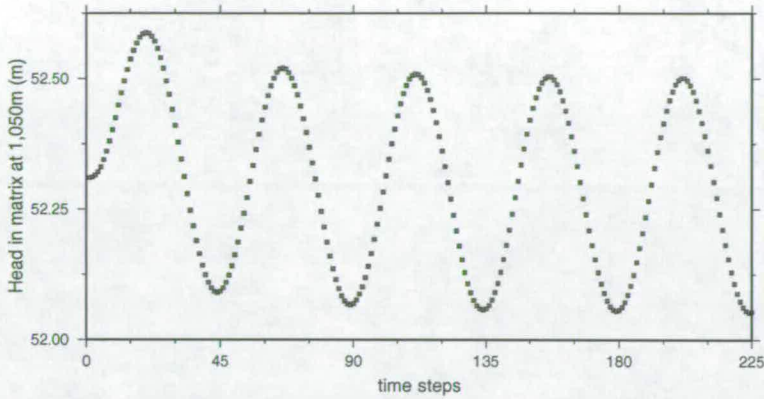


Figure 7.13: Node at depth reaching oscillatory steady-state regime. Only after approximately 180 time steps (each time step has a length of 8 days) does the piezometric head reach an oscillatory steady-state regime.

The value of D that was determined by matching the observed delay between the peak in water level in the reservoir and the maximum seismic activity using the procedure described in Figure 7.12, was $5.5 \times 10^3 \text{ m}^2/\text{day}$. Given a value for intact rock for S of $1.0 \times 10^{-8} \text{ m}^{-1}$ this corresponds to a values for K of $5.5 \times 10^{-5} \text{ m/day}$ Figure 7.14a shows for these values the lake level variation and the resulting predicted head values at 1,950m depth. The 1,950m depth corresponds to the observed hypocentral depth in 1995 and the time lag corresponds to that observed within the real seismological data in 1995.

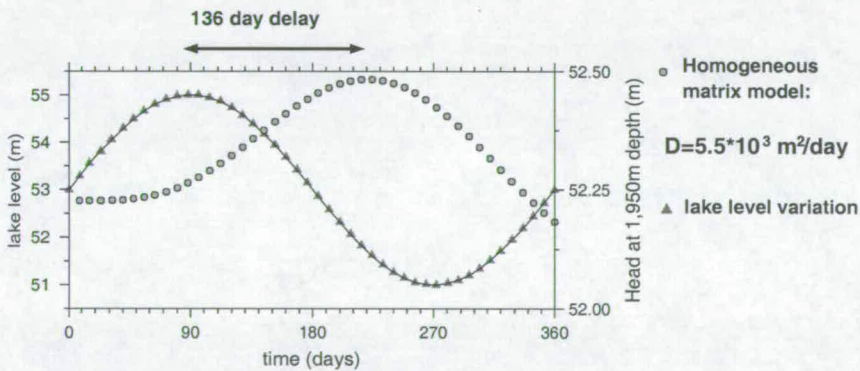


Figure 7.14: An idealised reservoir water level with a one-year period (triangles) plotted together with the predicted head values, at 1,950m depth. The left-hand side y-axis measures the variation of the lake level, whilst the right-hand side y-axis measures the piezometric head response at 1,950m depth.

Values of D have been previously derived by other authors using seismicity-based methods (Talwani and Acree, 1984/85; Scholz, 1990; Shapiro *et al.*, 1997; Talwani *et al.*, 1999; Shapiro *et al.*, 1999; Shapiro, 2000). The majority of the D values found by these authors lie between 8.6×10^2 and $8.6 \times 10^4 \text{ m}^2/\text{day}$ so the value derived here is consistent with these.

Given a value of $S = 1.0 \times 10^{-8} \text{ m}^{-1}$ for intact crystalline rock, a corresponding value of $5.5 \times 10^{-5} \text{ m/day}$ for K represents the upper limit of values reported in the literature for hard rock Singhal and Gupta (1999). In other words, the rock would be heavily fractured/fissured. Data from the literature for hard

rock show a range of values of S from 10^{-7} - $10^{-5}m^{-1}$ with even larger values for fissured and jointed rock. The value taken for S of $1.0 \times 10^{-8}m^{-1}$ is at least one order of magnitude lower than any reported value. However, any greater values will necessarily increase the value of K beyond physically realistic bounds for crystalline rocks since $D = K/S$. In addition, if the rockmass storativity is small, it follows that the degree of fracturing must be small. However, intact rock would correspond to a very low value of K , this contradict the predictions that the values of K are on the upper limit of those reported in the literature. In other words, the calculated values of K and S required to fit the data are not self-consistent and produce a physically unrealistic homogeneous media.

It is interesting here to mention a recent approach that has been used to determine large-scale *in situ* permeability tensors for rocks using induced seismicity (Shapiro *et al.*, 1997, 1999). In this approach, it is assumed that microseismic events reflect zones where the pore pressure has been increased because of fluid injections, so that the locations of the front of the microseismicity cloud provides a good description of the motion of the pressure front in the rock mass. The authors propose correlating the change in shape of the seismic cloud with the large-scale permeability of the intact rock.

From Shapiro *et al.* (1997, 1999) the diffusivity D_{homog} of this homogeneous equivalent media can be written as:

$$D_{homog} = N \frac{K}{\rho g} \quad (7.3)$$

g and ρ are respectively the gravity acceleration and the density of water. N is a poroelastic modulus defined by:

$$N = \left(\frac{\phi}{\mathcal{K}_f} + \frac{\alpha}{\mathcal{K}_g} \right)^{-1} \quad (7.4)$$

where $\alpha = 1 - \frac{\mathcal{K}_d}{\mathcal{K}_g}$, ϕ is the porosity and \mathcal{K}_d , \mathcal{K}_g and \mathcal{K}_f are, respectively, bulk moduli of the dry frame, the grain material and the fluid. From the knowledge that $D = K/S$, an homogeneous equivalent value for the storativity can also be found:

$$S_{homog} = \frac{\rho g}{N} \quad (7.5)$$

Using the values of $N \approx 2.0 \times 10^{13}$ Pa, as used by Shapiro *et al.* (1997), $S_{homog} = 5.0 \times 10^{-8}m^{-1}$. The values for K_{homog} in Shapiro *et al.* (1997, 1999) range from 3.0×10^{-5} to $1.1 \times 10^{-2} m/day$. From the discussion above it is not possible to find a fractured crystalline rock with such high value of hydraulic conductivity and a low value of storativity, as those found by Shapiro *et al.* (1997, 1999). Therefore, it can be concluded that the interpretation made by Shapiro *et al.* (1997, 1999) is also not physically plausible.

The results presented here demonstrate that it is not possible to produce a physically realistic model using a 3-D homogeneous rock matrix to explain the triggering of seismicity in the Açu reservoir. Thus an alternative model formulation is required. The most obvious alternative is to invoke the presence of a high permeability fault plane within the homogeneous matrix. The inclusion of such a fault within the regional and refined models is discussed in the next section.

7.4 The matrix and fault model

Faults within PARADIGM are represented using single planes located in the 3D matrix mesh. A plane can be at any location and orientation, and interaction with the matrix flow is provided in the fully implicit flow solution by allowing leakage between fault nodes and the nearest matrix nodes. Figure 7.15 shows a schematic representation of a fault within a matrix model. The fault plane is located in space by the coordinate O of the top left hand corner, together with its angle of strike ϕ in relation to the x -axis and by its dip angle, defined by α . Figure 7.15b shows the geometry of the fault given by the the number of rows n_r and the number of columns n_c . Several intersecting planes may be used

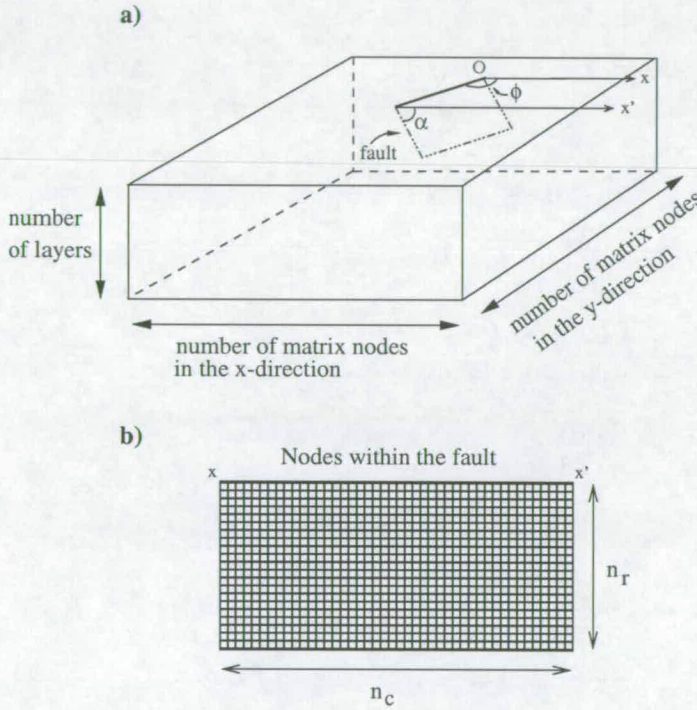


Figure 7.15: Schematic diagram showing how fault planes are defined within PARADIGM.

to mimic non-planer fault structures and parts of the fault mesh can be assigned zero permeability to allow for any shape of fault. Moreover, the fault mesh can be fully heterogeneous in its values of K and S .

Each fault node is hydraulically connected to the nearest matrix node by a user-defined conductivity. This allows for representation of the conductivity of the fault-filling materials.

The equation for flow within a single fault plane, f , is given by:

$$S_f \frac{\partial h}{\partial t} = \nabla \cdot (T \nabla h_f) + q_{m \rightarrow f} \tag{7.6}$$

Here it is necessary to explain the definitions T , S_f , $q_{m \rightarrow f}$ in equation 7.6. If a fault has thickness e (perpendicular to the fault plane itself), as shown in Figure 7.16, the flow Q within the fault in the

direction x' is given by:

$$Q = \int_0^e U_{x'} dz' = -\nabla h \int_0^e \mathbf{K}_F dz' \quad (7.7)$$

where $U_{x'}$ is the velocity component in the x' direction. \mathbf{K}_F is the hydraulic conductivity tensor in the $x' - y'$ plane of the fault and ∇h is the hydraulic gradient in this plane.

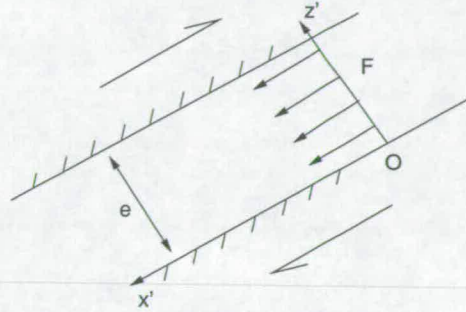


Figure 7.16: Flow in a fault.

The last integral in 7.7 is called transmissivity, T :

$$T_f = \int_0^e \mathbf{K}_F dz' \quad (7.8)$$

If \mathbf{K} is isotropic and constant along Oz (i.e. throughout the fault thickness), equation 7.8 reduces to:

$$T_f = Ke \quad (7.9)$$

Transmissivity has dimensions of [$length^2 time^{-1}$].

Fault transmissivity values are directly related to the fracture aperture of the fault. If the flow is confined to a few fractures and these fractures are assumed to be planar features, the fault transmissivity is given by (Rutqvist *et al.*, 1998):

$$T_f = \frac{b_h^3 \rho g}{12\eta} \quad (7.10)$$

where b_h is called the hydraulic aperture, g is the gravity acceleration and ρ and η are the fluid density and viscosity respectively.

Typical values of b_h for faults in crystalline rock are between 10 and 100 μm (Rutqvist *et al.*, 1998; Zimmermann *et al.*, 2000). Typical values of T_f for crystalline rock, are between 10^{-2} and 10^{-5} m^2/day (Rutqvist *et al.*, 1998; Gudmundsson, 2000).

S_f is the fault storativity. The fault storativity describes the increase in the weight of water per unit

area of the fault in response to a unit increase in pressure:

$$S_f = eS \quad (7.11)$$

Since S_s has [$length^{-1}$] units, fault storativity is dimensionless.

The quantity $q_{m \rightarrow f}$ represents leakage between the matrix and the fault. This is calculated as a constant conductivity (the user defined conductivity mentioned above) multiplied by the pressure gradient between the matrix and the fault. The term linking the matrix and the fault is given by:

$$q_{m \rightarrow f} = \frac{K_m}{L}(h_f - h_m) \quad (7.12)$$

$1/L$ represents the conductivity of fault gouge divided by a distance for zone thickness. L is not a physical quantity, since L is not measurable in a real rockmass.

As described in equation 7.12, in the matrix-to-fault link term L controls how much flow is allowed between the matrix and fault nodes. This link is needed because in PARADIGM the faults are not described in the 3D matrix; they are independent but interacting grids. This implies a loss in physicality with the introduction of the term L , as it is not measurable. However, there is gain in the structural flexibility, as the faults described by this scheme can be introduced at any orientation and dip, and still be modelled by a coherent mesh within the fault plane itself. In reality, how ever faults are described in a model, the only possible approach for determining a conductivity between matrix and fault (pump test) is to calibrate the value with field or synthetic data since no method has so far been identified for direct field conductivity measurement. Since, at Açu, no flow data are available, a range of values for L have been considered.

7.4.1 Placing the seismogenic fault in the numerical model

To investigate the impact of fluid flow through a fault in the triggering of earthquakes in the Açu reservoir, a discrete fault plane is introduced in the 3D mesh.

Figure 7.17 shows the 3D mesh and the location of the fault. Here, a fault of strike $\phi = 135^\circ$ and dip $\alpha = 90^\circ$ is employed. The position and orientation of this fault are based on epicentral and focal mechanism determinations from Chapter 3. The number of nodes in the fault in the x direction is 100 and the number of nodes in the y direction is 50. For the fault, the discretisation used was 30 m in the x direction and 100 m in the y direction. The fault is then a 3,000x5,000 m plane embedded in the 14,826x14,826x8,000km model domain.

7.5 Sensitivity Analysis

In this section a sensitivity analysis to T_f and S_f is presented. In this analysis, the term L in equation 7.12 is 10^{10} , which is a large value, resulting in no flow between the fault and the matrix. In other words, the fault is entirely sealed. Hence, only the effect of the T_f and S_f ratios on the flow inside the

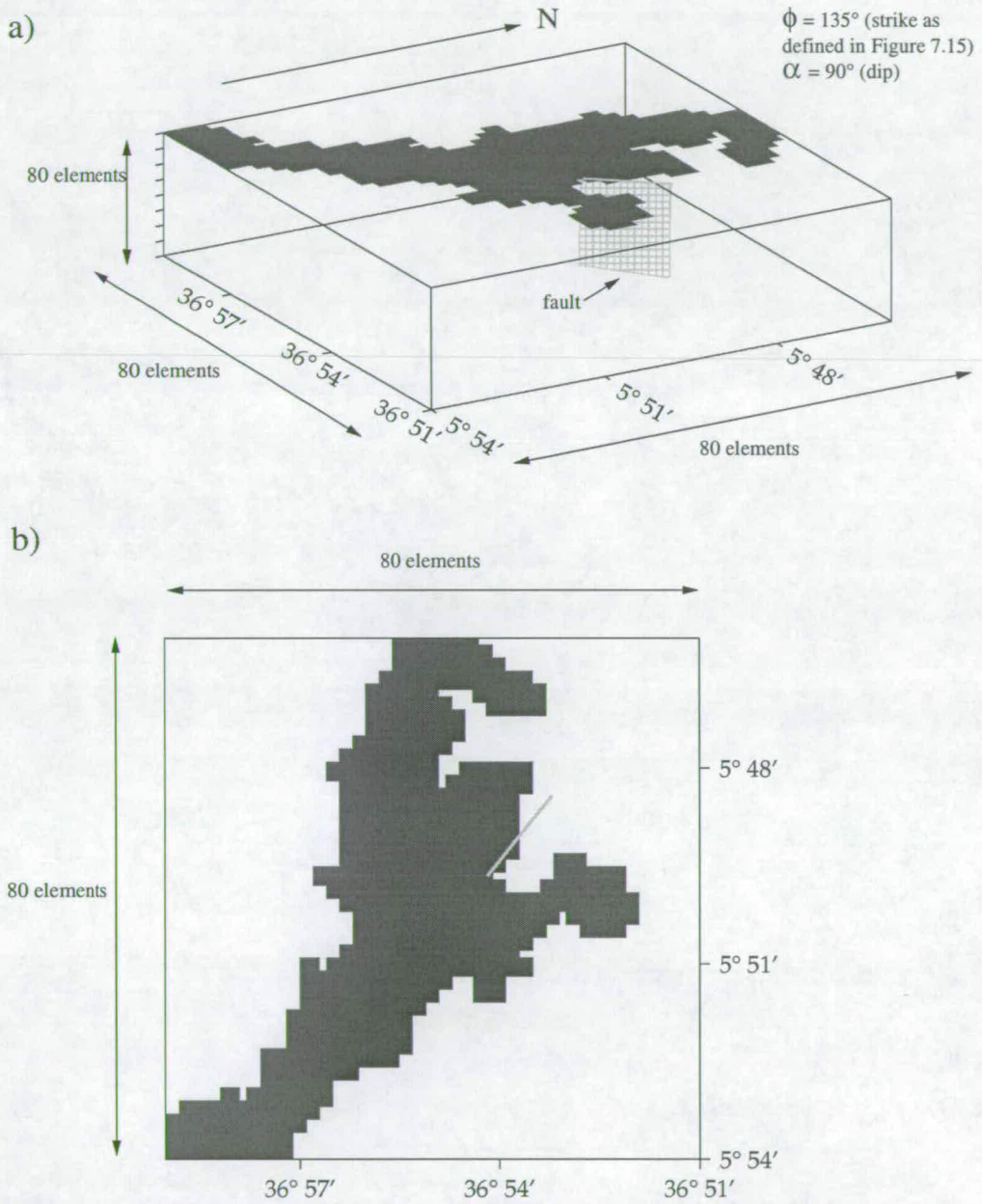


Figure 7.17: Refined groundwater model of the centre of the seismic activity in the Açu reservoir with the inclusion of a highly permeable fault. The output from sections A, B, C and D (Figure 7.2) from the regional model were used as boundary conditions for this refined local model. The location of the fault is marked in this figure.

fault will be presented in this section. Later, in section 7.6, the effect of reducing the value of L will be discussed.

Figure 7.18 shows the results for a series of numerical runs changing T_f and S_f (all the head output nodes are at 2,050m depth and $x=1,500\text{m}$). Figure 7.18a shows the lake level input with a one-year period. In Figure 7.18b, T_f is constant and equal to $2.0 \times 10^{-4} \text{m}^2/\text{day}$. S_f ranges from 4.10^{-9} to 4.10^{-6} , which means that the hydraulic diffusivity D ranges from 5.0×10^{-1} to $5.0 \times 10^4 \text{m}^2/\text{day}$. As S_f decreases (and hence, D increases), the amplitude of the change in the piezometric head increases. In addition, the time delay between the maximum water level in the surface and the maximum in the piezometric head is decreased. The straight lines on this figure occur because of very high values of S_f that reduce the hydraulic diffusivity to such an extent that the head variation at depth becomes negligible.

In Figure 7.18c S_f is constant and equal to 4.0×10^{-8} , and T_f spans from $2.0 \times 10^{-7} \text{m}^2/\text{day}$ to $2.0 \times 10^{-3} \text{m}^2/\text{day}$. Here, D ranges from 5.0 to $5.0 \times 10^4 \text{m}^2/\text{day}$. Here, as T_f decreases (D decreases), the amplitude of the change in the piezometric head decreases. The time delay between the maximum water level at the surface and the maximum in the piezometric head is increased. The straight lines on this figure arise because of very low values of T_f again reducing the hydraulic diffusivity such that the head variation at depth becomes negligible.

The reason for choosing these values of T_f and S_f is because they are typical values found in the literature (Rutqvist *et al.*, 1998; Singhal and Gupta, 1999) and also because the values of hydraulic diffusivity they provide are in the range of seismicity-based values reported in the literature (Talwani and Acree, 1984/85; Scholz, 1990; Shapiro *et al.*, 1997; Talwani *et al.*, 1999; Shapiro *et al.*, 1999; Shapiro, 2000). All these seismicity-based studies assume that the pore pressure diffusion is the main mechanism for the triggering of seismicity. The sensitivity analysis shows that as D_f increases, the time lag between the maximum in water level and the the maximum in the prediction of the piezometric head change decreases. This is accompanied by corresponding increase in the amplitude of the piezometric head change at depth. Increasing D_f can be achieved by either keeping T_f constant and reducing S_f , or by keeping S_f constant and reducing T_f . So, one can get different piezometric head predictions in the fault by changing the value of S_f or T_f and hence of D_f .

Figure 7.19 shows a typical flow pattern in the fault for the sensitivity analysis described in Figure 7.18. Because there is no flow between the host matrix and the fault, i.e. $L = 10^{10}$, the flow circulates within the fault. Recent studies, however, indicate that faults largely control groundwater flow in bedrock (Barton *et al.*, 1995; Gudmundsson, 2000). This is because in a real rock mass, there is flow between the matrix and the high-conductivity fractures (Gudmundsson, 2000). In other words, the fault is not completely sealed. Therefore, it is useful to explore other values of L to see the effect on the flow within the fault and in the temporal response of the piezometric head predictions at depth. The existence of flow between the fault and the matrix requires the full spatially varying form of the groundwater equations to be used (equation 5.11 as opposed to 5.12), since there is no longer a single diffusivity value.

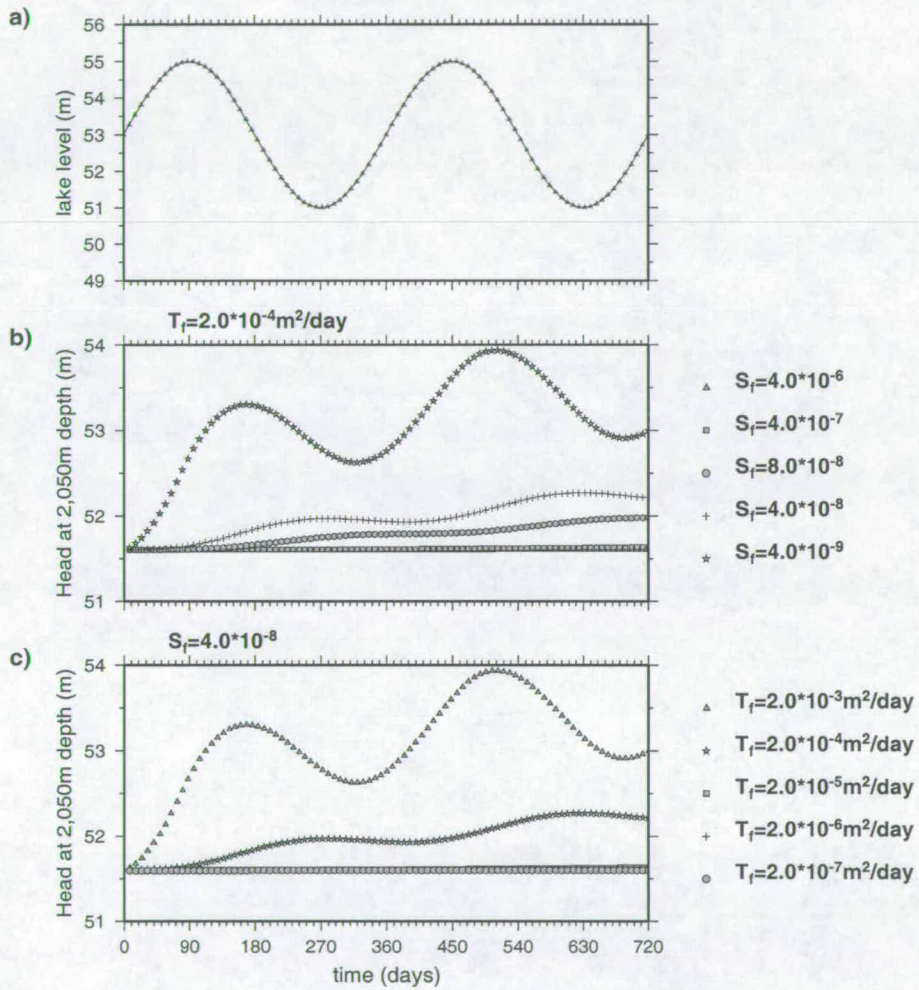


Figure 7.18: T_f and S_f . a) shows shows the lake level input with an one-year period. b) T_f is kept constant and S_f varies. c) S_f is kept constant and T_f varies. All the head output nodes are at 2,050m depth and $x=1,500\text{m}$.

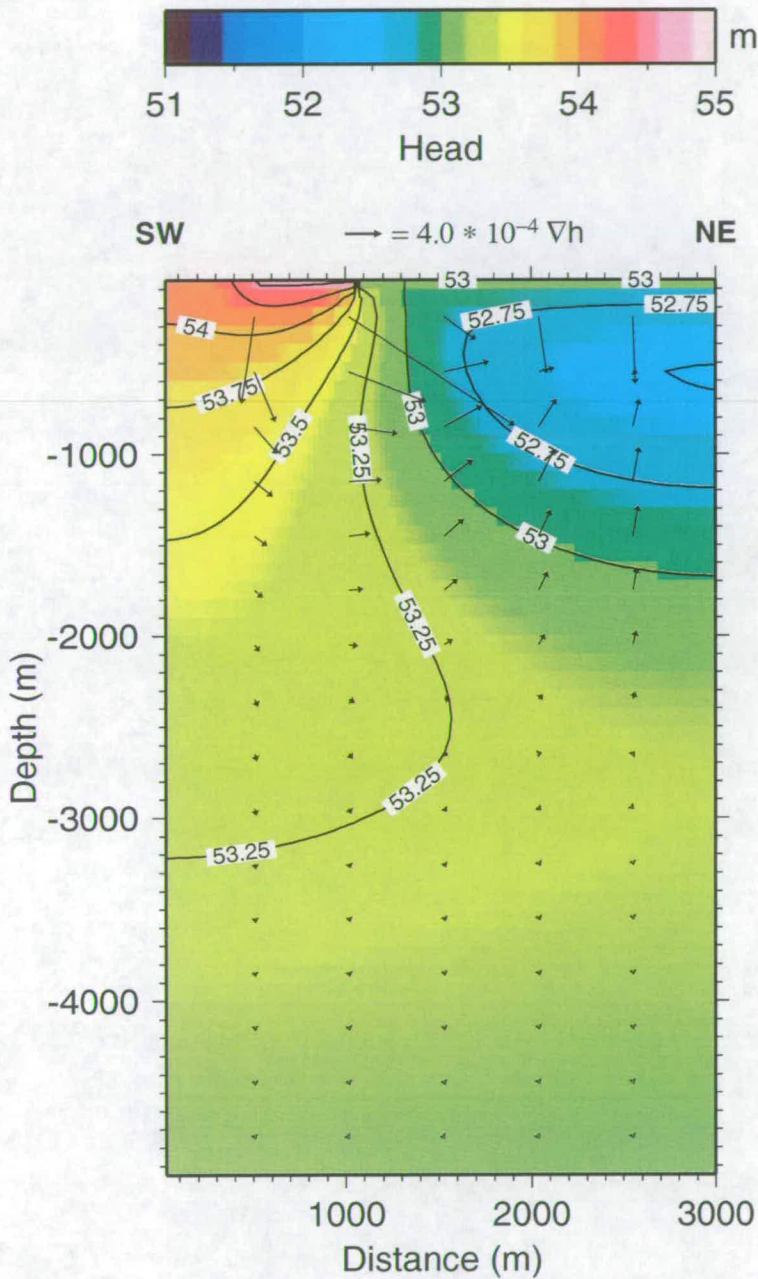


Figure 7.19: Example of piezometric head predictions in the fault shown in figure 7.17. Here, $L=10^{10}$. Because no flow is allowed between the fault and the matrix in this case, the flow circulates within the fault. The arrows indicate the direction and magnitude of the piezometric head gradient.

7.6 The matrix-to-fault link

The effect of varying L in the temporal response of the piezometric head predictions at depth is shown in Figure 7.20. For all the numerical simulations output in figure 7.20b, $T_f=2.0 \times 10^{-4} \text{ m}^2/\text{day}$ and $S_f=4.0 \times 10^{-8}$.

For each of the simulations in Figures 7.20 and 7.21, the initial head conditions in the fault calculated by solution of the steady-state groundwater equation vary according to the different values of L . When L is very large, and no fluid leaks out of the fault, all the nodes in the fault have, as initial head values, the value of the lake level (53m) used when solving the steady-state solution. When flow is allowed between the matrix and the fault, $L = 10^4$ for instance, the heads in the fault nodes are predicted to be smaller than 53m, indicating flow out of the reservoir. In other words, groundwater recharge is occurring from the reservoir via the high conductivity fault. This explains why each of the simulations in Figure 7.20 starts with a different value.

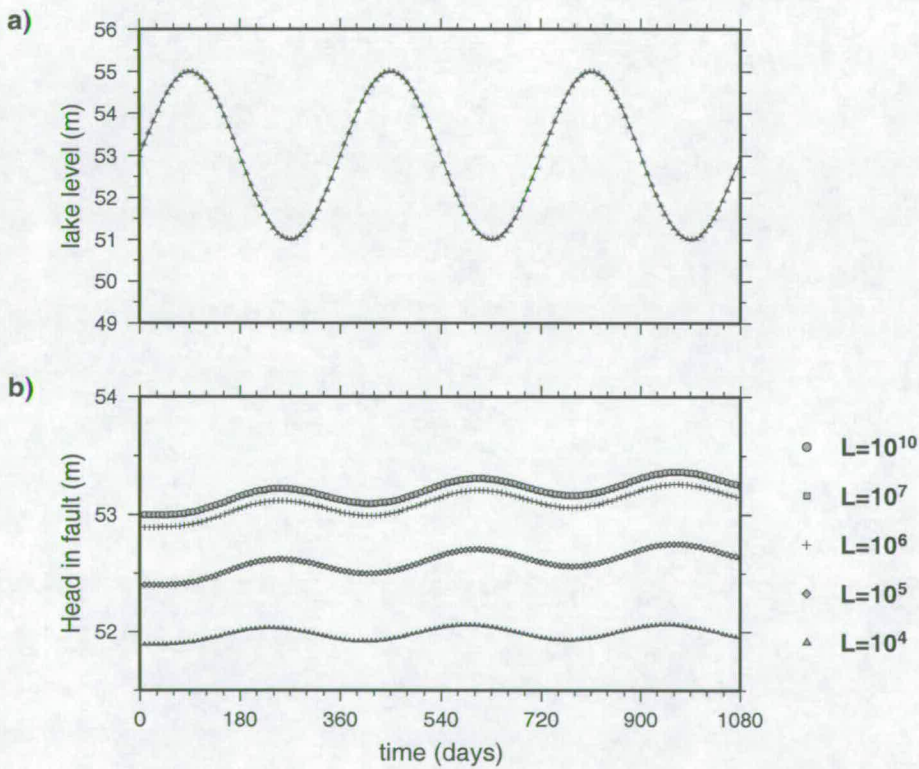


Figure 7.20: a) shows an idealised reservoir water level with a one-year period. b) shows the time varying outputs for numerical runs with different matrix-to-fault links. For these runs, the nodes output are at 2,050 m depth and $x=1,500\text{m}$. Here, $T_f=2.0 \times 10^{-4} \text{ m}^2/\text{day}$ and $S_f=4.0 \times 10^{-8}$

The numerical simulations shown in Figure 7.20 show that the larger the value of L (small matrix-to-fault flow), the longer the piezometric head predictions take to reach an oscillatory steady-state regime. For values of 10^7 and 10^{10} , the flow between the matrix and the fault is negligible. Therefore, fluid circulates within the fault as in Figure 7.19. As L decreases, and matrix-to-fault flow is allowed, this

circulatory effect vanishes. To illustrate this effect, Figure 7.21 shows the piezometric head predictions in the fault for different values of L . For values of 10^4 and below, the circulation has gone and flow is

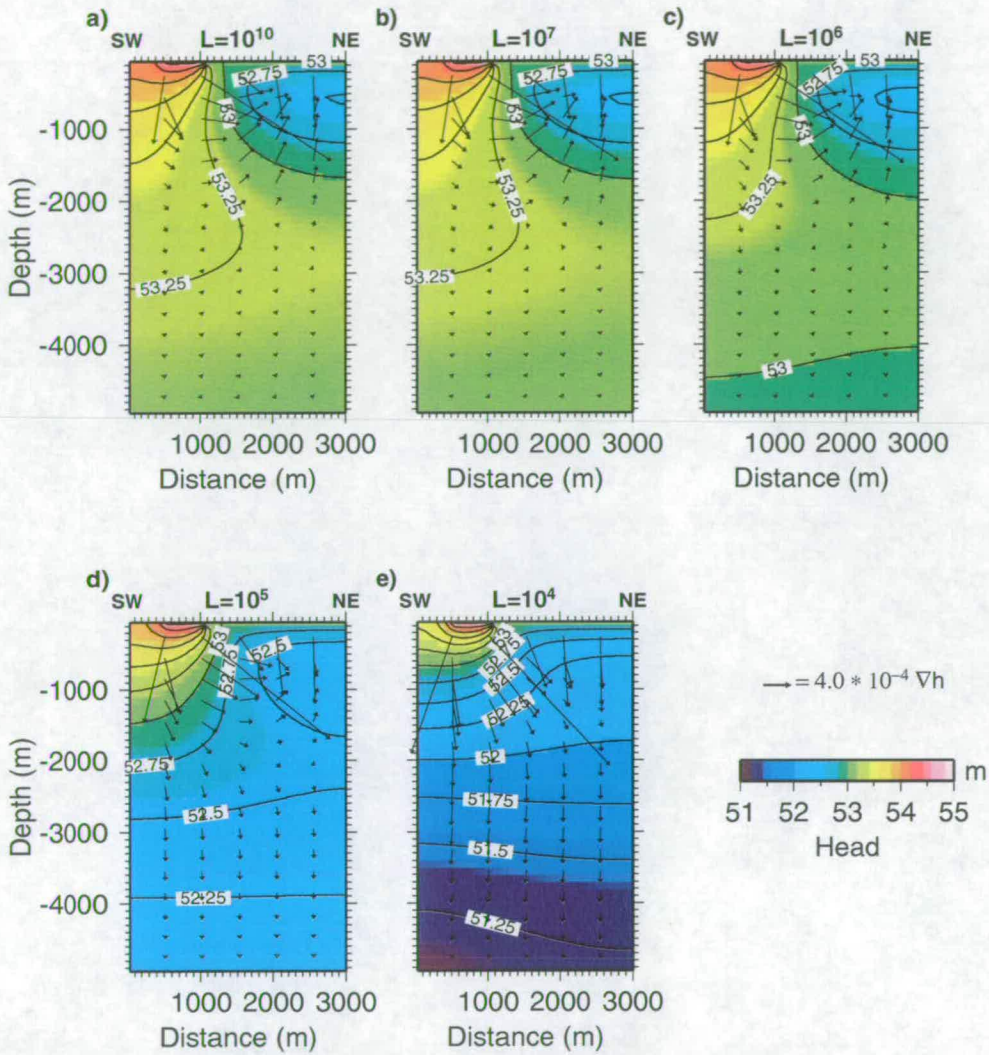


Figure 7.21: Piezometric head predictions in the faults for different values of L . The head predictions are output after 1080 days have elapsed.

now recharging groundwater in the matrix as documented in the literature (Haneberg, 1995; Matthäi and Roberts, 1997; Gudmundsson, 2000).

In real rock, L is more likely to vary spatially, since the distribution of fault gouge and the fault architecture (discussed in Chapter 8) vary spatially (Caine *et al.*, 1996). However, field data do not exist for a single value let alone a heterogeneous distribution. In our numerical simulations, the chosen value is $L = 10^4$ since with this value, the fault nodes reach a oscillatory steady-state quickly. More importantly, it is physically realistic to assume that flow exists between the matrix and fault. Values of L lower than 10^4 will behave in a similar fashion, so this value has been selected as being representative

of a physically realistic regional flow regime.

Figure 7.22 shows the effect of varying T_f and S_f now that flow is allowed between the matrix and the fault ($L = 10^4$). Figure 7.22a shows an idealised reservoir water level with a one-year period. In Figure 7.22b, the values of T_f and S_f have been varied, but the fault diffusivity remains the same ($D_f = \frac{T_f}{S_f}$). The figure shows piezometric head predictions at 2,050m depth. Despite D_f being the same, the piezometric head predictions are different. The amplitude change and the time lag between the maximum in water level and the maximum head prediction is not the same. For lower values of S_f , the same value of D_f leads to a reduction in the time lag between the maximum in water level and the maximum head, and also to a reduction in the amplitude of the piezometric head prediction. In

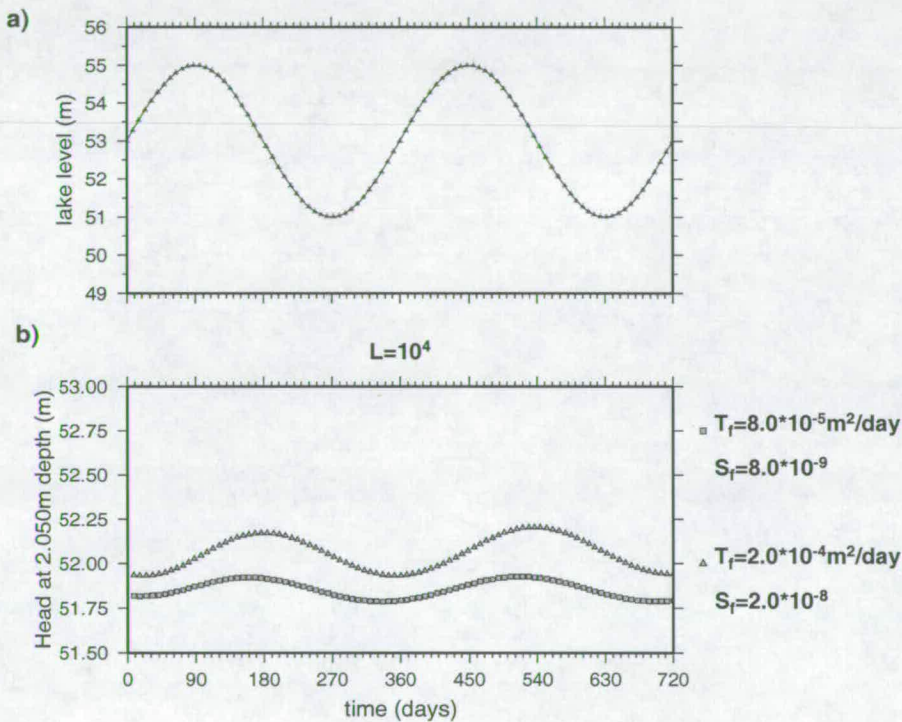


Figure 7.22: Effect of L in the numerical runs. a) shows an idealised reservoir water level with a one-year period. Here, a two year cycle is shown. b) $L = 10^4$ and D_f is the same, and different values of T_f and S_f are used. c) $L = 10^{10}$ and D_f is the same and different values of T_f and S_f are used.

figure 7.18 however, runs with the same values of D_f , but with differing T_f and S_f , produce exactly the same output.

This difference can be explained by writing equation 7.6 for a single fault with constant T_f and S_f :

$$\nabla \cdot (T_f \nabla h) = S_f \frac{\partial h}{\partial t} - \underbrace{\frac{K_m}{L} (h_f - h_m)}_{q_{m \leftrightarrow f}} \tag{7.13}$$

So, when L is large, the term $q_{m \leftrightarrow f}$ tends to zero, and therefore equation 7.13 can be written as:

$$\underbrace{\frac{T_f}{S_f}}_{D_f} \nabla^2 h = \frac{\partial h}{\partial t} \quad (7.14)$$

In other words, when L is big ($L = 10^{10}$), it is possible to write D_f as T_f/S_f , since the approximation presented in 7.14 is valid. That situation is presented in Figure 7.18. For different values of T_f and S_f , but keeping D_f the same, the results are the same.

On the other hand, when L is relatively small (10^4), the term $q_{m \leftrightarrow f}$ does not vanish. Rearranging the terms in 7.13:

$$D_f \nabla^2 h = \frac{\partial h}{\partial t} - \underbrace{\frac{q_{m \leftrightarrow f}}{S_f}}_{\text{source/sink term}} \quad (7.15)$$

So, when L and S_f are small, the source/sink term becomes more significant and the approximation used in equation 7.14 is no longer valid. In other words, D_f can no longer be simply written as the ratio between T_f and S_f . That situation is shown in Figure 7.22b; despite D_f being the same, the results are not the same. A decrease in S_f leads to a decrease in both the time delay and the amplitude, whereas an increase in S_f leads to an increase in both the time delay and the amplitude.

This result is not just due to the representation of fault within PARADIGM as a separate mesh with a flow between matrix and fault. If the fault were represented within the matrix nodes, T would in effect be spatially varying and hence could not be removed from the spatial derivative form. A single value of D_f , therefore, could still not be defined.

7.7 Finding the time lag with the matrix and fault model

In this section, the hydraulic properties of the fault (i.e. fault transmissivity T_f and fault storativity S_f) are calibrated to match the observed delay between the peak water level in the reservoir and the maximum seismic activity. Throughout all this section, $L = 10^4$. The values $T_f = 2.0 \times 10^{-4} \text{ m}^2/\text{day}$ and $S_f = 4.0 \times 10^{-8}$ are found to best match the 136-day time delay. This corresponds to $D_f = 5.0 \times 10^3 \text{ m}^2/\text{day}$. Figure 7.23a shows the idealised water level with a one-year period, and Figure 7.23b shows the predicted head values at 2,050m depth. The node which is output is located in the 50th column. Table 7.3 shows the model parameter data for the numerical experiment output in Figure 7.23. When a fault is included in the model, the values of transmissivity and storativity in the fault are $2.0 \times 10^{-4} \text{ m}^2/\text{day}$ and 4.0×10^{-8} . Rutqvist *et al.* (1998) found values of transmissivity of 3.0×10^{-4} and $1.2 \times 10^{-4} \text{ m}^2/\text{day}$ with fault storativities of 2.0×10^{-8} and 9.1×10^{-9} respectively. This is consistent with our estimates for T_f and S_f . In other words, with the incorporation of the fault plane, the flow model can explain the seismic activity with realistic values for the hydraulic properties in the fault. The presence of a discrete fault plane is therefore a more realistic model compared with that of the matrix-only model presented above. Those results show that, in reality, the flow is dominated

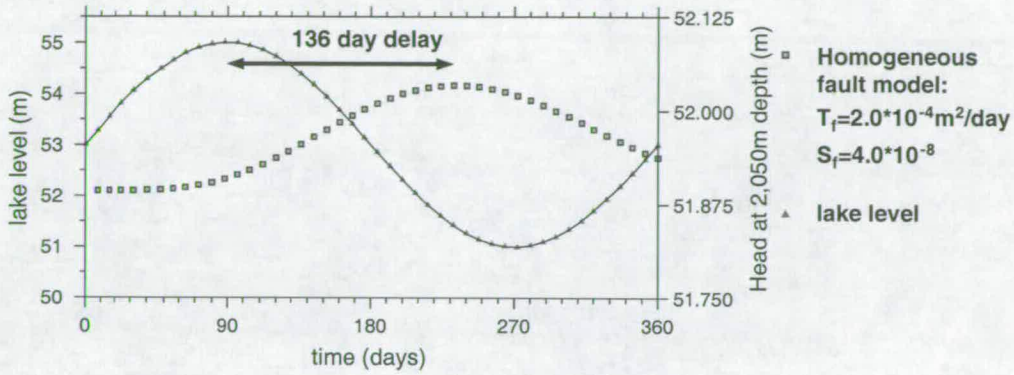


Figure 7.23: *x*-axis show the time in days. The *y*-axis on the left shows an idealised reservoir level variation, where as the *y*-axis on the right shows the piezometric head prediction at 2,050m depth.

Model data for the matrix	
Number of time steps	45
Time step length	8 days
Discretisation in the <i>x</i> and <i>y</i> directions	185.325 m
Discretisation in the <i>z</i> direction	100 m
Number of nodes in the <i>x</i> and <i>y</i> directions	80
Number of nodes in the <i>z</i> direction	80
Matrix hydraulic conductivity	8.5×10^{-7} m/day
Matrix storativity	$10^{-6} m^{-1}$
Model data for the fault	
Discretisation in the <i>x</i> direction	30 m
Discretisation in the <i>y</i> direction	100 m
Number of nodes in the <i>x</i> and direction	100
Number of nodes in the <i>z</i> direction	50
Fault transmissivity	$2.0 \times 10^{-4} m^2/day$
Fault storativity	4.0×10^{-8}
Fault strike (degrees)	135
Fault dip (degrees)	90

Table 7.3: Model parameter data for the numerical experiment output in Figure 7.23.

by a highly permeable fault beneath the Açu reservoir. In Shapiro *et al.* (1997, 1999), the authors are actually describing the fluid flow in a fault plane and not in an equivalent homogeneous media.

An example of the predictions of the piezometric head prediction within the fault is given in Figure 7.24. Figure 7.24a, 7.24b, 7.24c and 7.24d are the piezometric predictions in the fault output taken after 88, 176, 264 and 360 days have elapsed respectively. As the lake level (and shape) changes, the boundary conditions on the top of the 3D matrix grid changes accordingly. Therefore, the top nodes of the fault plane experience different boundary conditions depending upon the lake level. In Figure 7.24a, the piezometric head prediction is shown after 88 days have elapsed. At this time, the lake level is at its maximum (55 m). Thus, most of the fault is under the lake and higher isovalues of piezometric head on the top nodes of the fault are observed. Figures 7.24b, 7.24c and 7.24d show output from piezometric head predictions in which the reservoir and fault nodes are such that only a fraction of the fault is directly under the reservoir. The extent of the reservoir in each different piezometric output is also shown in each of these figures. The isovalues of heads are higher towards the southwestern end of the fault because of the regional groundwater gradient. In general, water is flowing out of the lake into the high conductivity fault plane. From here it flows into the surrounding rock matrix, recharging the regional groundwater. Figure 7.25 shows piezometric head predictions for fault nodes located at $x=1,500$ m (50th column). The depths are 950, 1,950 and 2,950 m. As the depth increases, the amplitude of the piezometric variation at a particular node decreases. The time delay between the maximum water level in the lake and the maximum piezometric head in the fault node increases as the depth increases. For depths near 3,000 m the increase in piezometric head due to the lake oscillation is 0.05 m. The time delay for the 2,950m depth node is between 200 and 216 days (≈ 7 months). This time delay is greater than that found in the seismological observations. According to the seismological observations, cluster b had seismic activity between 2.7 and 3.0 km depth 6.0 months after the peak in water level (see Table 4.2). To fit with the seismological observations, a higher value of D_f in the fault plane than that used in the numerical simulations would be necessary. This would then result in too rapid response for the observed seismicity at 2km depth. Thus whilst this homogeneous fault model explains more of the data, it does not provide a complete model and further models will be explored in Chapter 8.

7.8 Summary

In this Chapter, a numerical model was built in PARADIGM to simulate the pressure diffusion beneath the Açu reservoir. A description of PARADIGM's numerical scheme to solve for flow was also presented. A regional scale model was set up to determine physically realistic boundary conditions to, a second, more refined model of the area of seismic activity. Simulations with the refined model, both with and without including a highly permeable fault in the flow model were performed. In both cases, the hydraulic properties (hydraulic conductivity K and specific storativity S for the matrix, and transmissivity T_f storativity S_f for the fault) were calibrated to simulate the observed delay between the peak water level in the reservoir and the maximum seismic activity. For the flow model with no fault, the values of K and S calibrated are not self consistent and are physically unrealistic. When a highly permeable fault is included in our model, the values of T_f and S_f are in close agreement with realistic

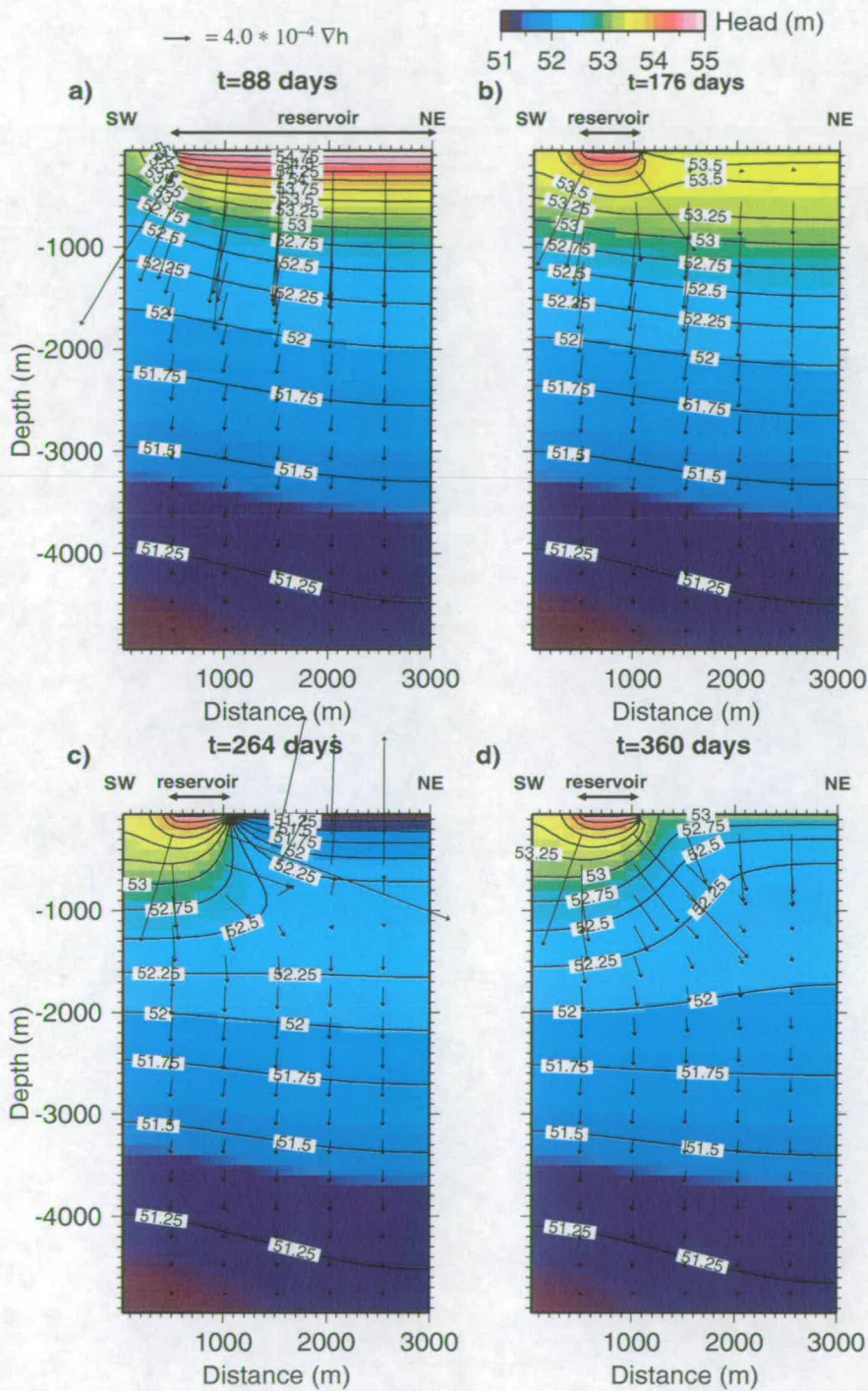


Figure 7.24: Examples of piezometric head predictions in the fault shown in Figure 7.17. The arrows indicate the direction and magnitude of the piezometric head gradient. The double headed arrow indicates the location of the reservoir. a, b, c and d are the piezometric predictions in the fault after 88, 176, 264 and 360 days have elapsed, respectively.

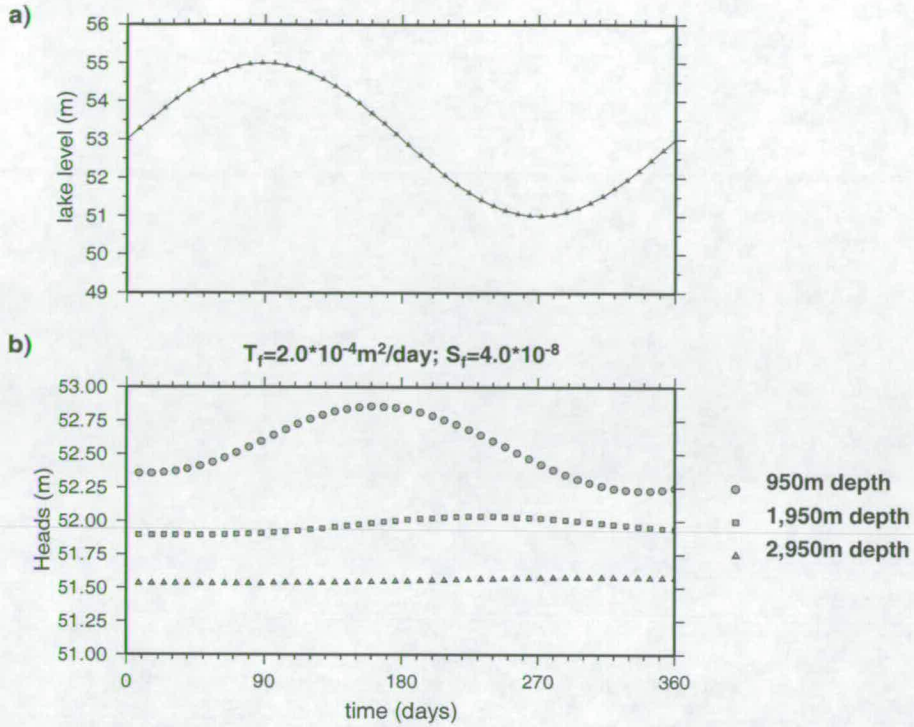


Figure 7.25: a) shows an idealised reservoir water level with a one-year period. b) shows the time varying output for nodes at 1,050, 2,050 and 3,050 m.

data from the literature. As a consequence, it was shown that the use of an equivalent homogeneous media to explain RIS is invalid and leads to wrong interpretations of fluid-induced seismicity in many cases.

8 GROUNDWATER MODELLING - HETEROGENEOUS MODEL

So far, the numerical experiments used a highly permeable fault with constant values for the hydraulic properties. With such a fault, it was possible to correctly predict the delay between the peak in water level in the reservoir and the peak in seismic activity at 2km depth. However, the earthquake spatio-temporal data (Chapter 4) in the Açu reservoir shows migration between different faults and also activation of different zones of a particular fault. The time delay predicted by the homogeneous fault at 3km depth is larger than the one observed in the spatio-temporal data (see end of Section 7.7). In addition, the homogeneous fault model does not predict activation of well defined spatial clusters in the fault, since this model simply predicts the same pore pressure change for all locations at the same depth in the fault. Therefore, a homogeneous fault with respect to its hydraulic properties is not a fully realistic way to describe a seismogenic fault and to explain the patterns observed in RIS.

There are several factors effecting the nature of K within a single fault plane. A large number of laboratory and in situ tests on fractured rocks show that mean hydraulic conductivity declines with increasing stress and hence depth (Brace *et al.*, 1968; Brace, 1980; de Marsily, 1986; Singhal and Gupta, 1999; Morrow and Lockner, 1994). This decrease can be explained by the general compression and reduction of hydraulic fracture aperture with increased stress at depth (Rutqvist *et al.*, 1998). Additionally, it is also known, that faults are lithologically heterogeneous and structurally anisotropic. Fault zones may act as barriers, conduits, or combined conduit-barriers systems that enhance or impede fluid flow (Scholz, 1990; Caine *et al.*, 1993; Antonellini and Aydin, 1994; Caine *et al.*, 1996). In order to simulate pore pressure diffusion in a more realistic fault zone, the fault within PARADIGM will incorporate: (1) - the effect of hydraulic conductivity decrease with depth; (2) - lithological heterogeneity.

The relationship between depth and hydraulic conductivity can be expressed by (de Marsily, 1986; Singhal and Gupta, 1999):

$$K = K'_0 d^{-\alpha} \quad (8.1)$$

This equation is equivalent to equation 5.16, where $K'_0 = K_0(\rho g)^\alpha$. ρ and g are the density of the overburden rock and g is the gravity acceleration. K_0 is the value of the hydraulic conductivity when no stress is applied (i.e. at the ground surface) and α is a constant that measures how the hydraulic conductivity drops off with increasing depth and d is the depth. Based on field or laboratory data about the variation of the hydraulic conductivity with depth, K_0 and α can be found by linear regression (de Marsily, 1986; Lunn and Mackay, 1997; Singhal and Gupta, 1999).

8.1 Evidence for the heterogeneous hydraulic structure of faults

The purpose of this section is to describe the field and laboratory evidence to support a heterogeneous hydraulic conductivity structure within a single fault zone.

Field and microstructural studies of fault zones demonstrate that fault zones are composed of distinct compartments: a fault core and a damage zone, as shown in Figure 8.1. In the **fault core** most of the displacement is accommodated. Fault cores may include single slip-surfaces, unconsolidated clay-rich gouge zones, brecciated and geochemically altered zones, or highly indurated, cataclasis zones (Caine *et al.*, 1996; Evans *et al.*, 1997). A **damage zone** is the network of structures that bound the fault core and may enhance fault zone hydraulic conductivity relative to the core and undeformed protolith (Chester and Logan (1986); Caine *et al.* (1996); Evans *et al.* (1997)). Fault-related subsidiary structures include small faults, veins, fractures, cleavage, and folds that cause heterogeneity and anisotropy in the hydraulic conductivity structure and elastic properties of the fault zone (Caine *et al.*, 1996; Evans *et al.*, 1997). Fracture density in the fault core is usually significantly less than in the damage zone.

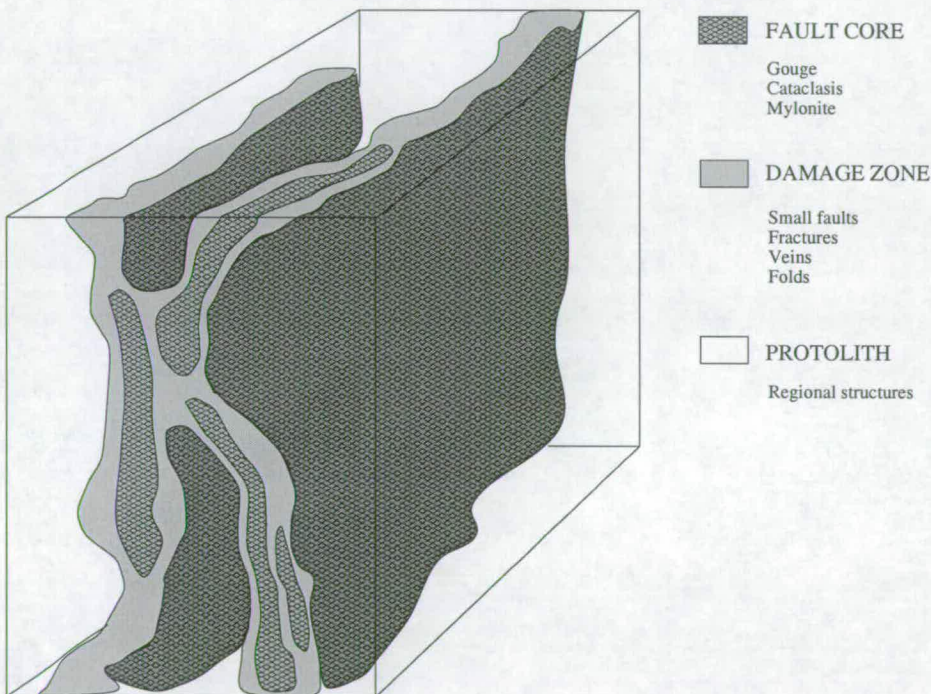


Figure 8.1: Conceptual model of fault zone with removed protolith removed (after Caine *et al.* (1996))

Therefore, boundaries between the damage zone and fault core are typically sharp, whereas the damage zone to protolith transition is usually gradational (Evans *et al.*, 1997).

Caine *et al.* (1996) also presented a conceptual scheme for fault-related fluid flow. According to the proportion of damage zone to the proportion of fault core, they built the diagram shown in Figure 8.2. Each of the four end-member architectural styles is associated with a characteristic hydraulic conductivity structure. (Caine *et al.*, 1996). The hydraulic conductivity structures comprise localised conduits, distributed conduits, localised barriers and combined conduit-barriers. Table 8.1 shows for each of these hydraulic conductivity structures its architectural style and the main characteristics of

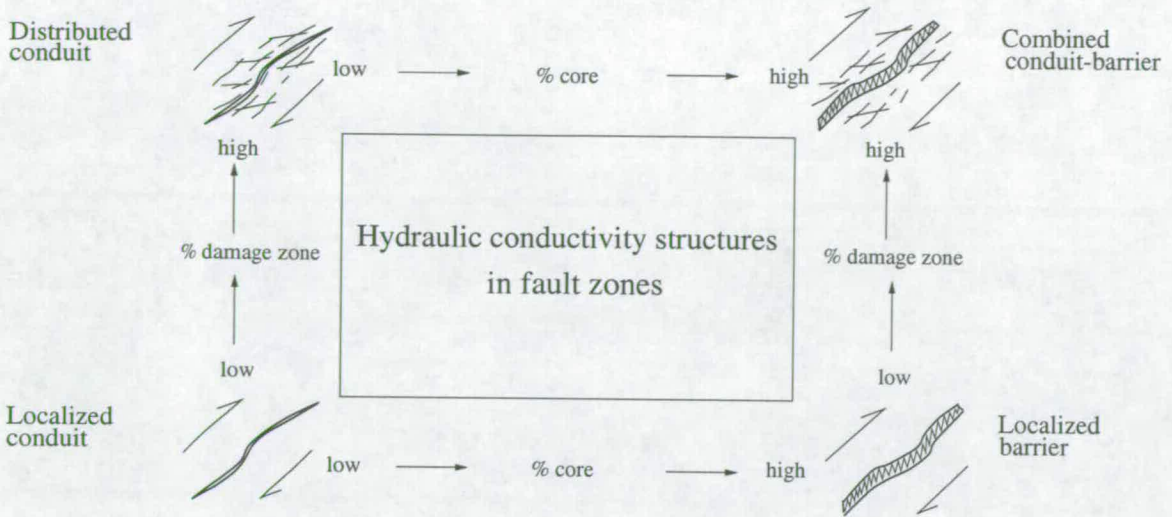


Figure 8.2: Conceptual scheme of fault-related fluid flow (after Caine *et al.* (1996))

the fault core and damage zone. This structure results in heterogeneity of hydraulic conductivity in the plane, both due to the existence of the core and the heterogeneous nature of the fractured damage zone. Seismically active faults in Precambrian basement observed elsewhere (e.g., Figure 8.3 and Dawers and Seeber (1991)) are typically characterised by zones of intense fracturing that show both opening and shear displacements. Dawers and Seeber (1991) called them “joint-zones”, and what is significant is that these zones exhibit very little displacement across them, and are poorly developed in terms of the formation of a fault core. In other words, there is no localisation of shear displacement and fault gouge development, which characterises larger displacement structures. In terms of the classification scheme proposed by Caine *et al.* (1996), these types of faults are best described as *distributed conduit*.

In this research, both the decrease in hydraulic conductivity with increasing confining stress and the more heterogeneous hydraulic conductivity structure within the fault will be included in the groundwater model. The hydraulic conductivity structure of the damage zone is modelled because the faults in the Açu area are thought to behave as distributed conduits. In such faults, the hydraulic conductivity structure is dominated by the hydraulic structure of the damage zone. It is anticipated that these two factors will alter the fluid flow pattern and, therefore, will provide an earthquake triggering pattern that has similar characteristics to the one provided by the actual earthquake data. The implementation of each of these two factors in PARADIGM are presented in turn.

8.2 Including the depth vs. hydraulic conductivity dependence

Many laboratory tests performed in fractured rocks show that hydraulic conductivity declines with increasing confining stress for samples containing either single, or multiples fractures (Brace *et al.*, 1968; Brace, 1984; Walsh and Brace, 1984; Morrow and Lockner, 1994; Guéguen and Palciauskas, 1994). However, fewer studies have been dedicated to studying how the pressure-hydraulic conductivity relationships might vary within the different components of the fault zones.

Hydr. cond. structure	Architectural style	Fault core	Damage zone
Localised conduit	Localised slip along a single surface or along discrete segmented planes.	Absent or poorly developed.	Absent or poorly developed.
Distributed conduit	Distributed slip accommodated along distributed surfaces and fractures.	Absent or poorly developed as discontinuous, narrow and discrete bands.	Developed discrete slip surface and associated fracture networks.
Localised barriers	Localised slip accomodeted within cataclatic zone.	Developed fault core cataclasites.	Absent or poorly developed.
Combined conduit-barrier	Deformation accommodated within a localised cataclastic zone and distributed zones of auxiliary structures.	developed fault core cataclasites.	Developed discrete slip surface and associated fracture networks.

Table 8.1: Fault zone architectural styles and their corresponding hydraulic conductivity structures. From Caine *et al.* (1996)



Figure 8.3: Exposure of a brittle fault zone in Pre-Cambrian basement at a locality to the south of Açu reservoir. This provides a possible analogue for active faults in the Açu area. Note the 2m wide zone of sub-vertical fractures to the right of the person in the photo. Photo taken by P. Cowie.

Evans *et al.* (1997), presents a study using basement rocks in which stress-hydraulic conductivity relationships are determined for different fault components via laboratory measurements of samples from the different fault components. They also investigate the pressure-hydraulic conductivity relationship as a function of orientation relative to fault slip for a net effective stress of 3.4 MPa. According to these tests at this net effective stress, the hydraulic conductivity of samples oriented parallel to the slip vector is about one order of magnitude greater than that of samples oriented perpendicular to slip. Evans *et al.* (1997) also suggest that each compartment of the fault may exhibit a three-dimensional hydraulic conductivity anisotropy. The minimum hydraulic conductivity values are associated with values perpendicular to the fault plane, maximum values parallel to the slip vector, and intermediate values within the fault plane, perpendicular to slip.

Figure 8.4 shows the fitted values of Equation 8.1 from Evans *et al.* (1997) using Equation 5.16. The reason for fitting Equation 8.1 and not an exponential law as in the work of Evans *et al.* (1997) is that at the field scale, equation 8.1 is more widely used and is a better fit to the field data. Figure 8.4 shows the measurements of hydraulic conductivity vs effective stress, for the damage zone, as a function of the structural position within the fault zone. In figure 8.4, the fitted values of K_0 and α are also presented.

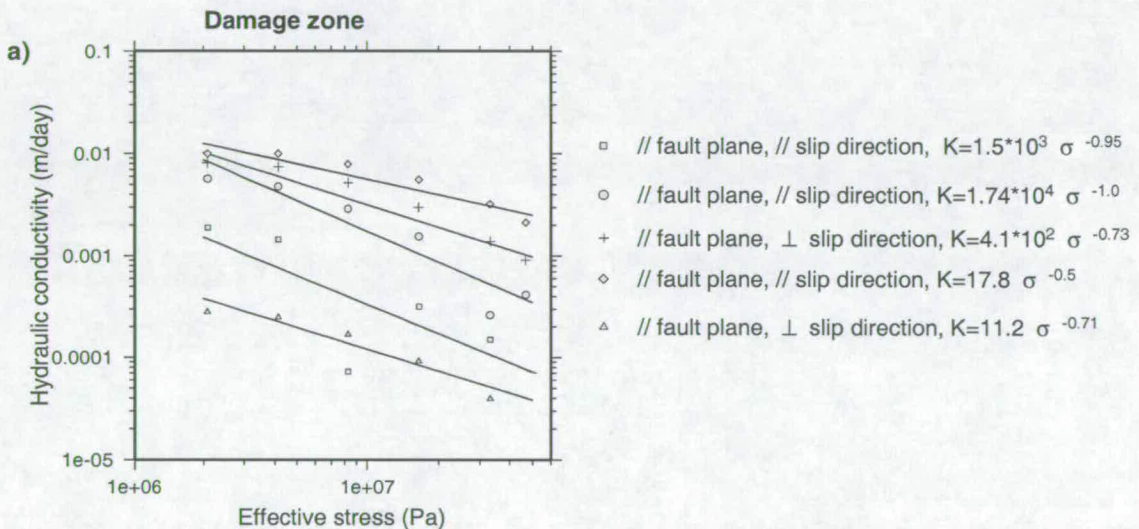


Figure 8.4: Fits of Equation 5.16 for the damage zone. Data from Evans *et al.* (1997).

In this research, it has already been demonstrated that the pressure diffusion in a discrete fault from the bottom of the Açu reservoir to hypocentral depths is the most likely mechanism for RIS in this site. The value of α for measurements of hydraulic conductivity parallel to the fault plane, perpendicular to the slip direction in Figure 8.4, as is the case in Açu, is 0.73 for the damage zone. This value does not differ from the mean value: 0.78. As mentioned before, I assume that the hydraulic conductivity of the faults in the region is controlled by the hydraulic conductivity of the damage zone.

For the numerical simulations in this Chapter, the fault grid used is different from that employed in the numerical simulations conducted in Chapter 7 (table 7.3). The new model parameter data for the fault is presented in Table 8.2. The new fault grid is a 4x4km plane, with 80x80 nodes (50m each). The reason for change is to increase the discretisation in the vertical to allow better definition in the

Discretisation in the x direction	50m
Discretisation in the y direction	50m
Number of nodes in the x direction	80
Number of nodes in the y directions	80
Fault transmissivity	$2.0 \times 10^{-4} \text{ m}^2/\text{day}$
Fault storativity	4.0×10^{-8}
Fault strike (degrees)	135
Fault dip (degrees)	90

Table 8.2: Model parameter datafor the fault grid used in the numerical simulations presented in this Chapter.

heterogeneous hydraulic conductivity structure. Given this increased number of nodes in the fault plane, the depth of the plane has been limited to 4km to keep simulation times to a minimum. This should not effect the results since it is still well bellow the deepest recorded seismic event (in cluster a) at 3.0km. Figure 8.5 shows an output of the predictions of the piezometric head in the fault. This output was taken after the head in all the nodes exhibited an oscillating steady state (1,080 days), (as in stage 2 of the flow diagram of Figure 7.12). It should be noted that the values of the piezometric head with the new fault plane grid do not differ from those using the previous grid (Figure 7.21e).

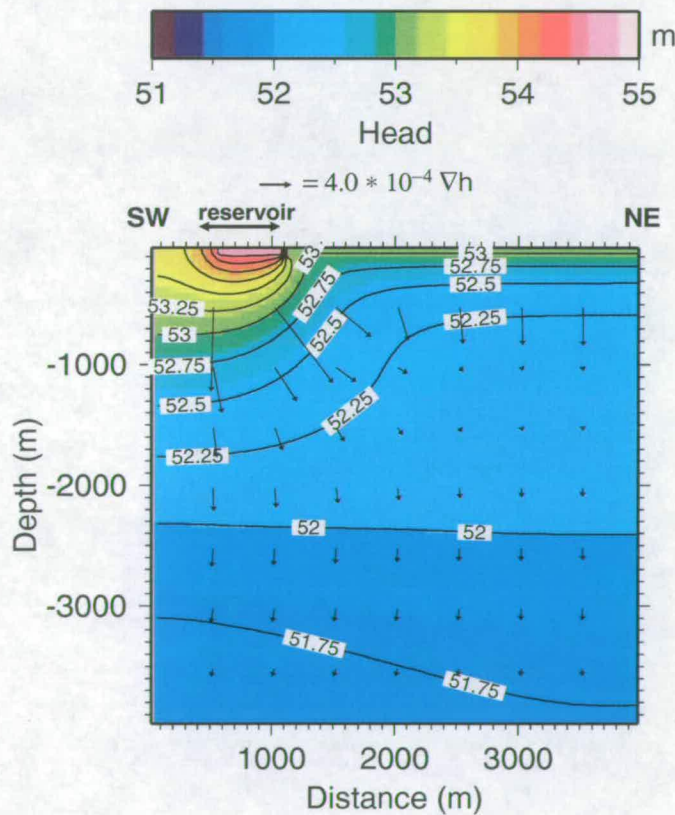


Figure 8.5: Example of piezometric head prediction in the seismogenic fault. The arrows indicate the direction and magnitude of the piezometric head gradient. The double headed arrow indicates the location of the reservoir.

In PARADIGM, equation 8.1 is used to determine hydraulic conductivity over depth. The values of

fault transmissivity over depth in PARADIGM are calculated in an analogous way:

$$T_f = T_0 d^{-\alpha} \quad (8.2)$$

The values of K_0 and T_0 are found by matching the observed delay of 4.5 months between the maximum in water level and the maximum in pore pressure at 2,050m depth. The value of α is 0.73 taken from Evans *et al.* (1997).

8.2.1 Matrix only model with dependence of K over depth

The procedure adopted here is analogous to the one described in the flow diagram shown in Figure 7.12. Note that there is no fault as yet, I am simply adding the effect of stress as a function of depth. Firstly, a value of K_0 was found with the regional model. The value of K_0 was found to be 8.0×10^{-3} m/day ($\alpha=0.73$). Figure 8.6a shows the fitted values of hydraulic conductivity over depth (the continuous line) plotted together with the single value of hydraulic conductivity K_{fit} from Chapter 7 that fits the delay using the homogeneous model, i.e., no dependence of K over depth exists. In the case of the homogeneous matrix shown in Chapter 7, $K_{fit}=5.5 \times 10^{-5}$ m/day was found to be a physically unrealistic value of hydraulic conductivity. In reality, typical values of hydraulic conductivity are of 8.5×10^{-7} m/day. The matrix model incorporating stress dependence does not produce physically realistic values of K either. The values of K over depth are still too high to represent a physically realistic rock matrix.

In order to bring K_0 down to a typical mean value for the protolith for subsequent simulation (Section 8.2.2), K_0 has to be reduced by the same factor that K_{fit} was reduced in Chapter 7, 64.7. Therefore, the K_0 that will be used in the following simulations will be $8.0 \times 10^{-3} / 64.7 = 1.2 \times 10^{-4}$ m/day. Figure 8.6b shows the hydraulic conductivity over depth for $K_0=1.2 \times 10^{-4}$ m/day. The observed mean value of hydraulic conductivity, 8.5×10^{-7} m/day, is also plotted.

8.2.2 Matrix and fault model with dependence of K and T_f over depth

A model was now developed within PARADIGM analogous to that in Section 7.4, but with stress dependent conductivity/transmissivity in the matrix and fault respectively.

The value of T_0 was calibrated using the procedure shown in figure 7.12. The value of T_0 was found to be $3.2 \times 10^{-2} m^2 / day$. This was the same for both the old and new fault plane meshes. Therefore, for the numerical simulations in this Chapter, only the new fault plane grid simulations were carried out. Figure 8.6c shows the variation of the fault transmissivity T_f with depth having fitted T_0 (the value of T_f from Chapter 7 that fitted the observation with no stress effect is also plotted). For text clarity reasons, in the remainder of this thesis the fault in which the value of the transmissivity is function of depth only is called a *non-uniform fault*. The fault with a single value of transmissivity (as mentioned in Chapter 7) is called a *uniform fault*.

For depths smaller than 1km, the fluids go faster than predicted in the uniform fault (Chapter 7).

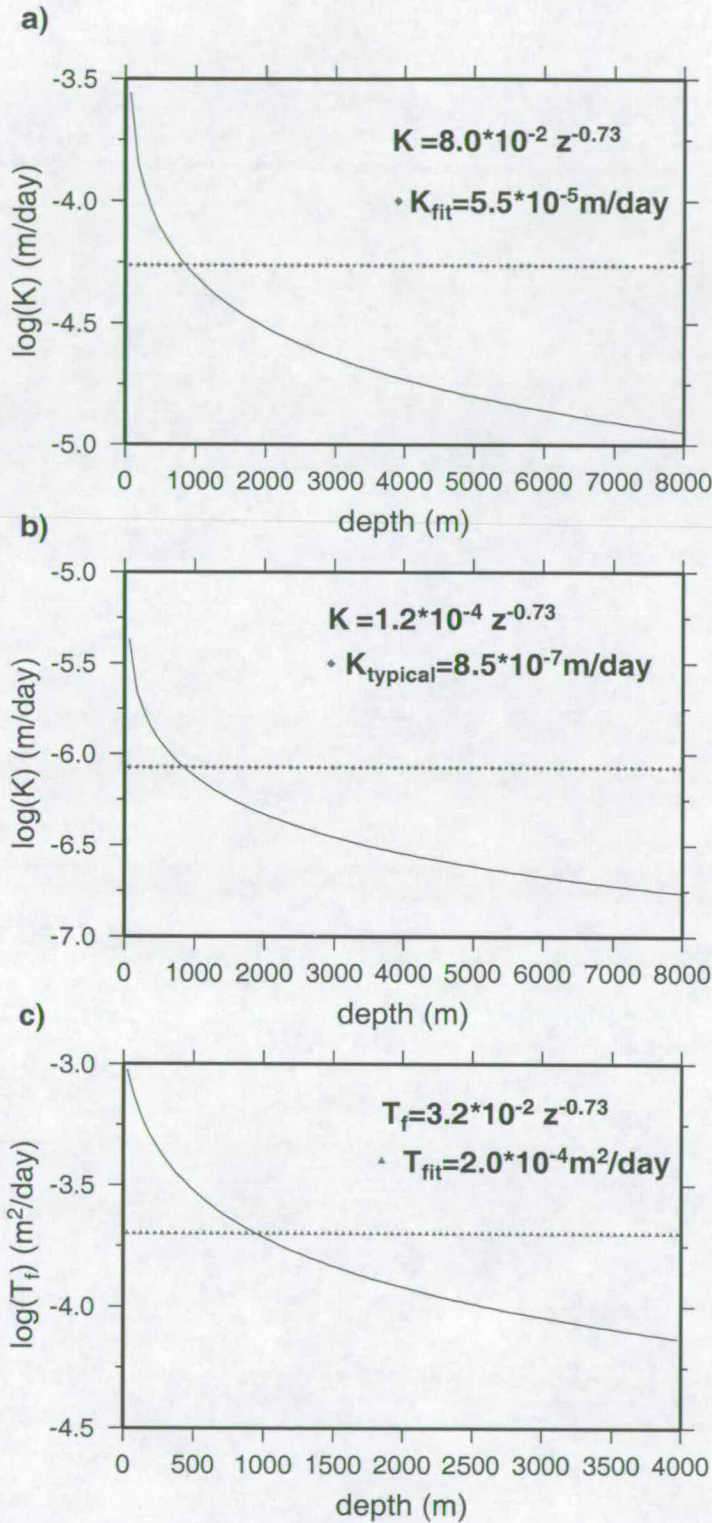


Figure 8.6: a) shows the dependence of K over depth (continuous line) that fits the seismic data and its comparison with K_{fit} (small dots). b) shows the depth dependence of K for realistic values of hydraulic conductivity. $K_{typical}$ is the typical values of hydraulic conductivity plotted to allow comparison with the curve. c) shows the dependence of T_f over depth (continuous line) in the non-uniform fault and the value of T_{fit} for the uniform fault.

This implies that as expected, the intersection of the lines in Figure 8.6c occurs at ≈ 1 km depth. Whereas for depths greater than 1 km, the fluid in the fault goes slower than predicted using the uniform transmissivity field. As was shown in Chapter 7, the fault is the main feature that promotes the diffusion of pressure to hypocentral depth. The non-uniform fault described on Figure 8.6c is still exhibits physically realistic values of T_f and S . More importantly, mean values of transmissivity are known to decrease with depth in fractured rock, so if this research aims to produce a more physically realistic model of fault transmissivity, this process must be included.

8.3 Including heterogeneous hydraulic properties in the fault

There is substantial field evidence that the transmissivity field in a fault is heterogeneous both because a fault zone is constituted by a damage zones with varying degrees of fracturing and hence, hydraulic properties as well as due to the effect of crack closure with increasing depth in the fault zone (Antonellini and Aydin, 1994; Caine *et al.*, 1996; Singhal and Gupta, 1999). Therefore, it is interesting to investigate the diffusion of pressure in fault zones using a heterogeneous transmissivity field to represent this fracturing in addition to modelling the closure of fractures with increase depth.

A code developed by Rebecca Lunn for the UK Environmental Agency in 1995 based on the Turning Bands Method (TBM) described by Mantoglou and Wilson (1982) is used for the simulation of the fault transmissivity random field. Random fields have been extensively researched in the simulation of natural hydrologic processes, particularly in groundwater flow and mass transport so the approach taken here is well established (Mantoglou and Wilson, 1982; Journel and Huijbregts, 1993; Kitanidis, 1997). The code will be used to generate transmissivity fields in the seismic fault. It is therefore convenient to present a brief review of the concept and properties of a random function.

8.3.1 Review of the properties of a stationary random function

The concept of a random function (or stochastic process) is a generalisation of a random variable. Let $\mathbf{x} = (x_1, x_2, \dots, x_n)$ be a point in n dimensional space, R^n , and $Z(\mathbf{x})$ a random variable corresponding to point \mathbf{x} . A random function on R^n is defined as the set $[\mathbf{x}, Z(\mathbf{x})] | \mathbf{x} \in R^n$. If $n = 2$, or $n = 3$, the random function is called a random field. When $n = 1$, the random function is called a unidimensional process, or a line process.

The mean function of a random function is defined as (Kreyszig, 1993):

$$m(\mathbf{x}) = \int_{-\infty}^{+\infty} Z(\mathbf{x})f(\mathbf{x})d\mathbf{x} = E[Z(\mathbf{x})] \quad (8.3)$$

where $f(\mathbf{x})$ is the probability density function of the random function $Z(\mathbf{x})$ and $E[]$ is the expectation operator. If $E[Z^2(\mathbf{x})]$ is finite for all \mathbf{x} , the covariance function can be defined as (Mantoglou and

Wilson, 1982):

$$\begin{aligned} C(\mathbf{x}_1, \mathbf{x}_2) &= E[(Z(\mathbf{x}_1) - m(\mathbf{x}_1))(Z(\mathbf{x}_2) - m(\mathbf{x}_2))] \\ &= E[Z(\mathbf{x}_1)Z(\mathbf{x}_2)] - m(\mathbf{x}_1)m(\mathbf{x}_2) \end{aligned} \quad (8.4)$$

A random process is called a *second-order stationary process* when the following conditions are satisfied (Kitanidis, 1997):

1. The mean is independent of the position of each point in R^n . In other words, the mean is a constant:

$$E[Z(\mathbf{x})] = m \quad (8.5)$$

2. The two point covariance function depends only on the distance between the two points:

$$C(\mathbf{x}_1, \mathbf{x}_2) = C(\mathbf{x}_1 - \mathbf{x}_2) = C(\mathbf{h}) \quad (8.6)$$

A second-order stationary process is called isotropic when the covariance function does not depend on the direction $\mathbf{h} = (\mathbf{x}_1 - \mathbf{x}_2)$ of the distance vector, but only on the length $|\mathbf{h}|$. So in this case, one can write:

$$C(\mathbf{h}) = C(r) \quad (8.7)$$

where $r = |\mathbf{h}|$.

All the processes dealt with in this Chapter are assumed to be second order stationary; field evidence supports this assumption for the distribution of hydraulic conductivity in natural systems (Journel and Huijbregts, 1993; de Marsily, 1986; Kitanidis, 1997). There are also many field and laboratory measurements supporting the assumption of a log-normal distribution of hydraulic conductivity (Abdel-Salam and Chrysikopoulos, 1996)

8.3.2 Spatial statistics

In order to characterise the transmissivity fields, some concepts of spatial statistics are briefly presented. It is beyond the scope of this thesis to provide a full review of spatial statistics. For further reading one may refer to the references presented in this section.

The variogram

A practical way to say how structured a field is via the *variogram*. Let us consider two numerical values of the correlated field $Z(\mathbf{x})$ and $Z(\mathbf{x} + \mathbf{h})$, at two points \mathbf{x} and $\mathbf{x} + \mathbf{h}$ separated by the vector \mathbf{h} . \mathbf{h} is also called the lag. The variability between those two quantities is characterised by the variogram

function, defined as (Journel and Huijbregts, 1993):

$$\gamma(x, h) = \frac{1}{2} E[Z(x) - Z(x + h)]^2 \quad (8.8)$$

If a data set is given, it is possible to estimate $\gamma(h)$ from the available data by the estimator $\gamma^*(h)$ which is the arithmetic mean of the square of the differences between two experimental point measurements $[z(x_i), z(x_i + h)]$ for any points separated by the distance vector h :

$$\gamma^*(h) = \frac{1}{2N(h)} \sum_{i=1}^{N(h)} [z(x_i) - z(x_i + h)]^2 \quad (8.9)$$

The variogram is related to the covariance by the equation:

$$\gamma(h) = \sigma^2 - C(h) \quad (8.10)$$

where σ^2 is the variance function.

Some properties of the covariance and the variance functions are useful to mention here (Journel and Huijbregts, 1993; Kitanidis, 1997):

Properties of the covariance

- $C(0) \geq 0$;
- $C(h) = C(-h)$, the covariance is an even function;
- $C(h) \rightarrow 0$, when $|h| \rightarrow \infty$; the correlation between $Z(x)$ and $Z(x + h)$ disappears when the distance h becomes too large. In practice, $C(h) = 0$, once $|h| \gg a$. The distance a beyond which $C(h)$ can be considered zero is called the *range* and it represents the transition from the state in which a spatial correlation exists ($|h| < a$) to the state in which the correlation no longer exists ($|h| > a$). Figure 8.7 illustrates this property. For the exponential covariance function I will adopt in this research, the range is approximately $3b^{-1}$.

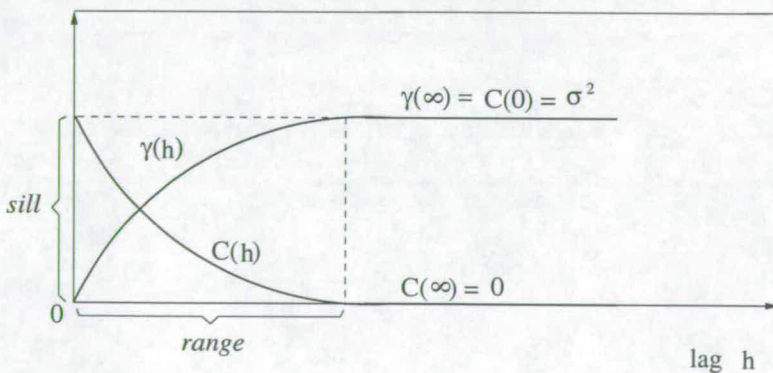


Figure 8.7: Covariance and variogram. This schematic illustration shows some of the properties of both the covariance and the variogram (after Journel and Huijbregts (1993)).

Properties of the variogram

- $\gamma(0) = 0$ and $\gamma(h) = \gamma(-h)$;
- transition phenomena; often, in practice, the variogram stops increasing around a limit value called the *sill*, which is simply the a priori variance of the random function, σ^2 . In mathematical terms: $\gamma(\infty) = C(0)$. Figure 8.7 also illustrates this property;
- zone of influence; in a transition phenomena, any data values $\xi(x)$ are said to be correlated with any other value falling within a radius a of x . This correlation and the influence of one value on the other will decrease as the distance between the two points increases. Therefore, the range a corresponds to the intuitive idea of a zone of influence of a random variable: beyond the distance $|h| = a$, the two points considered are uncorrelated.

Summarising, the field is defined by its covariance function, range and sill. If T_f field data were available, the experimental variogram could be calculated via 8.9. However, field measurements are not available at Açu and therefore the spatially correlated fields used in this research are simulated ones. A simple covariance (*simple isotropic exponential*) has been selected for the simulations. Since all the established functions for describing transmissivity fields behave in much the same way (just varying in shape and steepness as $h \rightarrow 0$), I do not expect this selection to influence my conclusions.

8.3.3 Simulation of the spatially correlated random fields

To present the Turning Bands Method, three assumptions are made: 1 - the field to be simulated is second-order stationary and isotropic; 2 - at each point the values of the field are normally distributed and 3 - the covariance $C(r)$ of the field to be simulated is known.

In the TBM the two- or three dimensional fields are not simulated directly. Instead, the TBM performs simulations along several lines, using a unidimensional covariance function. This unidimensional covariance function corresponds to the given two- three dimensional one. Then at each point of the two- three-dimensional field a weighted sum of the corresponding values of the line processes is assigned (Mantoglou and Wilson, 1982; Journel and Huijbregts, 1993). In this Chapter, only the two-dimensional simulations will be performed using the code developed by Rebecca Lunn in 1995. Mantoglou and Wilson (1982) provides a full description of the TBM in two and three dimensions.

As mentioned before, the two-dimensional function that will be dealt with will be the *simple isotropic exponential* (Journel and Huijbregts, 1993; Kitanidis, 1997):

$$C(r) = \sigma^2 e^{-br} \quad (8.11)$$

where the parameter b^{-1} has [*length*] units and is sometimes called the *correlation length*.

The upper panel of Figure 8.8 shows three examples of two-dimensional realisations of stationary fields generated by the turning bands method. The variance of the field is 0.25. The grid on which the realisation was generated has 80x80 nodes and each node is 50m apart. Figures 8.8a, b and c show

realisations with correlation lengths of 16.67, 166.67 and 500m, respectively. It can be noted that as the correlation length increases, the field obtained is more structured. In figure 8.8a, the correlation length is so small, in comparison to the grid size that the field is not structured and simply resembles a random field. As the correlation length increases, structure is present in the field and it presents clusters of high and low values. For each of the realisations a colour-coded histogram of the random field is presented in the middle panel. The colour code is the same as that used to plot the correlated field. In the bottom

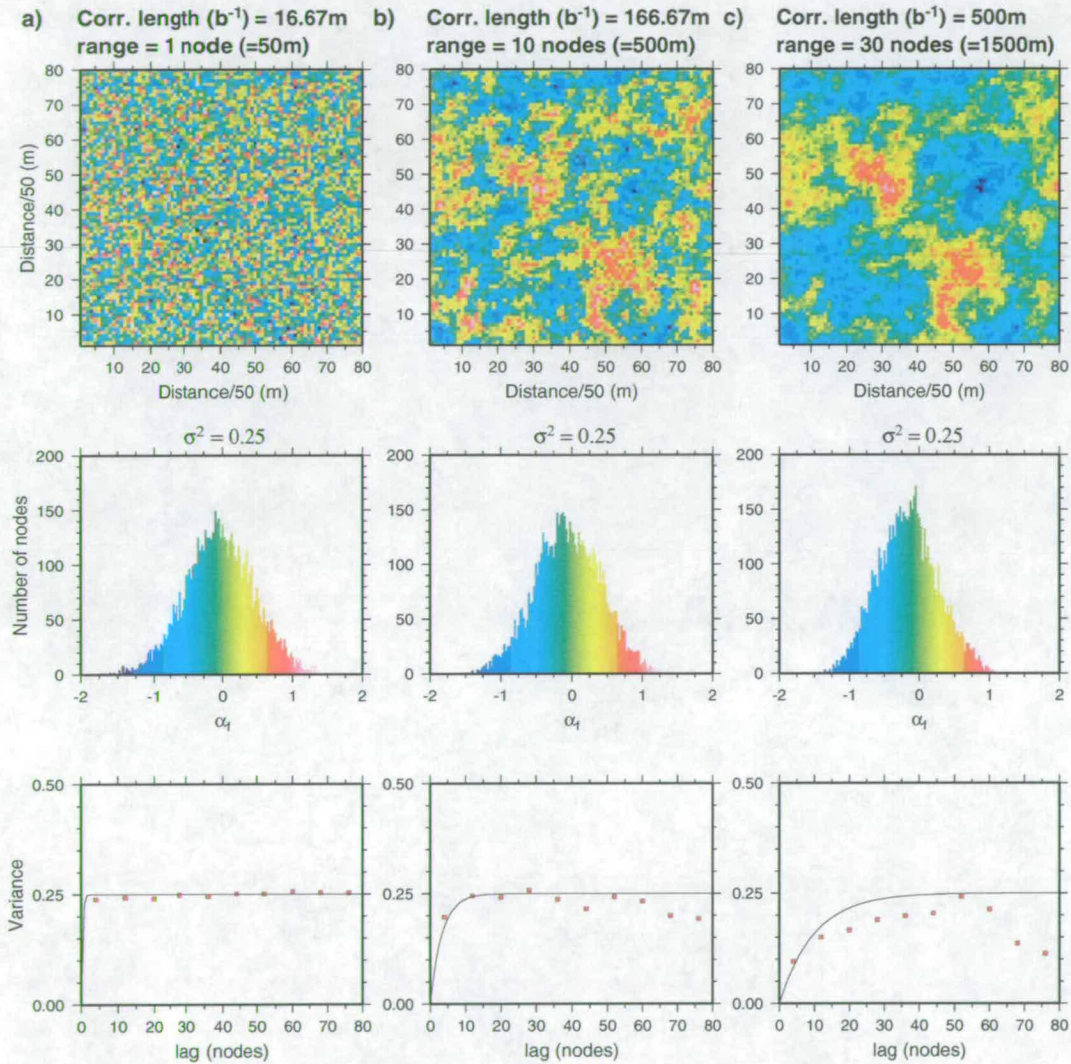


Figure 8.8: Examples of two-dimensional realisations of stationary fields generated by the turning bands method where $\sigma^2 = 0.25$. a), b) and c) show realisations with correlation lengths of 16.67, 166.67 and 500m, respectively. For each of the realisations the histogram of the random field is presented in the middle panel. The analytical (full lines) and experimental (red squares) variograms for each of the realisation are shown in the bottom panel. α_f is the values of the spatially correlated field with mean zero.

panel of each of the synthetic fields shown in Figures 8.8a, b and c, the theoretical variogram described by equation 8.8 (full line) is shown together with an experimental variogram computed via equation

8.9 (red dots). The theoretical variograms for each of the synthetic correlated fields with different correlation lengths exhibit the properties discussed above. In particular, it is worth noting that, as expected, as the correlation length increases, so does the sill of the variogram. The experimental variograms also behave in a similar fashion. However, as shall be observed in Figure 8.8a, b and c, the points computed via equation 8.9 deviate in places from the theoretical variogram. The reasons for this deviation are: 1 - finite size effects of the grid. As the correlation length approaches the total length of the grid, the number of experimental pairs is not big enough to provide reliable experimental statistics of $\gamma^*(\mathbf{h})$; 2 - each of the correlated fields shown in Figure 8.8 is **one** realisation of a random process. When more realisations were made, the average of the experimental variograms converged on the theoretical one.

To produce the transmissivity fields T_F to be used in the numerical simulations, the following approach is taken:

- A spatially correlated field α_f , with mean zero (Figure 8.8), is produced;
- the values of α_f are inverted to obtain transmissivity values: $T_{\alpha_f} = 10^{\alpha_f}$;
- T_{α_f} is multiplied by $T_0 z^{-\alpha}$, where $T_0 = 3.2 \times 10^{-2} \text{ m/day}$ and $\alpha = 0.73$ (from Section 8.2). The result of this final operation is T_f , the transmissivity field.

Figure 8.9 shows examples of correlated hydraulic fields in which the reduction of hydraulic transmissivity with increasing depth is included. Figures 8.9a, b, and c show T_f for three different correlation lengths: 16.67, 166.67 and 500m, respectively. For these three figures, $\sigma^2 = 0.25$. The plot on the right hand side of each of these figures shows: the mean values of T_f with depth as red triangles connected by a full continuous black line; the error bars show the standard deviation of T_f at depth; the green curve is the plot of the transmissivity distribution of the non-uniform fault ($T_f = 3.2 \times 10^{-2} z^{-0.73}$), also shown in Figure 8.6c. The full continuous line representing T_0 (from Chapter 7) is also plotted for completeness. These figures show that as the correlation length increases, the standard deviation of the transmissivity values at a particular depth increases. This occurs because, as the correlation length increases, the field becomes more structured and exhibits clusters of contrasting transmissivity values at the same depth. Figure 8.9d shows a correlated field with a 500m correlation length. Now, $\sigma^2 = 0.5$. As expected, as the background variance increases the standard deviation of the mean values over depth increases. Since the correlation length of the random field is the same as that in Figure 8.9c, the mean values of T_f are the same. The $T_f = 3.2 \times 10^{-2} z^{-0.73}$ curve (the green one) describes the theoretical transmissivity over depth. In all four realisations the reduction in the theoretical mean T_f is still mirrored by the behaviour of the experimental mean T_f (the full continuous black line).

8.4 Pore pressure diffusion in a non-uniform transmissivity field

To investigate the impact of heterogeneity on pore pressure diffusion in the seismogenic fault, simulations with transmissivity fields of different correlation lengths and with different variances were carried out. The correlation length selected for the transmissivity fields were 16.67, 166.67 and 500m,

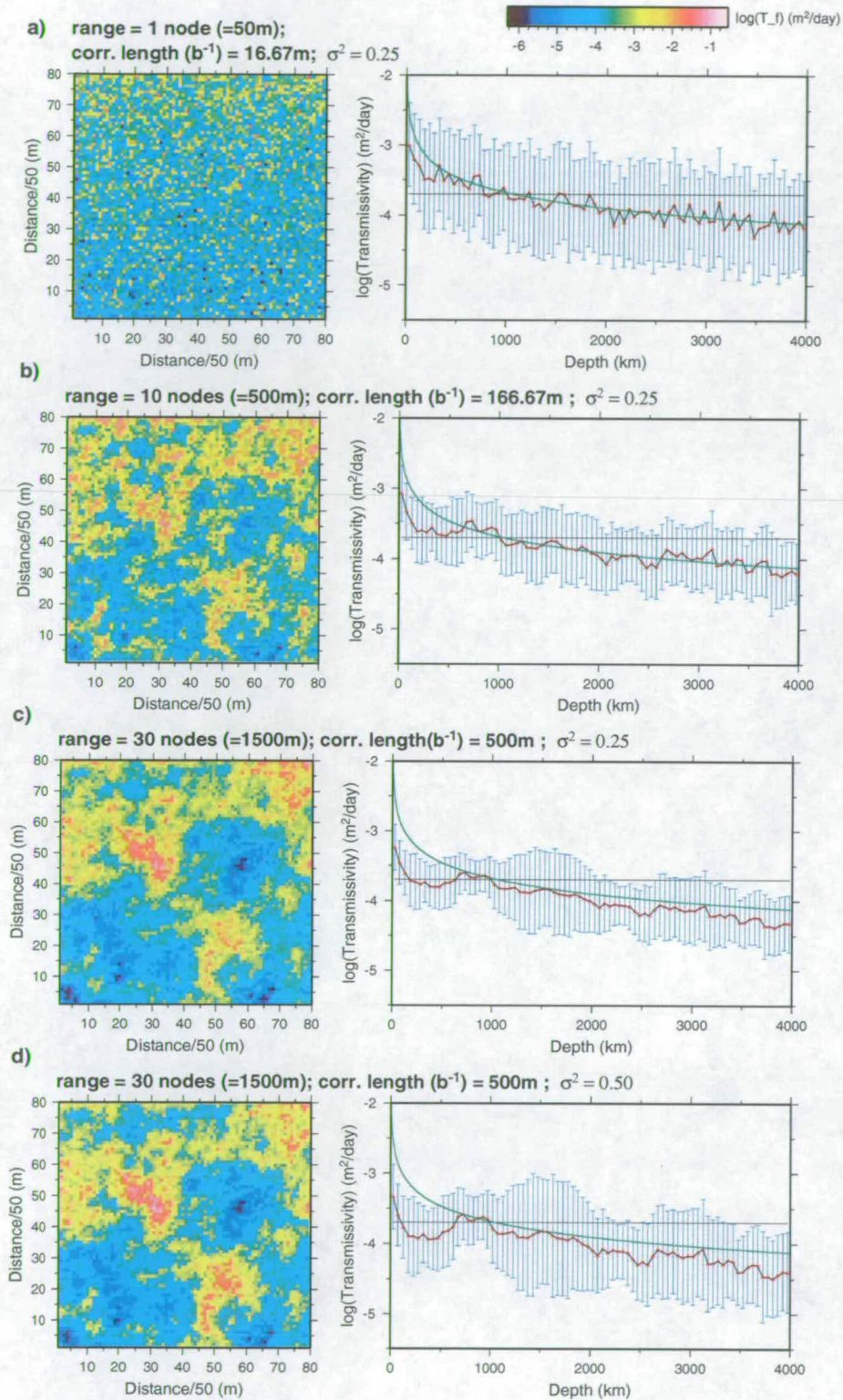


Figure 8.9: a, b and c show the transmissivity fields for three different correlation lengths:16.67, 166.67 and 500m, respectively. For those figures $\sigma^2 = 0.25$, On the right-hand side of each of the fields, the variation of the mean values of the transmissivity at each depth is plotted (red dots) together with the standard variation, the curve $3.2 \times 10^{-2} z^{-0.73}$ is the green curve. The full continuous horizontal line represents T_0 . d is a transmissivity field with 500m correlation length and $\sigma^2 = 0.50$.

corresponding to ranges of 50, 500 and 1500m, respectively. The choice of the largest range investigated was based on the size of the active seismic cluster a , shown in Figure 4.4: $\sim 1500m$. The lower values of correlation length were chosen to also see the impact of increasing correlation length in the numerical simulations.

The spatially correlated field generated for each simulation has a log-normal distribution with mean zero and variances of 0.25 and 0.5, corresponding to standard deviations of 0.5 and 0.71. The choice of a standard deviation, σ , of 0.5 and the fact that the field has a log-normal distribution, means that about 95.5% of the values of the generated field lie between -2σ and $+2\sigma$. Therefore, the extreme values of the field are 4σ apart. The choice of σ to be used in the simulations is based on the fact that the transmissivity values in crystalline rock range from $10^{-2} - 10^{-5}m^2/day$ (Rutqvist *et al.*, 1998; Gudmundsson, 2000). In other words, $\log(T_f)$ in real crystalline rocks varies by about 4σ , assuming that these values are also log-normally distributed (Abdel-Salam and Chrysikopoulos, 1996). The choice of a larger value of $\sigma^2 = 0.5$ is to investigate the impact of a larger variance in the pore pressure diffusion in the seismogenic fault. If was $\sigma^2 = 0.75$, it would imply in a transmissivity field lower than $10^{-5}m^2/day$. However, transmissivity values lower than $10^{-5}m^2/day$ are likely to occur, as most of the pump tests to obtain this hydraulic properties are only performed at shallow depths ($\approx 1km$). Therefore σ^2 is likely to be larger than 0.5.

To show the results of the numerical simulations performed for each realisation of transmissivity, a plot of the transmissivity field and the piezometric head predictions will be shown. Two other outputs of the numerical simulations will also be presented: the corresponding contour plot of the time lag between the maximum water level and the maximum piezometric head prediction for each node of the fault plane and a contour plot of the maximum variation of the piezometric head prediction at each node. To obtain these two extra outputs, an oscillatory steady-state variation of the piezometric head prediction was achieved in a similar fashion to that described by the flow diagram shown in Figure 7.12.

Figure 8.10 illustrates how the measurements of the time delay and the amplitude variation are made. The lake level is in black and the piezometric head prediction at a particular node is in red. In order to ensure that all the nodes in the fault have achieved the steady-state oscillatory regime, 226 time steps (5 years) are first simulated. The lake level and the piezometric head prediction at a node for these 226 time steps are displayed in Figure 8.10 as dashed lines. When the 6th year begins, the full lines, the measurements of both the time lag and the amplitude variation are made, for each node of the fault, as illustrated by the double-headed arrows.

Before analysing the results from the stochastic fields it is useful to plot contours of the time delay and the amplitude variations for results already obtained for the uniform fault (Chapter 7) and the non-uniform fault (stress dependent fault, seen in section 8.2.2). Figure 8.11 shows examples of time delay and amplitude measurements for the uniform and non-uniform faults. Figures 8.11a and 8.11b show the time delay and amplitude variation contour plots for the case in which the fault is uniform, $T_f=2.0 \times 10^{-4}m^2/day$. Figures 8.11c and 8.11d show the time delay and amplitude variation contour plots for the case in which T_f is non-uniform (function of depth): $T_f=3.2 \times 10^{-2}z^{-0.73}m^2/day$. In Figures 8.11a and 8.11c, it is possible to analyse the time delays over depth for different nodes of the

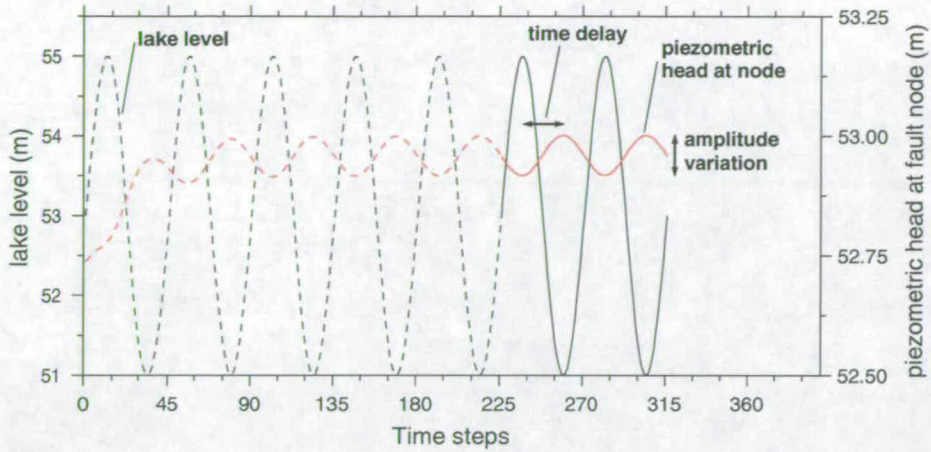


Figure 8.10: How the time lag and the amplitude variations are performed. Only after 226 time steps have been simulated (the dashed line), the measurements, for each node are made.

fault. At 2.0km depth, for both the uniform and non-uniform case, the calibrated time delay between the peak in water level and the increase in seismic activity made by seismological observation is the same at approximately 136 days. However, the spatial pattern of the two figures is not the same; in the uniform fault (Figure 8.11a), the time delay contours increase more slowly than in the non-uniform fault (figure 8.11c). This is caused by the decrease of T_f over depth in the non-uniform case. Another feature worth noting is that in the homogeneous case, the maximum time delay observed is 272 days for the deepest regions of the fault. For the non-uniform case, the time delay, for the same region of the fault reaches 328 days. The spatio-temporal analysis of the seismicity (Chapter 4) shows activation of seismic events at depths of 3.0 and 4.0 km at times delays of 180 and 210 days. So, the times observed in the Açu area are shorter than those predicted by both the uniform and the non-uniform model: 224 and 328 days. This constitutes an important reason to investigate models with heterogeneous transmissivity fields. In figures 8.11b and 8.11d, the amplitude variations for the homogeneous model and the non-homogeneous model are shown. The fault nodes that are directly beneath the reservoir experience amplitude variations as high as the amplitude variation of the reservoir level. The incorporation of the more physically realistic non-uniform transmissivity reduces the amplitude variation experienced at a given depth.

In order to compare the numerical simulation results with the real seismological data (presented in Chapters 3 and 4), it is necessary to generate some summary statistics from the real seismological data. A straightforward way to summarise data with a non-parametric distribution is to calculate the *range*, *median* and the *interquartile range*. The *range* is the difference between the largest and the smallest values. The *median* is the middle of a distribution: half the scores are above the median and half are below the median. The *interquartile range* (hereafter IQR) is a measure of spread. It is the distance, measured from the median, that covers half of the data. In other words, it is the range in which (the central) half of the data lies.

Figure 8.12 shows the histogram of the percentage of seismic events as a function of the time delay between the peak in water level on the 31st May 1995 and the time the earthquake occurs. The

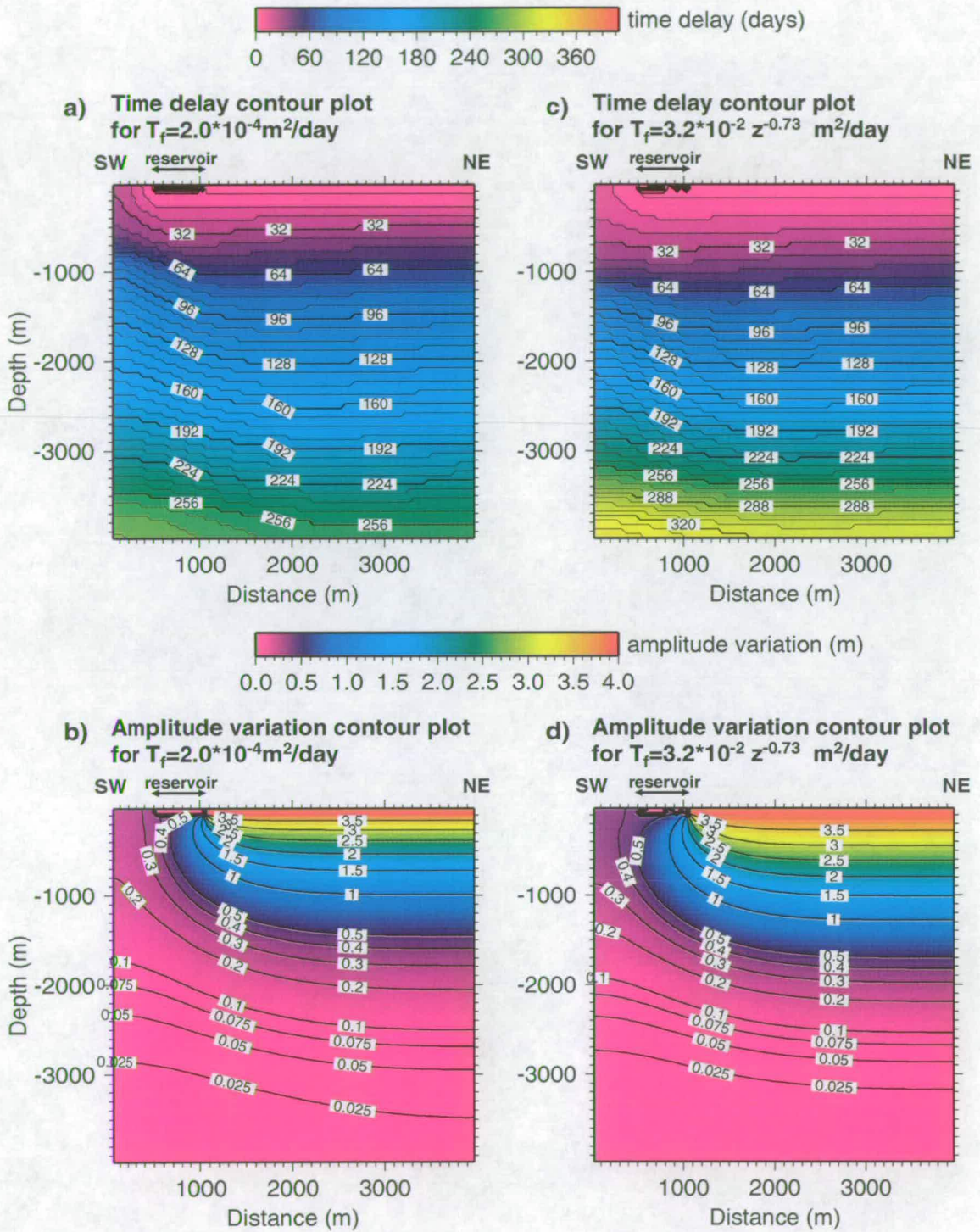


Figure 8.11: **a** and **b** show, respectively, the time delay and the amplitude variation contour plots for a homogeneous fault with $T_f=2.0 \times 10^{-4} \text{ m}^2/\text{day}$. **c** and **d** show, respectively, the time delay and the amplitude variation contour plots for a fault in which the transmissivity is a function of the depth: $T_f=3.2 \times 10^{-2} z^{-0.73} \text{ m}^2/\text{day}$. The time delay and amplitude variation for each fault node are measured as shown in Figure 8.10.

earthquakes considered here are those from cluster a. Each of the histograms - Figures 8.12a to 8.12d - correspond to the percentage of the total number of events. The total number of earthquakes considered is 190. For each depth range considered, the number of events, range, median and the IQR are shown.

Figure 8.12a corresponds to the shallowest depth range considered: 1400 - 1800 m depth. 15 earthquakes occur in this depth range. Most of the events in this depth range are at 128 days. Figure 8.12b comprises the majority of the seismic events considered. The frequency histogram shows that the peak of the frequency of the events in this depth range (1800 - 2200 m) has a time lag between 128 and 136 days. Besides that, it is possible to observe a large scatter in the frequency distribution, from 8 to 432 days. It is very unlikely that events were triggered by pore pressure diffusion, at this depth range, a month after the maximum in water level. Therefore, it is important to calculate the summary statistics for events which are likely to be caused by the pore pressure diffusion only. i.e., events with time a delay greater than 32 days. Table 8.3 presents the summary statistics of events with time delays greater than 32 days occurring at depth range of 1800 to 2200m. It should be noted that the range is smaller

number of events	125
range	405 days
median	148 days
IQR	68 days

Table 8.3: Summary statistics of events with time delay greater than 32 days occurring at depth range of 1800 to 2200m.

than when the events with time a delay smaller than 32 are not included in the computation. This illustrates how sensitive the range is to possible outliers in the data. On the other hand, the median and the interquartile range are less sensitive measures and therefore, they remain practically the same. In Figure 8.12c the depth range is from 2200 to 2600 m. At this depth range, fewer events are triggered (only 37 events) and a small peak in the frequency distribution is observed at around 136 days. A large scatter in the time lag is also observed. A priori, one does not know if all the events that occur in the 1,800 - 2,200 m range are induced by the pressure diffusion only. Again, it seems unlikely that the first group of events are caused by pressure diffusion. For the deepest depth range considered, Figure 8.12d, only seven events are available. All these seven events occur at zero time lag. Thus may be a response to the previous years increase in water level of the reservoir. A common feature of all the histograms described is the fact that in all depth ranges, there are periods of quiescence of up to 32 days.

The existence of very small time lags in all the depth ranges may be explained if the seismicity in the Açú reservoir is partially triggered by the undrained response, as discussed in section 2.2.2. In the numerical simulations I have conducted, only the diffusion effect (drained response) is calculated, since it is the dominant mechanism of RIS in the Açú reservoir. This research will consider to what extent the data can be explained by such a diffusion-only modelling approach. The following sections compare the frequency histogram of the real data with numerical simulated frequency histograms obtained from different correlated transmissivity fields. The aim is not to match the frequency histograms derived from the real data with the frequency histograms derived from the simulated pressure field, but to identify fault transmissivity parameters (variance and correlation length of the transmissivity field) that can reproduce a similar distribution shape and spread (for each depth) as that observed in the frequency histograms in Figure 8.12. In addition, since the amplitude variation is an important output from our

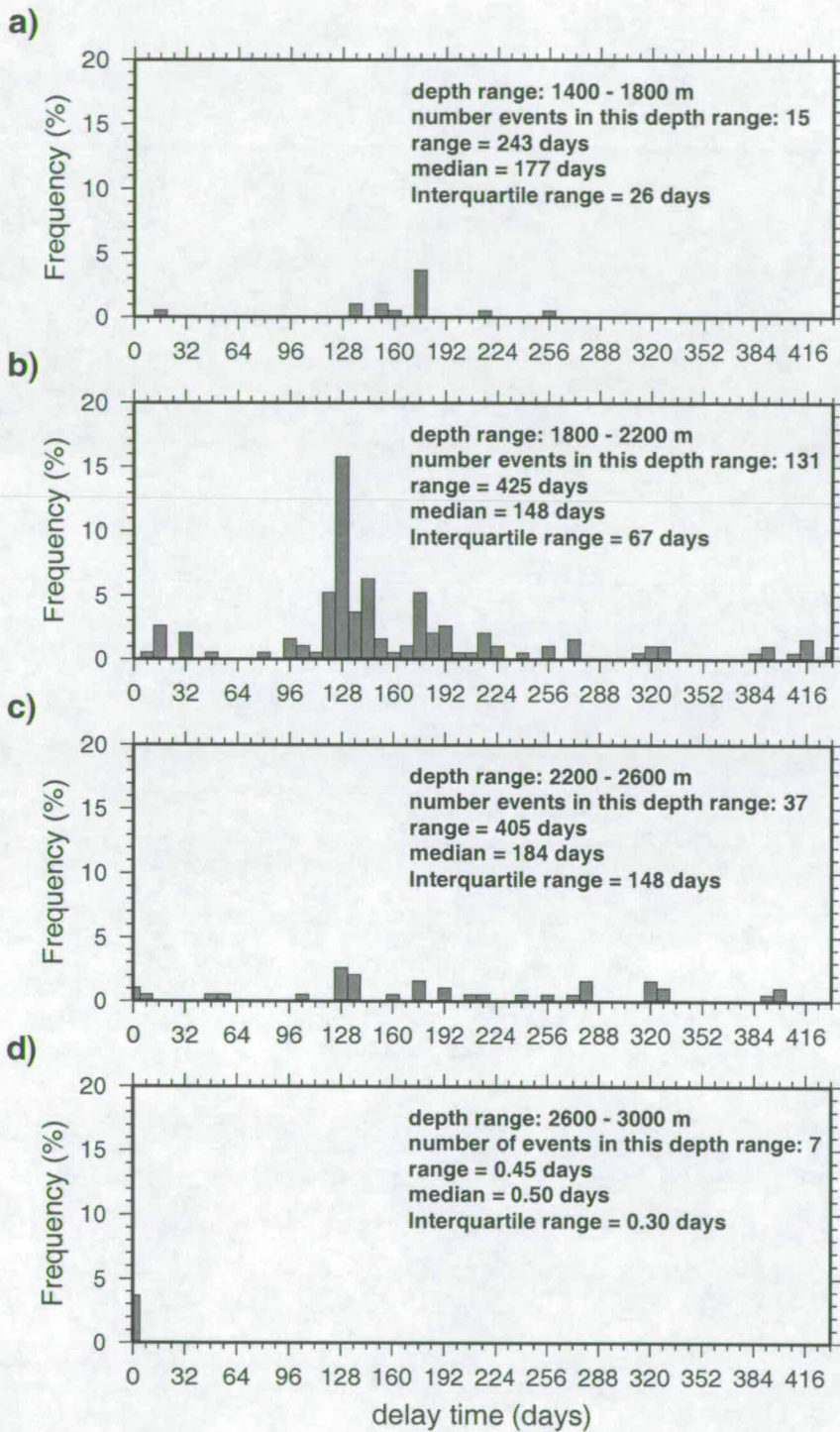


Figure 8.12: Frequency histogram of the percentage of events as a function of the time delay between the peak in water level in October 1995 and the time the earthquake occurs. Each histogram corresponds to a different depth range and the total number of earthquakes is 190. For each depth range summary statistics are also presented. The histograms and their statistics are calculated from the real earthquake data.

model, it will be displayed to illustrate the magnitude of the piezometric head causing seismicity in the fault. One underlying assumption is made that is relevant to this analysis: once a node experiences a maximum value in the piezometric head, this node is triggered, i.e. an earthquake occurs at that fault node. A priori, one does not know how much piezometric head variation is necessary to trigger an earthquake, therefore, the following research will also investigate the validity of this assumption.

In the following sections, the transmissivity field, maximum amplitude variation, time delay contour plot and the frequency histogram of the percentage of events as a function of the time delay between the maximum in water level and the maximum in piezometric head predictions will be presented. The approach used in this thesis is to first investigate a spatially correlated permeable fault in which the effect of the stress field is accounted for and then to add to this field more and more structure: increasing both the correlation length and the variance of the transmissivity field. The total number of numerical simulations is 23 and they are organised as shown in Table 8.4. For each of the numerical simulations, the transmissivity field, time delay contour plot, the maximum piezometric amplitude variation and the histogram of triggered nodes is presented and discussed.

Figure number	Transmissivity field characteristics	σ^2 (if pertinent)	number of runs
8.13	non-uniform	-	1
8.14	random field with stress effect	0.25	1
8.15	random field with stress effect	0.50	1
Correlation length			
E.1 - E.5	166.67m and stress effect	0.25	5
E.6 - E.10	166.67m and stress effect	0.50	5
E.11 - E.15	500m and stress effect	0.25	5
E.16 - E.20	500m and stress effect	0.50	5

Table 8.4: Transmissivity field parameters for the numerical simulations performed. Figures E.1 to E.20 are found in the appendix.

8.5 Numerical simulation with non-uniform and random transmissivity fields

In this section, a run with an uncorrelated random transmissivity field (Figure 8.13) is presented together with two other fields with a correlation length of 16.67m (Figures 8.14 and 8.15).

Figure 8.13a shows the simplest case of a non-uniform fault with no heterogeneity, i.e., only the reduction in transmissivity due to increasing stress over depth is included (non-uniform field). With this fault model, the transmissivity field ranges from $10^{-3.1} - 10^{-4.1} m^2/day$. The time delay to peak pressure change is shown in figure 8.13b. The maximum delay is 328 days in the deepest part of the

fault. The amplitude variation, shown in figure 8.13c shows the decay of the amplitude in pressure variation as depth increases. At 2.0km depth, the amplitude variation may range from 0.1 to 0.3m. As should be noted, for depths greater than 3,000m, the amplitude variation is not larger than 0.025m. Hence, it is very unlikely that earthquakes may be triggered for depths greater than 3,000m according to this model. The histograms shown in figure 8.13d show the time delays at different depth ranges. These histograms are presented for every 400 metres range, starting from the 1,400 - 1800 (top panel of figure 8.13d), down to 3,400 - 3,800m (the bottom panel in figure 8.13d). The total number of nodes in the whole set of histograms is 3840 and each histogram comprises 640 nodes. The deeper parts of the fault show a larger time delay. The distribution of the percentage of triggered nodes slightly diverges from a uniform distribution (which would be anticipated if all the contours were horizontal) due to the position of the fault relative to the lake and the regional groundwater gradient. The median of each histogram increases as depth increases, due to the latter arrival of the pressure front at deeper depths. The range at all depth ranges is the same since histogram distributions are near-uniform. The interquartile range is slightly increased for the histograms that include the greatest depths as the delay contours deviate more from the horizontal lines.

Figures 8.14 and 8.15 show the same plots for a fault with a random non-correlated transmissivity field with variances of 0.25 and 0.50. The input value for generation the random fields (the seed) for the random number generator is the same. The introduction of the stochastic field does not change significantly the patterns already present in figure 8.13 as demonstrated by the summary statistics shown for each depth range of each stochastic field in Figure 8.14. For $\sigma = 0.25$, the range and the median are slightly increased in comparison to the non-uniform field by 8 days (sometimes 16) at all depth ranges. The median remains practically the same. The increased $\sigma = 0.50$ of the stochastic field shown in Figure 8.15 also does not significantly alter the statistics. The median and the range are slightly shifted towards greater values (8 or 16 days). The IQR is not altered in comparison with the numerical simulation with $\sigma = 0.25$.

The values of range, median and IQR are very different for each of these simulations (8.13-8.15) from the ones observed in the real earthquake data. The IQR and the range: 56 and 16; of the simulated values are much smaller than those observed in the real earthquake data. It is clearly noted that the inclusion of an uncorrelated random stochastic field is not an appropriated model to explain the seismicity pattern. The most obvious alternative is to invoke the inclusion of correlated random fields. That will provide a range of structured highly permeable and impermeable flow paths.

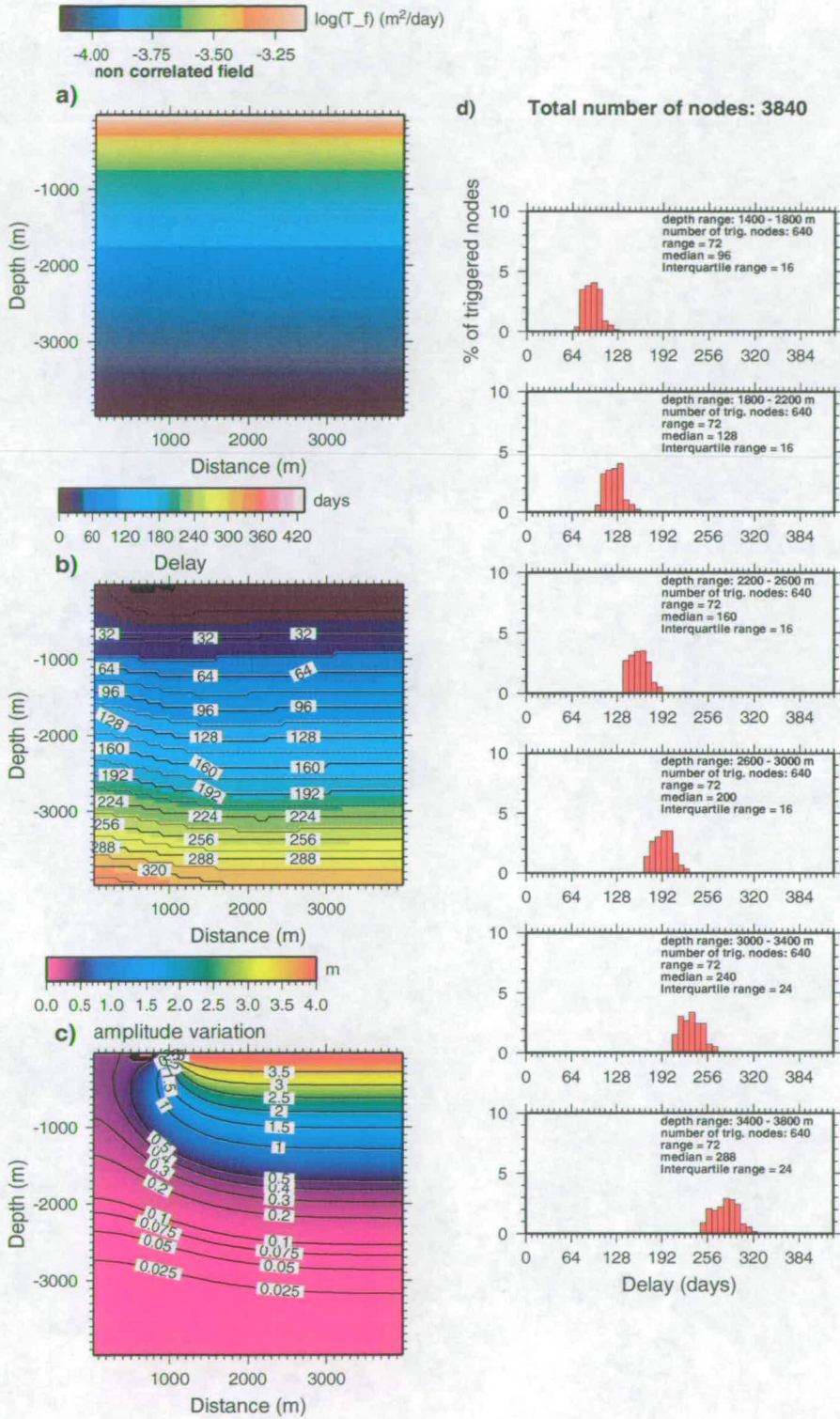


Figure 8.13: Output from a non-uniform fault without a random transmissivity field.

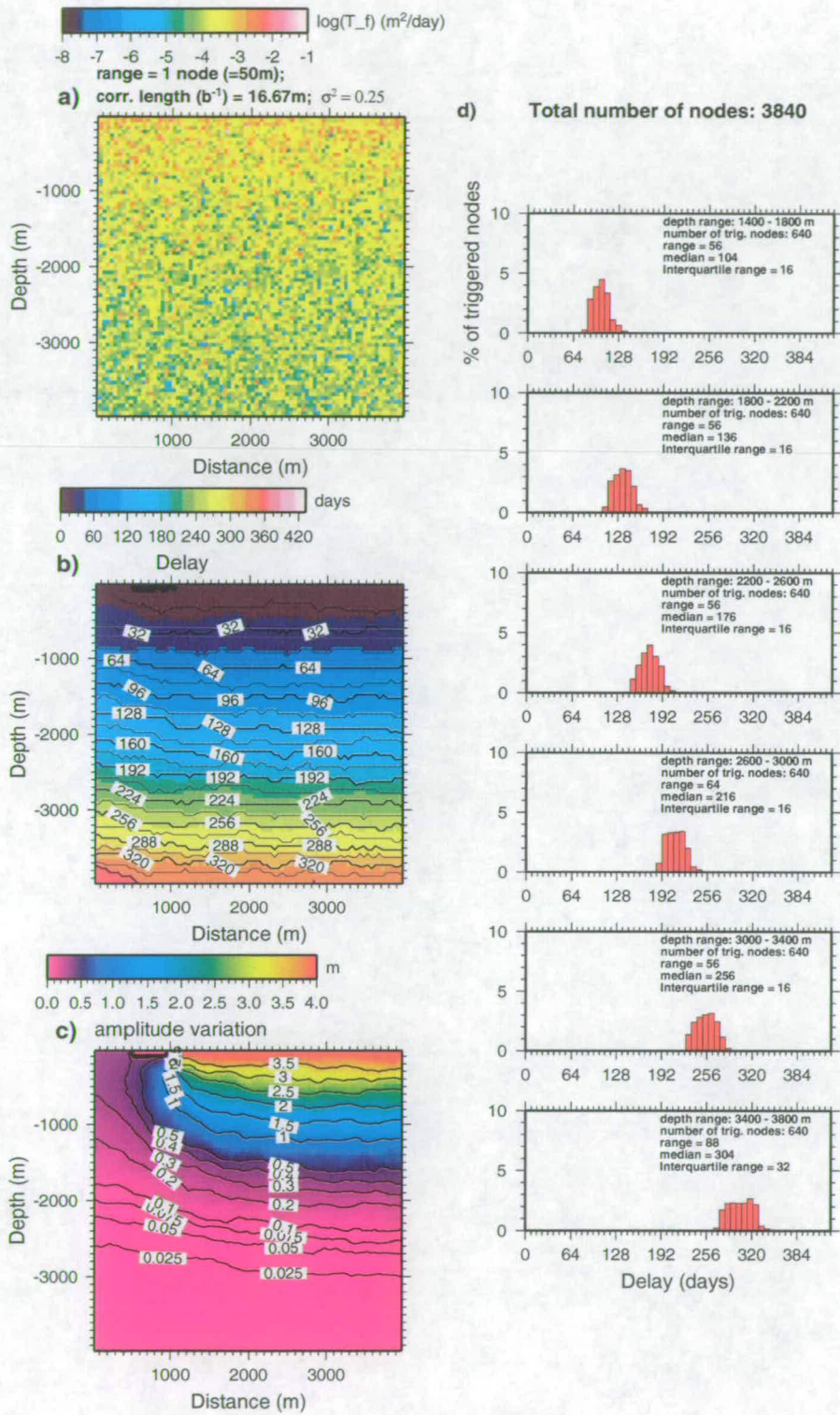


Figure 8.14: Output from a fault with a random transmissivity field and $\sigma^2=0.25$.

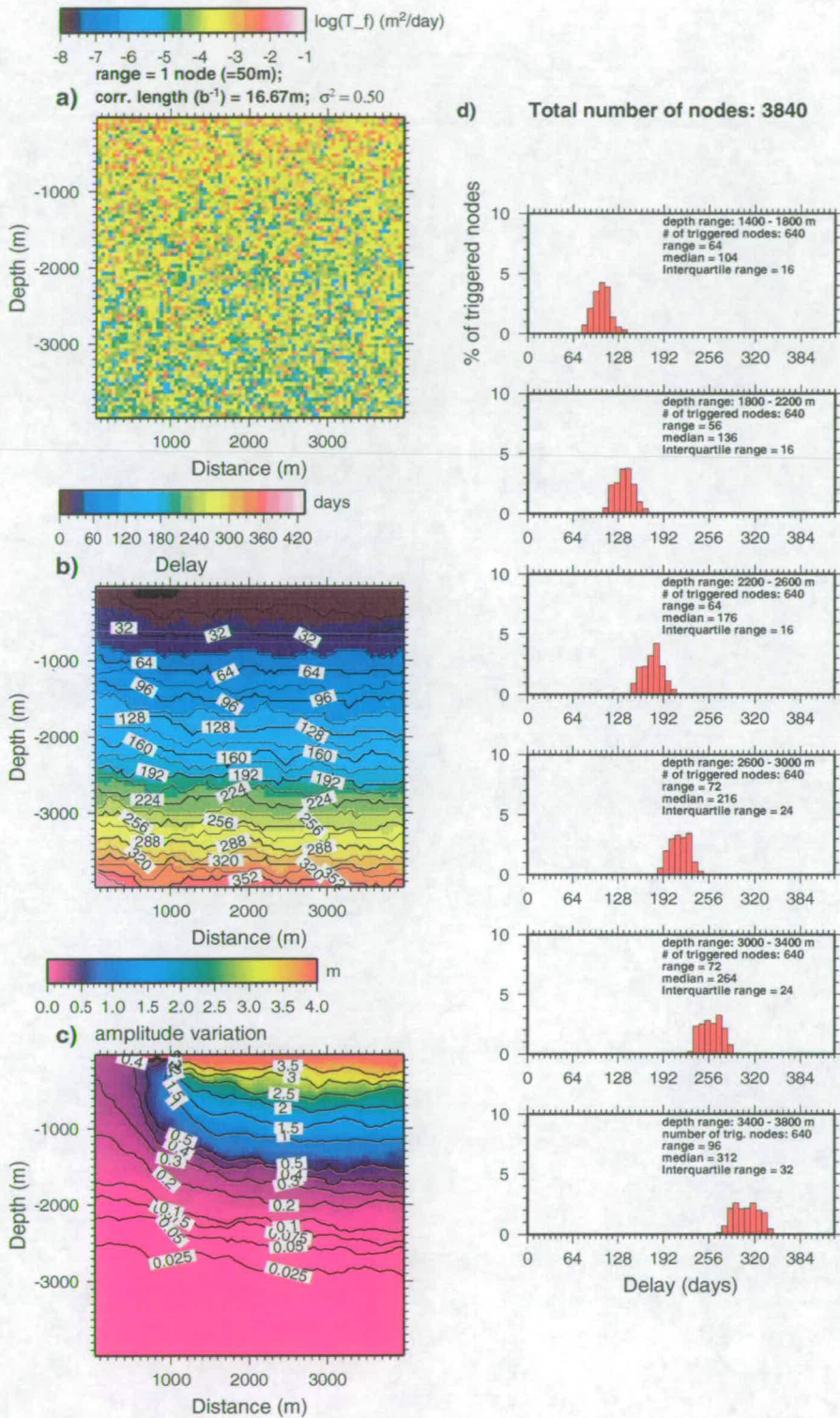


Figure 8.15: Output from a fault with a random transmissivity field and $\sigma^2=0.50$.

8.6 Numerical simulations with random correlated transmissivity fields

In order to give more structure to the transmissivity fields, the random transmissivity fields have a correlation length (b^{-1}). As mentioned before, the aim of this approach is to identify fault transmissivity parameters (b^{-1} and σ^2 of the transmissivity field) that can reproduce a similar distribution shape and spread (for each depth) as that observed in the frequency histograms of the real data (Figure 8.12). When dealing with stochastic field simulation it is important to bear in mind that the statistical analysis of a single realisation of the random field is not the most relevant aspect to be statistically analysed. This is because an individual realisation of the transmissivity field still is a single sample of the possible realisations. The values of range, median and IQR of a single realisation of the transmissivity field are not statistically significant. What is statistically analysed is the ensemble of calculated values of range, median and IQR. In other words, what is important to know is how, on average, the values of range, median and IQR behave. That is the underlying idea of the Monte Carlo simulation method.

In the problem that is dealt with in this thesis, a number of values of transmissivity fields have been generated for each pair of correlation length and variance. For each of these fields the range, median and the IQR are calculated for each depth range to be analysed. This is computationally expensive because 226 time steps are calculated before the measurements of time delay and amplitude variations are made (see figure 8.10). For the fault grid used in this research, the CPU time, for each transmissivity field, is around 8.5h on a SPARC1000. If 20 random realisations were made, one week of CPU time would be necessary for a single set of b^{-1} and σ^2 . Because of this considerable CPU time, only 5 runs were made for each set of b^{-1} and σ^2 . The way the simulations are organised is shown in Table 8.4.

In the following sections, for each set of b^{-1} and σ^2 simulations carried out, the cumulative distribution of the percentage of triggered nodes for each depth range are calculated. The summary statistics for these cumulative (or the ensemble) are then calculated. The random correlated transmissivity field, the time delay and amplitude variation plots and the summary statistics of each individual realisation are found in appendix E.

8.6.1 Correlation length of 166.67m and variance of 0.25

For this set of runs, the correlation length is 166.67m and the variance is 0.25. For each of these runs, a different seed of the random generator has been used. The seed for the field shown in figure E.1a is the same as the ones used in figures 8.14a and 8.15a. For this variance, 95.5% of the transmissivity field are between 2.0×10^{-6} and $2.0 \times 10^{-2} m^2/day$.

Figure 8.16 shows the of triggered node histograms for the ensemble of five realisations of the correlated transmissivity field. The summary statistics at each depth range are also shown. With five random realisations of the correlation field some conclusions on the behaviour of the range, median and IQR may be drawn. The range increases as the depth of the histogram also increases. This arises due to the presence of some structure in the random field, with regions of contrasting transmissivity values. This allows regions of the fault, within each depth range, to have different time delays and therefore, as the

fluid passes through each depth the range of possible arrival times increases. The median of the five realisations, as expected, increases as the depth of the depth range considered increases. The values found for the median at the different depth ranges for this ensemble are close to those found in the non-uniform fault (only the stress over depth effect, seen in Figure 8.13). If more simulations were carried out, the median of every depth range would converge to the ones found for the non-uniform fault. It is interesting that with five simulations the median is already converging. The IQR also increases as the depths of the depth range considered increase. This is also an effect due to the presence of correlation of the transmissivity over distance which allows the fluid to reach the same depth at different times. A comparison of these simulations with the non-uniform fault shows both the range and the IQR to be substantially greater at all depths.

The transmissivity distribution in a natural fault is a single realisation of a stochastic process. Therefore it should be recognised that histograms with shapes very different from those of Figure 8.16 can occur with a single random realisation. Figure 8.17 shows an example of a single random realisation of a transmissivity field from this ensemble. With this correlation length and this variance the clusters of contrasting transmissivity are apparent (Figure 8.17). The pattern of both the time delay and the amplitude variation is fairly different from the non-uniform case (Figures 8.17b, 8.17c, 8.13b and 8.13c). This is also reflected in the histograms shown in Figure 8.17d. However, most importantly, the histograms have for this single realisation a completely different shape to the ones calculated from the ensemble (Figure 8.16). The summary statistics in Figure 8.17d are also quite different from those of the calculated from the ensemble (Figure 8.16). This is because the summary statistics in Figure 8.17d are sample statistics from a single realisation and do not necessarily match the population statistics. The greater the number of realisations the closer the ensemble statistics will come to the population statistics.

Due to the difference between the statistics from a single realisation and those from a population, one has to be extremely cautious in inferring statistics from the real data. However, a general comparison is of interest. The values of range and IQR, at the 1,800 - 2,200m depth range, are 96 and 32 days (Figure 8.16b). This is much smaller than than the ones found by the real earthquake data: 405 and 68 days. As discussed, the values of correlation length and variance control the range and the IQR. Therefore, it is interesting to increase the value of b^{-1} and σ^2 to further investigate their effect on the results of the ensemble of random realisations considered.

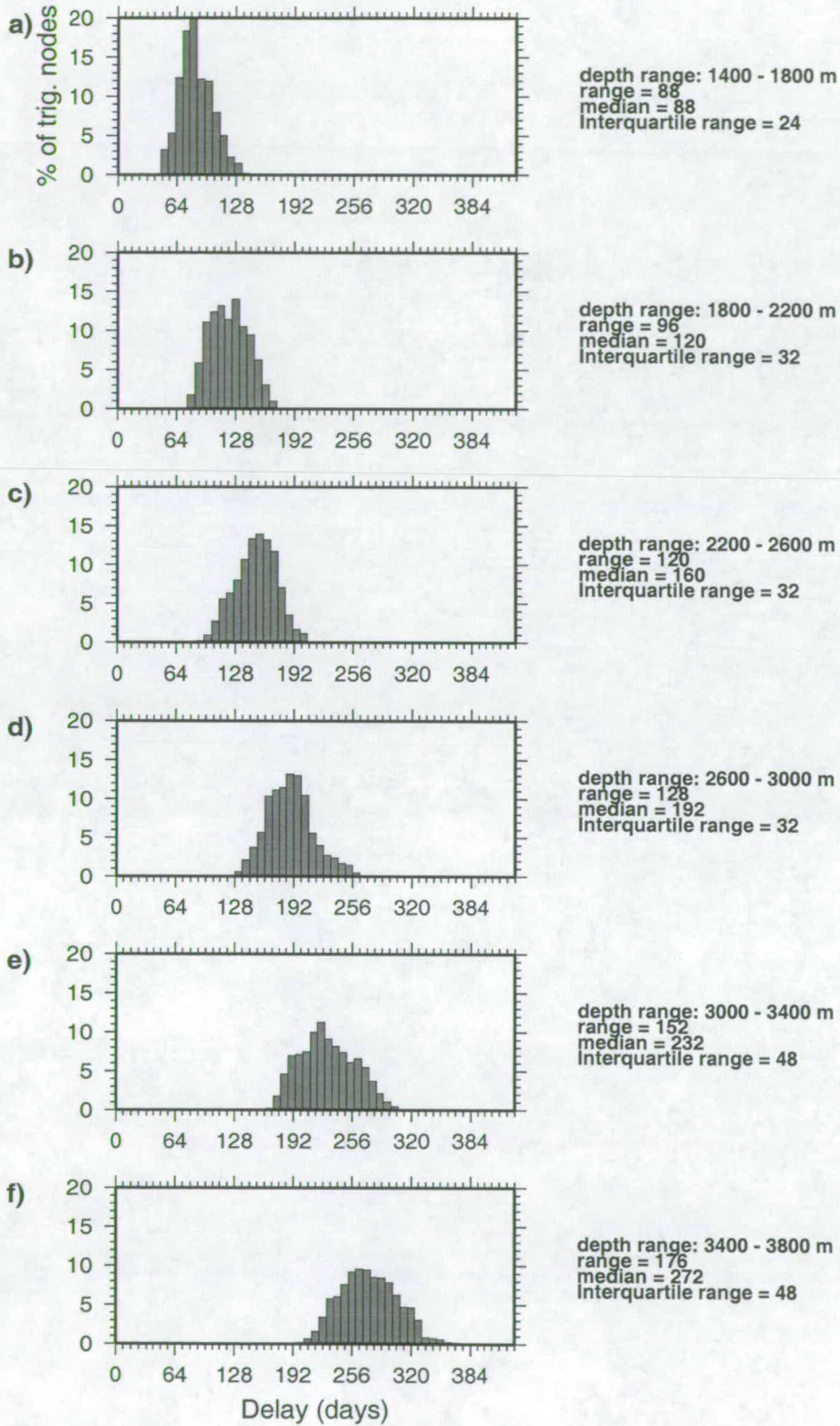


Figure 8.16: Histogram percentage of triggered nodes for an ensemble of five different correlated random fields. For these fields, $b^{-1} = 166.67m$ and $\sigma^2 = 0.25$.

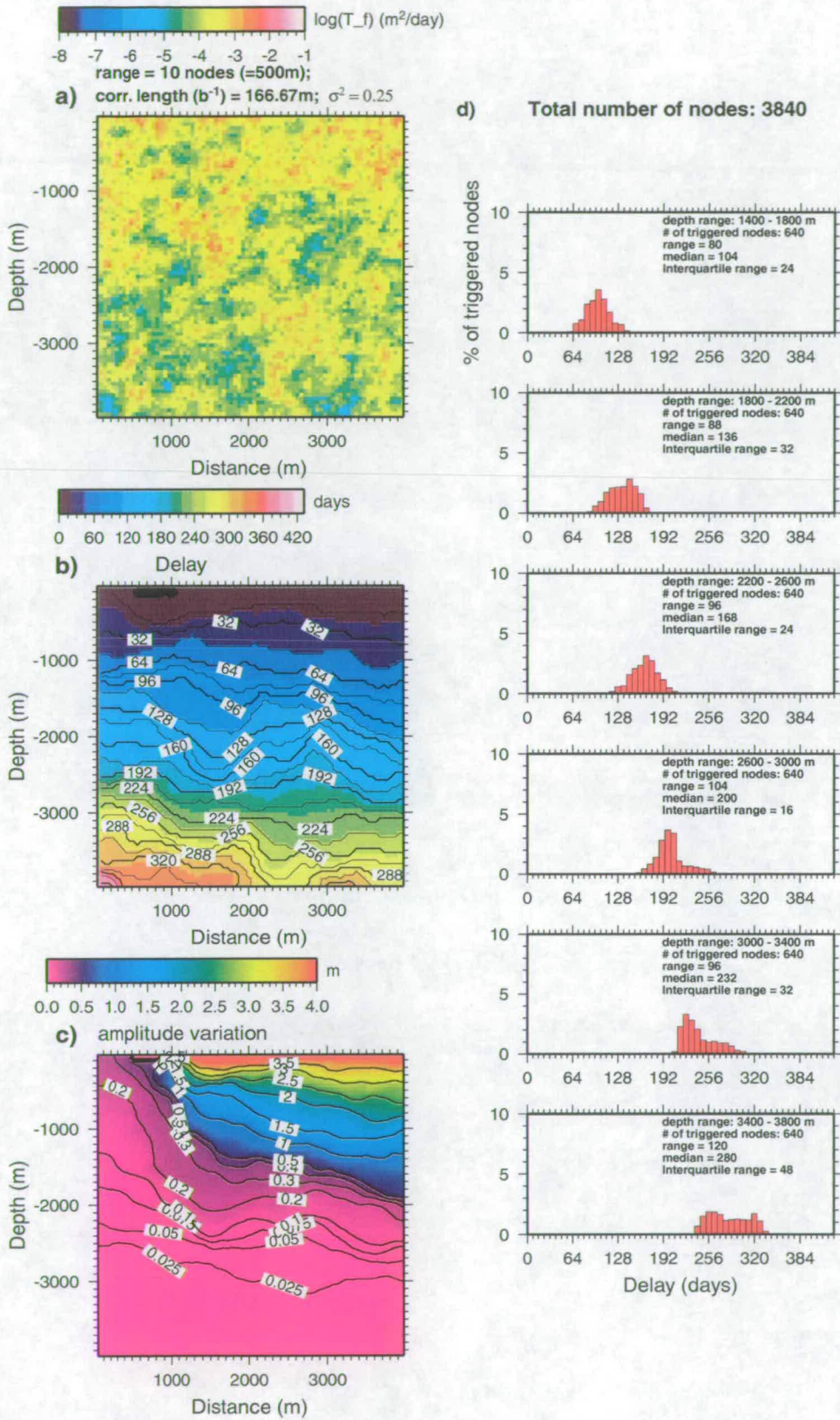


Figure 8.17: Single realisation of a random correlated field with $b^{-1} = 166.67m$ and $\sigma^2=0.25$.

8.6.2 Correlation length of 166.67m and variance of 0.50

With the increase in variance, 95.5% of the values of the transmissivity field now are between 3.0×10^{-7} and $7.0 m^2/day$. Five random realisations of the random correlated field are performed for this pair of b^{-1} and σ^2 considered.

Figure 8.18 shows the percentage of triggered nodes histograms for the ensemble of five random correlated transmissivity fields. The summary statistics for each depth range are also shown. For the same depth range, the summary statistics show that the median is practically the same as those found with a smaller variance (Figure 8.16). The IQR is slightly increased when the variance is increased. The range, on the other hand, has a significant increase. As the variance increased, clusters with higher contrasting values of transmissivity are formed producing a greater difference in the time delay of nodes at the same depth.

Figure 8.19 shows an example of a single realisation of a random correlated field to illustrate the effect of the increased variance. Figure 8.19a shows the transmissivity field single realisation. Despite holding a similar geometrical structure to the field shown in Figure 8.17 (due to the use of the same seed), the clusters exhibits a stronger contrast of transmissivity values. In the delay plot, the influence of the larger variance is noted by a steeper concentration of isovalues of delay time shown in figure 8.19. The contours of amplitude variation from this run with a large variance are rougher (Figure 8.19c). Again, it is worth pointing out that Figure 8.19 is a single realisation of a stochastic process and does not necessarily match the population statistics. Therefore, the histograms shown in Figure 8.19d, do not closely resemble the ones in Figure 8.18.

So far, the fields investigated have correlation lengths of 166.67m and variances of 0.25 and 0.50. The increase in the variance, as seen, has increased the range of the histograms of triggered nodes for the ensemble considered. The values of range and IQR, at the 1,800 - 2,200m depth range, are 120 and 48 days (Figure 8.18b). Which are smaller than the ones found by the real earthquake data: 405 and 68 days. An increase in the correlation length comes naturally as a way to increase geometrical structure. Because the clusters of seismic events are around 500m in diameter, it is interesting to run models in which the clustering of high transmissivity values is also of around 500m. An increase in the variance to add more complexity in the 166.67m correlation length fields, (e.g. $\sigma^2 = 0.75$) of the transmissivity field would lead to values in the transmissivity spanning from approximately $3.4 - 2.9 \times 10^{-8} m^2/day$. Such a range of transmissivity values is far greater than the values reported by the literature (Rutqvist *et al.*, 1998; Gudmundsson, 2000). Moreover, such a high value of variance would generate neighbouring nodes with contrasting transmissivity values of up to 10^7 , which is non-physical. Hence, only an increase in the correlation length is investigated.

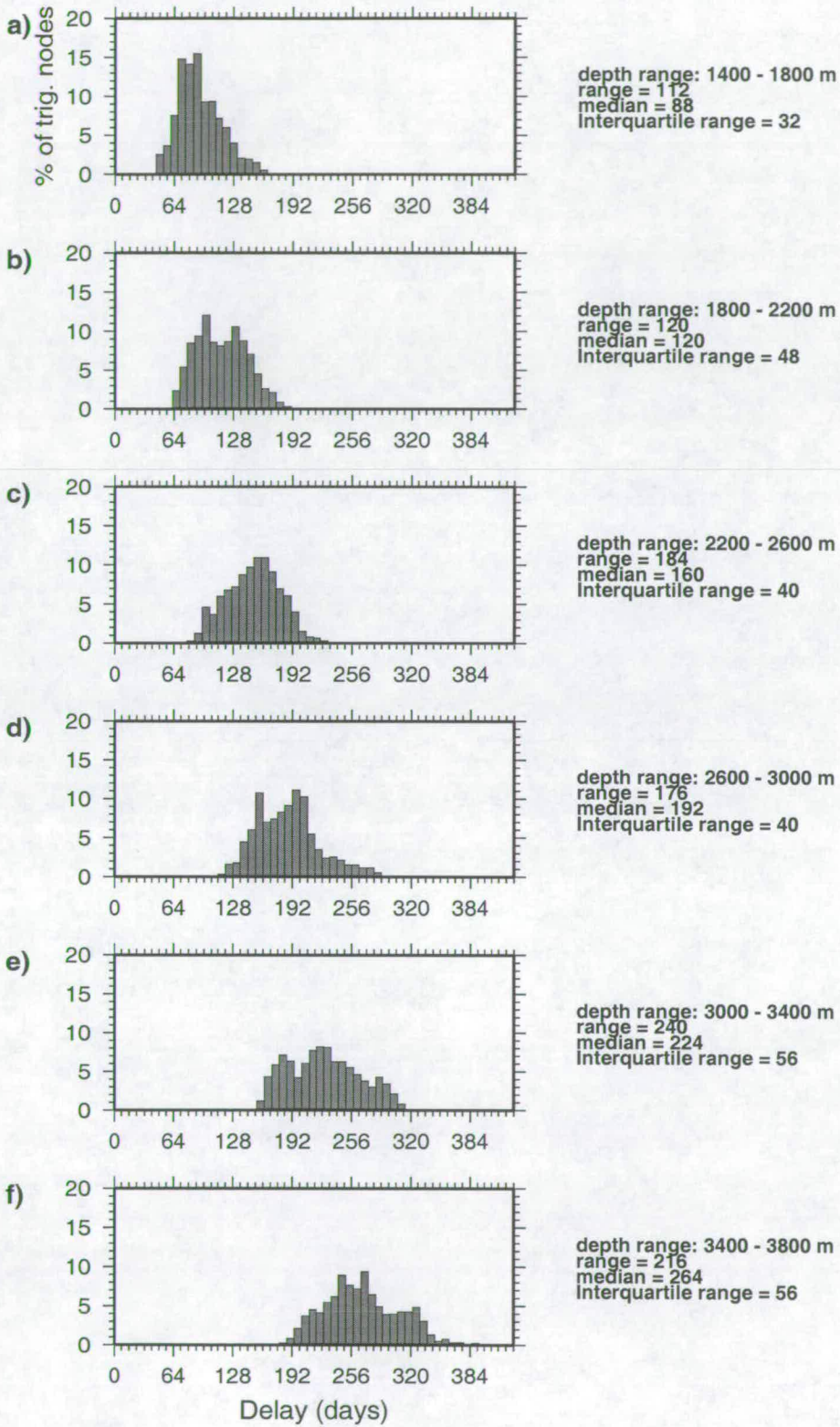


Figure 8.18: Histogram of percentage of triggered nodes from an ensemble of five different correlated random fields. For these fields, $b^{-1} = 166.67m$ and $\sigma^2 = 0.50$.

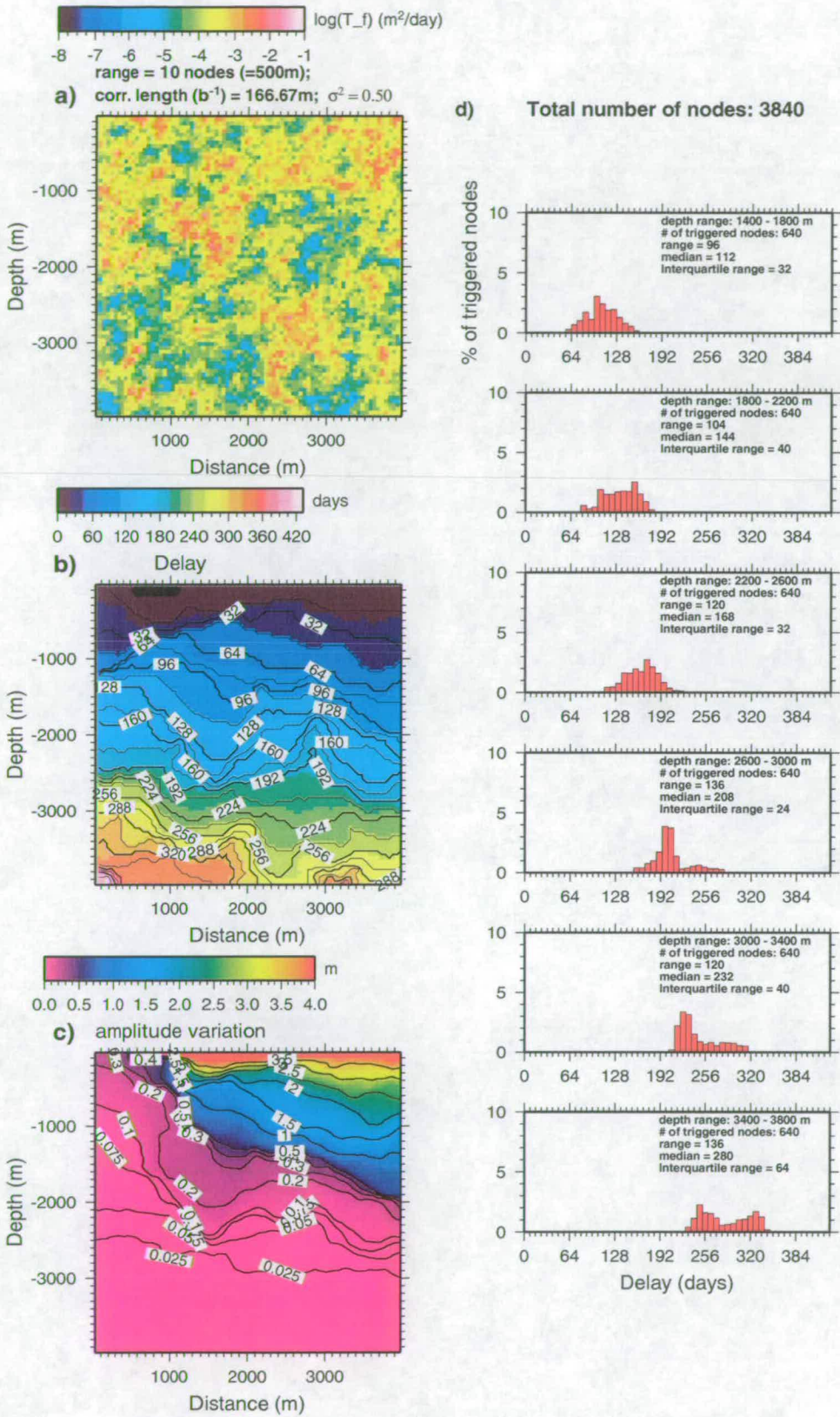


Figure 8.19: Single realisation of a random correlated field with $b^{-1} = 166.67m$ and $\sigma^2=0.50$.

8.6.3 Correlation length of 500m and variance of 0.25

For the runs shown in this section, the correlation length is increased to 500m and the variance is 0.25. The main reason for increasing the correlation length is due to the intuitive notion that the clusters of high/low transmissivity are associated with the size of the seismic cloud observed in the real earthquake data beneath the Açu reservoir (Chapter 4). The transmissivity fields with a larger correlation length do produce larger clusters of contrasting values high/low transmissivity values. For the ensemble considered, the values of range and IQR, at the 1,800 - 2,200m depth range, are 160 and 40 days. These are still much smaller than than the ones found by the real earthquake data: 405 and 68 days.

Figure 8.20 shows the of the percentage of triggered nodes histograms for the ensemble of five random correlated transmissivity field. Again, for each depth range the summary statistics are presented. Now, a comparison of the summary statistics of this ensemble with the summary statistics of the last two ensembles (see Figures 8.16 and 8.18) can be made. The increase in the correlation length produced a greater increase in the range and also in the IQR, than the increase in the variance only (Figure 8.18). As discussed above the range and the IQR are only slightly changed when the variance is increased, whereas the values of range and IQR for the ensemble shown in Figures 8.16 and 8.20 are significantly changed when the correlation length is increased. For all the ensembles considered, the median is roughly the same throughout as expected.

Figure 8.21a shows the transmissivity field of a single realisation of a random transmissivity field with $b^{-1} = 500m$ and $\sigma^2=0.25$. It is possible to note that the clusters of high/low values of transmissivity are larger than the ones previously presented (Figures 8.17a and 8.19a). These larger clusters change the distribution of time delay over depth and amplitude variation even further from the non-uniform case, as shown in Figures 8.17c and d. The histograms of triggered nodes and the summary statistics for this single realisation are shown to, once again, illustrate how the single sample statistics are unlikely to be the same as those from the population or the ensemble.

To further investigate the behaviour of the triggering pattern, the next runs will have a correlation length of 500m and the variance will be increased to 0.5. The combination of a longer correlation length and a greater variance may explain the values of range and IQR presented in the earthquake data.

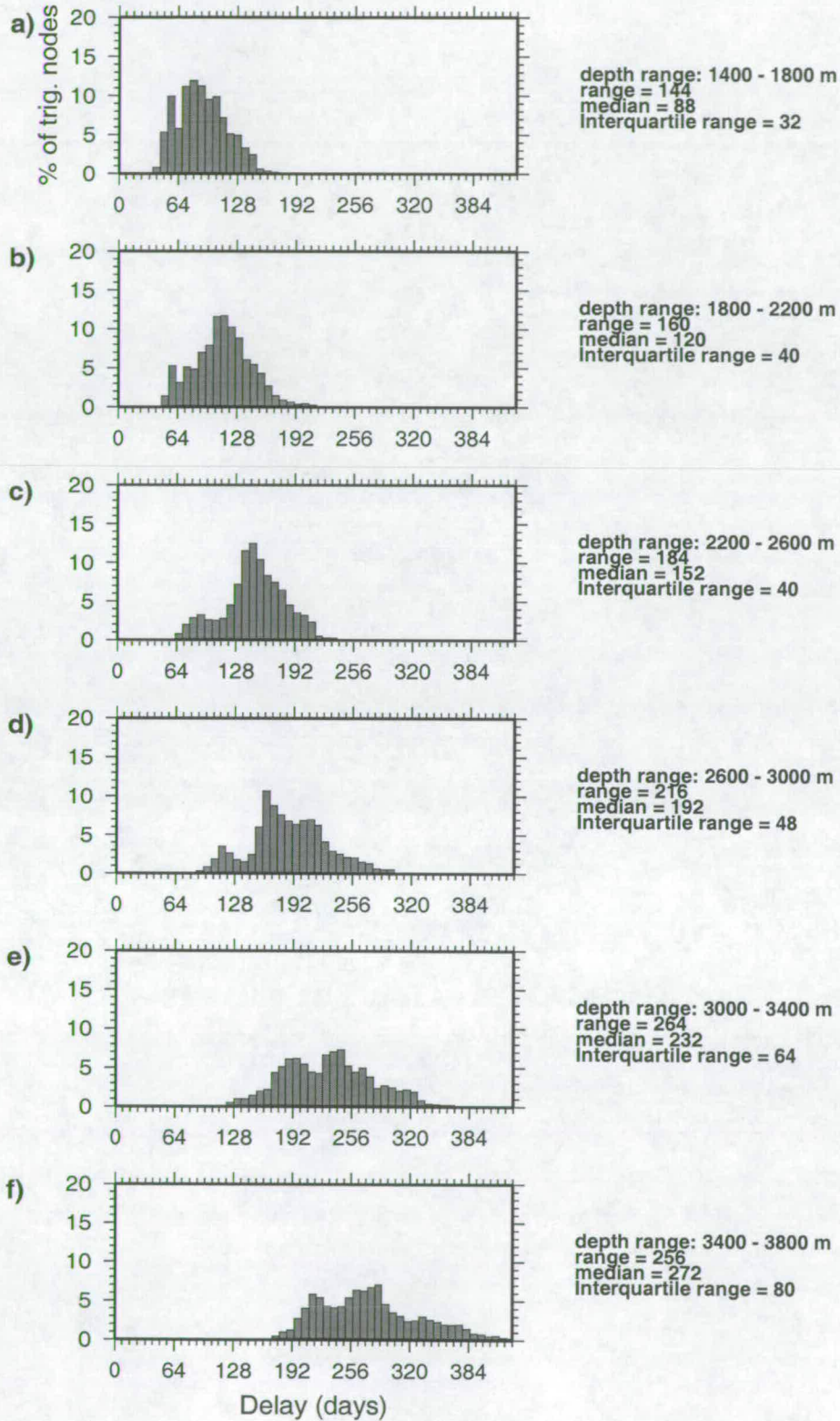


Figure 8.20: Histogram of percentage of triggered nodes for an ensemble of five different correlated random fields. For these fields, $b^{-1} = 500m$ and $\sigma^2 = 0.25$.

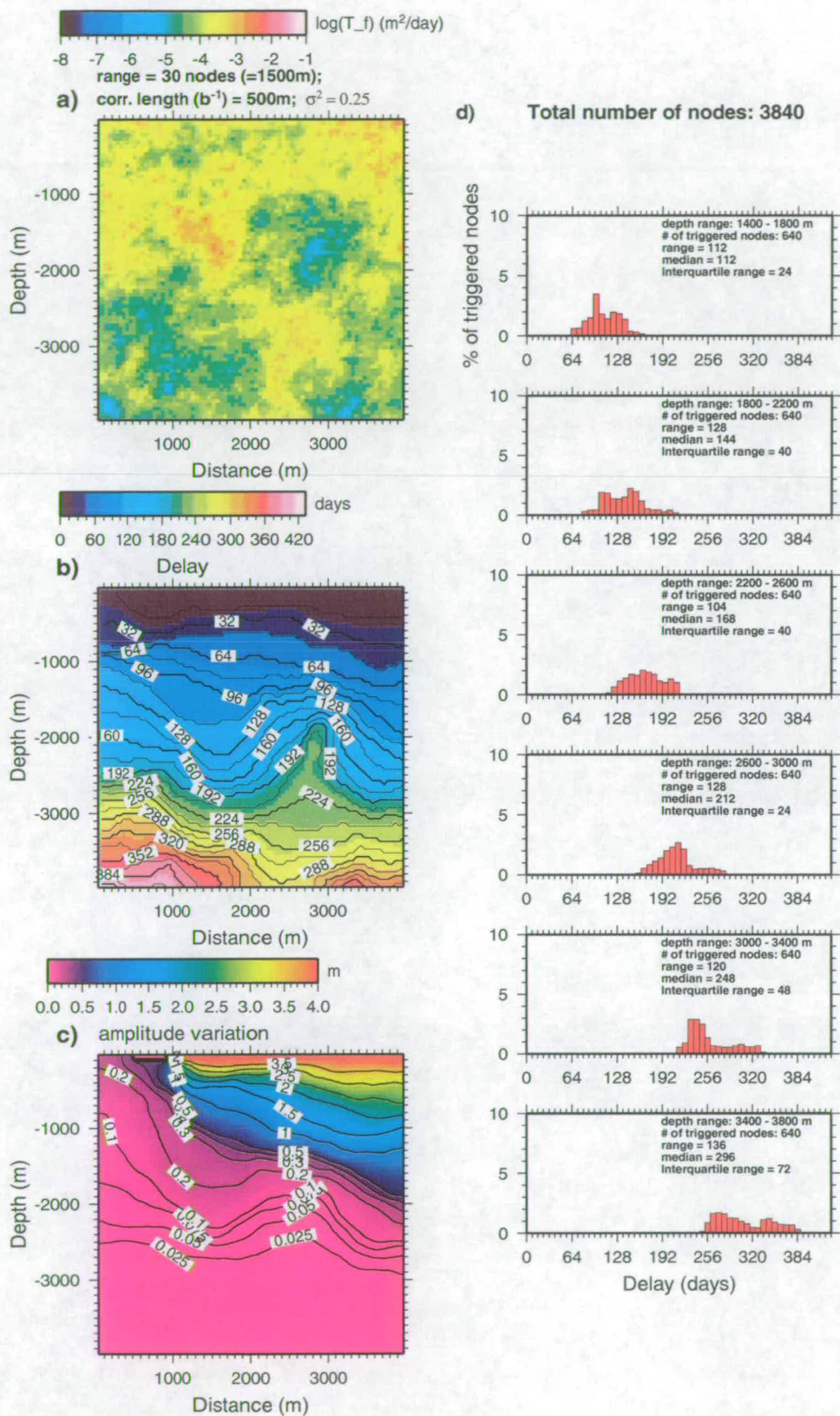


Figure 8.21: Single realisation of a random correlated field with $b^{-1} = 500m$ and $\sigma^2 = 0.25$.

8.6.4 Correlation length of 500m and variance of 0.50

In this section, fields with the largest correlated length and the largest variance are investigated. Figure 8.22 shows the histograms, for different depth ranges, of the ensemble of random correlated fields. The summary statistics for every depth are also shown in Figure 8.22. With $b^{-1} = 500m$ and $\sigma^2=0.50$, a great increase in the range of the ensemble of triggered nodes, in comparison with previous simulations, is observed. The reason for the great increase in the range arises from the fact that it is a measure of dispersion that is very sensitive to extreme values. The IQR is less sensitive to variations in the extremes. Nevertheless, the IQR for $b^{-1} = 500m$ and $\sigma^2=0.50$ is also increased in comparison to previous runs. For the ensemble considered, the values of range and IQR, at the 1,800 - 2,200m depth range, are 224 and 48 days. which is smaller than than the ones found by the real earthquake data: 405 and 68 days. However, inspection of the individual realisation E.16 to E.20 shows a great difference in sample statistics even between those realisations. In fact, in these 5 realisations, the IQR ranges from 28 to 56 days at 2.0km depth. Since the real world is a single realisation, it is very possible that such values could be generated from the population statistics for a single realisation given a large number of realisations.

Figure 8.23a shows a single realisation of the random correlated field with $b^{-1} = 500m$ and $\sigma^2=0.50$. One of the impacts of the increase in the variance of the transmissivity field in the delay plot is the same as the one already discussed in section 8.6.2: there is a general increase in the gradient of isovalues of time delay over the same depth. Another interesting effect is the presence of “pockets” of isovalues of time delay in all five transmissivity fields investigated. The presence of such a “pocket” is indicated on Figure 8.23b. The presence of such a “pocket” is indicated on Figure 8.23b. The reason for these pockets is because the transmissivity field now has pockets low transmissivity that are extensive enough to impede the flow. The diameter of the pocket is approximately equal to the diameter of the cluster of low transmissivity. The existence of these pockets of time delay means that certain regions which are at the same depths may have very different time delays. As a matter of fact, the presence of a bimodal distribution in Figure 8.23b in the 1,800 - 2,200m depth range is caused by the presence of a pocket of low transmissivity adjacent to a pocket of high transmissivity.

8.7 Interpretation of the numerical simulations

The simulations carried out by PARADIGM using different transmissivity fields mimic the main characteristics of the real earthquake data: a spread of the distribution of earthquakes over time for a given depth. In the simulations, seismicity was assumed to be triggered at a fault node when it reached the peak in piezometric head. The time delay for each node is the time between the peak in water level variation in the reservoir and the time at which it is triggered. This assumption of time to peak pressure change represents an upper bound on the time taken for seismicity to be triggered since no data exist on the actual stress change required to induce an event at a particular location. More detailed investigation on the effect of periodic loading in the triggering of earthquakes can be found in Perfettini and Schmittbuhl (2001); Lockner and Beeler (1999). In addition, the introduction of stochastic correlated field does provide faster pathways for flow and therefore, greater changes in amplitude variations may

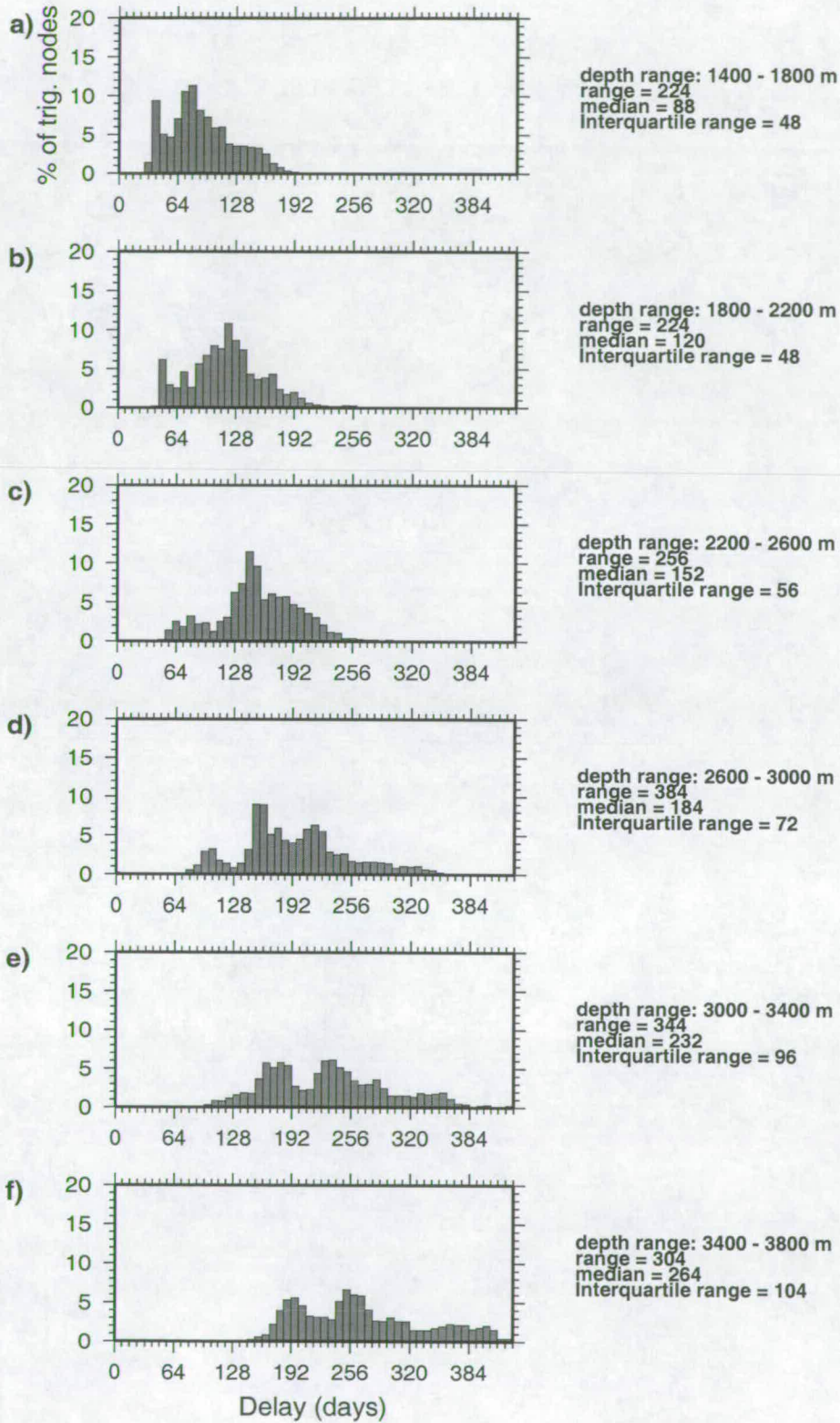


Figure 8.22: Histogram percentage of triggered nodes for an ensemble of five different correlated random fields. For these fields, $b^{-1} = 500m$ and $\sigma^2 = 0.50$.

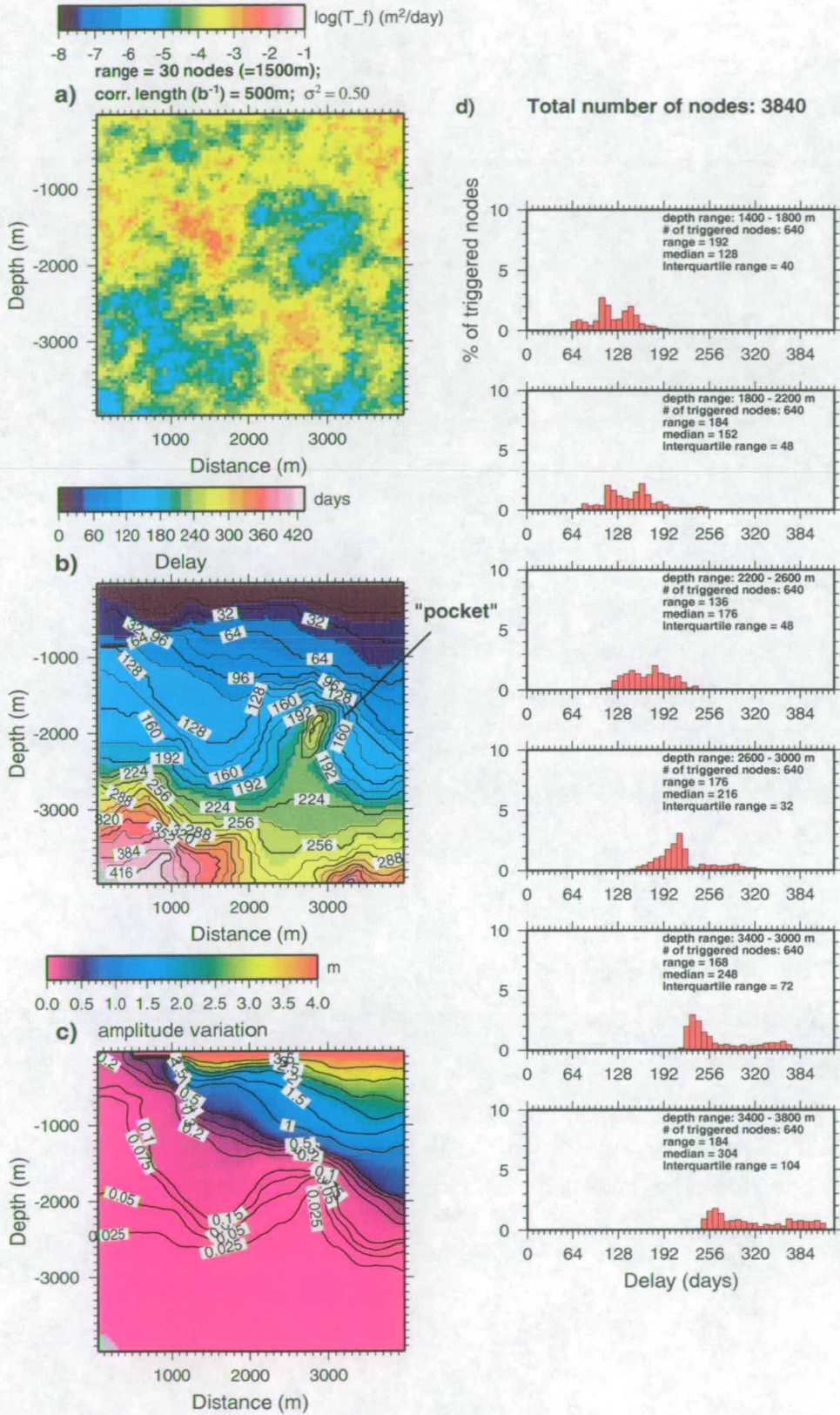


Figure 8.23: Single realisation of a random correlated field with $b^{-1} = 500m$ and $\sigma^2 = 0.50$.

happen at greater depths.

The analysis of the results shows that fields with $b^{-1} = 500m$ and $\sigma^2=0.50$ are the most likely to describe the transmissivity field of the seismogenic fault in Açu. This is because the spread and IQR are the closest to the ones in the real earthquake data. If more than five realisation were made (say 1,000), the likelihood of obtaining the real values derived from the seismic data in a single realisation could be quantified.

The recognition of the stochastic nature of the transmissivity field of a real fault has lead to an interesting interpretation of the migratory pattern observed in the Açu area. As shown in the spatio-temporal analysis of the earthquake data, each different fault activated in the area is activated at different times (migration from one fault to another). For some periods, the seismic activity occurs simultaneously at two different faults. Table 8.5 shows the activation period of events recorded by the digital seis-

Period of activation	Active seismic cluster
August/1994 - December/1995	$\approx 7.5km$ from BA1, a and possibly b
Nov. 1994 - 15/Aug./1996	a
15/Aug./1996 - 21/Oct./1996	a
21/Oct./1996 - 22/Nov./1996	b
25/Nov./1996 - 30/Dec/1996	c, b
30/Dec./1997 - May/1997	a, b

Table 8.5: Activation period of events recorded by the digital seismic network and by the station BA1. With precise hypocentre determination, it is possible to observe migration of seismic events between different faults and within individual faults over different time periods. When only the $(t_S - t_P)$ are available (station BA1), the distance from the event to the station can be estimated.

mic network and by the station BA1. With precise hypocentre determination, it is possible to observe migration of seismic events between different faults and within individual faults over different time periods. When only the $(t_S - t_P)$ are available (station BA1), the distance from the event to the station can be estimated.

Since each transmissivity field of the active seismic cluster is a single realisation of a stochastic process, the observed spatio-temporal behaviour is its natural consequence. The fact that the summary statistics in the real data do not match one of the single realisations of the simulated random correlated field is not relevant. The relevant aspect is to realise that this migratory behaviour is mimicked by the description of a fault as a single realisation of a stochastic process. Further, the presence of clusters in the data at Açu could be explained by pockets of high and low transmissivity.

8.8 Summary

In this Chapter, I presented the modelling of fluid flow using heterogeneous transmissivity fields as an explanation for the triggering pattern observed in the Açu reservoir.

It is demonstrated that a non-uniform transmissivity field (stress effect over depth only) fails to provide a mechanism that explains the seismicity pattern observed in the Açu reservoir. Migration of

seismicity within a single fault would get uniformly deeper over time, which it does not. Moreover, the seismicity migrates from fault to fault. The introduction of an uncorrelated random field does not alter considerably the scenario obtained with the non-uniform fields. Therefore, a correlated stochastic field with different values of correlation length (b^{-1}) and variance (σ^2) is introduced. The aim is to obtain values of correlation length and variance that can reproduce a similar distribution shapes and spread (for each depth) as that observed in the real earthquake data. In order to obtain values of correlation length and variance which are statistically meaningful for comparison, the population summary statistics must be estimated. Simulations for an ensemble of five different realisations for each pair of values of correlation length and variance were carried out. The range and the IQR are only slightly changed when the variance is increased from 0.25 to 0.50 ($b^{-1} = 166.67m$), whereas the values of range and IQR for the ensemble are significantly increased when the correlation length is increased from 166.67 to 500m. The values of correlation length and variance that are closest to the observations are obtained with $b^{-1} = 500m$ and $\sigma^2=0.50$. For all the ensembles considered, the median is roughly the same as the non-uniform fault (stress effect only) throughout all the groups of ensembles.

Since each fault is a random realisation of the random transmissivity field, a migratory behaviour of the active seismic clusters can be naturally mimicked. This arises because each realisation of a fault exhibits different time delay patterns for different depths. In other words, the migratory behaviour is a natural consequence of the fault heterogeneity. The earthquake data is, in reality, a single realisation and its sample statistics do not necessarily match the population statistics.

9 SUMMARY AND DISCUSSIONS

This thesis has combined both seismological and hydrogeological analysis to investigate the RIS associated with the Açú reservoir in NE Brazil. This combination of expertise has provided a unique approach to the study of RIS. For the first time a 3D numerical groundwater model incorporating hydrogeological information to study the role of pressure in a RIS area has been carried out.

From a purely seismological point of view, it has been shown in Chapter 3 that the hypocentral locations are very good due to the simple seismic velocity structure beneath the Açú reservoir. This leads to well constrained focal mechanism determinations and has also allowed seismic anisotropy studies to be carried out. The focal mechanism studies have also independently confirmed the presence of seismic anisotropy in the area. The seismic anisotropy in the area is controlled by the foliation of the Precambrian basement and not by anisotropy of stress-aligned fluid-filled cracks. The results of the seismic anisotropy studies are in close agreement with other seismic anisotropy observational and theoretical studies Gledhill (1991); Brocher and Christensen (1990); Barruol and Mainprice (1993); Zhang and Schwartz (1994); Menke *et al.* (1994); do Nascimento *et al.* (2002).

The spatio-temporal analysis in Chapter 4 suggests that the RIS in the Açú area is controlled by the mechanism of pore pressure diffusion. Another result from the spatio-temporal analysis is that the seismicity in the Açú reservoir occurs in well-defined seismic zones. The seismicity in these well defined zones is observed to migrate between different zones and within individual zones over different periods of time.

In order to build a groundwater model of the Açú reservoir, the hydrological regime of the area was characterised in Chapter 6. Despite the scarcity of hydrological data for this area, the most important features of a semi-arid hydrological regime are present in the data. The purpose of this hydrological characterisation is to present the relevant hydrological and geological data that justify the choice of parameters for the model used in Chapters 7 and 8.

In Chapter 7, to model the pressure diffusion beneath the Açú reservoir, the 3D groundwater flow code PARADIGM is used. PARADIGM was specifically developed to solve for flow in porous media and interacting fault planes (Lunn and Mackay, 1997). In PARADIGM, the flow equations are solved for a 3D porous medium within which discrete planar objects (fractures or faults) with their own 2D meshes can be placed. This allows the flow to be represented within each fault within a three-dimension matrix without limitations on the fault geometry. In PARADIGM the matrix and fault grids are solved separately, by iterating to achieve a consistent fully implicit solution between the grids. Flow between the fault and the matrix is governed by the head gradient between the two and the permeability of the fill material within the fault. PARADIGM also allows for a fully heterogeneous hydraulic conductivity distribution in both the matrix and/or the fault planes.

Firstly, a regional model (33.7x41.1x8.0 km) was built using PARADIGM with a grid resolution of 91x111x80 elements. This regional scale model was built in order to determine physically realistic boundary conditions for a more detailed flow model of the area of seismic activity. Using piezometric head predictions from the regional model as boundary conditions, a second, more refined model has been developed. The refined model is 14.8x14.8x8.0 km with 80x80x80 grid elements and is centred around the area of maximum seismic activity. Simulations were conducted with the refined model, both with and without including a highly permeable fault plane in the flow model. In both cases, the hydraulic properties (hydraulic conductivity K and specific storativity S for the matrix, and transmissivity T_f storativity S_f for the fault) were calibrated to simulate the observed delay between the peak water level in the reservoir and the maximum seismic activity. For those numerical simulations, the water level variation is a synthetic sinusoidal oscillation with a one-year period. The choice of a synthetic lake level variation was made to simplify the analysis results.

The numerical simulations showed that the time delay between the peak in the reservoir water level and an increase in pressure at hypocentral depths can be reproduced in both models. However, in the model with no fault plane the values of K and S , $5.5 \times 10^{-5} \text{ m/day}$ and 10^{-8} m^{-1} , required to fit the observations are not physically realistic. In other words, the calculated values of K and S required to fit the data are not self-consistent and produce a physically unrealistic equivalent homogeneous media. On the other hand, when a highly permeable fault is included in our model, the fitted values of transmissivity and storativity in the fault ($2.0 \times 10^{-4} \text{ m}^2/\text{day}$ and 4.0×10^{-8} , respectively) are in close agreement with the values in the literature (Rutqvist *et al.*, 1998).

The recognition that an homogeneous equivalent media cannot explain the induced seismicity is a very important point to discuss. In induced seismicity literature, a lot of attention is given to the values of hydraulic diffusivity and permeability (or hydraulic conductivity), but not a lot of attention is given to the relation these have with the storativity. Therefore, wrong interpretations of the results are made resulting in inappropriate conclusions. In fact, if Shapiro *et al.* (1997, 1999) had calculated the value of the storativity of the homogeneous equivalent media they found via equation 7.5, they may have realised that an homogeneous media with such properties is not possible. In this thesis, attention was given to the definitions of the hydraulic conductivity and storativity and its significance to fluid flow and their value ranges in real rock. Hence, it was possible to point out and correct misinterpretations such as those made by Shapiro *et al.* (1997, 1999), discussed in sections 7.3 and 7.7

The inclusion of a homogeneous fault proved to be a more promising model to describe the RIS in the Açu reservoir. However, from the spatio-temporal analysis of seismic activity performed in Chapter 4, it is clear that the spatio-temporal evolution of the earthquake data is complex and is not fully described by a simple homogeneous fault. The simple homogeneous model predicts that the migration of seismicity within a single fault would get uniformly deeper over time, which does not happen in the real fault. The spatio-temporal analysis shows activation of seismic events at depths of 3.0 and 4.0 km at time delays of 180 and 210 days. Those times observed in the Açu area are smaller than those predicted by the non-uniform model (stress effect only): 224 and 328 days. That constitutes an important reason to investigate models with heterogeneity because the non-uniform model (stress effect over depth included), despite being more realistic than the fully uniform transmissivity field, cannot explain the time activation of seismic clusters described in Chapter 4. Moreover, seismicity migrates

from fault to fault. In order to mimic the complexity exhibited by the real earthquake data, complex structure was introduced into the fault, as described in Chapter 8. In reality, fault zones are composed of distinct components: fault core where most of the displacement is accommodated and an associated damage zone mechanically related to the growth of the fault (Chester and Logan, 1986; Caine *et al.*, 1996). The fault core is relatively impermeable, the damage zone however, may include small faults, veins, fractures, cleavage and folds which may significantly enhance fault zone permeability relative to the fault core and the intact rock (Caine *et al.*, 1996). The hydraulic conductivity structure of the damage zone only is modelled because the faults in the Açu area are thought to behave as distributed conduits. In such faults, the hydraulic conductivity structure is dominated by the hydraulic structure of the damage zone. The heterogeneous hydraulic properties of the damage zone were incorporated via a synthetic correlated fault transmissivity field. Numerical simulations with different values of both the correlation length and the variance of the fault transmissivity field were performed in PARADIGM. In order to compare the real earthquake data with the simulated faults in PARADIGM, seismicity was assumed to be triggered at a fault node when it reached the peak in piezometric head. The delay time for that particular node is the time between the peak in water level variation in the reservoir and the time it is triggered. This assumption of time to peak pressure change represents an upper bound on the time taken for seismicity to be triggered since no data exist on the actual stress change required to induce an event at a particular location. The introduction of a stochastic correlated field does provide faster pathways for flow and therefore, greater changes in pressure (larger amplitudes of oscillation) happen at greater depths.

The analysis of the numerical simulations with heterogeneous transmissivity fields shows that the complexity of the triggering pattern of the real earthquake data is mimicked by the simulations carried out using the heterogeneous field. In the real data, whilst the general trend is an increasing time lag over depth, this is not a uniform trend; many events within the same depth range trigger at different time lags. These time lags range from 32 to 432 days. The simulations show a spread in the time lag that is similar to the one observed in the data. These effects observed in the real earthquake data are reproduced due to the heterogeneity in the correlated fields. The areas of contrasting transmissivity provide complex pathways for fluid flow and therefore provide a complex triggering pattern.

Simulations for an ensemble of five different realisations for each pair of values of correlation length and variance were carried out. The range and the IQR of delay times to triggering are only slightly changed when the variance is increased from 0.25 to 0.50 ($b^{-1} = 166.67m$), whereas the values of range and IQR for the ensemble are significantly increased when the correlation length is increased from 166.67 to 500m. The values of correlation length and variance that are closest to the observations are $b^{-1} = 500m$ and $\sigma^2=0.50$. For the ensemble with $b^{-1} = 500m$ and $\sigma^2=0.50$, the values of range and IQR, at the 1,800 - 2,200m depth range, are 224 and 48 days, which are smaller than the ones found by the real earthquake data: 405 and 68 days. However, inspection of the individual realisation E.16 to E.20 shows a great difference in sample statistics even between those realisations. In fact, in these 5 realisations, the IQR ranges from 28 to 56 days at 2.0km depth. Since the real world is a single realisation, it is very possible that such values could be generated from the population statistics for a single realisation given a large number of realisations. The discrepancy observed in the range and IQR may arise from the fact that a priori, one does not know if all the events that occur in the 1,800 - 2,200 m range are induced by the pressure diffusion only. It could also be that, once that the rupture occurs,

the values of transmissivity and storativity change at this location and this might weaken the fault even more, leading to later failure. For all the ensembles considered, the median is roughly the same as the non-uniform fault (stress effect only) throughout all the groups of ensembles, reflecting the calibrated values of 128 days at 2km depth.

It is interesting to note that the maximum pressure variation simulated to trigger events is not that great (0.05 - 0.15m). So, tectonic stress conditions must be very close to critical values. According to Grasso and Sornette (1998) the "critical" nature of the state of the crust is characterised by the property of a large susceptibility to small perturbations. In other words, small external perturbations may lead to large responses in some parts of the system. The seismicity induced by pressure diffusion can be rationalised in the framework described by Grasso and Sornette (1998). This argument is more strongly supported in the Açu reservoir case because the reservoir is relatively shallow and it lies in a stable cratonic area where the effect of the reservoir itself is more evident.

The recognition that the transmissivity fields in seismically active faults can be described as a correlated field has important implications for explaining the complex triggering pattern in the Açu reservoir. As was observed in Chapter 4, the seismicity in 1989 and 1990/91 and from August 1994 until March 1997 occurred in at least six different seismic zones (see Figure 4.7). It is possible that each of these faults is described by a statistically identical correlated transmissivity field. In other words, each fault could have the same correlation length and the same variance, but be a different realisation. This would still result in each of the faults having distinct fluid flow pathways that would activate earthquakes at different times and depths. Since each fault is a random realisation of the random transmissivity field, a migratory behaviour of the active seismic clusters can be naturally mimicked. This arises because each fault will exhibit different time delay patterns for different depths. In other words, the migratory behaviour is a natural consequence of the fault heterogeneity.

10 SYNTHESIS AND CONCLUSIONS

10.1 Conclusions

During the presentation and interpretation of the induced seismicity of the Açú area and the modelling of the pore pressure diffusion beneath this reservoir, a number of conclusions were reached. These are itemized below:

Earthquake location, focal mechanism and anisotropy

Three spatially distinct earthquake clusters were active from 1994 until 1997. Therefore their migration may be correlated to the water level of the Açú reservoir. The focal mechanism of the earthquakes located (regardless of which cluster they belong to) indicates a nearly pure right-lateral strike-slip fault oriented NE-SW. The solutions of focal mechanisms in this region is consistent with compression stresses with an E-W orientation and extension with a N-S orientation (Assumpção, 1992; Ferreira *et al.*, 1998). The seismic anisotropy is aligned with the metamorphic fabric of the region, and not with anisotropy of stress-aligned fluid cracks.

Spatio-temporal analysis

The seismicity in Açú reservoir mostly occurs in well defined seismic zones. The seismicity in such zones is observed to migrate between these zones and within individual zones over different periods of time. Not all the events fit this simple picture but the majority do. When hypocentral data were available, the activation of clusters is consistent with the diffusion of pressure throughout the rockmass.

Groundwater modelling - Homogeneous modelling

For the flow model with no fault, the values of K and S calibrated for this model are not self consistent and are physically unrealistic. When a highly permeable fault is included in our model, the values of T_f and S_f are in close agreement with realistic data from the literature. As a consequence, it was shown that the use of an equivalent homogeneous media to explain the seismicity is invalid and leads to wrong interpretations of fluid-induced seismicity cases.

Groundwater modelling - heterogeneous modelling

The migration of seismic activity within a fault and between faults is controlled by the heterogeneity of the fault transmissivity field. The introduction of a random correlated transmissivity field results in complex fluid migration that explains the migration of seismicity with in a fault and potentially from fault to fault. The amplitude variation of pressure at seismogenic depth is minute (equivalent head of 5 - 15cm). This corroborates the notion that the tectonic stress conditions must be very close to critical values.

10.2 Future work

The value of both a detailed seismological analysis and a groundwater modelling study in a RIS area have been demonstrated in this thesis, a number of improvements and suggestion for future work can be made. They may be divided into seismological aspects and modelling aspects.

Seismological Aspects

- Include in the study of the spatio-temporal analysis the magnitude of the events to determine if the activation of a cluster is associated with the magnitude of the early events in a particular cluster;

Modelling Aspects

- Better constrain the values of K and S used for the modelling. Pumping tests in the crystalline basement would provide these data.
- Apply the real water level variation to the simulations already performed with the synthetic sinusoidal water level variation.
- Investigate the effect of seismicity on permeability structure - why do earthquakes 'stop' at a particular location?
- Increase the variance of the stochastic field. This is to investigate the impact of a larger range of hydraulic property values for depths beyond the ones presented in pump tests.

REFERENCES

- Abdel-Salam, A. and Chryssikopoulos, C. V.**, 1996. Unsaturated flow in a quasi-three-dimensional fracture medium with spatially variable aperture. *Water Resour. Res.*, **32**:pages 1531–1540.
- Aki, K. and Richards, P.**, 1980. Quantitative seismology: theory and methods, volume I and II. Freeman & Co., San Francisco.
- de Almeida, F. F. M., Hasui, Y., Neves, B. B. B., and Fuck, R. A.**, 1981. Brazilian structural provinces: an introduction. *Earth Sci. Rev.*, **17**:pages 1–29.
- ANEEL**, 2001. Agência Nacional de energia Elétrica. Data available online at <http://hidroweb.aneel.gov.br>.
- Antonellini, M. and Aydin, A.**, 1994. Effect of faulting on fluid flow in porous sandstone: Petrophysical properties. *Am. Assoc. Petrol. Geol. Bull.*, **79**:pages 355–377.
- Assumpção, M.**, 1992. The regional intraplate stress field in south america. *J. Geophys. Res.*, **97**(B8):pages 11889–11903.
- Barruol, G. and Mainprice, D.**, 1993. A quantitative evaluation of the contribution of crustal rocks to the shear-wave splitting of teleseismic SKS waves. *Phys. Earth Planet. Int.*, **78**:pages 281–300.
- Barton, C. A., Zoback, M. D., and Moos, D.**, 1995. Fluid flow along potential active faults in crystalline rock. *Geology*, **23**(8):pages 683–686.
- Bear, J. and Verruijt, A.**, editors, 1987. Modeling groundwater flow and pollution. Kluwer Academic Publishers Group, Dordrecht, Holland.
- Beck, J. L.**, 1976. Weight-induced stresses and recent seismicity at lake oroville and california. *Bull. Seism. Soc. Am.*, **66**(4):pages 1121–1131.
- Bell, M. L. and Nur, A.**, 1978. Strength changes due to reservoir-induced pore pressure and stresses and applications to lake oreville. *J. Geophys. Res.*, **83**(B9):pages 4469–4482.
- Brace, W. F.**, 1980. Permeability of crystalline and argillaceous rocks. *Int. J. Rock. Mech. Min. Sci. Geomech. Abst.*, **17**:pages 241–251.
- Brace, W. F.**, 1984. Permeability of crysalline rocks: new in situ measurements. *J. Geophys. Res.*, **89**:pages 4327–4330.

- Brace, W. F., Walsh, J. B., and Frangos, W. T.,** 1968. Permeability of granite under high pressure. *J. Geophys. Res.*, **73**(6):pages 2225–2236.
- Brocher, T. M. and Christensen, N. I.,** 1990. Seismic anisotropy due to preferred mineral orientation observed in the shallow crust in southern Alaska. *Geology*, **18**:pages 737–740.
- Caine, J. S., Evans, J. P., and Forster, C. B.,** 1996. Fault zone architecture and permeability structure. *Geology*, **24**(11):pages 1025–1028.
- Caine, J. S., Foster, C. B., and Evans, J. P.,** 1993. A classification scheme for permeability structure in fault zones. *EOS*, **74**:pages 677.
- Carder, D. S.,** 1945. Seismic investigations in the Boulder Dam area, 1940–44 and the influence of reservoir loading on local earthquake activity. *Bull. Seism. Soc. Am.*, **35**(4):pages 175–192.
- Cassidy, J. F. and Bostock, M. G.,** 1996. Shear-wave splitting above the subducting Juan de Fuca plate. *Geophys. Res. Lett.*, **23**(9):pages 941–944.
- Chester, F. M. and Logan, J. M.,** 1986. Composite planar fabric of gouge from the Punchbowl fault, California. *J. Struct. Geol.*, **9**:pages 621–634.
- Cornet, F. H. and Yin, J.,** 1992. Induced seismicity and flow paths associated with forced fluid percolation. *Geothermal resources Council TRANSACTIONS*, **16**:pages 287–295.
- Costa, W.,** 1986. Análise dos fatores que influenciam no aquífero fissural: área piloto dos estados da Paraíba e Rio Grande do Norte. Ph.D. thesis, Universidade de São Paulo, São Paulo, Brazil.
- CPRM,** 1999. Serviço Geológico do Brasil. Data available online at <http://www.cprm.gov.br/rehi/dhid00.html>.
- Crampin, S.,** 1978. Seismic-wave propagation through a cracked solid: polarisation as a possible dilatancy diagnostic. *Geophys. J. R. astron. Soc.*, **53**:pages 467–496.
- Crampin, S.,** 1981. A review of wave motion in anisotropic cracked elastic-media. *Wave Motion*, **3**:pages 343–391.
- Crampin, S.,** 1987. Geological and industrial implications of extensive-dilatancy anisotropy. *Nature*, **328**(6130):pages 491–496.
- Crampin, S., Chesnokov, E. M., and Hipkin, R. G.,** 1984a. Seismic anisotropy - the state of the art: I. *Geophys. J. R. astron. Soc.*, **76**:pages 1–16.
- Crampin, S., Evans, R., and Atkinson, B. K.,** 1984b. Earthquake prediction: a new physical basis. *Geophys. J. R. astron. Soc.*, **76**:pages 147–156.
- Crampin, S. and Lovell, J. H.,** 1991. A decade of shear-wave splitting in the earth's crust: what does it mean? what use can we make of it? and what should we do next? *Geophys. J. Int.*, **107**:pages 387–407.
- Dawers, N. H. and Seeber, L.,** 1991. Intraplate faults revealed in crystalline bedrock in the 1983 Goodnow and 1985 Ardsley epicentral area, New York. *Tectonophysics*, **186**:pages 115–131.

- de Marsily, G.**, 1986. Quantitative Hydrology. Academic Press.
- Detournay, E. and Cheng, A. H.-D.**, 1993. Fundamentals of poroelasticity, volume 2 of *Comprehensive Rock Engineering Principle, Practice & Projects*. Pergamon Press.
- DNPM**, 1983. Departamento Nacional de Produção Mineral - Projeto RADAMBRASIL - Levantamento de recursos naturais. vol. 2.
- DNPM, UFRN, PETROBRAS, and Governo do Estado do Rio Grande do Norte**, 1998. Mapa Geológico do Estado do Rio Grande do Norte.
- do Nascimento, A. F.**, 1997. Estudo da sismicidade induzida pelo reservatório da barragem do Assu (RN). Master's thesis, PPGG - UFRN.
- do Nascimento, A. F., Pearce, R. G., and Takeya, M. K.**, 2002. Local shear-wave observations in João Câmara, NE Brazil. *J. Geophys. Res.* Accepted for publication.
- Evans, J. P., Forster, C. B., and Goddard, J. V.**, 1997. Permeability of fault-related rocks, and implications for hydraulic structure of fault zones. *J. Struct. Geol.*, **19**(11):pages 1393–1404.
- Evans, R.**, 1984. Effects of the free surface on shear wave trains. *Geophys. J. R. Astron. Soc.*, **76**:pages 165–172.
- Ferreira, J. M.**, 1997. Seismicity and stresses in NE Brazil. Ph.D. thesis, University of São Paulo, Brazil. In Portuguese.
- Ferreira, J. M., Oliveira, R., Takeya, M. K., and Assumpção, M.**, 1998. Superposition of local and regional stresses in northeast Brazil: evidence from focal mechanism around the Potiguar marginal basin. *Geophys. J. Int.*, **134**:pages 341–355.
- Ferreira, J. M., Oliveira, R. T., Assumpção, M., Moreira, J. A. M., Pearce, R. G., and Takeya, M. K.**, 1995. Correlation of seismicity and water level - an example from northeastern Brazil. *Bull. Seismol. Soc. Am.*, **85**:pages 1483–1489.
- Gledhill, K. R.**, 1991. Evidence for shallow and pervasive seismic anisotropy in the Wellington region, New Zealand. *J. of Geophys. Res.*, **96**:pages 21503–21516.
- Gough, D. I.**, 1969. Incremental stress under a two-dimensional artificial lake. *Can. J. Earth Sci.*, **6**:pages 1067–1075.
- Gough, D. I. and Gough, W. I.**, 1970. Load-induced earthquakes at Lake Kariba - ii. *Geophys. J. R. Astron. Soc.*, **21**:pages 79–101.
- Grasso, J.-R. and Sornette, D.**, 1998. Testing self-organized criticality by induced seismicity. *J. Geophys. Res.*, **103**(B12):pages 29965–29987.
- Gudmundsson, A.**, 2000. Active fault zones and groundwater flow. *Geophys. Res. Lett.*, **27**(18):pages 2993–2996.
- Guéguen, Y. and Palciauskas, V.**, 1994. Introduction to the physics of rocks. Princeton University Press, Princeton, New Jersey.

- Gupta, H. K.**, 1992. Reservoir-induced-earthquakes, volume 64 of *Developments in Geotechnical Engineering*. Elsevier.
- Haneberg, W. C.**, 1995. Steady state groundwater flow across idealised faults. *Water Resour. Res.*, **31**(7):pages 1815–1820.
- Healy, J. H., Rubey, W. W., Griggs, D. T., and Raleigh, C. B.**, 1968. The denver earthquakes. *Science*, **161**(3848):pages 1301–1310.
- Hubbert, M. K. and Rubey, W. W.**, 1959. Role of fluid pressure in mechanics of overthrusting faulting. *Bull. Geol. Soc. Am.*, **70**:pages 115–166.
- Journel, A. G. and Huijbregts, C. J.**, 1993. Mining geostatistics. Academic Press Limited, London, UK.
- Kalpna, R. C.**, 2000. Green's function based stress diffusion solutions in the porous elastic half space for time varying finite reservoir loads. *Phys. Earth Planet. Int.*, **120**:pages 93–101.
- Karnasopoulou, A., Pearce, R. G., and Booth, D. C.**, 1996. A method to determine microearthquake focal mechanisms in the presence of seismic anisotropy. *Tectonophysics*, **261**:pages 115–126.
- Kessels, W. and Kuck, J.**, 1995. Hydraulic communication in crystalline rock between two boreholes of the continental deep drilling project in Germany. *Int. J. Rock. Mech. Min. Sci. Geomech. Abstr.*, **32**:pages 37–47.
- Kisslinger, C. and Engdahl, E. H.**, 1973. The interpretation of the wadati diagram with relaxed assumptions. *Bull. Seism. Soc. Am.*, **63**:pages 1723–1736.
- Kitanidis, P. K.**, 1997. Introduction to Geostatistics. Applications in Hydrogeology. Cambridge University Press, Cambridge, UK.
- Kreyszig, E.**, 1993. Advanced Engineering Mathematics. John Wiley & Sons, Inc, New York.
- Landau, L. D. and Lifshitz, E. M.**, 1959. Fluid Mechanics, volume 6 of *Course on Theoretical Physics*. Pergamon Press.
- Lee, M.-K. and Wolf, L. W.**, 1998. Analysis of fluid pressure propagation in heterogeneous rocks: Implications for hydrologically-induced earthquakes. *Geophys. Res. Lett.*, **25**(13):pages 2329–2332.
- Lee, W. H. K. and Lahr, J. C.**, 1975. HYPO71 (revised): a computer program for determining hypocenter and magnitude and first motion pattern of local earthquakes. Open File Rep. 75-311. U. S. Geological Survey.
- Lockner, D. A. and Beeler, N. M.**, 1999. Premonitory slip and tidal triggering of earthquakes. *J. Geophys. Res.*, **104**:pages 20133–20151.
- Lunn, R. J. and Mackay, R.**, 1997. An investigation of coupled hydromechanical effects in the Borrowdale group, Sellafield, UK. In Findikakis, A. N., editor, *Water for a changing global community*, pages 150–155. XXVII IAHR. Groundwater: an endangered resource, Am. Soc. Civ. Eng., San Francisco.

- Mantoglou, A. and Wilson, J. L.**, 1982. The turning bands method for simulation of random fields using line generation by a spectral method. *Water Resour. Res.*, **18**(5):pages 1379–1394.
- Matthäi, S. K. and Roberts, S. G.**, 1997. Transient versus continuous fluid flow in seismically active faults: an investigation by electric analogue and numerical modelling. In Jamtveit, B. and Yardley, B. W. D., editors, *Fluids flow and transport in rocks - mechanics and effects*, Chapter 16, pages 263–295. Chapman & Hall, London.
- Menke, W., Brandsdottir, B., Jakobsdottir, S., and Stefansson, R.**, 1994. Seismic anisotropy in the crust at the mid-atlantic plate boundary in the south-west iceland. *Geophys. J. Int.*, **119**:pages 783–790.
- Morrow, C. A. and Lockner, D. A.**, 1994. Permeabilities differences between surface-derived and deep drillhole in core samples. *Geophys. Res. Lett.*, **21**:pages 2151–2154.
- Murdie, R. E., Prior, D. J., Flint, S. S., Pearce, R. G., and Agar, S. M.**, 1993. Seismic responses to ridge-transform subduction: Chile triple junction. *Geology*, **21**:pages 1095–1098.
- Nur, A. and Booker, J. R.**, 1972. Aftershocks caused by pore fluid flow? *Science*, **175**:pages 885–887.
- Nuttli, O. W.**, 1961. The effect of the earth's surface on the s wave particle motion. *Bull Seism. Soc. Am.*, **51**:pages 237–246.
- Ohtake, M.**, 1974. Seismic activity induced by water injection at Matsushiro, Japan. *J. Physic. Earth*, **22**:pages 163–176.
- Pearce, R. G.**, 1977. Fault plane solutions using relative amplitude methods of P and pP. *Geophys. J. Roy. Astr. Soc.*, **50**:pages 381–394.
- Pearce, R. G.**, 1980. Fault plane solutions using relative amplitudes of P and pP: further studies. *Geophys. J. Roy. Astr. Soc.*, **60**:pages 469–487.
- Pearce, R. G. and Rogers, R. M.**, 1989. Determination of earthquake moment tensors from teleseismic relative amplitude observations. *J. Geophys. Res.*, **94**:pages 775–786.
- Perfettini, H. and Schmittbuhl, J.**, 2001. Periodic loading on a creeping fault: implications for tides. *Geophys. Res. Lett.*, **28**:pages 435–438.
- Rajendran, K. and Talwani, P.**, 1992. The role of elastic and undrained and drained responses in triggering earthquakes at monticello reservoir and south carolina. *Bull. Seism. Soc. Am.*, **82**(4):pages 1867–1888.
- Raleigh, C. B., Healy, J. H., and Bredehoeft, J. D.**, 1976. An experiment in earthquake control at Rangely, Colorado. *Science*, **191**:pages 1230–1237.
- Reasenber, P. and Oppenheimer, D.**, 1985. FPFIT, FPLOT, FPPAGE: Fortran computer programs for calculating and displaying earthquake fault-plane solutions. U. S. Geological Survey. Openfile Report 85-739.
- Rice, J. R. and Cleary, M. P.**, 1976. Some basic stress diffusion solutions for fluid-saturated elastic porous media with compressible constituents. *Rev. Geophys. Space Phys.*, **14**(2):pages 227–240.

- Roeloffs, E. A.**, 1988. Fault stability changes induced beneath a reservoir with cyclic variations in water level. *J. Geophys. Res.*, **93**(B3):pages 2107–2124.
- Roeloffs, E. A.**, 1998. Persistent water level changes in a well near parkfield and california and due to local and distant earthquakes. *J. Geophys. Res.*, **103**(B1):pages 869–889.
- Rowlands, H. J.**, 1995. Shear-wave anisotropy in the New Madrid seismic zone. Ph.D. thesis, The University of Edinburgh.
- Rutqvist, J., Noorishad, J., Tsang, C., and Stephansson, O.**, 1998. Determination of fracture storativity in hard rocks using high-pressure injection testing. *Water Res. Res.*, **34**(10):pages 2551–1560.
- Scherbaum, F.**, 1996. Of poles and zeros. Fundamentals of digital seismology. Kluwer Academic Publishers.
- Scholz, C. H.**, 1990. The mechanics of earthquakes and faulting. Cambridge University Press, Cambridge.
- Schön, J. H.**, 1996. Physical Properties of Rocks: fundamntals and principles of petrophysics, volume 18. Elsevier Science Ltd, Oxford, UK, first edition.
- Shapiro, S. A.**, 2000. An inversion for fluid transport properties of three-dimensionally heterogeneous rocks using induced microseismicity. *Geophys. J. Int.*, **143**:pages 931–936.
- Shapiro, S. A., Audigane, P., and Royer, J.-J.**, 1999. Large-scale in situ permeability tensor of rocks from induced microseismicity. *Geophys. J. Int.*, **137**:pages 207–213.
- Shapiro, S. A., Huegens, E., and Borm, G.**, 1997. Estimating the crust permeability from fluid-injection-induced seismic emission at the ktb site. *Geophys. J. Int.*, **131**:pages F15–F18.
- Shearer, P. M.**, 1999. Introduction to Seismology. Cambridge University Press, 1st edition.
- Simpson, D. W., Leith, W. S., and Scholz, C. H.**, 1988. Two types of reservoir-induced seismicity. *Bull Seism. Soc. Am.*, **78**(6):pages 2025–2040.
- Simpson, D. W. and Narasimhan, T. N.**, 1992. Inhomogeneities in rock properties and their influence on reservoir induced seismicity. In Knoll, P., editor, *Induced seismicity*, pages 345–359. Balkema, Rotterdam.
- Singhal, B. B. S. and Gupta, R. P.**, 1999. Applied hydrogeology of fractured rocks. Kluwer Academic Publishers, The Netherlands.
- SUDENE**, 1970. Superintendência do Desenvolvimento do Nordeste. Folha SB-24-L-III. Departamento de Recursos Naturais. Divisão de Cartografia.
- Tadokoro, K. and Ando, M.**, 2000. Induced earthquakes accompanying the water injection experiment at the nojima fault zone, Japan: Sesismicity and its migration. *J. Geophys. Res.*, **105**(B3):pages 6089–6104.
- Talwani, P.**, 1976. Earthquakes associated with the Clark Hill Reservoir, South Carolina - a case of induced seismicity. *Eng. Geol.*, **10**:pages 239–253.

- Talwani, P.**, 1995. Speculations on the cause of continuing seismicity near Koyna reservoir, India. *Pageoph*, **145**(1):pages 167–174.
- Talwani, P.**, 1997. On the nature of reservoir-induced seismicity. *Pageoph*, **150**:pages 473–492.
- Talwani, P.** and **Acree, S.**, 1984/85. Pore pressure diffusion and the mechanism of reservoir-induced seismicity. *Pageoph*, **122**:pages 947–965.
- Talwani, P., Cobb, J. S., and Schaeffer, M. F.**, 1999. In situ measurements of hydraulic properties of shear zone in northwestern South Carolina. *J. Geophys. Res.*, **104**:pages 14993–15003.
- Tapley, W. C. and Tull, J. E.**, 1991. SAC - Seismic Analysis Code and Users Manual and Revision 3. Regents of the University of California.
- USGS**, 2001. USGS EROS Data Center. Data available online at <http://http://edcdaac.usgs.gov/gtopo30/gtopo30.html>.
- Vavryčuk, V.**, 1993. Crustal anisotropy from local observations of shear-wave splitting in West Bohemia and Czech Republic. *Bull. Seism. Soc. Am.*, **83**(5):pages 1420–1441.
- Walsh, J. B. and Brace, W. F.**, 1984. The effect of pressure on porosity and the transport properties of rock. *J. Geophys. Res.*, **89**(B11):pages 9425–9431.
- Ward, R. R. and Robinson, M.**, 1990. Principles of Hydrology. McGrall Hill, UK, third edition. 365 pp.
- Wessel, P. and Smith, W. H. F.**, 1998. New, improved version of Generic Mapping Tools released. *EOS Trans. Am. Geophys. U.*, **79**(47):pages 579.
- Zhang, Z. and Schwartz, S. Y.**, 1994. Seismic anisotropy in the shallow crust of the loma prieta segmet of the san andreas fault system. *J. Geophys. Res.*, **99**(B5):pages 9651–9661.
- Zimmerman, R. W. and Bodvarsson, G. S.**, 1996. Hydraulic conductivity of rock fractures. *Transport in Porous Media*, **23**:pages 1–30.
- Zimmermann, G., Körner, A., and Burkhardt, H.**, 2000. Hydraulic pathways in the crystalline rock of the KTB. *Geophys. J. Int.*, **142**:pages 4–14.
- Zoback, M. D. and Hickman, S.**, 1982. In situ study of the physical mechanisms controlling induced seismicity at monticello reservoir and south carolina. *J. Geophys. Res.*, **87**(B8):pages 6959–6974.

A POLARISATION MEASUREMENTS

Here, it is shown the hypocentre details of the events that provided 39 splitting measurements in which it was possible to obtain the polarisation direction and the delay.

station name	date and time	distance (km)	polarisation (N°E)	delay (s)	depth (km)	azimuth (°)	i.a. (°)
BACA	960102 1525	2.7	45.	0.025	4.63	337.5	150.0
BACP	941130 2054	2.5	40.	0.03	2.70	323.4	137.2
BACP	941212 0501	2.1	40.	0.03	2.10	328.2	135.1
BACP	950108 1957	2.5	45.	0.025	2.87	336.5	139.3
BACP	950109 1858	2.5	45.	0.025	2.83	339.5	138.8
BACP	950112 1136	2.6	35.	0.01	2.88	334.7	137.7
BACP	950117 0822	2.5	47.	0.025	2.78	340.0	137.7
BACP	950127 1705	2.4	40.	0.01	2.78	349.7	138.9
BACP	950414 1300	2.3	20.	0.01	2.92	299.9	141.7
BACP	950523 1816	2.4	25.	0.03	2.57	297.0	136.4
BACP	950725 0248	2.4	30.	0.03	2.56	306.1	136.8
BACP	951202 0935	2.3	40.	0.02	2.70	322.1	139.6
BAPO	960424 0318	1.9	45.	0.004	2.61	181.7	144.6
BARV	961209 0924	3.7	35.	0.004	4.36	131.4	139.4
BARV	961229 0908	1.0	30.	0.006	5.44	172.2	169.6
BARV	961230 0627	3.3	35.	0.01	4.68	136.8	145.2
BASQ	951004 0743	1.9	155	0.01	1.97	188.1	135.6
BASQ	951005 1744	1.5	35	0.01	2.06	181.9	143.6
BASQ	951005 2325	1.6	40	0.01	1.99	183.2	141.7
BASQ	951006 1127	1.6	47	0.01	2.09	181.9	143.0
BASQ	951006 1342	1.6	37	0.01	1.98	184.9	141.9
BASQ	951010 1159	1.6	40	0.025	2.24	182.4	145.2
BASQ	951010 1821	1.6	37	0.01	2.11	181.8	143.3
BASQ	951013 0526	1.5	40	0.010	2.24	179.8	145.7
BASQ	951013 0538	1.5	47	0.01	2.26	179.8	145.7
BASQ	951013 1608	1.6	39	0.01	2.10	181.1	142.8
BASQ	951015 1528	1.7	45	0.01	1.94	185.4	138.4
BASQ	951020 1232	1.7	40	0.01	2.18	182.3	142.5
BASQ	951029 2058	1.4	50	0.010	2.15	176.1	146.4
BASQ	951115 1653	1.5	231	0.010	2.65	167.3	150.6
BASQ	951125 1843	1.6	20	0.010	1.92	184.3	141.1
BASQ	951208 1224	1.2	40	0.010	1.83	173.0	146.3
BASQ	951212 0530	1.0	40	0.01	1.81	182.7	150.1
BASQ	951215 1354	1.3	50	0.010	1.96	171.4	146.7
BASQ	960106 1748	1.1	44	0.01	1.98	178.4	150.2
BASR	951029 0920	1.6	145.	0.015	2.13	35.8	142.6
BASR	960217 0550	1.1	155.	0.015	2.07	33.0	152.5
BASR	960424 0414	0.3	30.0	0.006	2.57	249.0	172.9
BASR	970217 0449	1.4	40.	0.04	2.43	338.3	149.5

Table A.1: Splitting measurements for 40 event-station raypaths within the shear-wave window. The parameters measured are self-explanatory.

B NETWORK CONFIGURATIONS

Here, the PDAS network configuration is shown. As mentioned in section 3.1, the network had five different configuration, shown in table B.1. Table B.2 shows the stations codes, names and locations. Figures B.1, B.2, B.3, B.4 and reffig:config5 show the map of the different configurations. The top map of each of these figures, show a map plotting the hypocentres on the horizontal plane and the lake contour. The bottom left shows the projection of the hypocenters in a plane striking 47° from north, whilst the bottom right shows is a projection of the same hypocenters in a plane perpendicular to the one shown on the bottom left. The starting point of both projections is indicated by the star in the left hand corner of each top map in each figure.

Configuration	Deployment period
A	29/10/1994 to 06/02/1995
B	07/02/1995 to 19/10/1995
C	20/10/1995 to 17/01/1996
D	18/01/1996 to 06/02/1996
E	07/12/1996 to 18/07/1997

Table B.1:

Station code	Station name	Location	
		Lat. S	Long. W
BASQ	Saquinho	5° 49.94 S	36° 53.87 W
BABV	Boa Vista	5° 48.41 S	36° 51.74 W
BACH	Cachoeirinha	5° 49.67 S	36° 52.29 W
BASR	São Rafael	5° 48.40 S	36° 53.35 W
BACP	Cordão de Pedra	5° 47.83 S	36° 54.44 W
BAIL	Ilha	5° 49.25 S	36° 55.44 W
BACB	Cavalo Bravo	5° 45.85 S	36° 52.81 W
BACA	Caiçarinha	5° 49.86 S	36° 56.84 W
BASF	São Fernando	5° 52.26 S	36° 51.63 W
BASO	Saco da Onça	5° 48.35 S	36° 56.58 W
BAPO	Porcino	5° 49.32 S	36° 53.30 W
BA1	IPA	5° 41.77 S	36° 51.22 W

Table B.2:

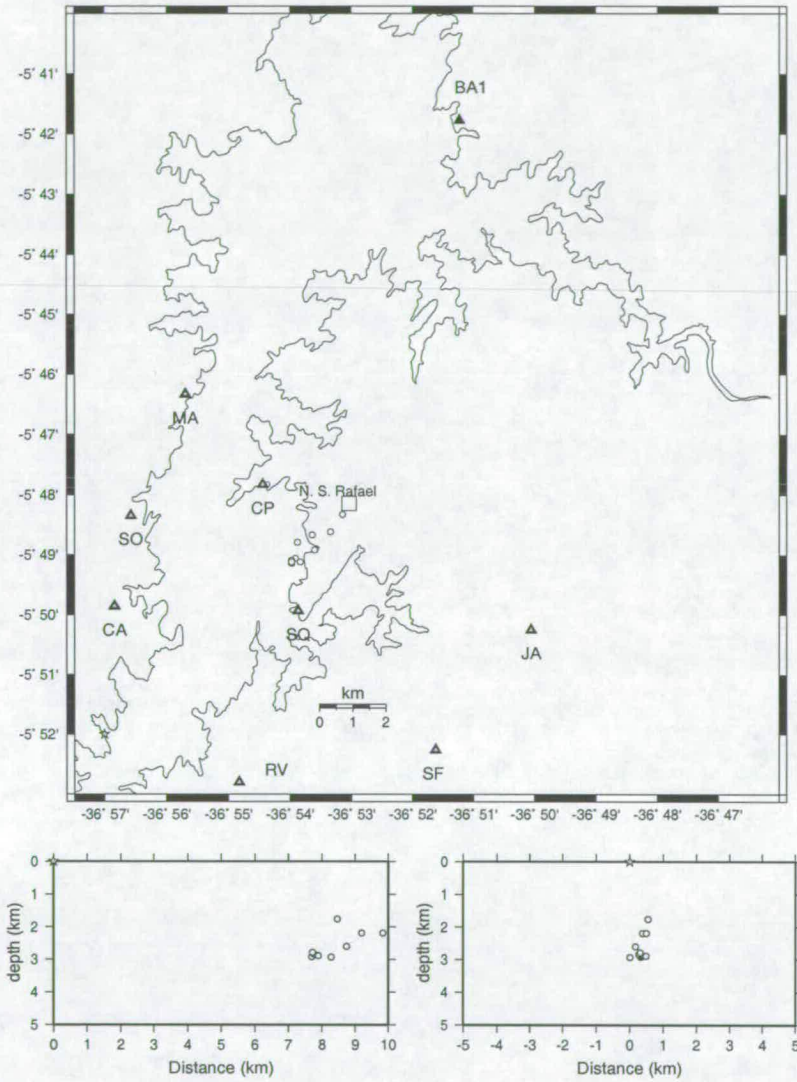


Figure B.1: Network configuration A. From 29/10/1994 to 06/02/1995.

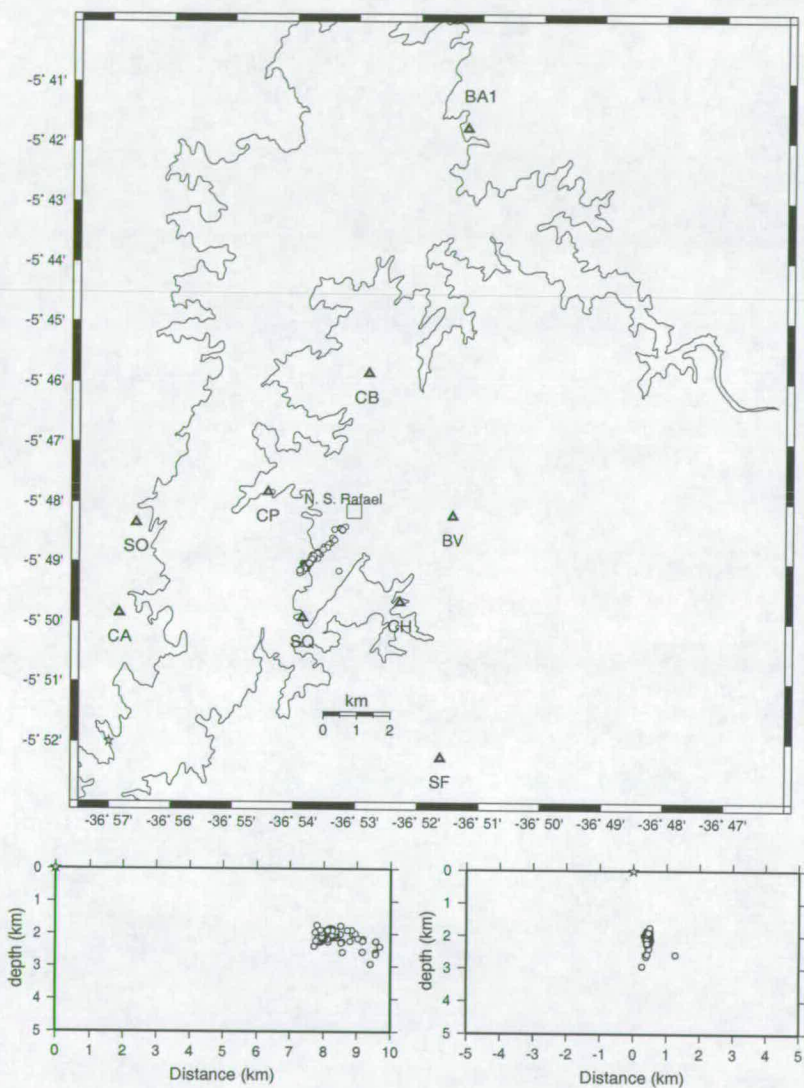


Figure B.2: Network configuration B. From 07/02/1995 to 19/10/1995.

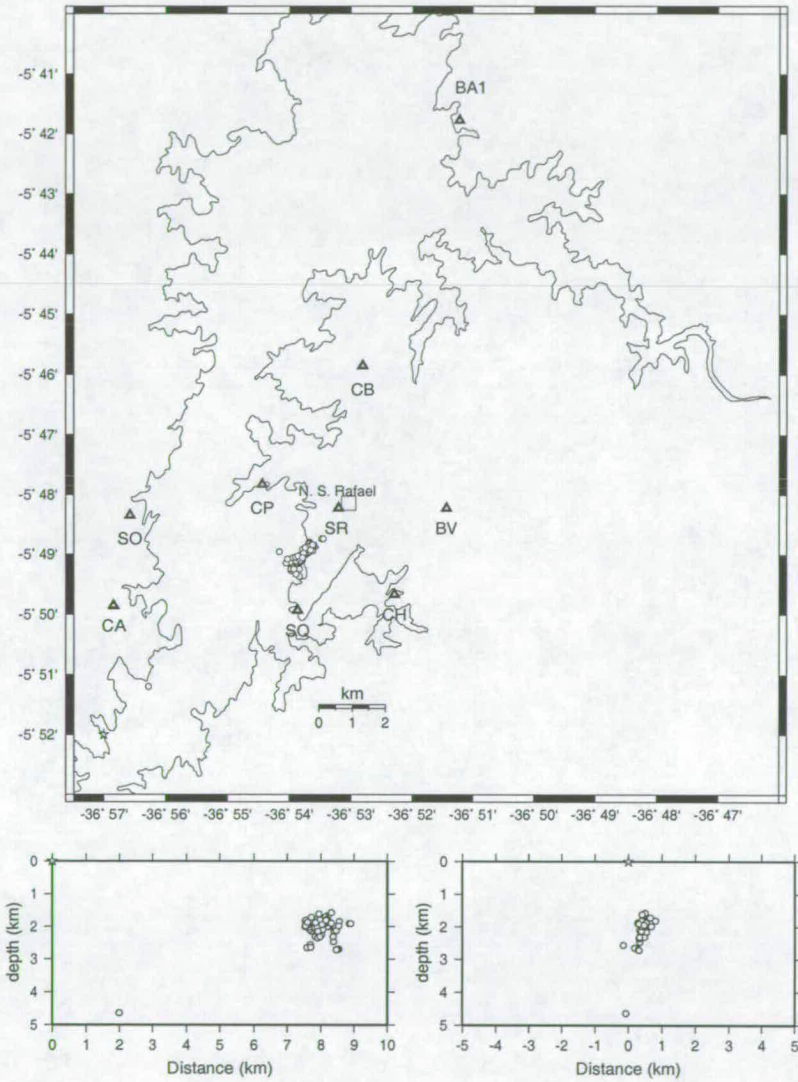


Figure B.3: Network configuration C. From 20/10/1995 to 17/01/1996.

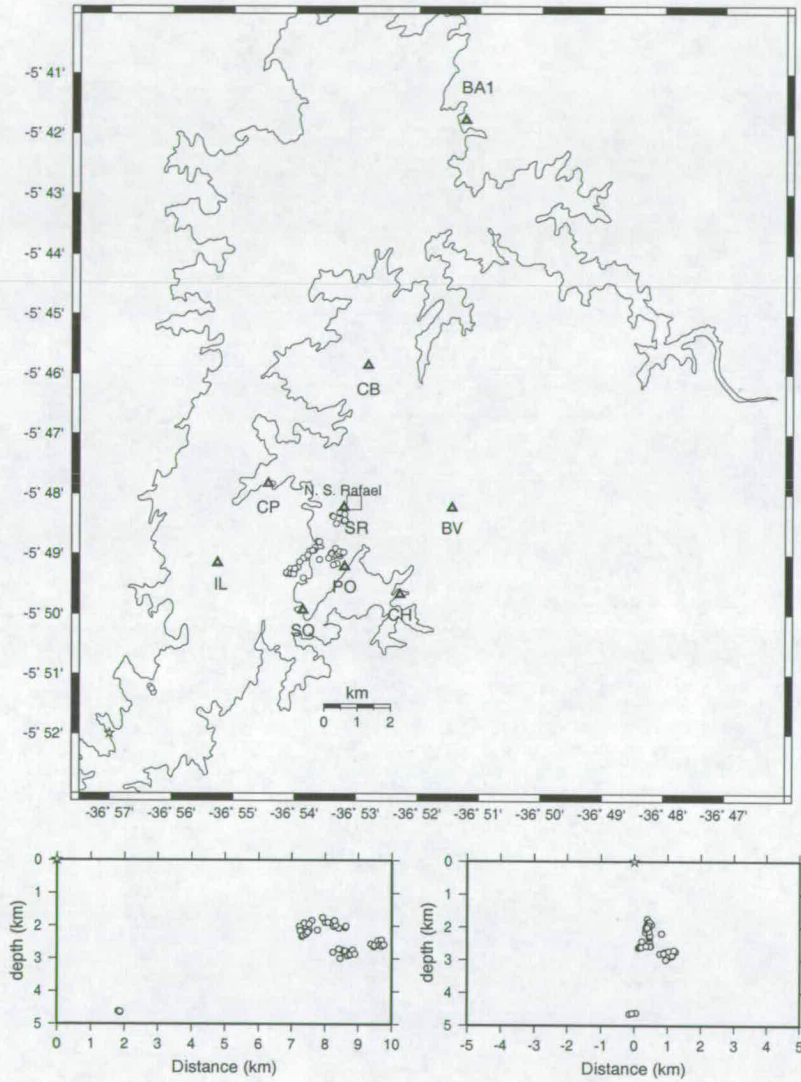


Figure B.4: Network configuration D. From 18/01/1996 to 06/02/1996.

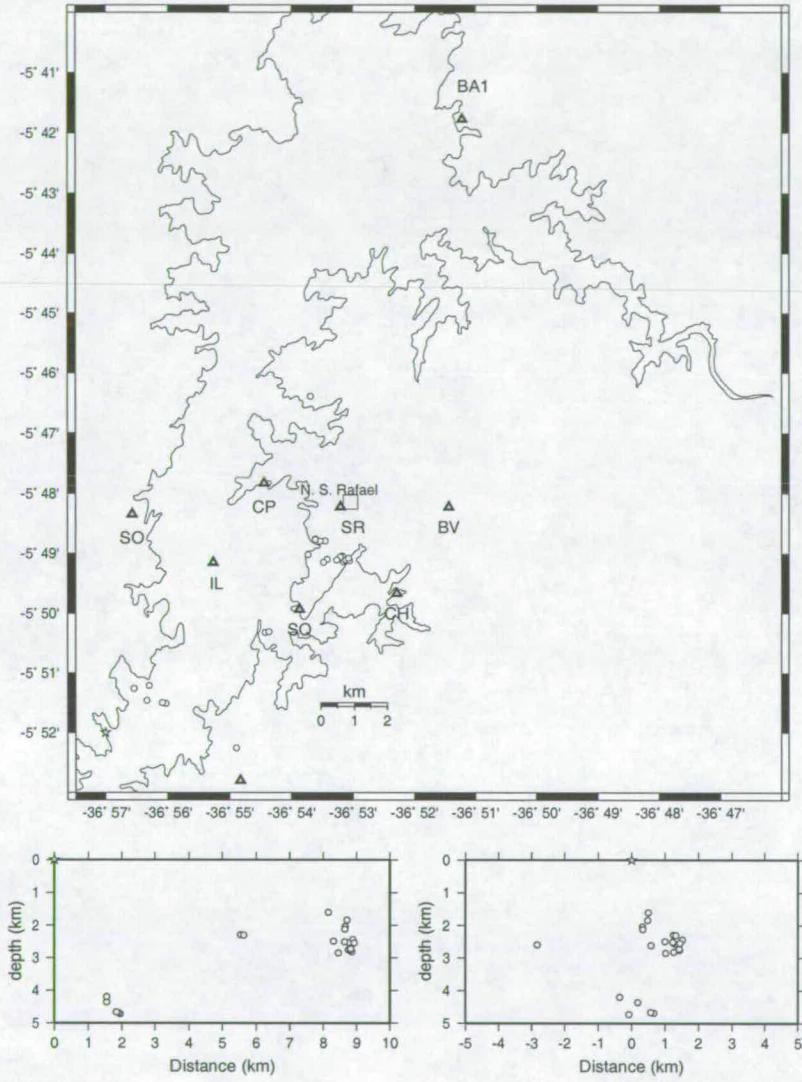


Figure B.5: Network configuration E. From 07/12/1996 to 18/07/1997.

C EARTHQUAKE LOCATIONS

The following list of earthquakes is basically the summary output of the location program HYPO71 (Lee and Lahr, 1975). This list contains information on the 286 earthquakes recorded in at least 3 stations by the PDAS network from August 1994 until September 1997.

DATE ORIGIN: Date of earthquake: year, month and day, followed by origin time.

LAT S: Latitude of epicentre in degrees and minutes.

LONG W: Longitude of epicentre in degrees and minutes.

DEPTH: Focal depth in *km*.

NO: Number of station readings used in locating the earthquake.

GAP: Largest azimuthal separation in degrees between stations.

DMIN: Epicentral distance to the nearest solution.

RMS: Root mean square error of the time residual in seconds.

$rms = (R_i^2 / NO)^{1/2}$, where R_i is the time residual for the i^{th} station.

ERH: Error of the epicentre in *km*. If ERH is an *, this means that ERH cannot be computed because of insufficient data..

ERZ: Error of the focal depth in *km*. If ERZ is an *, this means that ERH cannot be computed because of insufficient data.

Q: Solution quality of hypocentre. It is a measure to indicate the general reliability of the solution, as shown in table C.1.

Q	Epicentre	Focal depth
A	excellent	good
B	good	fair
C	fair	poor
D	poor	poor

Table C.1:

DATE ORIGIN	LAT S	LONG W	DEPTH	NO	GAP	DMIN	RMS	ERH	ERZ	Q
941105 0517 15.62	5-48.33	36-53.14	2.19	11	174	2.6	0.02	0.1	0.3	B1
941130 2054 49.38	5-48.92	36-53.63	2.70	10	186	1.9	0.04	0.3	0.2	C1
941203 0045 10.62	5-48.93	36-53.67	2.72	11	183	1.9	0.04	0.2	0.2	C1
941209 0313 10.26	5-48.97	36-53.70	2.78	12	143	1.8	0.04	0.2	0.2	B1
941212 0330 28.22	5-48.62	36-53.34	2.19	12	162	2.5	0.02	0.2	0.2	B1
941212 0501 49.99	5-48.80	36-53.84	2.10	10	143	2.1	0.05	0.4	0.4	B1
941212 1632 58.65	5-48.79	36-53.88	2.93	7	144	2.0	0.02	0.3	0.3	B1
941212 0501 49.95	5-48.75	36-53.91	2.23	11	141	2.0	0.05	0.3	0.4	B1
941213 2220 54.88	5-49.14	36-53.97	2.91	11	137	1.5	0.03	0.2	0.2	B1
941215 1534 58.34	5-49.34	36-54.19	2.55	11	129	1.3	0.05	0.2	0.3	B1
941216 2027 46.66	5-48.67	36-53.64	2.60	9	155	2.4	0.02	0.2	0.2	B1
950108 1957 27.67	5-49.06	36-53.91	2.87	13	131	1.6	0.03	0.1	0.2	B1
950109 1858 36.22	5-49.09	36-53.97	2.83	11	164	1.6	0.03	0.2	0.2	B1
950112 1136 10.90	5-49.12	36-53.83	2.88	11	132	1.5	0.02	0.1	0.1	B1
950117 0822 58.03	5-49.12	36-53.97	2.78	9	163	1.5	0.01	0.1	0.1	B1
950118 1729 30.86	5-49.00	36-53.74	2.01	5	311	1.8	0.00	0.1	0.0	C1
950122 0638 24.83	5-48.95	36-53.70	1.87	5	182	1.9	0.00	0.2	0.1	C1
950125 0455 48.59	5-48.48	36-53.19	1.93	5	220	2.6	0.00	0.2	0.2	C1
950126 0441 07.96	5-48.92	36-53.60	1.76	6	187	1.9	0.01	0.1	0.2	C1
950127 1705 30.51	5-49.12	36-54.21	2.78	7	151	2.4	0.03	0.3	0.4	B1
950213 0706 22.90	5-48.56	36-53.52	2.20	6	243	2.6	0.02	1.0	1.2	C1
950227 1917 21.13	5-48.61	36-53.37	2.16	8	193	2.6	0.00	0.1	0.1	C1
950303 0947 03.65	5-48.41	36-53.18	2.39	15	82	2.6	0.02	0.1	0.1	A1
950303 0949 06.96	5-48.47	36-53.22	2.24	9	150	2.5	0.01	0.1	0.1	B1
950402 1727 35.60	5-48.95	36-53.70	2.12	13	73	1.9	0.01	0.0	0.1	A1
950414 1300 26.22	5-48.45	36-53.36	2.92	12	101	2.3	0.02	0.1	0.1	B1
950501 0255 02.32	5-48.68	36-53.41	2.15	8	132	2.5	0.01	0.0	0.1	B1
950511 0908 02.60	5-48.66	36-53.97	3.29	10	155	1.8	0.12	0.7	0.8	B1
950513 1425 29.04	5-45.07	36-54.10	0.60	9	264	2.8	0.13	1.1	4.7	C1
950523 1816 34.02	5-48.43	36-53.26	2.57	14	79	2.4	0.02	0.1	0.1	A1
950523 1153 06.33	5-48.75	36-53.52	2.23	9	124	2.3	0.01	0.1	0.1	B1
950530 1709 13.83	5-48.44	36-53.25	2.63	10	94	2.5	0.02	0.1	0.2	B1
950603 0048 15.45	5-48.83	36-53.62	2.25	11	128	2.1	0.02	0.1	0.1	B1
950603 0133 03.59	5-48.85	36-53.62	2.28	11	128	2.1	0.01	0.1	0.1	B1
950610 0057 36.79	5-48.46	36-53.22	2.23	9	151	2.5	0.01	0.1	0.1	B1
950616 1051 07.59	5-48.94	36-53.67	2.12	9	134	1.9	0.01	0.1	0.1	B1
950617 0405 33.64	5-48.88	36-53.60	1.76	7	127	2.0	0.01	0.1	0.2	B1
950617 0407 44.41	5-48.93	36-53.68	2.04	9	135	1.9	0.01	0.1	0.1	B1
950617 0457 53.99	5-48.95	36-53.71	1.85	7	137	1.9	0.00	0.0	0.0	B1
950617 0629 42.28	5-48.86	36-53.63	2.02	9	129	2.0	0.02	0.1	0.2	B1
950620 0642 19.05	5-48.94	36-53.63	2.12	9	130	1.9	0.01	0.1	0.1	B1
950624 1624 40.08	5-48.95	36-53.69	1.90	8	136	1.9	0.00	0.0	0.0	B1
950705 1539 26.56	5-48.91	36-53.68	2.06	15	63	1.9	0.01	0.0	0.0	A1
950708 1539 14.52	5-48.97	36-53.74	1.83	6	147	1.8	0.00	0.0	0.0	B1
950708 1746 02.10	5-48.95	36-53.73	2.01	10	140	1.8	0.01	0.0	0.1	B1
950710 2014 21.21	5-48.94	36-53.71	1.94	13	92	1.9	0.01	0.0	0.1	B1
950720 2229 10.14	5-48.96	36-53.74	1.85	12	94	1.8	0.01	0.0	0.1	B1
950725 0248 50.51	5-48.60	36-53.39	2.56	8	137	2.4	0.02	0.1	0.2	B1
950730 0425 04.60	5-48.63	36-53.35	2.22	6	136	2.5	0.01	0.1	0.1	B1
950821 1308 59.32	5-48.94	36-53.72	1.87	7	179	2.4	0.00	0.0	0.1	B1
950910 0804 28.78	5-48.73	36-53.47	2.02	14	67	2.4	0.02	0.1	0.1	A1
950910 1530 36.21	5-48.70	36-53.45	1.99	14	68	2.4	0.01	0.0	0.1	A1
950911 0450 06.64	5-48.76	36-53.47	1.89	10	125	2.3	0.01	0.1	0.2	B1

950914 1232 19.08	5-48.96	36-53.70	1.88	10	101	1.8	0.01	0.0	0.1	B1
950918 1220 18.19	5-49.06	36-53.83	2.12	8	110	1.6	0.00	0.0	0.0	B1
950919 0429 48.46	5-49.01	36-53.76	2.25	13	96	1.7	0.02	0.1	0.1	B1
950924 2316 28.30	5-49.01	36-53.75	1.85	6	145	1.7	0.00	0.0	0.0	B1
950926 1411 20.23	5-49.15	36-53.28	2.57	9	87	1.8	0.02	0.1	0.2	A1
950930 1120 00.80	5-49.02	36-53.86	1.98	10	124	1.7	0.01	0.1	0.1	B1
950930 1120 07.70	5-49.02	36-53.82	1.90	8	195	1.7	0.01	0.1	0.1	C1
951003 0457 27.47	5-49.04	36-53.85	2.12	12	79	1.7	0.02	0.1	0.2	A1
951004 0743 01.97	5-48.90	36-53.72	1.97	15	65	1.9	0.02	0.1	0.1	A1
951004 1100 22.34	5-49.07	36-53.81	2.05	7	138	1.6	0.00	0.0	0.1	B1
951005 1744 53.13	5-49.12	36-53.84	2.06	13	74	1.5	0.01	0.1	0.1	A1
951005 2325 52.76	5-49.09	36-53.82	1.99	6	151	1.6	0.00	0.0	0.1	B1
951006 0839 22.89	5-49.02	36-53.74	2.05	11	103	1.7	0.02	0.1	0.2	B1
951006 1127 16.86	5-49.09	36-53.84	2.09	12	103	1.6	0.01	0.1	0.1	B1
951006 1342 24.60	5-49.10	36-53.80	1.98	13	71	1.6	0.01	0.1	0.1	A1
951007 1727 38.75	5-49.08	36-53.85	2.11	8	153	1.6	0.01	0.0	0.1	B1
951007 0635 36.55	5-49.09	36-53.83	2.03	13	73	1.6	0.01	0.1	0.1	A1
951007 1050 29.95	5-49.08	36-53.81	2.05	13	71	1.6	0.02	0.1	0.1	A1
951007 1402 13.12	5-49.08	36-53.79	2.05	13	70	1.6	0.01	0.1	0.1	A1
951007 1539 57.23	5-49.05	36-53.79	1.99	13	70	1.7	0.01	0.1	0.1	A1
951009 0050 19.90	5-48.88	36-53.71	1.99	13	64	2.0	0.02	0.1	0.2	A1
951009 0414 52.60	5-48.90	36-53.72	2.05	12	93	1.9	0.02	0.1	0.2	B1
951009 0728 51.52	5-49.11	36-53.81	2.06	11	98	1.5	0.02	0.1	0.2	B1
951009 0917 27.79	5-49.01	36-53.78	2.17	12	98	1.7	0.02	0.1	0.2	B1
951009 1959 20.13	5-49.07	36-53.82	1.99	12	101	1.6	0.01	0.1	0.1	B1
951009 2152 13.90	5-49.08	36-53.83	2.09	9	151	1.6	0.01	0.0	0.1	B1
951010 0910 43.11	5-49.11	36-53.82	1.91	10	102	1.5	0.01	0.0	0.1	B1
951010 1159 44.73	5-49.10	36-53.83	2.24	11	93	1.6	0.01	0.1	0.1	B1
951010 1235 44.73	5-49.03	36-53.76	1.93	13	68	1.7	0.01	0.1	0.1	A1
951010 1253 23.84	5-49.07	36-53.80	1.93	13	71	1.6	0.01	0.1	0.1	A1
951010 1310 20.16	5-49.09	36-53.82	2.04	13	72	1.6	0.01	0.1	0.1	A1
951010 1821 12.49	5-49.09	36-53.84	2.11	12	103	1.6	0.01	0.1	0.1	B1
951010 2025 40.27	5-49.17	36-53.89	1.95	6	159	1.4	0.00	0.0	0.0	B1
951011 1725 07.88	5-48.79	36-53.54	1.89	12	65	2.2	0.01	0.1	0.1	A1
951011 1803 22.13	5-48.95	36-53.71	1.94	12	93	1.9	0.01	0.1	0.1	B1
951011 1854 45.69	5-48.96	36-53.72	2.04	13	65	1.8	0.02	0.1	0.2	A1
951011 1923 44.63	5-49.05	36-53.81	2.13	13	71	1.6	0.02	0.1	0.1	A1
951011 2005 58.75	5-49.06	36-53.84	2.12	11	153	1.6	0.01	0.1	0.1	B1
951011 2325 56.49	5-48.90	36-53.69	1.92	12	72	1.9	0.01	0.0	0.1	A1
951011 2335 25.30	5-48.96	36-53.72	1.89	13	65	1.8	0.01	0.1	0.1	A1
951012 2022 11.83	5-49.13	36-53.88	2.14	10	95	1.5	0.01	0.1	0.1	B1
951013 0230 41.25	5-49.09	36-53.86	2.23	13	75	1.6	0.01	0.1	0.1	A1
951013 0231 31.32	5-49.08	36-53.85	2.18	12	104	1.6	0.01	0.1	0.1	B1
951013 0247 21.20	5-49.10	36-53.87	2.24	13	76	1.5	0.02	0.1	0.1	A1
951013 0526 47.77	5-49.11	36-53.87	2.24	13	76	1.5	0.01	0.1	0.1	A1
951013 0538 39.95	5-49.11	36-53.87	2.26	13	76	1.5	0.01	0.1	0.1	A1
951013 1330 26.55	5-49.07	36-53.84	2.02	9	152	1.6	0.00	0.0	0.1	B1
951013 1608 10.86	5-49.07	36-53.85	2.10	13	74	1.6	0.01	0.1	0.1	A1
951013 1928 26.41	5-49.08	36-53.84	1.96	11	152	1.6	0.01	0.1	0.1	B1
951014 1338 33.20	5-48.95	36-53.72	1.90	10	108	1.8	0.00	0.0	0.1	B1
951015 0040 42.67	5-49.16	36-53.87	1.74	7	156	1.4	0.00	0.0	0.0	B1
951015 0321 01.04	5-49.11	36-53.84	1.88	9	152	1.5	0.00	0.0	0.1	B1
951015 0658 33.36	5-49.18	36-53.91	2.38	13	80	1.4	0.02	0.1	0.2	A1
951015 1528 12.08	5-49.01	36-53.78	1.94	13	69	1.7	0.02	0.1	0.2	A1
951017 2008 09.65	5-49.12	36-53.89	2.25	13	78	1.5	0.01	0.0	0.1	A1
951017 2011 46.34	5-49.14	36-53.91	2.22	12	109	1.5	0.01	0.1	0.1	B1
951017 2035 28.61	5-48.43	36-52.88	1.77	6	223	2.5	0.05	0.7	1.0	C1
951018 0627 53.88	5-49.02	36-53.76	1.89	7	144	1.7	0.01	0.1	0.2	B1
951019 2335 09.57	5-49.14	36-53.84	2.07	13	74	1.5	0.02	0.1	0.2	A1
951020 1045 24.11	5-49.11	36-53.81	2.17	13	72	1.5	0.02	0.1	0.2	A1
951020 1212 16.72	5-49.10	36-53.79	1.90	13	71	1.6	0.02	0.1	0.2	A1
951020 1232 17.03	5-49.03	36-53.83	2.18	11	95	1.7	0.01	0.1	0.1	B1
951020 1725 03.76	5-49.02	36-53.84	2.25	12	72	1.7	0.02	0.1	0.1	A1
951027 0501 01.92	5-48.98	36-53.70	1.87	13	74	1.2	0.02	0.1	0.1	A1

951027 1343 45.37	5-48.96	36-53.73	2.01	13	72	1.2	0.01	0.0	0.1	A1
951027 1602 18.95	5-48.94	36-53.71	1.95	13	72	1.2	0.01	0.0	0.1	A1
951027 1428 50.37	5-48.96	36-53.73	1.96	10	74	1.2	0.00	0.0	0.0	A1
951027 2044 01.12	5-48.95	36-53.71	1.87	11	73	1.2	0.01	0.0	0.0	A1
951027 2053 41.13	5-48.96	36-53.72	2.01	9	114	1.2	0.02	0.1	0.1	B1
951027 1324 31.17	5-48.97	36-53.74	2.00	12	95	1.3	0.01	0.1	0.1	B1
951028 1959 26.09	5-49.12	36-53.88	2.10	10	157	1.5	0.01	0.0	0.1	B1
951028 1959 26.21	5-49.12	36-53.88	2.08	10	157	1.5	0.01	0.1	0.1	B1
951029 0920 24.83	5-49.12	36-53.86	2.13	13	76	1.5	0.02	0.1	0.1	A1
951029 0928 21.26	5-49.11	36-53.81	2.18	13	74	1.5	0.02	0.1	0.1	A1
951029 2058 19.47	5-49.17	36-53.92	2.15	13	81	1.4	0.02	0.1	0.1	A1
951029 1909 45.73	5-49.15	36-53.98	2.10	8	227	1.5	0.01	0.1	0.1	C1
951105 0142 06.11	5-49.12	36-53.84	1.78	12	74	1.5	0.01	0.1	0.1	A1
951105 1043 56.50	5-49.24	36-53.97	1.89	10	169	1.3	0.00	0.0	0.0	B1
951105 2349 23.50	5-49.17	36-53.89	1.83	12	109	1.4	0.01	0.0	0.1	B1
951106 2217 03.50	5-49.02	36-53.81	2.10	12	77	1.4	0.01	0.1	0.1	A1
951106 2339 34.79	5-48.99	36-53.72	1.67	12	74	1.3	0.01	0.1	0.1	A1
951111 0205 26.69	5-49.23	36-53.91	2.03	12	81	1.3	0.01	0.0	0.1	A1
951115 1552 56.39	5-48.96	36-54.16	2.56	9	220	1.8	0.01	0.1	0.1	C1
951115 1653 41.72	5-49.15	36-54.05	2.65	9	88	1.5	0.02	0.1	0.2	A1
951116 0703 47.68	5-48.96	36-53.67	1.58	9	87	1.2	0.02	0.1	0.2	A1
951119 0047 50.57	5-49.08	36-54.03	2.64	13	85	1.6	0.01	0.1	0.1	A1
951119 0238 49.01	5-49.03	36-53.84	1.87	6	217	1.5	0.00	0.0	0.1	C1
951122 0846 13.76	5-49.14	36-53.87	2.05	9	80	1.5	0.01	0.1	0.1	A1
951122 1420 42.60	5-48.80	36-53.67	2.69	6	161	2.1	0.00	0.0	0.0	B1
951125 1808 28.31	5-49.02	36-53.78	1.80	14	72	1.4	0.01	0.0	0.1	A1
951125 1843 43.23	5-49.10	36-53.81	1.92	8	149	1.5	0.01	0.1	0.1	B1
951125 1904 35.24	5-49.06	36-53.84	1.80	6	215	1.5	0.00	0.0	0.1	C1
951126 0053 46.30	5-49.02	36-53.76	1.91	8	143	1.4	0.01	0.1	0.1	B1
951126 0339 46.50	5-49.12	36-53.84	2.04	6	213	1.5	0.00	0.0	0.0	C1
951126 0530 05.32	5-49.01	36-53.74	1.80	9	82	1.3	0.01	0.0	0.1	A1
951127 0130 43.31	5-49.01	36-53.76	1.71	14	73	1.4	0.01	0.1	0.1	A1
951127 1502 05.80	5-49.10	36-53.84	2.23	13	73	1.6	0.01	0.0	0.1	A1
951127 1502 39.75	5-49.11	36-53.83	2.15	10	152	1.5	0.01	0.0	0.1	B1
951128 0413 32.55	5-48.85	36-53.60	1.85	9	93	0.9	0.01	0.0	0.1	B1
951128 2228 48.59	5-48.74	36-53.48	1.91	13	79	0.7	0.01	0.1	0.1	A1
951128 2229 44.35	5-48.74	36-53.45	1.91	8	120	0.7	0.00	0.0	0.0	B1
951201 1924 16.96	5-48.99	36-53.75	1.78	14	72	1.3	0.02	0.1	0.1	A1
951201 0828 10.65	5-49.18	36-53.95	1.79	5	210	1.4	0.00	0.1	0.1	C1
951201 1455 43.69	5-49.11	36-53.89	2.31	8	158	1.5	0.01	0.0	0.1	B1
951201 2225 38.02	5-49.07	36-53.85	1.62	6	215	1.5	0.01	0.1	0.1	C1
951202 0935 12.56	5-48.81	36-53.68	2.70	14	68	1.0	0.01	0.0	0.1	A1
951202 1202 28.71	5-48.83	36-53.69	2.71	9	115	2.1	0.01	0.0	0.0	B1
951202 1944 28.17	5-48.87	36-53.71	2.46	8	136	1.1	0.00	0.0	0.0	B1
951205 1436 02.73	5-49.27	36-53.97	2.01	11	106	1.3	0.02	0.1	0.1	B1
951205 2351 07.58	5-48.93	36-53.74	1.88	12	95	1.2	0.02	0.1	0.2	B1
951206 1709 03.86	5-49.22	36-53.96	1.96	10	90	1.3	0.01	0.1	0.1	B1
951208 1224 33.90	5-49.28	36-53.95	1.83	8	120	1.2	0.02	0.2	0.2	B1
951212 0530 02.02	5-49.37	36-53.84	1.81	9	116	1.0	0.02	0.1	0.2	B1
951213 0100 06.75	5-48.94	36-53.62	2.16	10	181	1.9	0.02	0.1	0.2	C1
951213 0917 34.82	5-50.05	36-53.82	2.18	5	198	0.2	0.00	0.1	0.0	C1
951215 1354 49.50	5-49.25	36-53.97	1.96	9	121	1.3	0.02	0.1	0.2	B1
951217 0032 06.43	5-48.92	36-53.79	1.86	9	125	1.9	0.02	0.2	0.3	B1
951217 0646 32.71	5-48.90	36-53.65	2.23	5	182	2.0	0.00	0.2	0.1	C1
951217 2227 48.41	5-48.86	36-53.66	2.13	6	185	2.0	0.01	0.2	0.2	C1
951218 0036 59.63	5-48.93	36-53.66	2.31	8	122	1.9	0.01	0.1	0.1	B1
951226 1656 06.01	5-49.06	36-53.94	1.88	6	125	1.6	0.01	0.2	0.2	B1
960102 1525 51.52	5-51.20	36-56.28	4.63	11	268	2.7	0.01	0.1	0.1	C1
960102 1940 35.31	5-48.98	36-53.77	1.81	11	95	1.3	0.01	0.1	0.1	B1
960102 1525 42.38	5-50.04	36-53.97	3.00	5	258	0.3	0.21	0.2	0.1	C1
960103 2302 36.10	5-49.05	36-53.90	2.35	9	124	1.6	0.01	0.1	0.1	B1
960104 1224 06.76	5-48.84	36-53.62	1.98	6	161	2.1	0.00	0.0	0.0	B1
960105 0152 29.58	5-49.25	36-53.84	1.72	7	102	1.3	0.01	0.2	0.1	B1
960106 0117 11.29	5-49.03	36-53.86	2.31	13	74	1.5	0.02	0.1	0.1	A1

960106 1748 15.30	5-49.33	36-53.89	1.98	11	87	1.1	0.02	0.1	0.2	A1
960107 2034 16.69	5-49.25	36-53.93	1.87	9	90	1.3	0.01	0.1	0.1	A1
960110 2315 53.36	5-48.89	36-53.74	1.90	10	96	1.2	0.01	0.0	0.1	B1
960111 2038 11.96	5-50.45	36-53.19	2.43	4	258	1.6	0.00	*	*	C1
970114 2228 06.48	5-45.95	36-52.91	3.00	10	168	0.3	0.51	2.1	2.3	D1
960115 0614 29.64	5-49.06	36-53.79	1.94	9	78	1.5	0.02	0.1	0.2	A1
960116 2132 42.87	5-48.95	36-53.73	2.02	10	74	1.8	0.01	0.0	0.1	A1
960117 1623 12.70	5-48.88	36-53.64	1.78	4	158	2.0	0.00	*	*	C1
960120 1506 14.49	5-51.01	36-49.86	4.39	4	315	5.1	0.02	*	*	C1
960126 1736 20.16	5-49.20	36-53.92	1.58	4	269	2.7	0.00	*	*	C1
960127 1346 04.66	5-49.32	36-55.77	0.04	6	323	3.7	0.29	4.5	469.5	D1
960129 1728 04.68	5-49.04	36-53.90	2.44	5	262	2.4	0.00	0.2	0.2	C1
960131 1550 39.44	5-49.05	36-53.86	2.15	5	262	2.5	0.00	0.0	0.1	C1
960215 0246 49.77	5-48.50	36-53.32	2.55	10	76	0.2	0.01	0.1	0.1	A1
960215 2233 09.83	5-49.06	36-53.81	1.89	13	79	1.1	0.01	0.1	0.1	A1
960216 0249 27.85	5-49.07	36-53.86	1.75	11	83	1.1	0.01	0.1	0.1	A1
960217 0550 30.30	5-48.89	36-53.67	2.07	10	69	1.0	0.01	0.1	0.1	A1
960301 0658 41.39	5-48.96	36-53.76	1.90	8	74	1.8	0.02	0.2	0.2	A1
960301 0938 37.06	5-48.94	36-53.69	1.97	8	135	1.9	0.00	0.0	0.1	B1
960301 1300 45.38	5-48.94	36-53.71	1.84	8	138	1.9	0.00	0.0	0.1	B1
960302 1616 45.18	5-48.45	36-53.21	2.44	9	80	2.5	0.01	0.1	0.1	A1
960307 1214 59.28	5-48.37	36-53.39	2.63	7	176	3.0	0.01	0.1	0.1	B1
960307 2008 26.33	5-48.38	36-53.37	2.59	7	175	3.0	0.01	0.1	0.1	B1
960308 0224 41.95	5-48.33	36-53.26	2.53	8	170	2.8	0.01	0.1	0.2	B1
960309 1735 18.62	5-48.32	36-53.26	2.42	6	170	2.8	0.01	0.1	0.1	B1
960416 2319 23.99	5-49.25	36-54.07	2.02	8	181	1.3	0.00	0.0	0.0	C1
960417 1007 29.29	5-49.02	36-53.79	1.89	7	146	1.4	0.00	0.0	0.0	B1
960417 2304 07.58	5-49.24	36-54.00	2.14	11	100	1.3	0.01	0.1	0.1	B1
960421 0401 35.60	5-48.44	36-53.18	2.57	10	136	0.3	0.01	0.1	0.1	B1
960422 0855 48.85	5-48.44	36-53.19	2.58	10	135	0.3	0.01	0.1	0.1	B1
960424 0318 34.03	5-48.31	36-53.27	2.61	8	148	0.2	0.01	0.1	0.1	B1
960424 0414 15.24	5-48.34	36-53.19	2.57	8	137	0.3	0.01	0.1	0.1	B1
960425 2011 40.38	5-49.13	36-53.92	2.13	6	133	1.2	0.01	0.2	0.1	B1
960426 1520 58.42	5-48.26	36-53.31	2.57	6	173	0.3	0.01	0.4	0.1	B1
960427 1846 39.92	5-54.55	36-43.47	3.00	4	352	21.0	4.90	*	*	D1
960428 2343 28.75	5-49.35	36-53.74	2.36	5	190	0.8	0.01	0.3	0.1	C1
960428 0904 28.08	5-48.96	36-53.40	1.93	5	159	0.7	0.01	0.3	0.1	C1
960508 0701 12.65	5-48.43	36-53.88	2.39	4	203	1.0	0.00	*	*	C1
960518 1824 40.10	5-49.16	36-54.07	2.23	4	223	1.9	0.00	*	*	C1
960620 0625 00.84	5-49.32	36-54.14	2.02	6	193	1.2	0.00	0.0	0.0	C1
960702 1605 04.47	5-49.32	36-54.12	2.14	7	190	1.2	0.01	0.1	0.1	C1
960702 1455 18.02	5-49.31	36-54.13	2.15	6	117	1.3	0.01	0.1	0.1	B1
960705 1029 22.32	5-49.33	36-54.07	2.32	9	111	1.2	0.01	0.1	0.1	B1
960709 1906 54.50	5-49.32	36-54.06	2.29	9	110	1.2	0.01	0.1	0.1	B1
960712 1026 28.75	5-49.29	36-54.02	2.25	8	105	1.2	0.01	0.1	0.1	B1
960718 0529 06.39	5-49.33	36-54.02	1.91	7	107	1.2	0.01	0.1	0.1	B1
960722 2035 51.26	5-49.22	36-53.95	1.84	9	95	1.2	0.02	0.2	0.2	B1
960722 2051 30.17	5-49.25	36-54.00	2.13	10	101	1.3	0.01	0.1	0.1	B1
960723 0449 42.87	5-49.24	36-54.00	1.94	6	173	1.3	0.00	0.0	0.0	B1
960807 0727 49.91	5-48.79	36-53.62	2.05	9	113	0.9	0.02	0.1	0.1	B1
960809 1218 51.87	5-49.40	36-53.86	2.19	6	111	1.0	0.01	0.2	0.1	B1
960815 0349 37.21	5-48.80	36-53.60	2.01	6	162	0.9	0.00	0.0	0.0	B1
961021 1737 34.57	5-49.04	36-53.38	2.78	7	139	1.2	0.01	0.1	0.1	B1
961023 0652 33.78	5-49.16	36-53.31	2.74	6	151	1.4	0.01	0.3	0.1	B1
961023 1603 07.09	5-49.00	36-53.41	2.80	8	136	1.1	0.01	0.1	0.1	B1
961023 0023 36.07	5-48.98	36-53.40	2.77	8	135	1.1	0.01	0.1	0.1	B1
961102 0120 58.48	5-50.35	36-54.48	1.39	7	246	1.4	0.02	0.3	0.4	C1
961104 0417 57.80	5-48.99	36-53.26	2.79	11	88	0.6	0.01	0.0	0.1	A1
961107 1200 18.90	5-49.00	36-53.40	2.76	13	102	0.6	0.02	0.1	0.1	B1
961109 0548 21.29	5-49.09	36-53.60	2.80	8	165	0.7	0.02	0.2	0.2	B1
961112 0159 34.69	5-49.02	36-53.33	2.90	13	95	0.6	0.01	0.1	0.1	B1
961113 0907 08.36	5-49.22	36-53.19	2.88	5	207	1.8	0.01	0.3	0.1	C1
961114 0416 53.09	5-49.03	36-53.26	2.87	11	90	1.2	0.02	0.1	0.1	B1
961115 1513 36.77	5-48.99	36-53.30	2.79	12	92	0.6	0.01	0.1	0.1	B1

961115 1454 45.86	5-49.00	36-53.26	2.80	10	88	1.1	0.01	0.1	0.1	A1
961115 1454 52.35	5-48.98	36-53.27	2.79	9	89	1.1	0.01	0.1	0.1	A1
961115 1116 16.78	5-48.91	36-53.34	2.79	11	98	0.8	0.02	0.1	0.1	B1
961115 1115 08.82	5-48.99	36-53.29	2.86	11	91	1.1	0.02	0.1	0.1	B1
961115 1614 37.07	5-48.96	36-53.27	2.73	6	140	1.0	0.01	0.1	0.1	B1
961116 0324 42.69	5-48.87	36-53.56	2.62	7	178	1.0	0.00	0.4	0.1	B1
961117 1912 29.36	5-48.97	36-53.21	2.85	12	83	0.7	0.01	0.1	0.1	A1
961121 1458 09.45	5-49.18	36-53.37	2.70	9	154	1.4	0.02	0.1	0.2	B1
961122 0052 17.48	5-49.07	36-53.45	2.99	10	147	1.2	0.02	0.1	0.2	B1
961125 1605 55.63	5-51.31	36-56.29	4.61	12	315	4.1	0.01	0.2	0.2	C1
961126 1021 12.30	5-50.67	36-57.21	2.85	10	324	4.2	0.07	0.9	0.9	C1
961126 0524 21.04	5-51.22	36-56.35	4.64	11	316	4.0	0.01	0.2	0.1	C1
961126 1141 47.36	5-49.00	36-55.42	2.41	5	277	0.5	0.00	0.1	0.0	C1
961201 2150 27.93	5-51.25	36-56.32	4.62	12	315	4.0	0.02	0.3	0.2	C1
961201 0025 29.97	5-51.21	36-56.30	4.72	11	315	3.9	0.01	0.2	0.1	C1
961208 1123 28.14	5-49.04	36-53.17	2.81	12	82	1.2	0.02	0.1	0.2	A1
961209 0924 53.93	5-51.46	36-56.34	4.36	12	251	3.7	0.01	0.1	0.1	C1
961215 1449 34.42	5-49.06	36-53.16	2.57	10	139	1.3	0.01	0.1	0.1	B1
961216 1902 20.15	5-48.79	36-53.45	2.61	6	174	0.7	0.01	0.2	0.2	B1
961217 1210 43.57	5-49.14	36-53.15	2.75	9	142	2.0	0.02	0.1	0.2	B1
961217 1206 28.75	5-49.12	36-53.12	2.75	10	142	2.1	0.03	0.2	0.3	B1
961217 1159 21.11	5-49.11	36-53.12	2.72	11	142	1.4	0.02	0.1	0.2	B1
961229 0805 34.38	5-52.26	36-54.89	5.44	10	178	1.0	0.03	0.2	0.2	B1
961230 0627 04.80	5-51.51	36-56.03	4.68	6	238	3.3	0.01	0.3	0.2	C1
961230 0622 06.18	5-51.50	36-56.08	4.66	6	240	3.3	0.01	0.3	0.2	C1
961230 0618 35.72	5-51.26	36-56.55	4.19	11	257	4.2	0.02	0.2	0.2	C1
970104 0809 03.59	5-49.06	36-53.21	2.53	8	131	1.2	0.00	0.0	0.0	B1
970107 0225 33.04	5-50.04	36-53.97	3.00	5	208	0.3	0.37	0.4	0.1	D1
970114 1048 58.82	5-49.10	36-53.42	2.84	7	99	1.3	0.01	0.1	0.0	B1
970125 0124 28.58	5-48.80	36-53.53	1.84	8	119	0.8	0.01	0.0	0.1	B1
970213 0341 04.02	5-49.02	36-53.73	1.61	8	129	1.3	0.02	0.1	0.2	B1
970217 0449 36.55	5-49.12	36-53.06	2.43	12	99	1.4	0.02	0.1	0.2	B1
970321 0440 21.58	5-50.32	36-54.42	2.29	8	243	1.2	0.02	0.2	0.2	C1
970331 0915 00.69	5-50.31	36-54.36	2.30	12	241	1.1	0.01	0.1	0.1	C1
970402 0959 03.23	5-46.39	36-53.69	2.59	12	305	3.0	0.01	0.1	0.1	C1
970409 0206 23.51	5-49.08	36-53.07	2.54	10	149	0.6	0.02	0.1	0.1	B1
970417 0233 08.99	5-48.76	36-53.61	2.04	6	193	1.2	0.00	0.0	0.0	C1
970418 0434 44.10	5-49.79	36-53.91	0.05	5	181	0.3	0.25	0.1	0.7	C1
970418 0940 33.15	5-48.77	36-53.61	2.12	6	192	1.2	0.00	0.0	0.0	C1
970523 0103 55.80	5-49.11	36-53.26	2.51	7	200	0.4	0.00	0.1	0.0	C1
970705 0904 43.17	5-49.15	36-53.48	2.49	8	117	0.4	0.01	0.1	0.1	B1

Table C.2:

D VECTORPLOTS AND SEISMOGRAMS

The compatible focal mechanism solutions, for assumption I is presented here, together with the respective seismograms showing the S wave waveforms (rotated into fast and slow direction) and its amplitude bounds used to calculate the focal mechanism with *RAMP2*. On the top left, the amplitude bounds for both assumptions (or interpretations) is shown. On the right side, I show a vector plot of all the solutions from *RAMP2* for the first assumption only (there is anisotropy) only. In this type of plot, the strike, dip and slip of the fault plane is plotted as a unit vector drawn at an angle given by the value of the strike of the fault plane, from the cartesian point given by the dip and the slip of the fault plane. Different combinations of dip and slip represents the various types of faulting and those are shown in figure D.1 with the equivalent lower hemisphere stereographic projections superposed on the plot (Pearce, 1977).

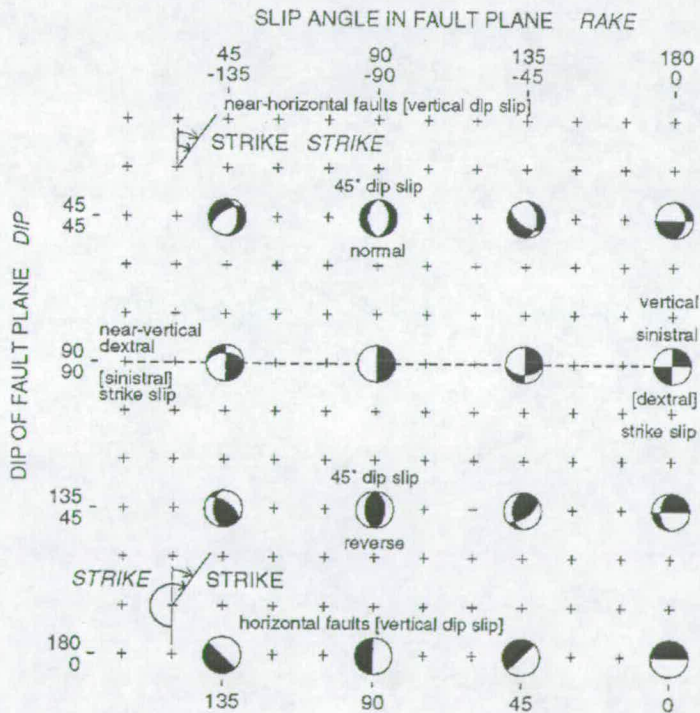


Figure D.1: Vectorplot for displaying focal mechanisms. Lower hemisphere stereographic projections indicate the type of fault plane orientation. Italicised words and lower numbers indicate Aki and Richards (1980) notation. Other angles are those from *RAMP* (Pearce, 1977).

Amplitudes

Method 1	Method 2
X: 40 to 100 (-)	X: 40 to 100 (-)
Y: 18 to 65 (-)	Y: 0 to 18 (U)

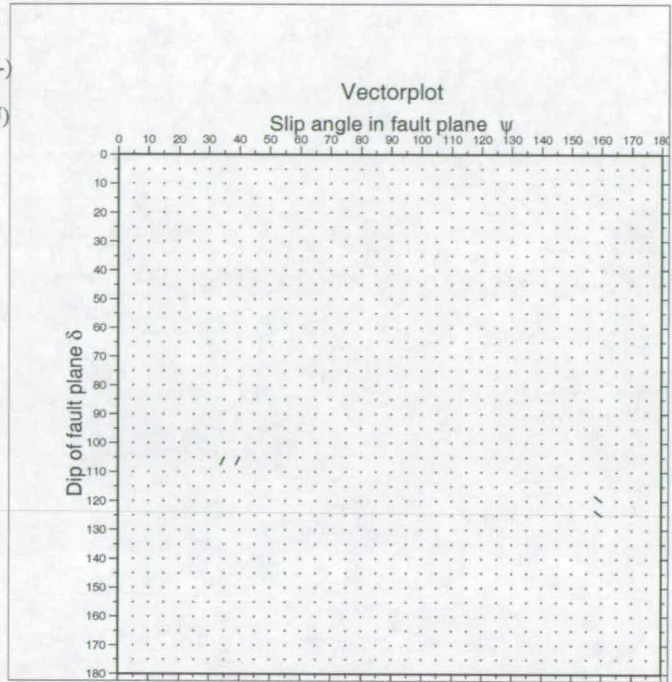
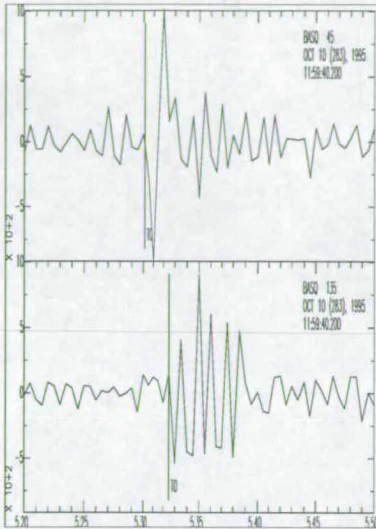


Figure D.2: Amplitude bounds, vectorplot and seismograms used to calculate the focal mechanism of the event of 10th October, 1995, at 11h56min.

Amplitudes

Method 1	Method 2
X: 40 to 100 (-)	X: 40 to 100 (-)
Y: 20 to 64 (+)	Y: 0 to 8 (U)

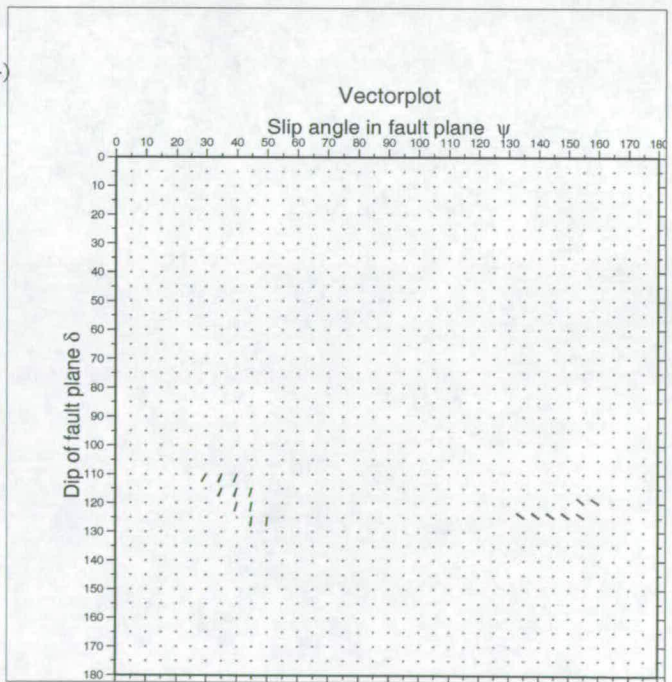
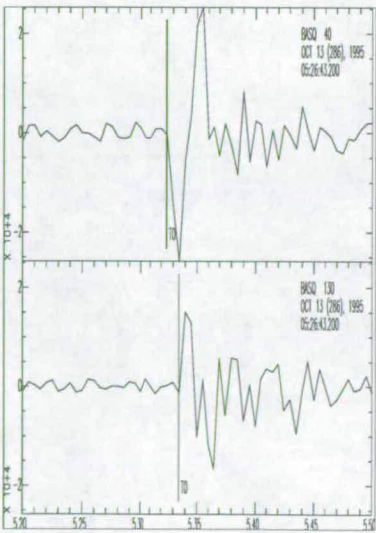


Figure D.3: Amplitude bounds, vectorplot and seismograms used to calculate the focal mechanism of the event of 13th October, 1995, at 05h26min.

Amplitudes

Method 1

Method 2

X: 40 to 100 (-)

X: 40 to 100 (-)

Y: 20 to 64 (+)

Y: 0 to 12 (U)

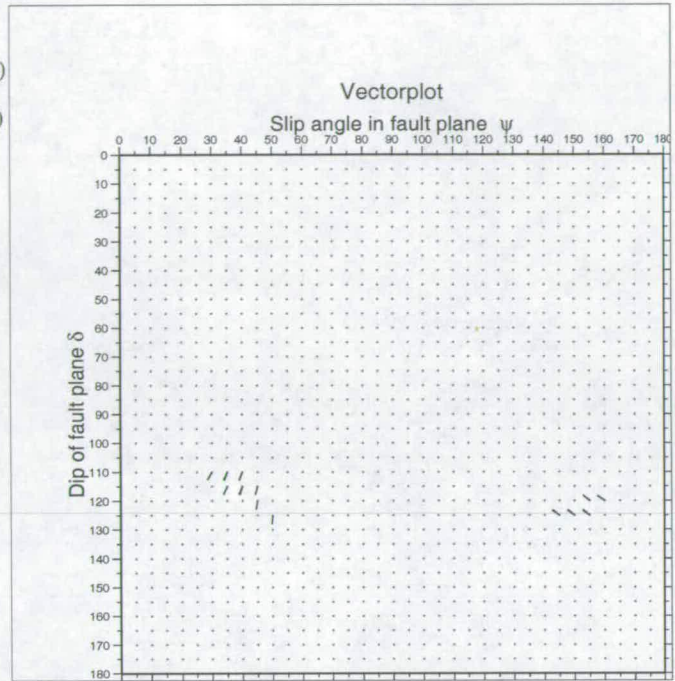
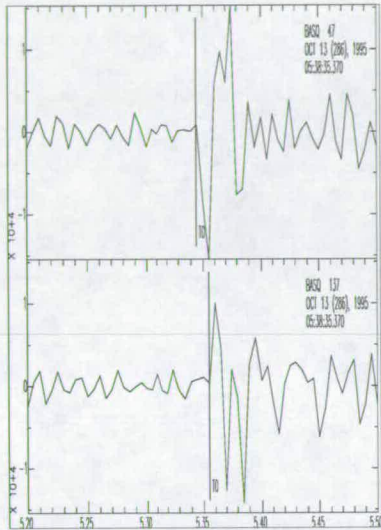


Figure D.4: Amplitude bounds, vectorplot and seismograms used to calculate the focal mechanism of the event of 13th October, 1995, at 05h38min.

Amplitudes

Method 1

Method 2

X: 40 to 100 (-)

X: 40 to 100 (-)

Y: 16 to 56 (-)

Y: 0 to 10 (U)

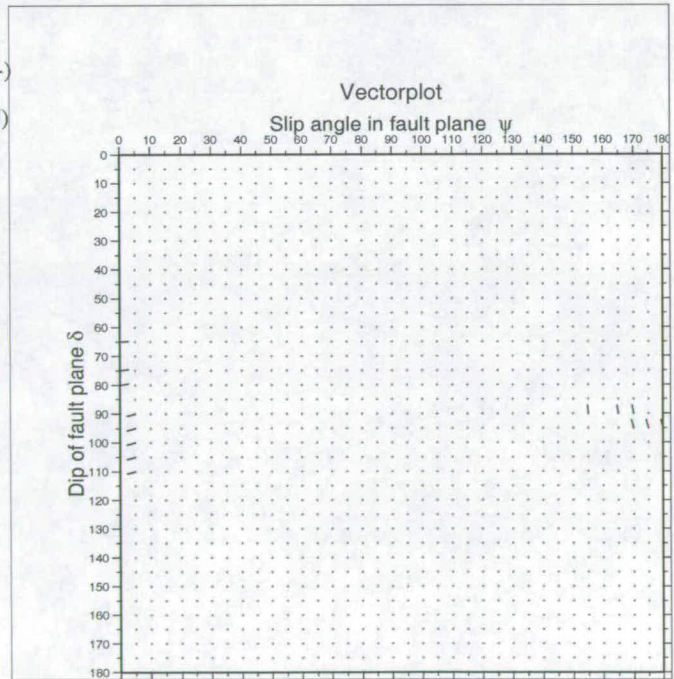
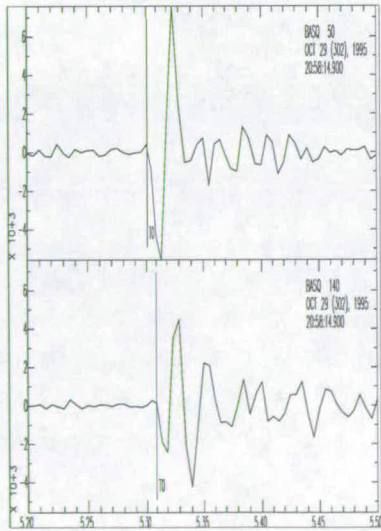


Figure D.5: Amplitude bounds, vectorplot and seismograms used to calculate the focal mechanism of the event of 29th October, 1995, at 20h58min.

Amplitudes

Method 1

Method 2

X: 47 to 100 (-)

X: 47 to 100 (-)

Y: 16 to 47 (-)

Y: 0 to 11 (U)

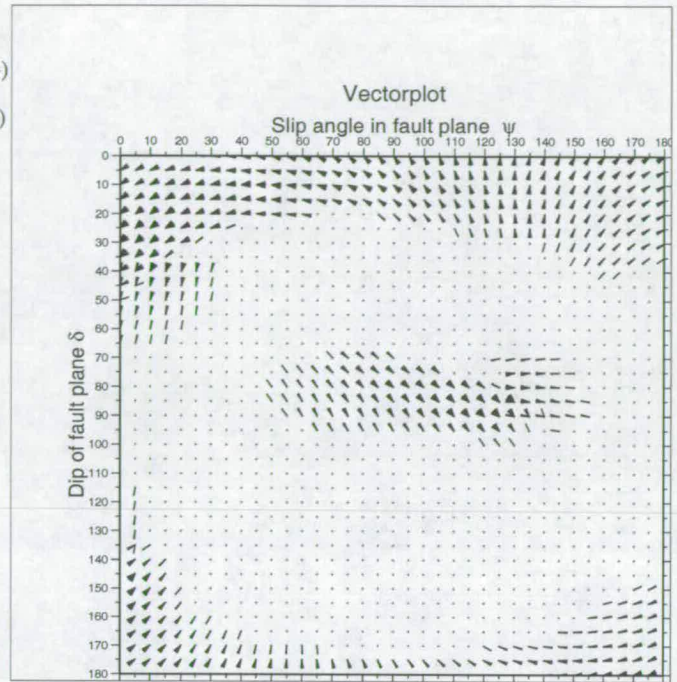
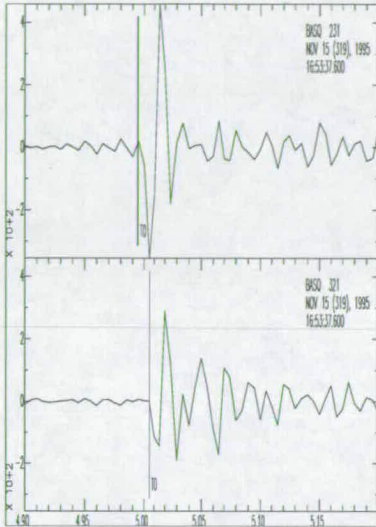


Figure D.6: Amplitude bounds, vectorplot and seismograms used to calculate the focal mechanism of the event of 15th November, 1995, at 16h53min.

Amplitudes

Method 1

Method 2

X: 10 to 33 (-)

X: 10 to 33 (-)

Y: 48 to 100 (+)

Y: 0 to 10 (U)

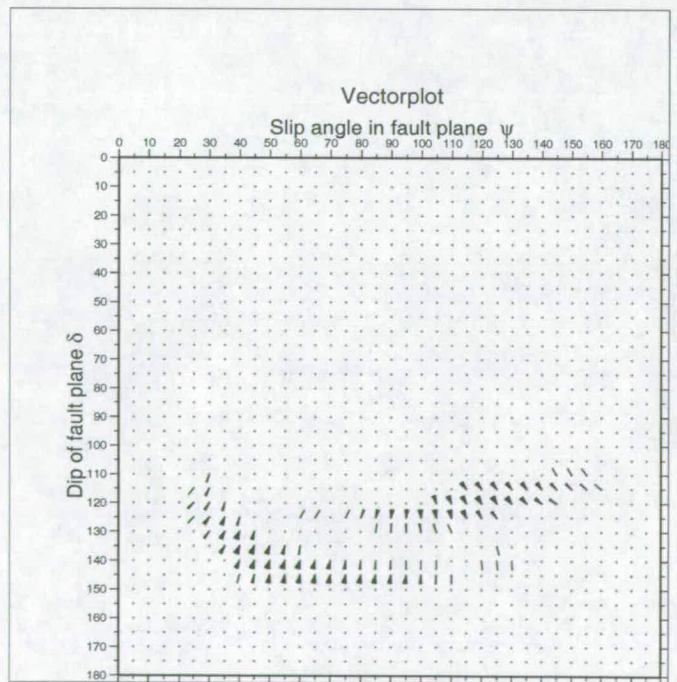
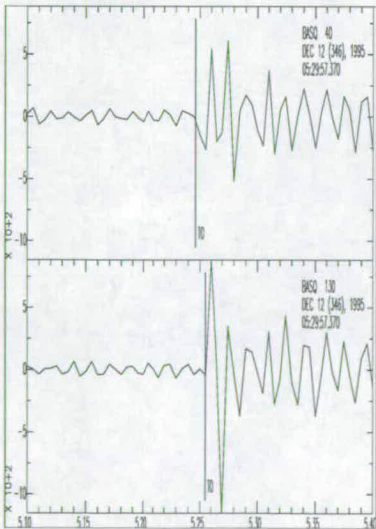


Figure D.7: Amplitude bounds, vectorplot and seismograms used to calculate the focal mechanism of the event of 12th December, 1995, at 05h29min.

Amplitudes

Method 1

X: 48 to 100 (-)

Y: 48 to 95 (+)

Method 2

X: 48 to 100 (-)

Y: 0 to 14 (U)

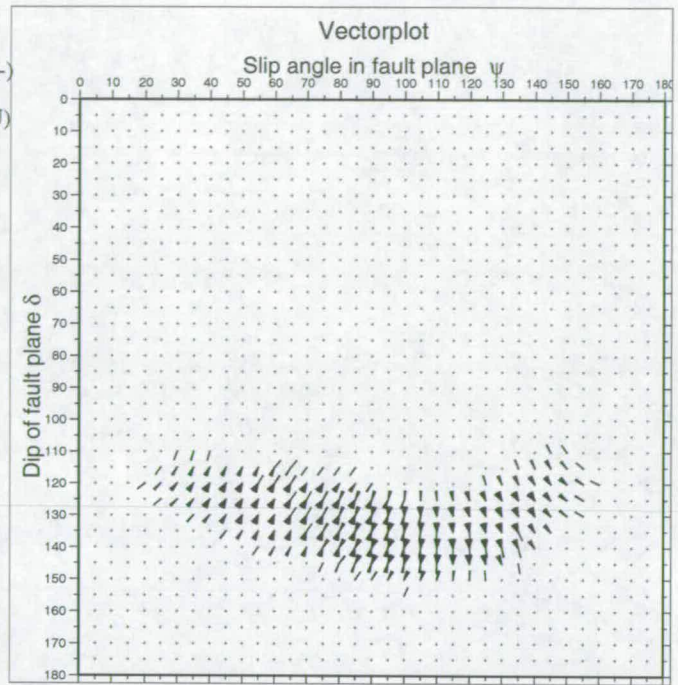
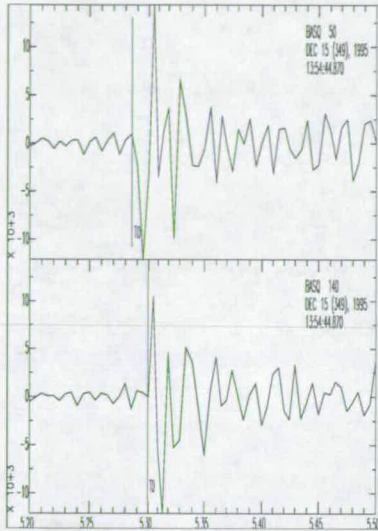


Figure D.8: Amplitude bounds, vectorplot and seismograms used to calculate the focal mechanism of the event of 15th December, 1995, at 13h54min.

Amplitudes

Method 1

X: 40 to 90 (-)

Y: 40 to 100 (+)

Method 2

X: 40 to 90 (-)

Y: 0 to 10 (U)

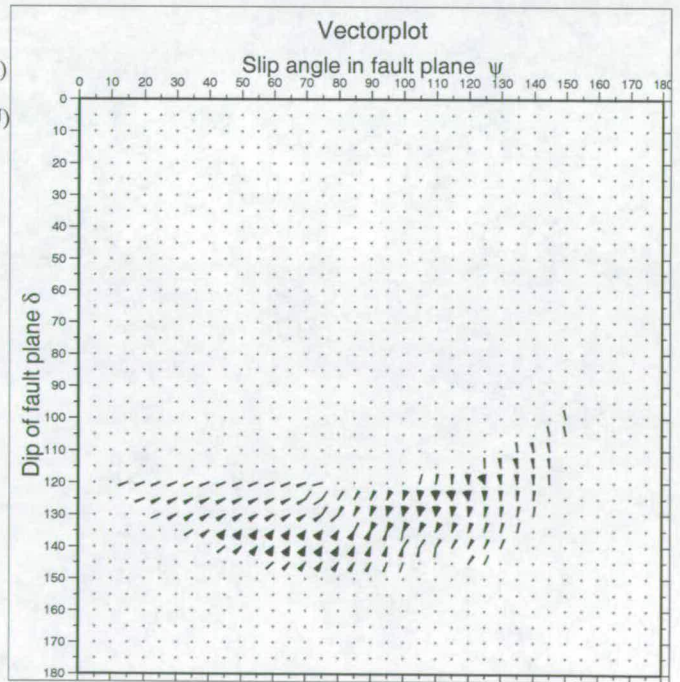
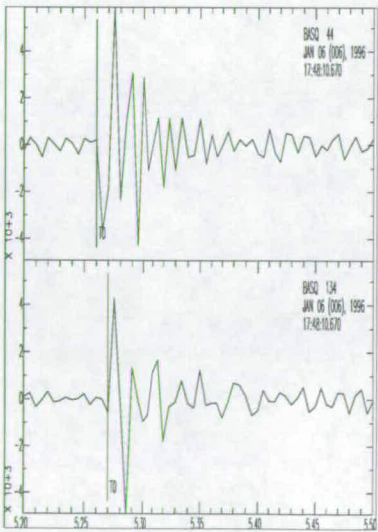


Figure D.9: Amplitude bounds, vectorplot and seismograms used to calculate the focal mechanism of the event of 6th January, 1996, at 17h48min.

Amplitudes

Method 1	Method 2
X: 28 to 100 (-)	X: 28 to 100 (-)
Y: 17 to 56 (-)	Y: 0 to 17 (U)

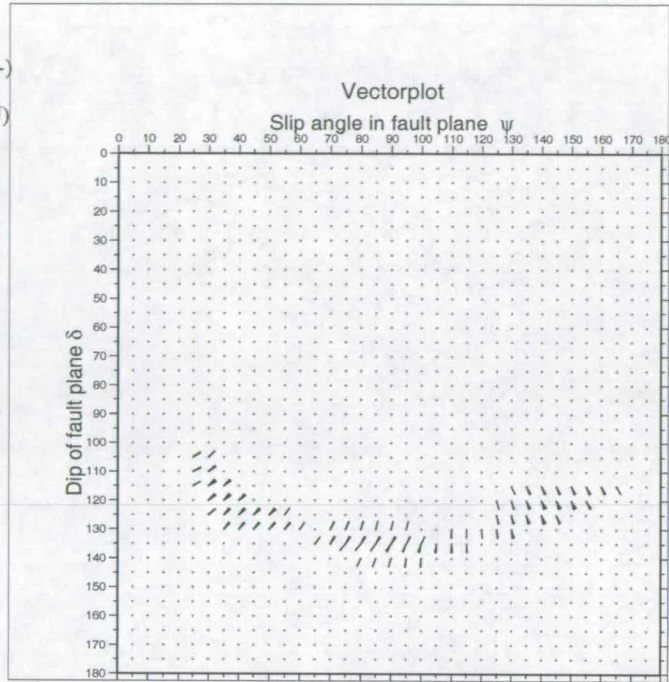
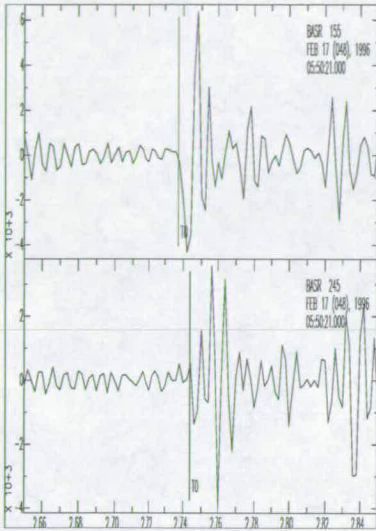


Figure D.10: Amplitude bounds, vectorplot and seismograms used to calculate the focal mechanism of the event of 17th February, 1996, at 05h20min.

Amplitudes

Method 1	Method 2
X: 30 to 90 (-)	X: 30 to 90 (-)
Y: 40 to 100 (-)	Y: 0 to 30 (U)

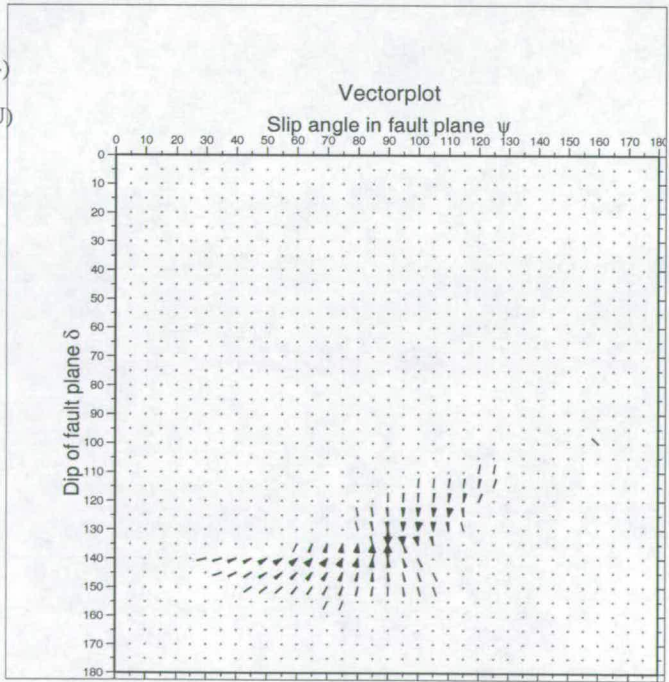
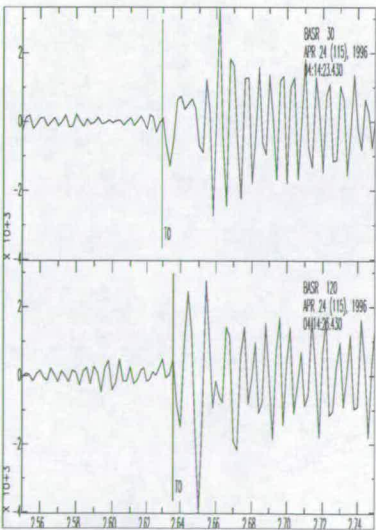


Figure D.11: Amplitude bounds, vectorplot and seismograms used to calculate the focal mechanism of the event of 24th April, 1996, at 04h14min.

E HETEROGENEOUS FAULT TRANSMISSIVITY FIELDS

E.1 Correlation length of 166.67m and variance of 0.25

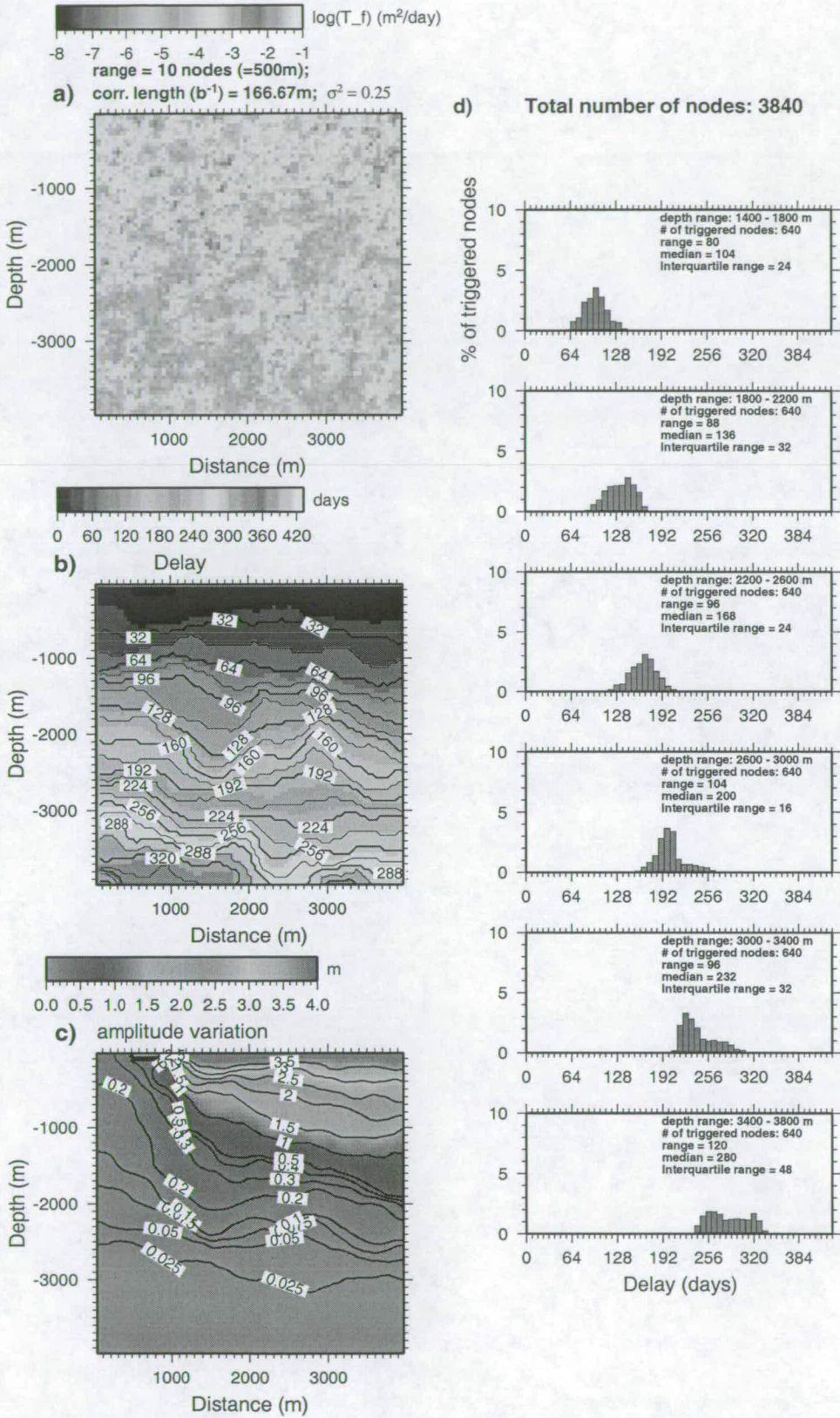


Figure E.1: Single realisation of a random correlated field with $b^{-1} = 166.67m$ and $\sigma^2=0.25$.

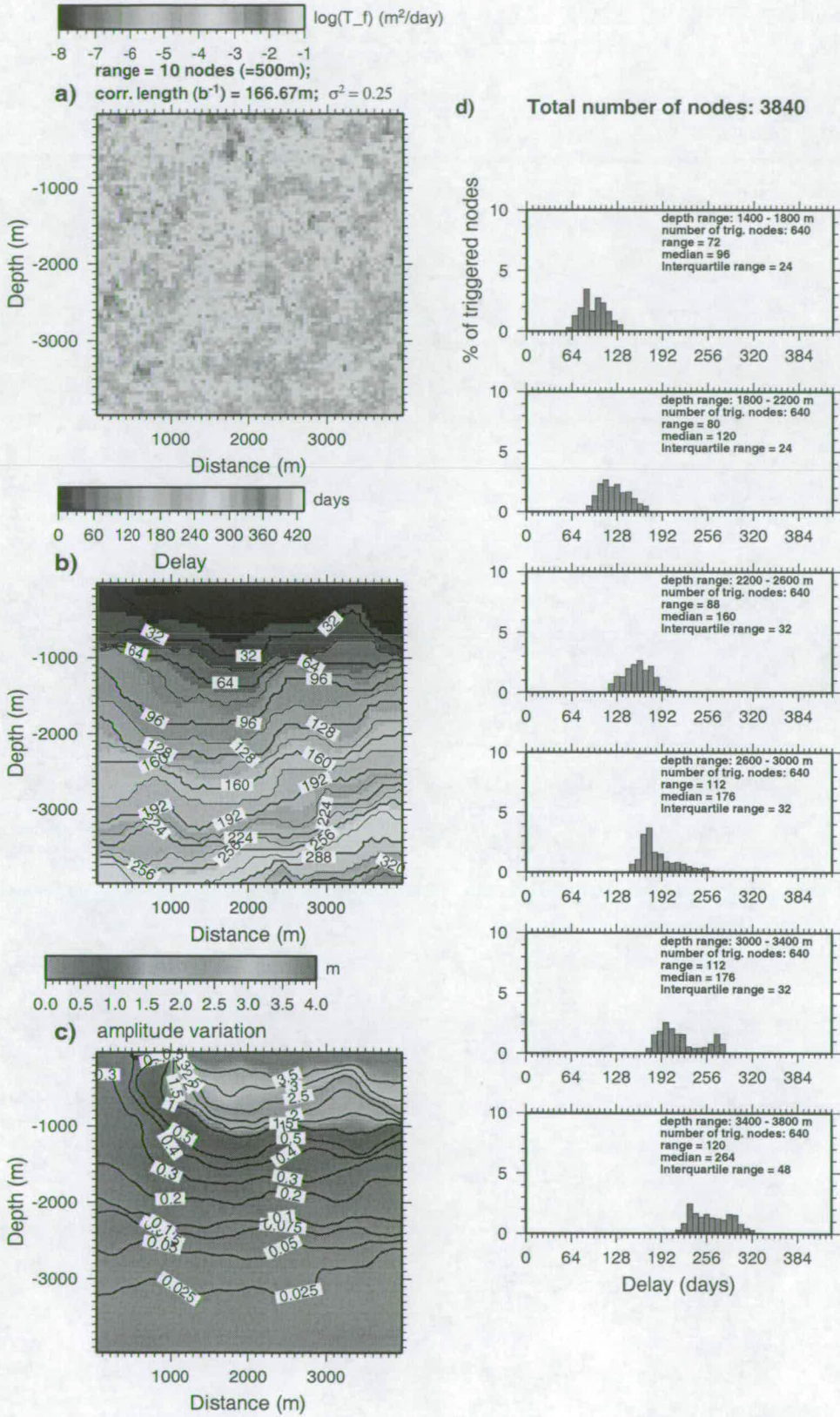


Figure E.2: Single realisation of a random correlated field with $b^{-1} = 166.67m$ and $\sigma^2=0.25$.

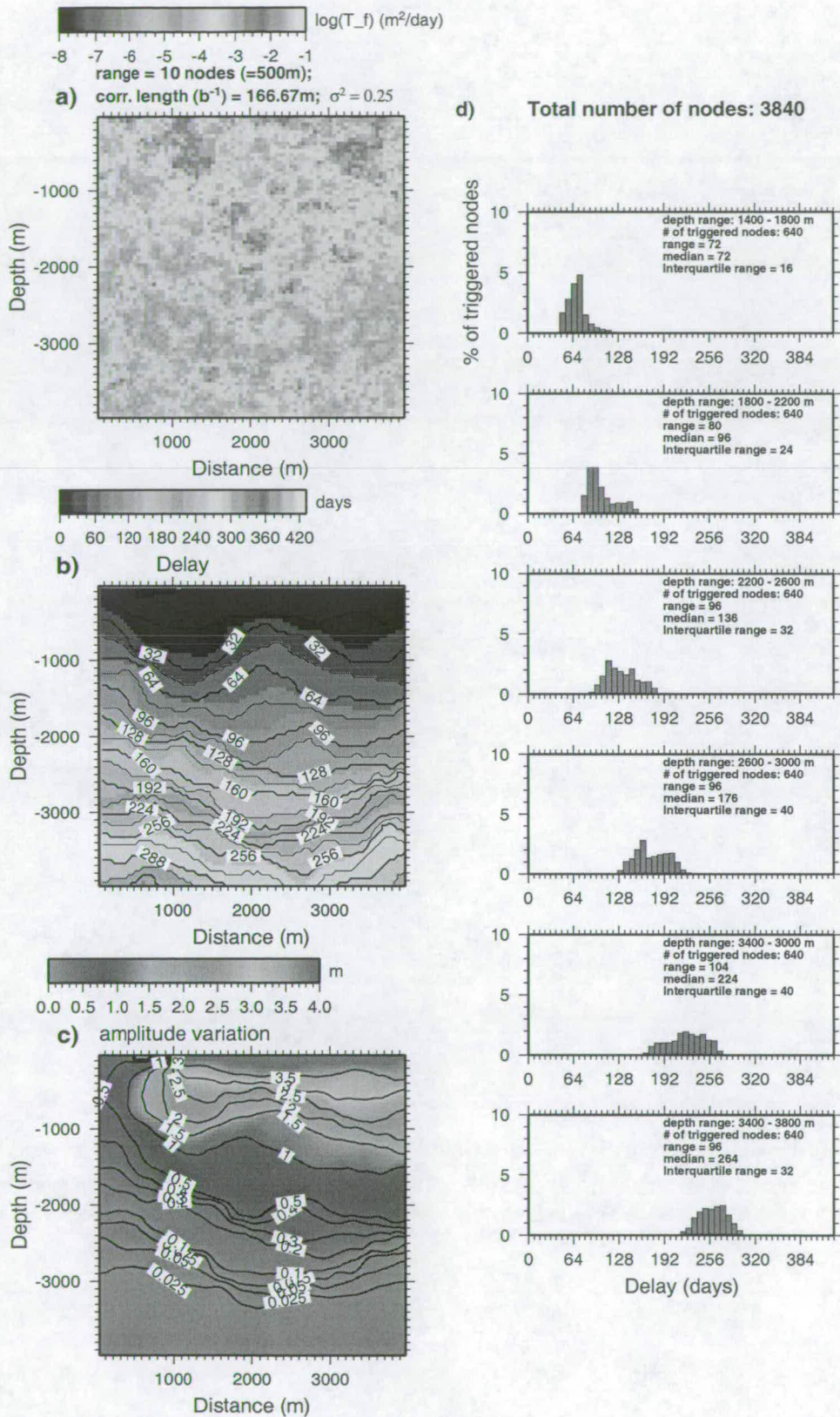


Figure E.3: Single realisation of a random correlated field with $b^{-1} = 166.67m$ and $\sigma^2=0.25$.

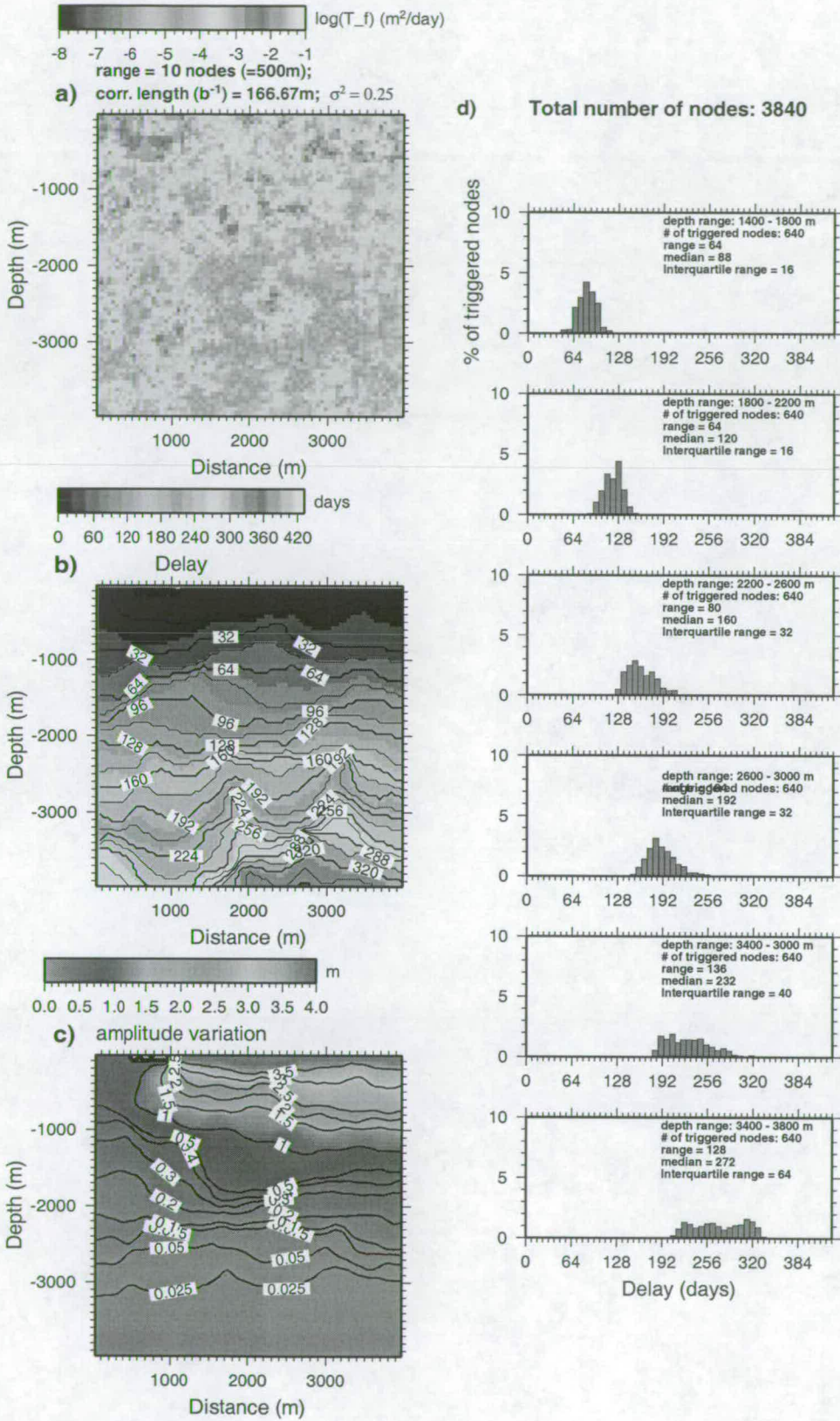


Figure E.4: Single realization of a random correlated field with $b^{-1} = 166.67m$ and $\sigma^2 = 0.25$.

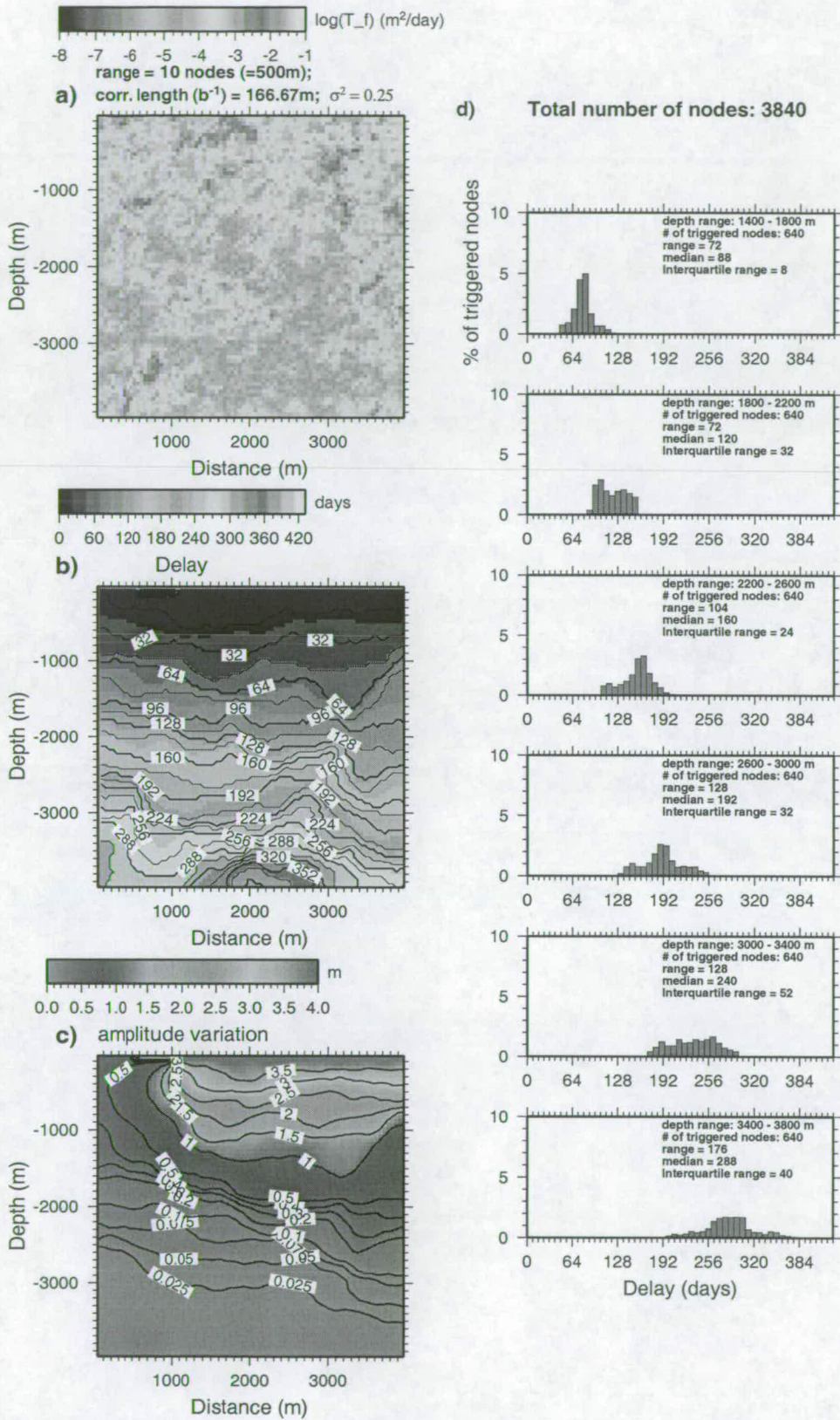


Figure E.5: Single realisation of a random correlated field with $b^{-1} = 166.67m$ and $\sigma^2 = 0.25$.

E.2 Correlation length of 166.67m and variance of 0.50

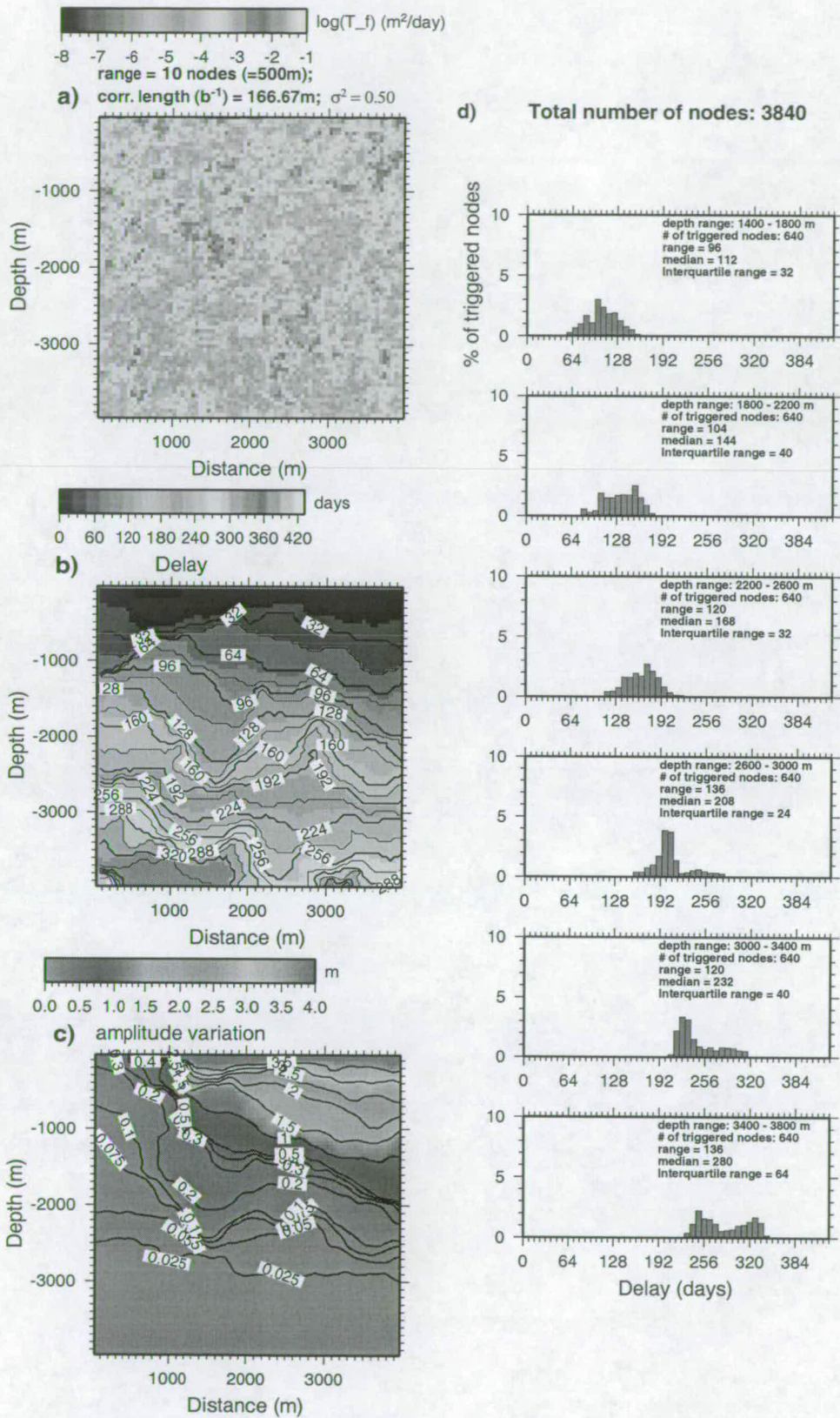


Figure E.6: Single realisation of a random correlated field with $b^{-1} = 166.67m$ and $\sigma^2 = 0.50$.

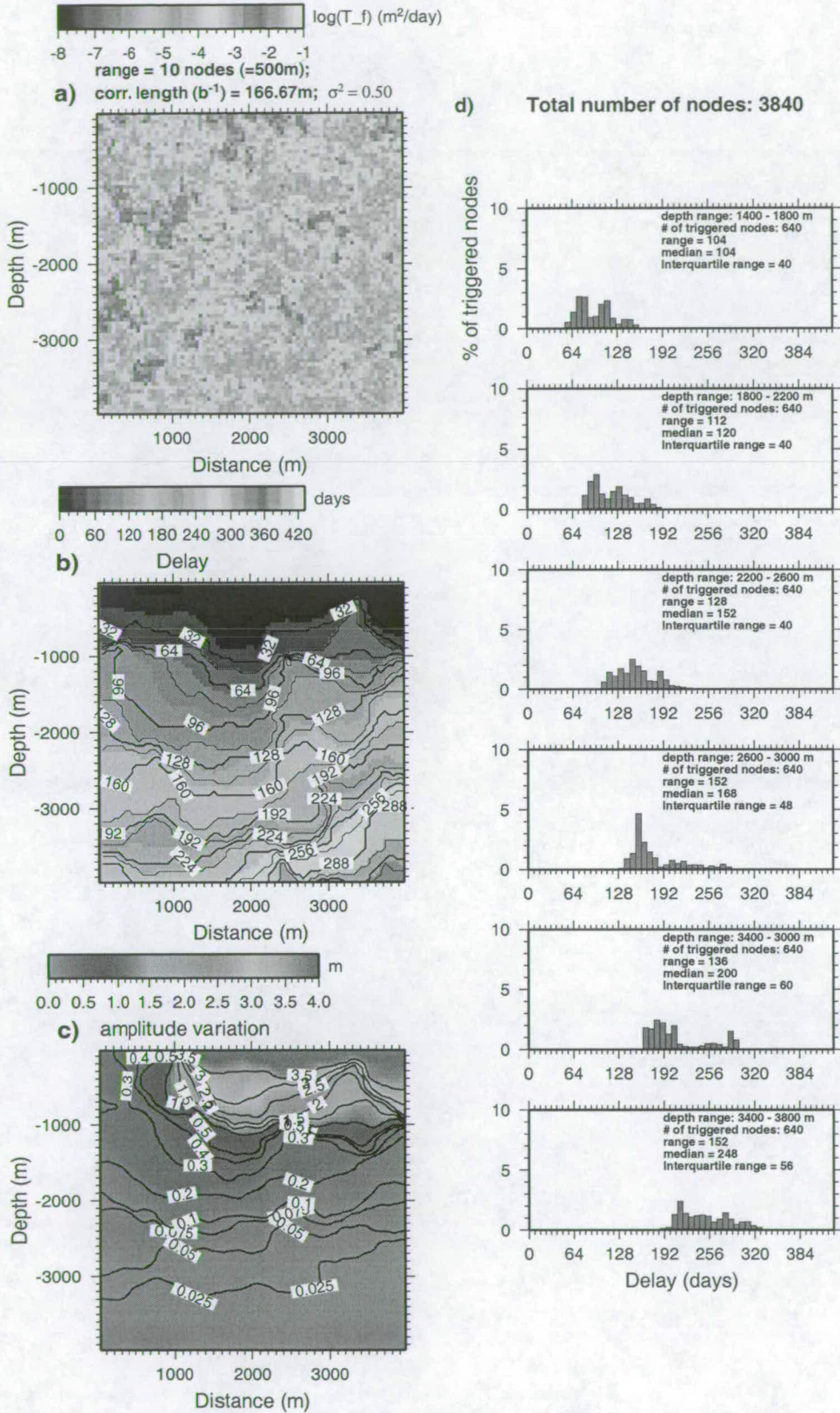


Figure E.7: Single realisation of a random correlated field with $b^{-1} = 166.67m$ and $\sigma^2=0.50$.

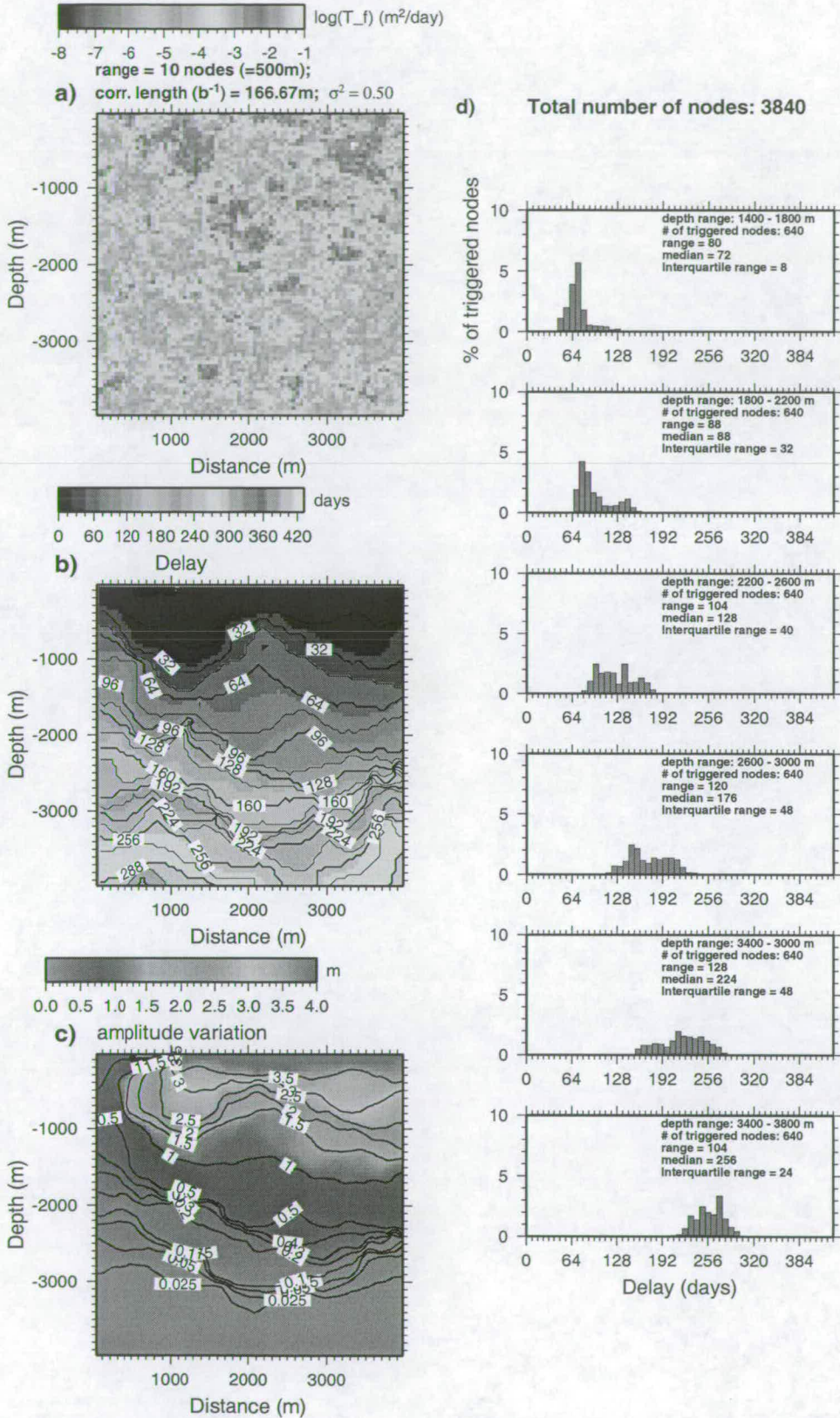


Figure E.8: Single realisation of a random correlated field with $b^{-1} = 166.67m$ and $\sigma^2=0.50$.

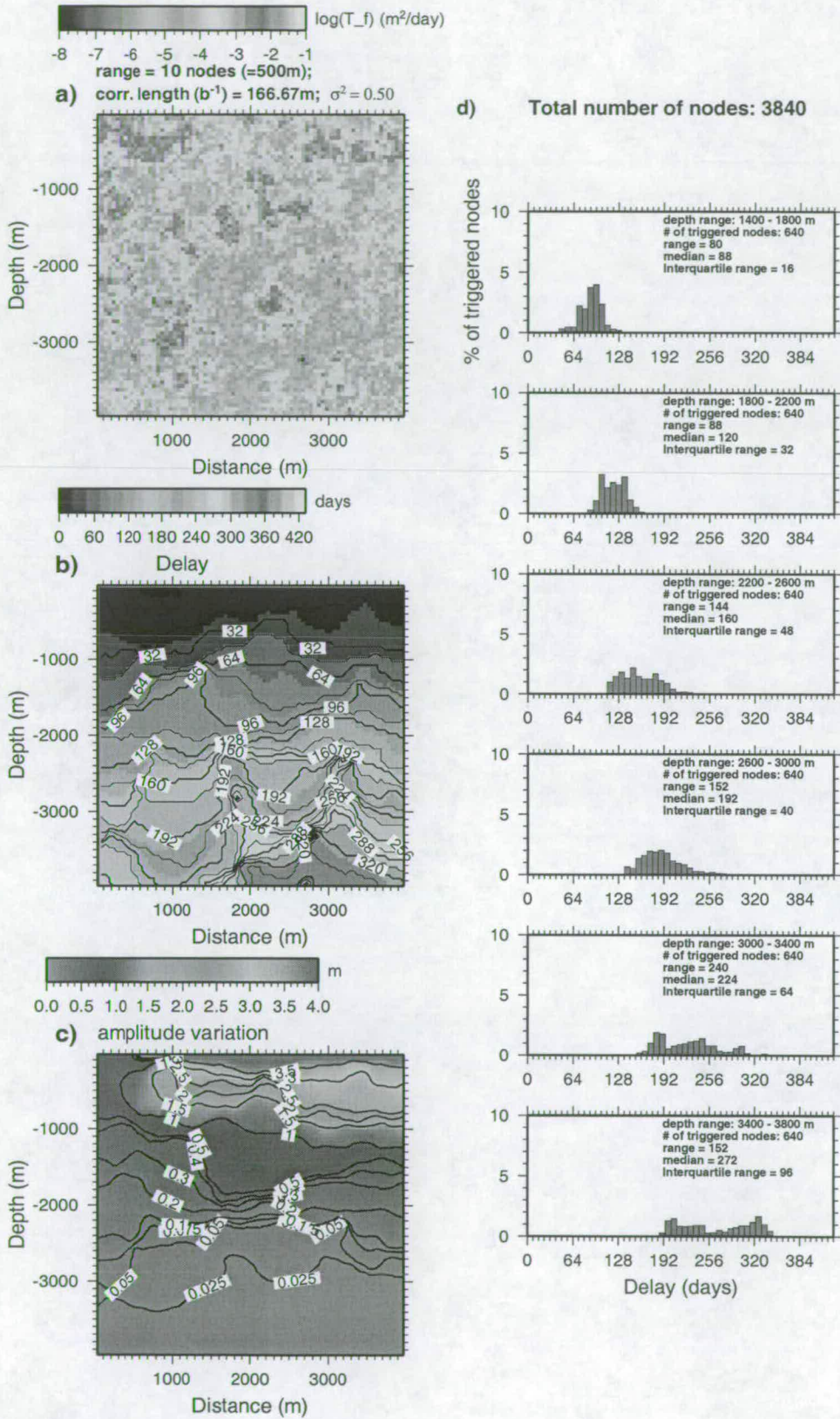


Figure E.9: Single realisation of a random correlated field with $b^{-1} = 166.67m$ and $\sigma^2=0.50$.

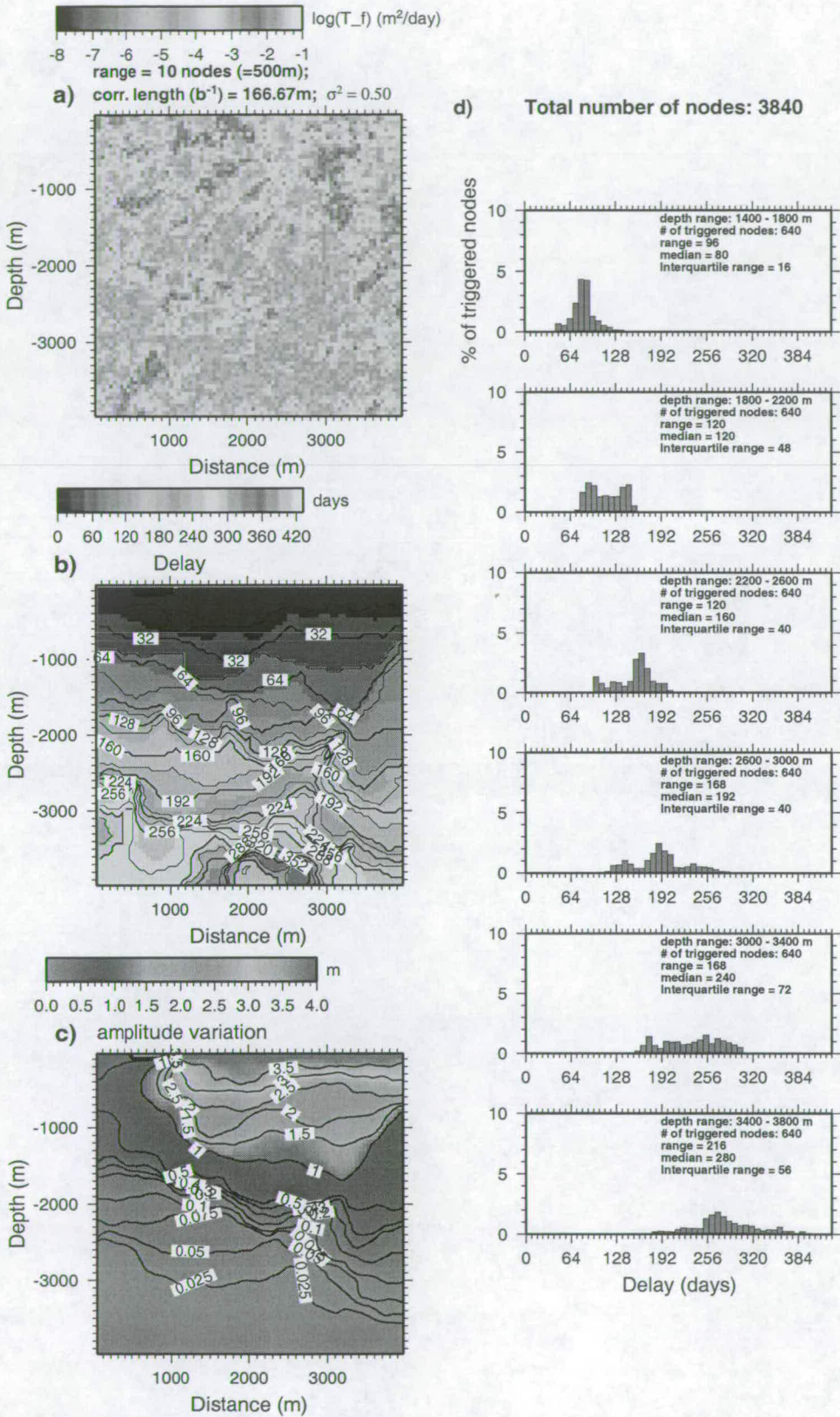


Figure E.10: Single realisation of a random correlated field with $b^{-1} = 166.67m$ and $\sigma^2 = 0.50$.

E.3 Correlation length of 500m and variance of 0.25

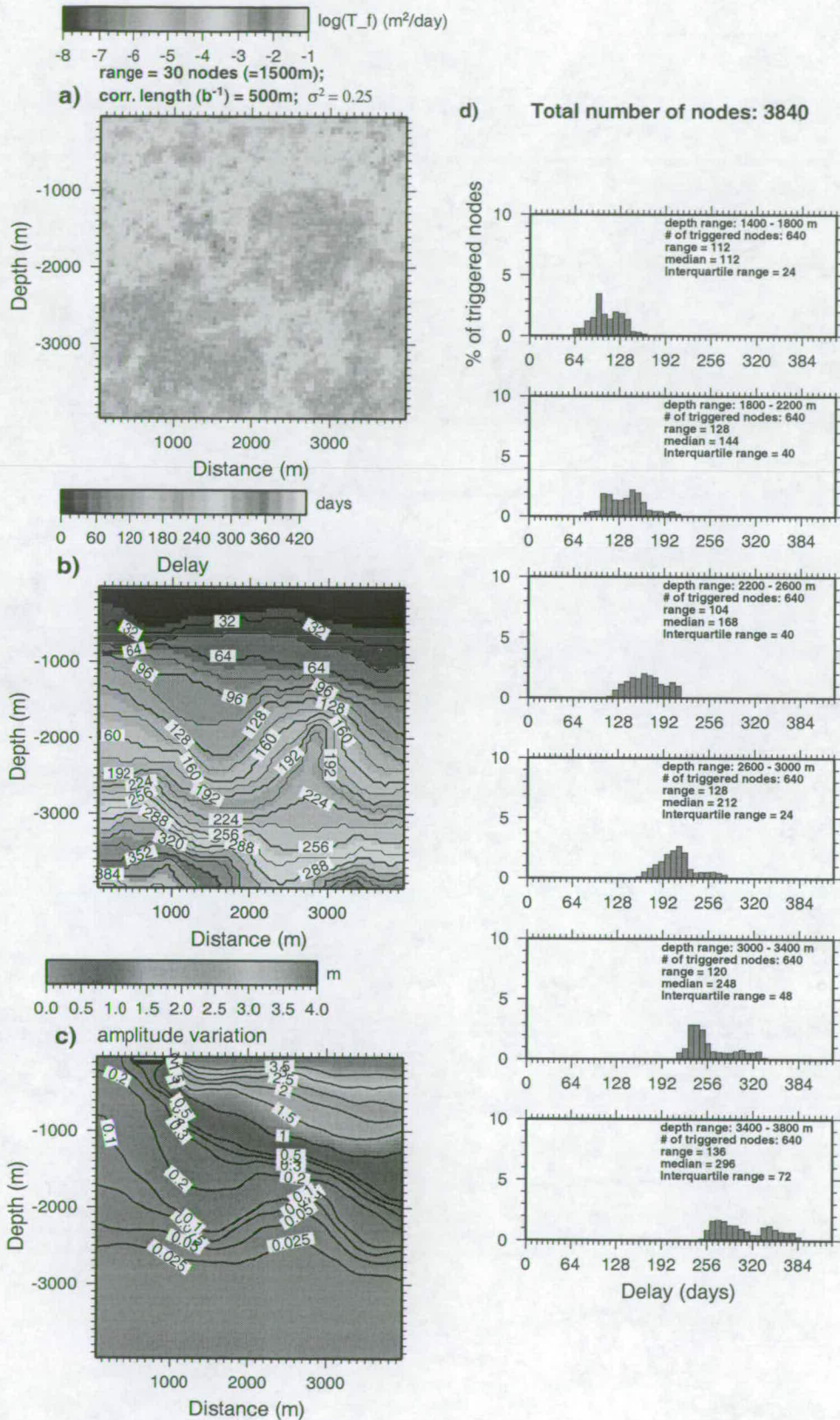


Figure E.11: Single realisation of a random correlated field with $b^{-1} = 500m$ and $\sigma^2 = 0.25$.

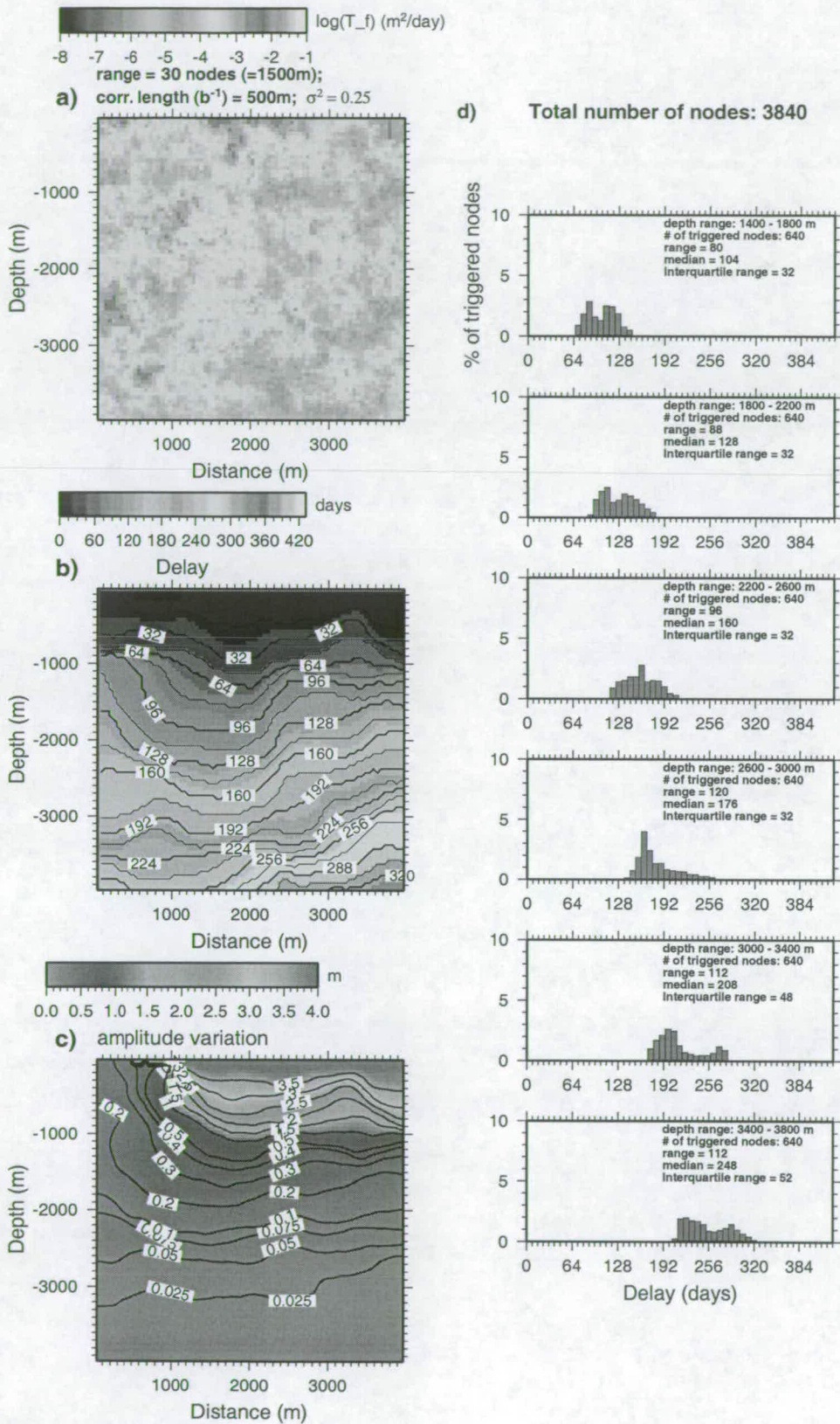


Figure E.12: Single realisation of a random correlated field with $b^{-1} = 500m$ and $\sigma^2 = 0.25$.

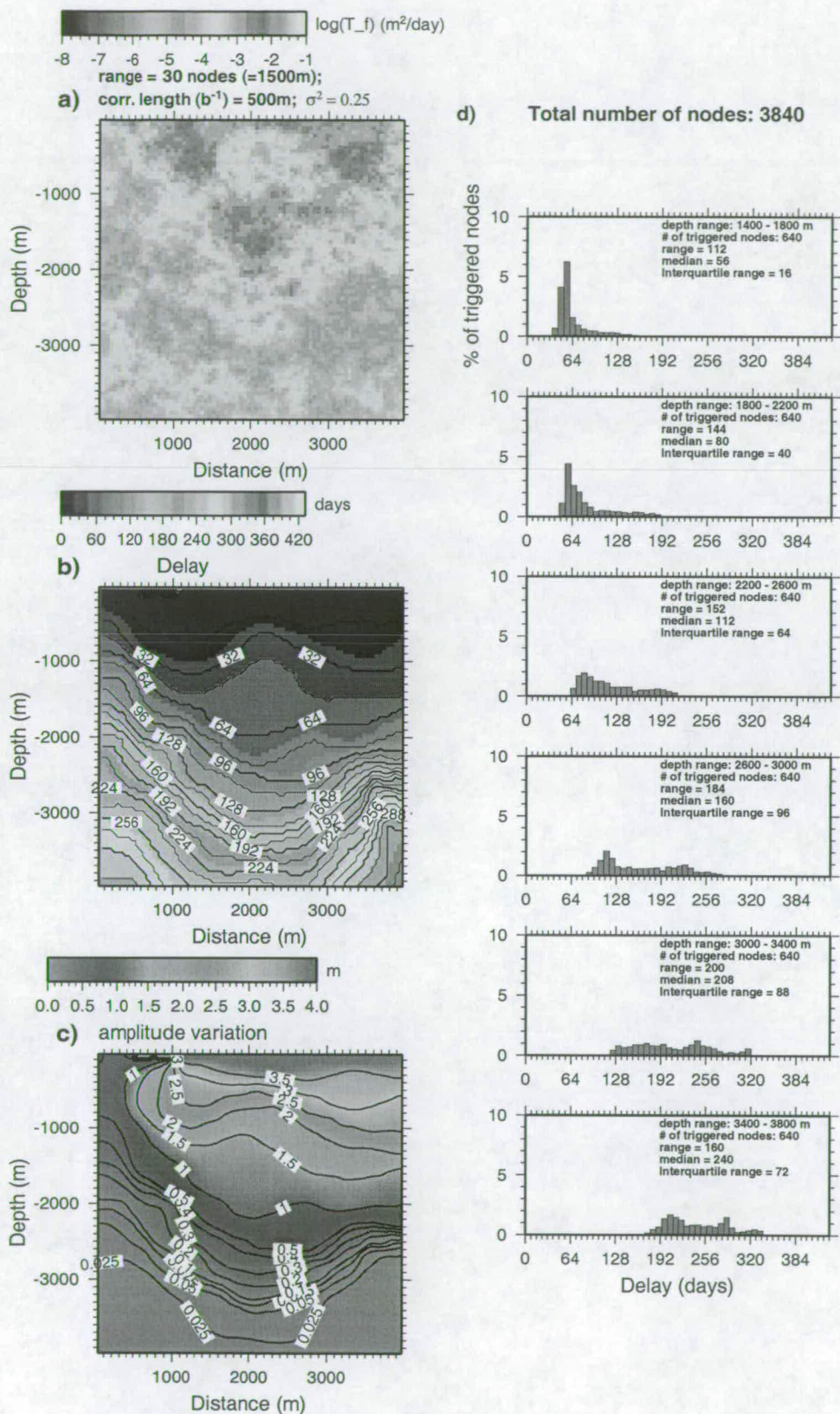


Figure E.13: Single realisation of a random correlated field with $b^{-1} = 500m$ and $\sigma^2 = 0.25$.

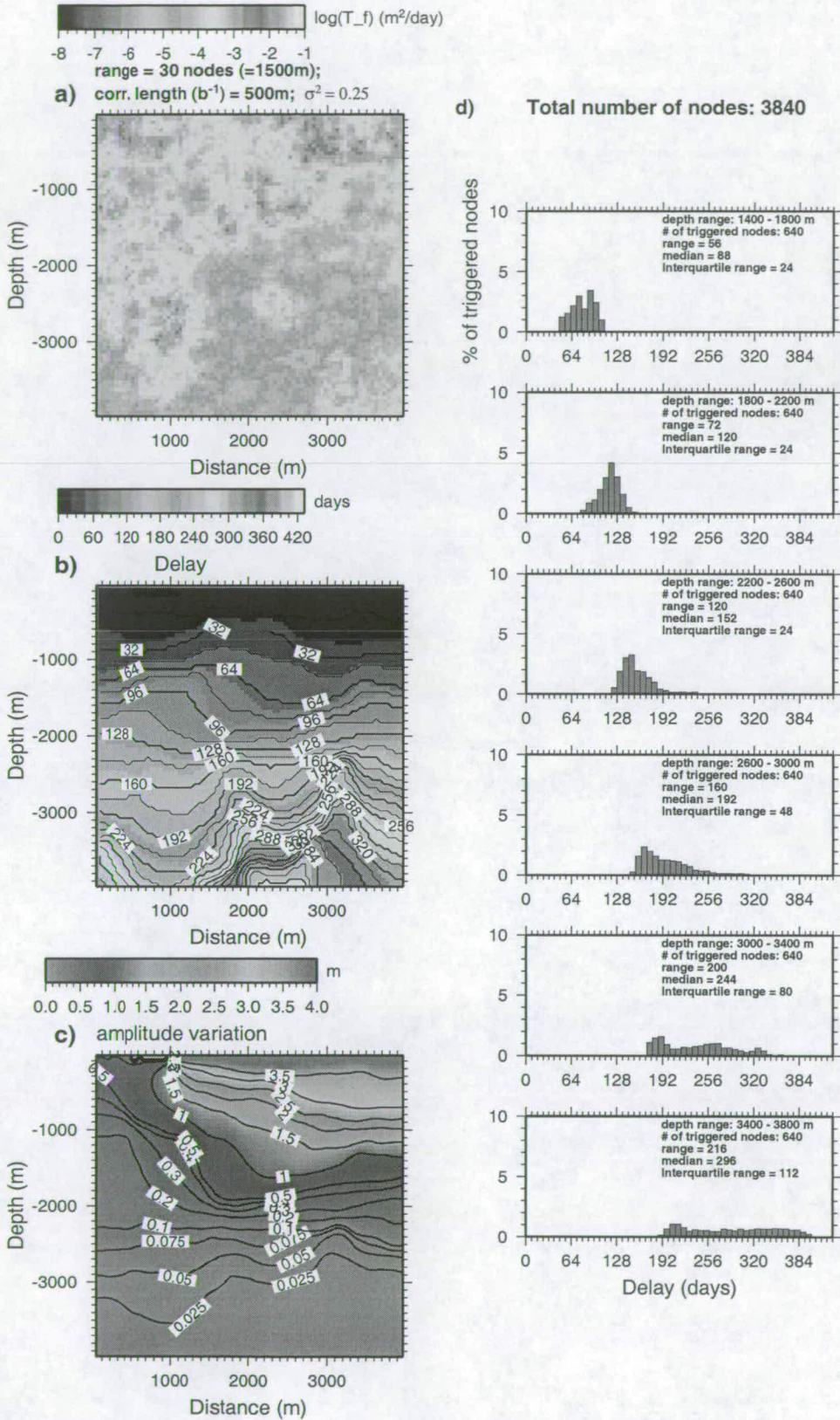


Figure E.14: Single realization of a random correlated field with $b^{-1} = 500m$ and $\sigma^2 = 0.25$.

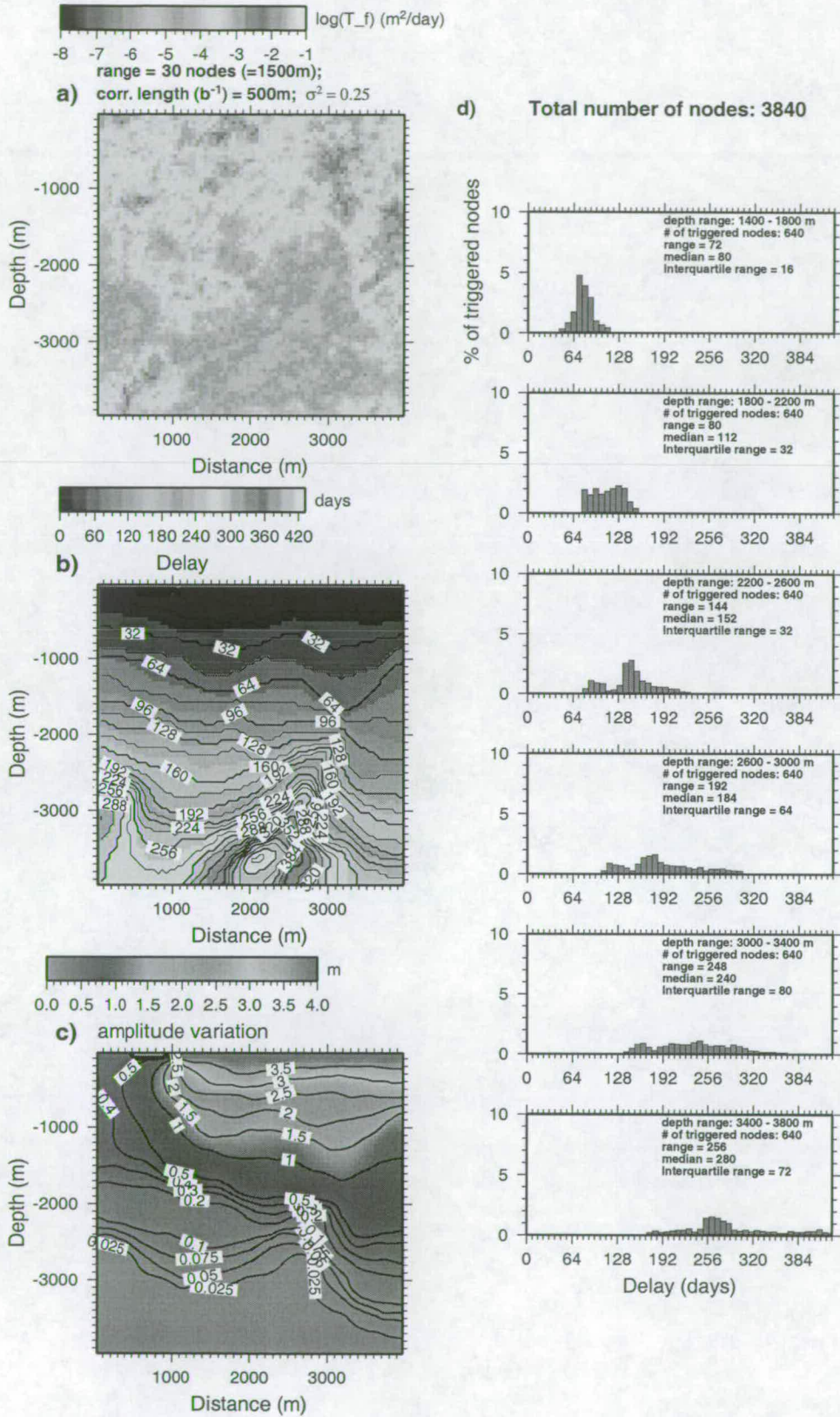


Figure E.15: Single realisation of a random correlated field with $b^{-1} = 500m$ and $\sigma^2=0.25$.

E.4 Correlation length of 500m and variance of 0.50

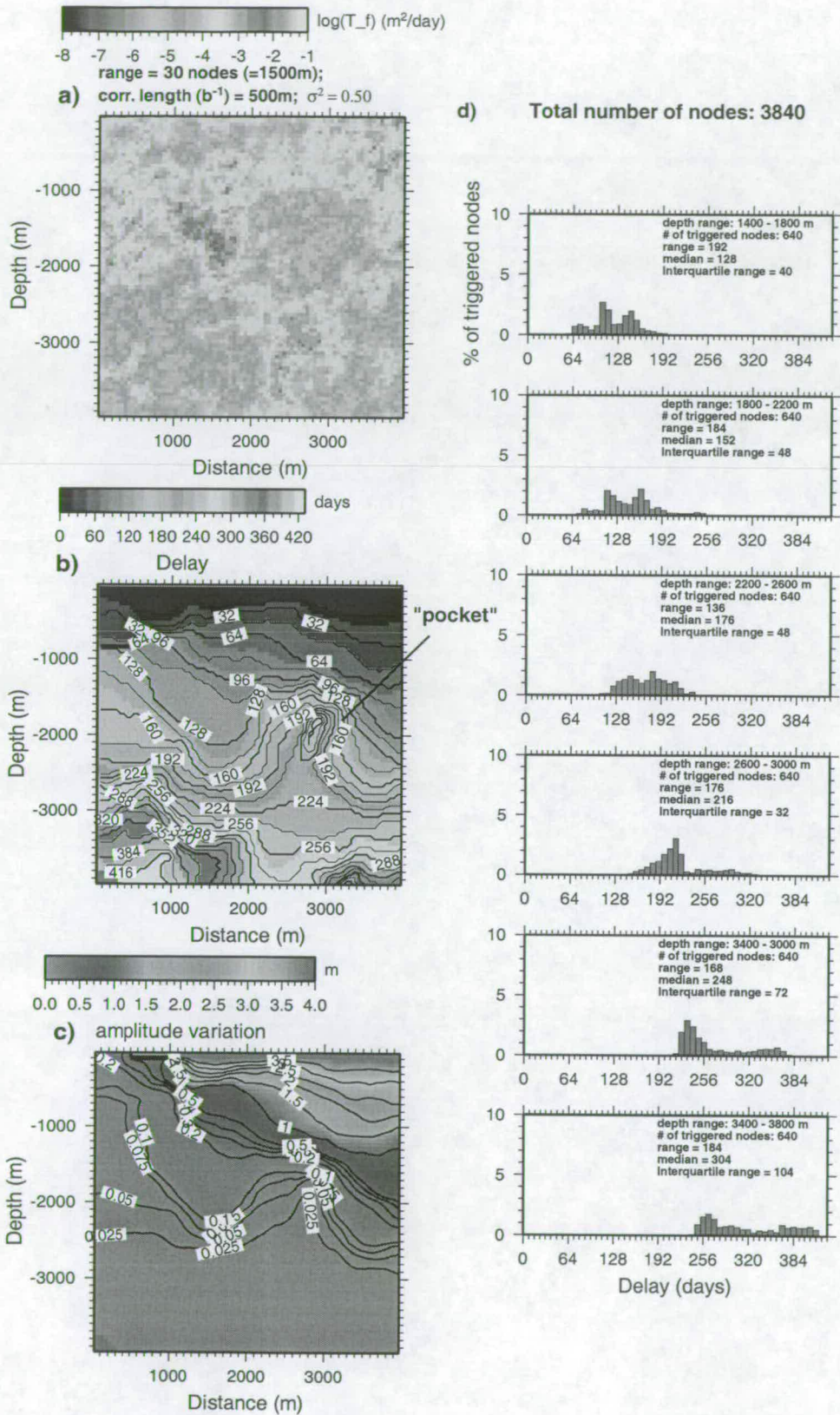


Figure E.16: Single realisation of a random correlated field with $b^{-1} = 500m$ and $\sigma^2=0.50$.

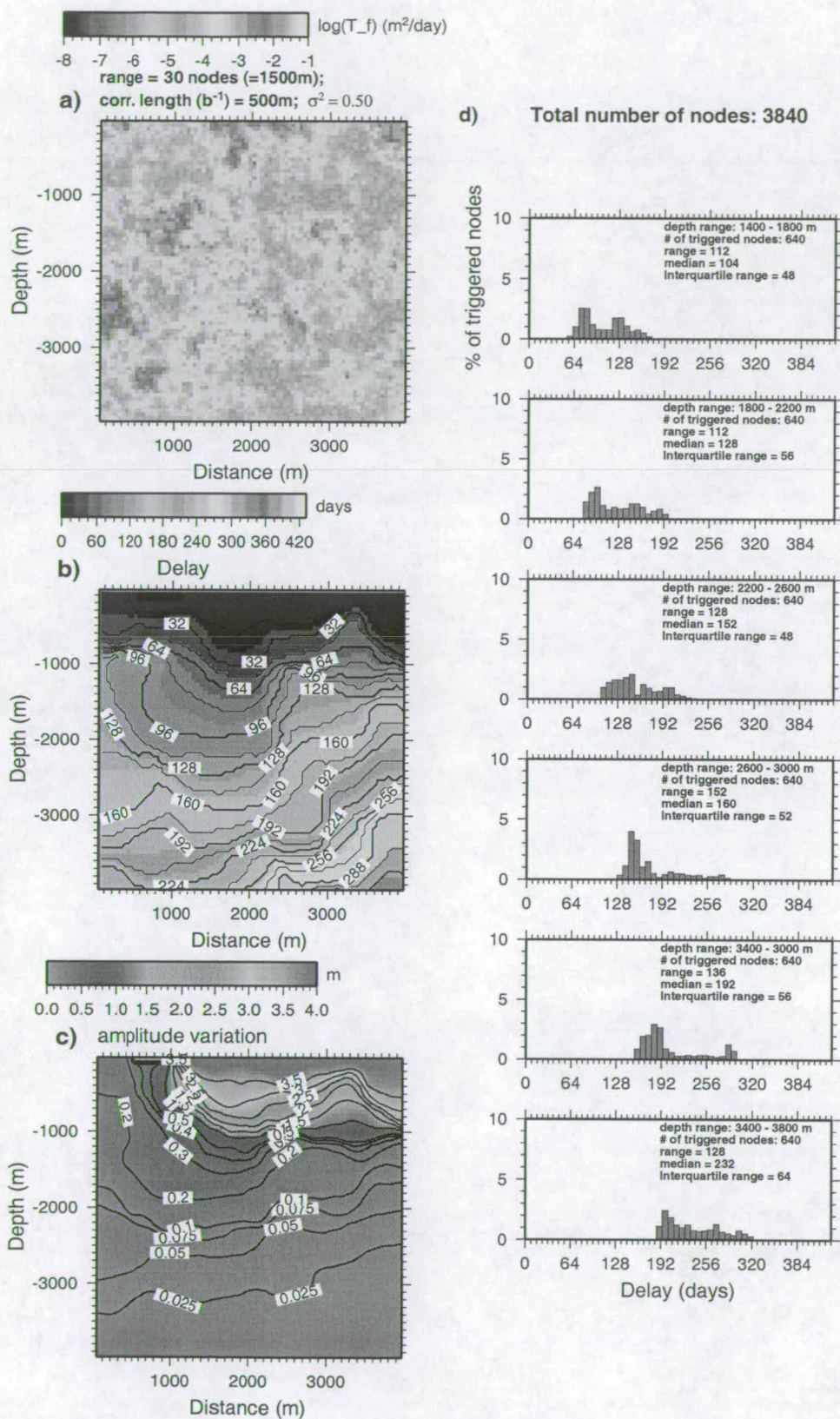


Figure E.17: Single realization of a random correlated field with $b^{-1} = 500m$ and $\sigma^2 = 0.50$.

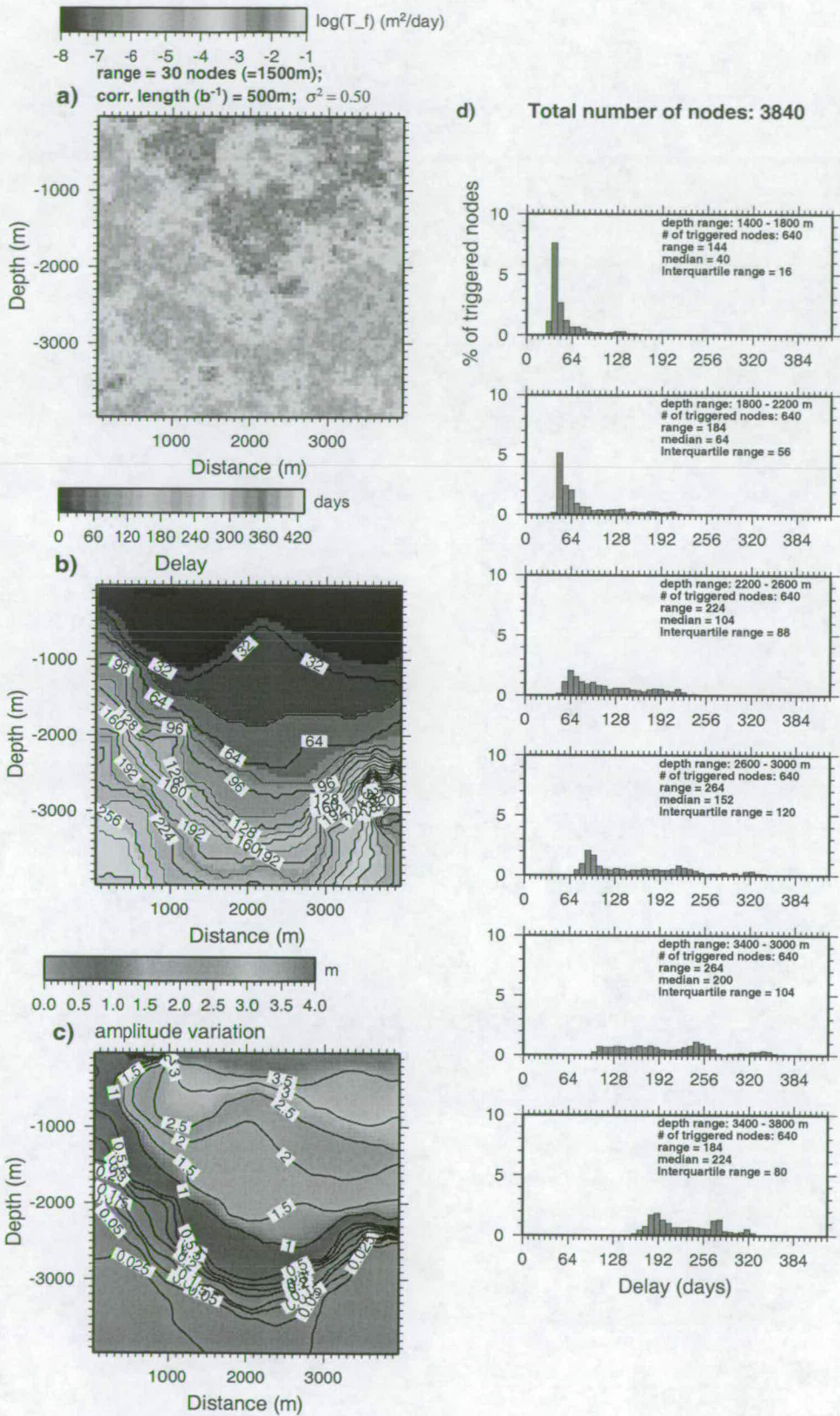


Figure E.18: Single realization of a random correlated field with $b^{-1} = 500m$ and $\sigma^2 = 0.50$.

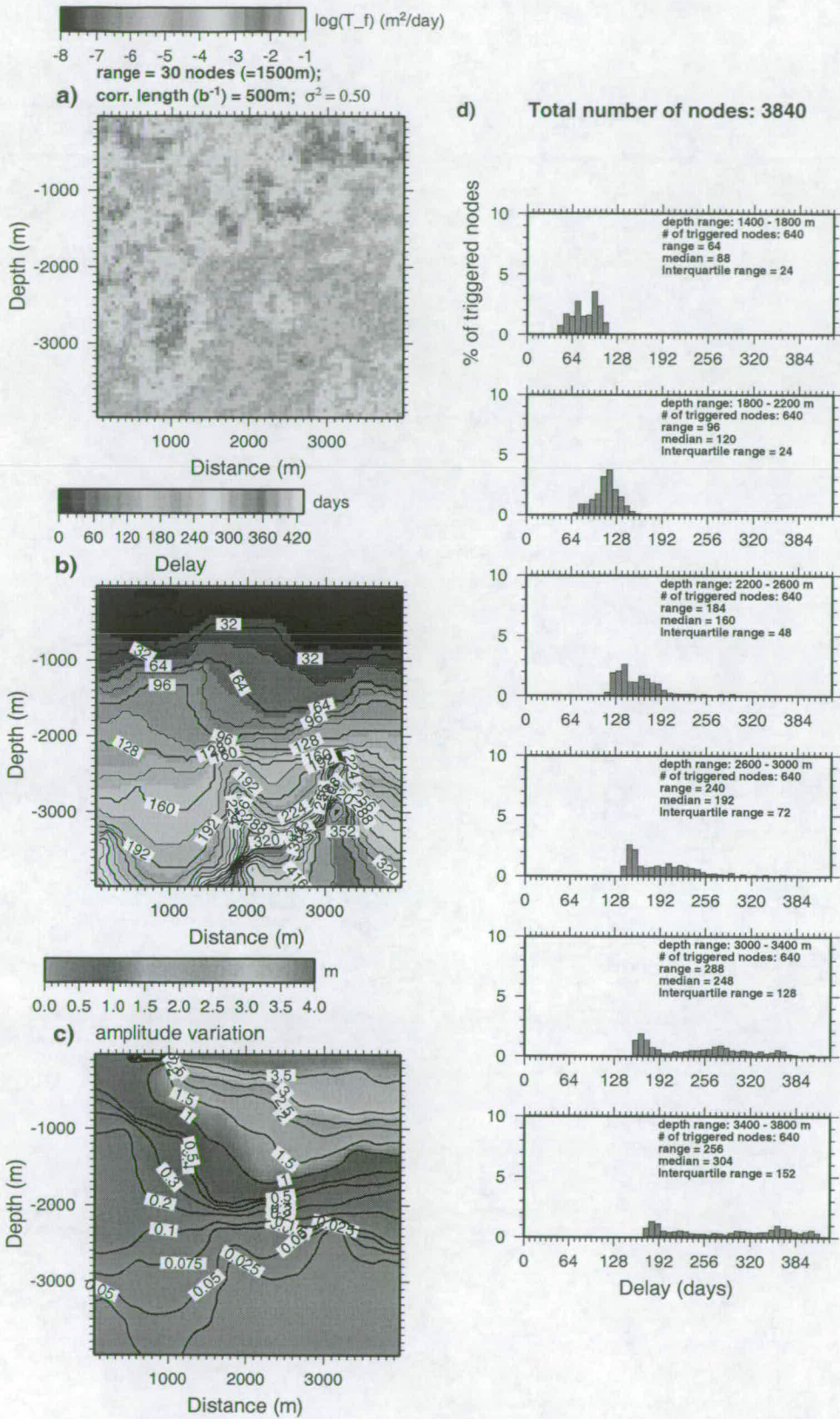


Figure E.19: Single realisation of a random correlated field with $b^{-1} = 500m$ and $\sigma^2 = 0.50$.

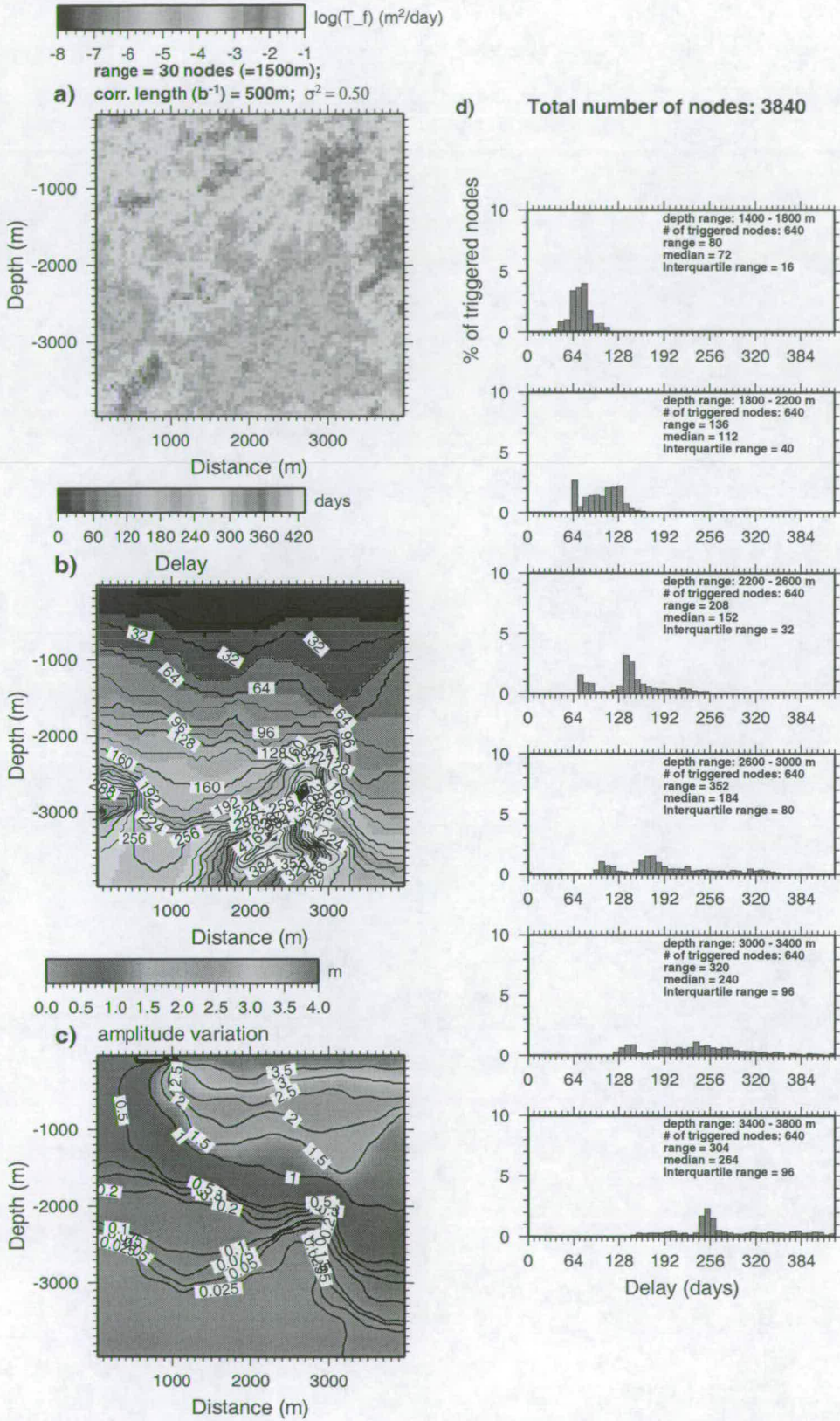


Figure E.20: Single realisation of a random correlated field with $b^{-1} = 500m$ and $\sigma^2 = 0.50$.

F PREPRINT OF DO NASCIMENTO *et al.* (2002)

In this appendix I present the article accepted for publication in the *Journal of Geophysical Research*. The work for this publication was done simultaneously with the PDAS data analysis presented in Chapter 3. The results of this article supports important conclusions about the seismic anisotropy in the Açú reservoir.

The work in this article aims exclusively to investigate seismic anisotropy in a different area in NE Brazil, and not reservoir-induced seismicity. Therefore, I have decided to include it as an Appendix and not as a Chapter of this thesis.

Local shear-wave observations in João Câmara, NE Brazil

A. F. do Nascimento

Department of Geology and Geophysics, The University of Edinburgh, UK¹

R. G. Pearce

Department of Geology and Geophysics, The University of Edinburgh, UK

M. K. Takeya

Departamento de Física Teórica e Experimental, Universidade Federal do Rio Grande do Norte, Brazil

Abstract. We present shear-wave splitting data from a 10 km aperture, 8-station digital three-component seismograph network which operated from December 1992 until August 1994 near João Câmara (5°33'S, 35°51'W), to record shear-waves from continuing microearthquake activity persisting six years after a mainshock in November 1986. Previous aftershock recording had shown remarkably impulsive simple seismograms and hypocentral errors of typically 200m in a structure of near-uniform wave speed, but only one station was three-component. The data reported here show consistent near-north-south polarisation directions for the fast split shear-wave in the north of the network, changing towards a NE-SW orientation at the southernmost stations. Results from the single three-component station in the previous network are also consistent. This pattern of polarisation directions is shown to be consistent with the trend of Precambrian foliation observed in the field. It is therefore concluded that these shear-wave observations are controlled by the seismic anisotropy associated with the Precambrian foliation, and hence bear the signature of the "palaeo-stress field", i.e., the Precambrian deformation regime. This conclusion has important implications for the interpretation of shear-wave splitting observations made in crustal crystalline rock, because other authors have asserted that shear-wave splitting normally results from the effect of stress-aligned fluid-filled cracks (extensive dilatancy anisotropy or EDA). EDA is, by contrast, a signature of the present-day stress field. In this region there is firm evidence that the present-day maximum compressive stress is east-west. This evidence comes from earthquake focal mechanisms and borehole break-out data and is summarised in the World Stress Map. We therefore conclude our present data are in maximum conflict with an interpretation in terms of EDA. Our interpretation is supported by the observation that delay times are consistent with those expected from modelling of elastic waves in the crust.

1. Introduction

From May 1987 to April 1988 a 30 km aperture nine-station analogue seismograph network was operated continuously around João Câmara (5°33'S, 35°51'W) in the Precambrian shield of Northeast Brazil, following a m_s 5.1 earthquake in a stable cratonic region [Takeya, 1992]. Results of that study will be reported elsewhere. As a secondary aim, that network included one three-component station deployed to record any shear-wave splitting. This station, JCAZ, is shown on the map in Figure 1, which also includes summary geological information. The polarisations observed at JCAZ showed a remarkably consistent direction close to north-south for the faster shear wave. Takeya [1992] noted that the direction of polarisation is associated with Precambrian foliation observed in the field, and that the shear-wave splitting may therefore be a signature of the "palaeo-stress field", i.e., the Precambrian deformation regime. Other authors [Crampin, 1987; Crampin and Lovell, 1991] have asserted that shear-wave splitting is normally caused by seismic anisotropy associated with the stress alignment of fluid-filled cracks, known as extensive dilatancy anisotropy (EDA). If the seismic anisotropy observed at JCAZ were caused by EDA, one would

expect the faster shear-wave polarisations to be parallel to the well-known east-west compressive stress determined from fault plane solutions and some borehole breakout data in the region [Ferreira *et al.*, 1987; Sophia, 1989; Assumpção, 1992; Ferreira *et al.*, 1998]. Here, the present-day maximum compressive stress and the Precambrian foliation are nearly perpendicular, so it is possible to discriminate between these possible causes of the observed shear wave anisotropy [Zhang and Schwartz, 1994].

¹ Now at Departamento de Física Teórica e Experimental, Universidade Federal do Rio Grande do Norte, Campus Universitário Lagoa Nova, Natal, RN, 59072-970, Brazil.

Copyright by the American Geophysical Union.

Paper number
0148-0227/02/089.00

2

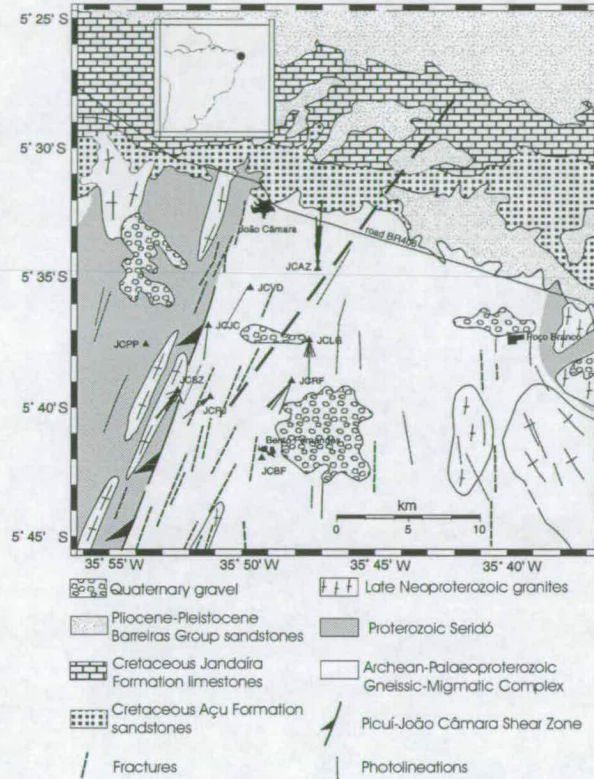


Figure 1. The João Câmara area, showing the locations of the analogue station JCAZ and the eight stations of the digital network. Also shown is the summary geological information and other features referred to in the text. Rose diagrams of the polarisation directions of shear-wave first arrivals from Figure 6 are also shown for each station. Long-dashed line shows the approximate location of the Samambaia fault which has been inferred from seismicity alone [Ferreira *et al.*, 1987; Takeya *et al.*, 1989]. Source of geological information: DNPM *et al.* [1998].

From December 1992 to August 1994, a three-component digital seismograph network of eight stations (also shown in Figure 1) was installed to provide additional shear-wave splitting data. It is shown that these new data corroborate Takeya's hypothesis; the shear-wave splitting is strongly correlated with the Precambrian foliation observed throughout the network.

2. Data selection for shear-wave splitting study

In this section, we present data recorded over 11 months for the analogue station JCAZ and the data recorded over 19 months for the eight digital stations. The analysis and discussion of both datasets is made in later sections. For both networks event locations were made with a two-layer model, consisting of an upper layer of 4.0 km thickness with P-wave

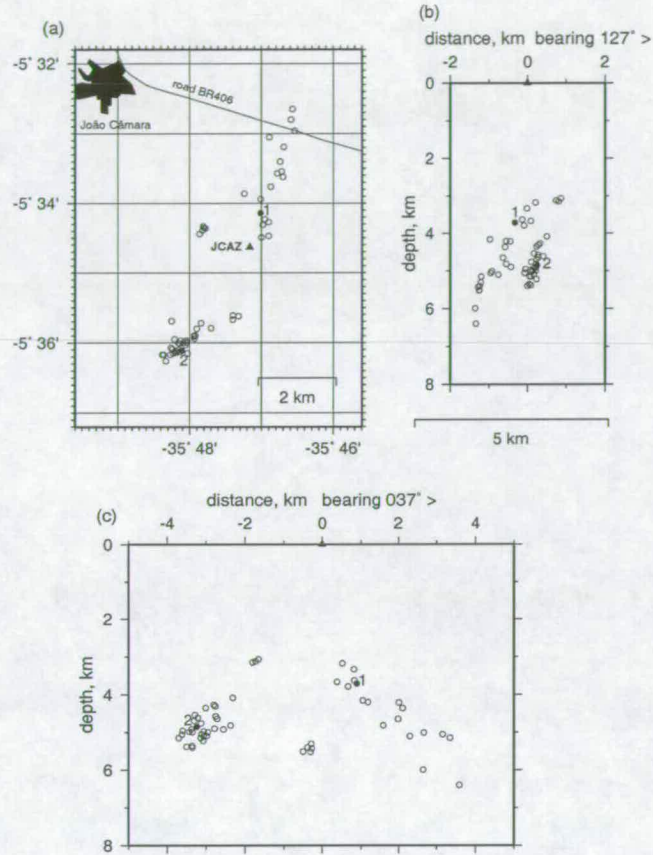


Figure 2. (a) Epicentre map of those events recorded at station JCAZ of the analogue network [Takeya, 1992] for which shear-wave splitting measurements were made. Circles represent epicentres and the filled triangle represents the three-component station JCAZ. (b) and (c) Vertical cross sections perpendicular to, and along, the Samambaia fault strike (Figure 1) showing that the emergent rays lie within the shear-wave window at station JCAZ. Examples 1 and 2 of Figure 5 are identified by filled circles; and represent events 05Jul87 17:39 and 26Jun87 14:08 respectively. The same horizontal and vertical scale are used throughout.

speed of 5.90 km/s, above a half-space with P-wave velocity of 6.10 km/s [Takeya, 1992].

For shear waves in the analogue network, Takeya [1992] used only events with an angle of emergence of less than 35.2° , and with vertical and horizontal location errors smaller than 0.5 km. Because the one three-component station (JCAZ) was at the centre of his network, the absolute hypocentres for these close events were particularly well determined; this means that even small events of around $m_b = 0.4$ and which were not recorded at all stations, had a sufficiently precise location to be included in this study. However, it turned

out that his one three-component station was located within a "gap" in aftershock seismicity; this reduced the number and azimuth range of usable signals. From a total of 140 events, some (typically above $m_b = 1.7$) were excluded because the recordings were saturated at JCAZ. In some other cases, the P-wave amplitude coda was too large to interpret the S-wave. Figure 2 shows the locations of the events used, which have magnitudes from 0.16 to $1.64 m_b$ calculated as duration magnitudes [Takeya, 1992].

For eight stations of the digital network, the shear-wave window was extended to include observations with emer-

4

gent angle of up to 45° (as predicted using the above two-layer model). This decision was based on the observation of waveforms, which showed that seismograms with emergence angles of up to 45° were indeed emerging at an angle subcritical to reflected P. We conclude that the emergent angle is somewhat less than that predicted by the model, due to a velocity gradient near the surface which is not apparent from the hypocentral error analysis. From the initial dataset

of 122 earthquakes, 41 seismograms from 22 earthquakes were recorded by stations inside our "extended" shear-wave window. A map showing the hypocentral locations of these 22 events is shown in Figure 3. A preliminary analysis of this new dataset was made by *Karnassopoulou* [1996]. She analysed 12 seismograms from 11 earthquakes analysed in this study. Her results are included in this paper.

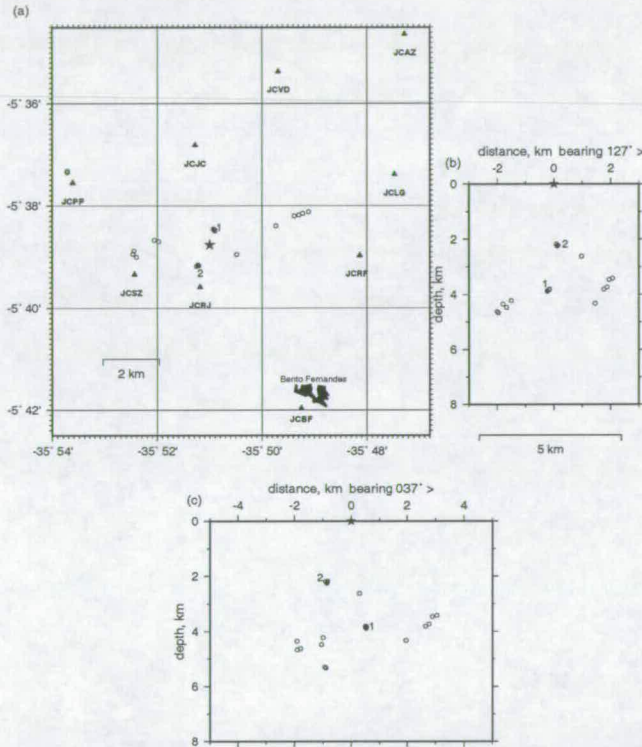


Figure 3. (a) Epicentre map of events recorded at stations of the digital network. Circles represent epicentre, and open triangles represent the three-component stations. JCAZ from the analogue network is shown with a filled triangle for reference. (b) and (c) Vertical cross sections perpendicular to, and along the Samambaia fault strike respectively. The reference point for the sections is indicated by an asterisk. Example 1 (Figure 7) and example 2 (Figure 8) are identified by filled circles, and represent events 01May94 07:23 and 12Jun94 04:56 respectively. The same horizontal and vertical scale is used throughout.

5

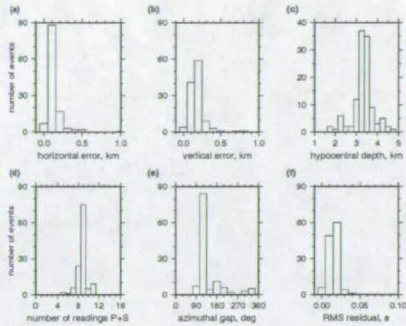


Figure 4. HYPO71 [Lee and Lahr, 1975] errors and location parameters. (a) and (b) show that most of the events have both vertical and horizontal errors of ≤ 0.2 km. (c) shows that the majority of events have hypocentral depth of less than 4 km. (d) shows that the majority of the located events have at least eight readings (P + S) which indicates the event was recorded at four or more stations. From (e) it is seen that the maximum azimuthal gap between two recording stations is 180° or less for most events. The low values for the RMS (≤ 0.02 s) shown in (f) supports the validity of the velocity model.

The location parameters from HYPO71 [Lee and Lahr, 1975] are shown in Figure 4. Figure 4a, b, c show that most events have both horizontal and vertical errors no greater than 0.2 km, and are located at between 3 and 4 km depth. Figure 4d shows that most of the events are recorded at four or more stations, and that the events are located within the network. Note that the peak in the azimuth gap distribution (Figure 4e) is 100° . Figure 4f shows that the rms residuals are not larger than 0.02 s for most events. This confirms the validity of applying the two-layer model of Takeya [1992] to the later (digital) dataset.

3. Shear-wave Analysis - Polarisation and delays

In general, shear wave splitting is difficult to identify on recorded seismograms, partly because the S-wave arrival is complicated by the effects of anelastic attenuation, scattering and near-surface velocity structure. In stable cratonic regions, Precambrian crystalline rocks predominate, and the seismic structure is not complicated significantly by sedimentary structures or extensive recent faulting. Signals may then exhibit high signal-to-noise ratio, very simple waveforms and impulsive P and S arrivals such as those in Figures 5, 7 and 8.

When analysing the analogue data (station JCAZ), Takeya [1992] digitised the horizontal seismograms and rotated them into the radial and transverse components with respect to the incoming ray. These were displayed together with polarisation diagrams to facilitate the picking of the fast and slow shear-waves, whose onsets were manually read from the seismograms. Figure 5 shows two examples from different az-

imuths. The polarisation direction of the first arrival in the horizontal plane is that of the fast split shear wave, and is determined from the horizontal polarisation diagrams (which contain most of the shear-wave energy). For shear waves at near-vertical incidence, the particle motion immediately following the onset of the fast split shear wave is usually sufficiently linear for the polarisation direction to be identified. The arrival of the second split S-wave is in general characterised by an abrupt change of particle motion, giving rise to a characteristic cruciform pattern on the particle-motion diagram. The horizontal components are then rotated again into the polarisation direction of the first shear wave and the direction normal to it; the first of these components then contains only the first split shear wave, and the other component is dominated by the second split shear wave. This facilitates reading of the arrival time of the second split shear wave, and hence calculation of the time delay.

At JCAZ it happens that the polarisation of the first shear wave is north-south, so that rotation from radial and transverse back to north and east is almost equivalent to rotation into fast and slow components.

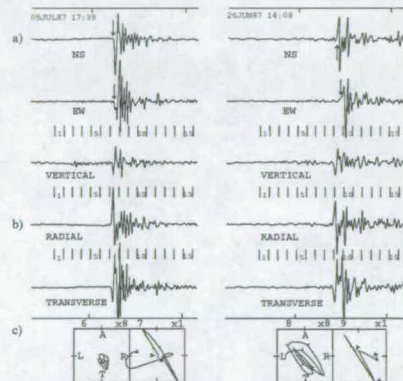


Figure 5. Two typical examples of shear-wave splitting at the analogue station JCAZ of the analogue network, (a) shows the conventional three-component seismograms, and (b) the two horizontal components rotated into radial and transverse directions. (c) Particle-motions diagram of the emerging signal in the horizontal plane with the ray-direction upwards ("T" and "A" refer to "towards" and "away" from the earthquake respectively, and "L" and "R" are to the "left" and "right" of the ray respectively). For each example, two consecutive 0.1 s polarisation time-windows are chosen to cover the S-wave arrival; these may be identified numerically from the time-interval graticule on the seismograms. Ticks on the particle-motion loci are every 0.01 s, and a relative gain factor (e.g. "x8" is shown above each diagram to allow comparison). Open and closed arrow heads mark the arrival of the first and second split shear-waves respectively. At the end of each locus an arrow-head indicates increasing time. In both examples the polarisation direction of the first split shear-wave is aligned almost exactly north-south, so the slow shear-wave arrivals can be seen separately on the unrotated horizontal components of (a) (see arrows).

6

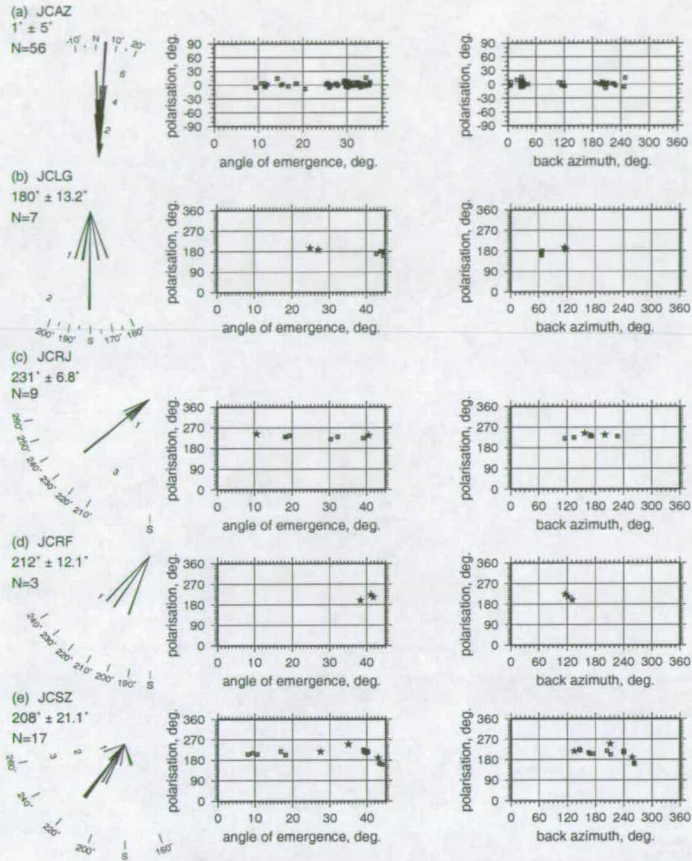


Figure 6. Rose diagrams showing the distribution of the polarisation directions of the fast split S-wave at stations with more than one shear-wave splitting observation. Directions are defined as lying between 90° and 270° . For each rose diagram these measurements are also plotted against angle of emergence and back azimuth; this confirms no evident correlation with these parameters. Asterisks on these plots are measurements made by Karnassopoulou [1996]. (a) and (b) show that the direction of polarisation of the fast shear-wave is in the north-south direction for stations JCAZ and JCLG. (c), (d) and (e) show that the direction of polarisation of the fast shear-wave for stations JCSZ, JCRJ and JCRF is in the northeast-southwest direction.

The exceptionally high signal-to-noise ratio and simplicity of the selected seismograms allowed the polarisation of the first shear-wave and the time delay between the two arrivals to be measured for all the selected events. Figure 6 shows a rose diagram of the measured first split shear-wave polarisation directions. The measurements are remarkably consistent, showing a first shear-wave polarised close to the north-south direction.

Figure 6 shows that there is no spurious correlation between the polarisation direction and either the backazimuth of the ray or its angle of emergence at the station. The absence of correlation between polarisation direction and azimuth provides confirmation that the observations are indeed split shear waves and not, for instance, conversions to P-waves beneath the receiver resulting from inhomogeneities in the subsurface. Particle-motion directions derived from observed three-component signals in Figures 5, 7 and 8 confirm that the first split shear-wave is not an S-to-P conversion

beneath the station, because such a conversion would be radially polarised.

In the shear-wave splitting analysis of the digital dataset (all stations other than JCAZ), the same method was used to determine polarisation directions as for JCAZ, described above. Figures 7 and 8 show two examples of S-wave split-

ting in the digital dataset. Although these data are recorded at 200 samples per second, it is evident that the data are nevertheless undersampled in view of the exceptionally high signal frequency.

All the shear-wave splitting measurements are shown in Figure 6. The measurements at each station have a standard deviation of less than 15° (Figure 6); at JCSZ the value is 21° .

Time delay is more difficult to measure than polarisation direction, because it is necessary to identify the onset of the second split shear-wave. This is assisted by the good quality of the signals and times that can be measured, as in the examples of Figures 7 and 8. In Takeya's analysis of JCAZ, the directions of the split S phases were approximately parallel

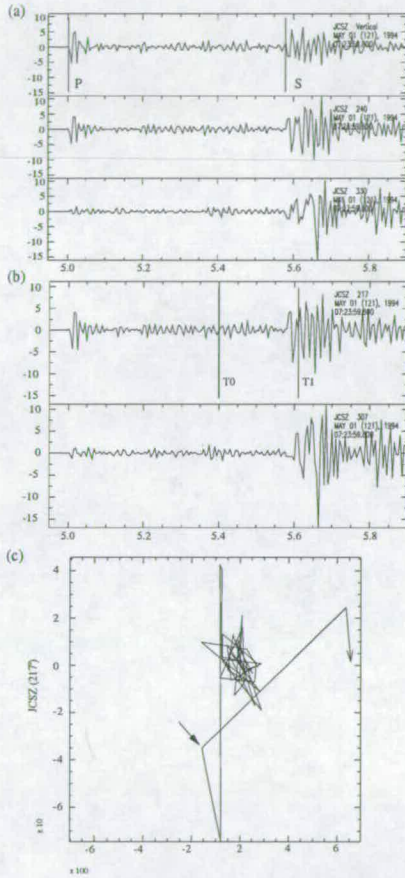


Figure 7. Typical example of shear-wave splitting at station JCSZ of the digital network. (a) shows the vertical component, followed by the horizontal components rotated to the radial and transverse directions. (b) shows the horizontal components rotated to the fast and slow S-wave polarisation directions. The azimuth of each horizontal-component seismogram is shown top-right next to the station code. The time marks "T0" and "T1" on the fast component denote the time interval corresponding to the polarisation diagram shown in (c), on which the arrival of the second split shear-wave is indicated by a filled arrow, and that of the particle motion by an open arrow.

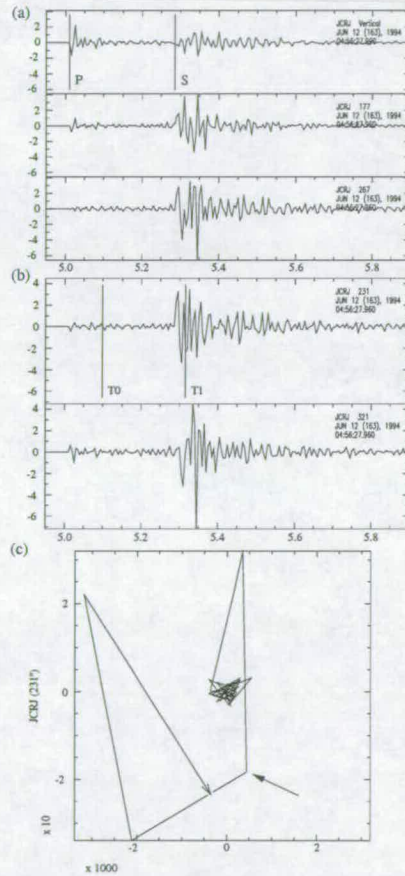


Figure 8. A typical example of shear-wave splitting at station JCRJ of the digital network. For explanation see Figure 7 caption.

8

to the seismometer orientations. That is, the slow split shear-wave coincided with the direction of the EW component. It was therefore possible to use the unrotated seismograms to check the delay of the second split shear-waves which were measured from the polarisation diagrams.

To determine delay times for the digital dataset, it was decided to do a visual inspection of each seismogram, to measure the delay of the second shear-wave. Figures 9 and 10 show two important aspects of the delays measured at all the stations. First, no clear correlation between delay time and the azimuth from event to station is observed. Secondly, the polarisation angle of the fast shear-wave does not depend upon the measured travel-time delay. Our interpretation of the observations in terms of shear-wave splitting is supported by the lack of correlation with these parameters, which also suggests the absence of complicating factors—in particular multiple layers of anisotropy or dipping interfaces.

4. Interpretation

Clear shear-wave splitting is observed in both the analogue and the digital datasets. Moreover, the polarisations of the first split shear-wave in both datasets are remarkably consistent for a variety of azimuths and incident angles—especially

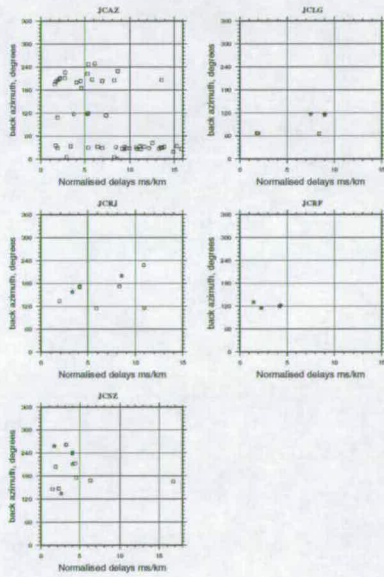


Figure 9. Normalised delay of the second split shear-wave, plotted against backazimuth (azimuth of the epicentre measured from the station); a plot is shown for each station in Figure 6. Asterisks are measurements made by *Karnassopoulou* [1996] as for Figure 7.

for stations JCAZ and JCSZ. This shear-wave splitting is indicative of seismic anisotropy along the ray path, and the consistent polarisation alignments are characteristic of hexagonal symmetry with a horizontal symmetry axis (TIH), as observed in many tectonic regions. Such anisotropy has been attributed to the presence of stress-aligned fluid-filled cracks (EDA) [*Crampin and Lovell*, 1991]. However, here there is convincing evidence that the stress field is dominated by east-west compression both locally and regionally. The composite fault-plane solutions for the João Câmara earthquakes determined by other authors [*Ferreira et al.*, 1987; *Sophia*, 1989; *Assumpção*, 1992; *Ferreira et al.*, 1998] are in close mutual agreement; they indicate a fault orientation

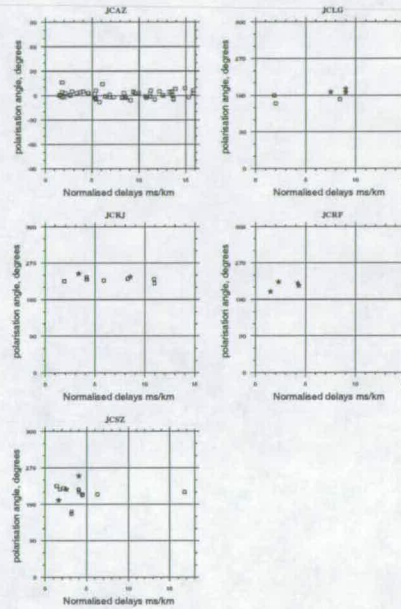


Figure 10. Normalised delay of the second split shear-wave, plotted against the polarisation angle of the fast split shear-wave; a plot is shown for each station appearing in Figure 6. Asterisks are measurements made by *Karnassopoulou* [1996].

Table 1. Station, maximum normalised delay, anisotropy and number of observations.

Station	Maximum normalised delay (ms/km)	anisotropy (%)	number of observations
JCAZ	16.0	5	56
JCLG	9.0	3	7
JCRJ	11.0	4	10
JCRF	4.0	1	4
JCSZ	17.0	6	17
JCJC	2.0	1	1

close to that inferred from the remarkably linear aftershock distribution along the Samambaia fault shown in Figure 1 [Takeya *et al.*, 1989]. These focal mechanisms indicate dextral strike-slip faulting with a small normal component, and an axis of maximum compressive stress close to east-west. Further evidence for such a regional stress orientation comes from other earthquake focal mechanisms [Ferreira *et al.*, 1987; Sophia, 1989] and from borehole breakout observations [Lima *et al.*, 1997]. This evidence is summarised in the World Stress Map [Mueller *et al.*, 2000]. Based upon this evidence of the present-day stress field, we would expect EDA cracks to result in fast shear waves polarised close to east-west. This is inconsistent with the orientation observed at all stations, and for JCAZ it is in maximum conflict (90°).

We now consider an alternative possibility that the observed shear-wave anisotropy arises from the Precambrian foliation, which would also result in hexagonal symmetry. The Precambrian basement of the area is part of the Borborema Province [de Almeida *et al.*, 1981], consisting of late Neoproterozoic (Brasiliano) granites, the Seridó Formation micaschists and the Gneissic-Migmatitic Complex.

The contact between the Seridó micaschists and older gneisses and micaschists is the Picuí-João Câmara Shear Zone (PJCSZ), shown in Figure 1. This shear zone has a north-south to north-northeast trend, dipping towards the west, and displays dextral transcurrent kinematics [Vauchez *et al.*, 1995; Coriolano *et al.*, 1997]. This deformation occurred in high temperature conditions, inferred by the occurrence of cordierite and sillimanite in the micaschists of the Seridó Formation and by felsic rocks mobilized in the Gneissic-Migmatitic Complex [Coriolano *et al.*, 1997].

We now compare the observed polarisation direction at each station with the trend of these shear zones. For comparison purposes, the polarisation rose diagrams of Figure 6 have been plotted also in Figure 1, and they show that the orientation of the fast split shear-wave follows closely the trend of the Picuí-João Câmara Shear Zone. The directions of the split shear wave agree with the north-south to north-northeast trend of the PJCSZ measured by Coriolano *et al.* [1997]. We therefore conclude that, by contrast with the EDA interpretation, this alternative is highly consistent with both seismological and geological observations.

This interpretation of the anisotropy in terms of the Precambrian structural trend is also supported by models of the effect of the whole crust on the splitting measurements of teleseismic SKS waves [Barruol and Mainprice, 1993]. They showed a strong correlation between the foliation orientation in the lower and middle crustal rocks and the observed delay. They concluded that a maximum delay time is systematically observed for waves propagating parallel to the foliation plane, and that the polarisation of the fast shear-wave is parallel to the lineation. The splitting is small when the waves propagate normal to the foliation. They estimated the amplitude of the delay due to mineral foliation in the lower and middle crust to be between 10 and 20 ms/km.

It is very difficult to see in this dataset a correlation between the geometrical orientation of the foliation and the measured time delays; one would need to correlate the direc-

tion of the incoming ray relative to the foliation to observe any such correlation. So, a correlation between these two factors with the present dataset was not made. However, most of our normalised delay values, as shown in Table 1, are well inside the range proposed by Barruol and Mainprice [1993]. These values of normalised time delays lead us to accept that in an area such as that of the present study, where the petrofabric of shallow rocks is controlling the anisotropy, the results of Barruol and Mainprice [1993] may perhaps be up-scaled and applied to the upper regions of the crust (as shallow as 5 km).

5. Discussion and conclusions

The consistency of the observed polarisation directions of the first split shear wave in all the six stations in this study is very high. The direction of polarisation is close to north-south at the most northern stations—namely JJC, JCAZ and JCLG, following the orientation of the shear zone. The other three stations (JCRF, JCSZ and JCRJ), show a preferential northeast-southwest orientation for the split shear-wave polarisations, which is also in agreement with the direction of the foliation in the shear zone. If the observed anisotropy was caused by EDA, one would expect an east-west direction for the fast split shear wave. In our observations, we show that the anisotropy is consistent with the tectonic structure (foliation, lineation) of the region, and not with anisotropy of stress-aligned fluid-filled cracks. Our results confirm those of several other authors [Gledhill, 1991; Brocher and Christensen, 1990; Zhang and Schwartz, 1994; Menke *et al.*, 1994; Bernard *et al.*, 1997], which also implies that the EDA hypothesis of Crampin *et al.* [1984], cannot explain all examples of crustal anisotropy. Here, the maximum horizontal compressive stress direction is almost perpendicular to the geological structures in the region, providing maximum differentiation between the two mechanisms. Moreover, delay times measured at different stations are consistent with previous work by Barruol and Mainprice [1993].

Acknowledgments. AFDN was supported by a scholarship from the Conselho Nacional de Desenvolvimento Científico e Tecnológico of Brazil (CNPq). The authors thank João da Mata Costa and Eduardo de Menezes for their effort in the field campaign. We also thank Drs. Patience Cowie, Emanuel F. Jardim de Sá and Anya Reading for suggesting improvements to the manuscript, and Dr. A. Vauchez and two anonymous reviewers for many helpful comments. Our thanks also go to Dr. Marcelo Assumpção for pointing out the importance of the time delay measurements in our analysis. GMT [Wessel and Smith, 1998] was used to display most of our results.

References

- Assumpção, M., The regional intraplate stress field in south America, *J. Geophys. Res.*, 97, 11,889–11,903, 1992.
- Barruol, G., and D. Mainprice, A quantitative evaluation of the contribution of crustal rocks to the shear-wave splitting of teleseismic SKS waves, *Phys. Earth Planet. Int.*, 78, 281–300, 1993.
- Bernard, P., G. Chouliaras, A. Tzanis, M. B. P. Briole, J. Telis, G. Stavrakakis, and K. Makropoulos, Evidence for shallow and pervasive seismic anisotropy in the Wellington region, New Zealand, *Geophys. Res. Lett.*, 24, 2227–2230, 1997.
- Brocher, T. M., and N. I. Christensen, Seismic anisotropy due to preferred mineral orientation observed in the shallow crust in southern Alaska, *Geology*, 18, 737–740, 1990.

10

- Coriolano, A. C. F., E. F. Jardim de Sá, P. A. Cowie, and C. A. Amaral, Estruturas frágeis no substrato de região de João Câmara (RN): correlação com a Falha Sísmica de Samambaias?, 1997, XVI Simpósio de Geologia do Nordeste, Fortaleza-CE, pp. 325-329. In Portuguese.
- Crampin, S., Geological and industrial implications of extensive-dilatancy anisotropy, *Nature*, 328, 491-496, 1987.
- Crampin, S., and J. H. Lovell, A decade of shear-wave splitting in the earth's crust: what does it mean? what use can we make of it? and what should we do next?, *Geophys. J. Int.*, 107, 387-407, 1991.
- Crampin, S., R. Evans, and B. K. Atkinson, Earthquake prediction: a new physical basis, *Geophys. J. R. Astron. Soc.*, 76, 147-156, 1984.
- de Almeida, F. F. M., Y. Hasui, B. B. B. Neves, and R. A. Fuck, Brazilian structural provinces: an introduction, *Earth Sci. Rev.*, 17, 1-29, 1981.
- DNPM, UFRN, PETROBRAS, and Governo do Estado do Rio Grande do Norte, Mapa Geológico do Estado do Rio Grande do Norte, 1998.
- Ferreira, J. M., M. Takeya, J. M. Costa, J. A. M. Moreira, M. Assumpção, J. A. V. Veloso, and R. G. Pearce, A continuing earthquake sequence near João Câmara, Northeastern Brazil—preliminary results, *Geophys. Res. Lett.*, 14, 1042-1045, 1987.
- Ferreira, J. M., R. Oliveira, M. K. Takeya, and M. Assumpção, Superposition of local and regional stresses in northeast Brazil: evidence from focal mechanism around the Potiguar marginal basin, *Geophys. J. Int.*, 134, 341-355, 1998.
- Gledhill, K. R., Evidence for shallow and pervasive seismic anisotropy in the Wellington region, New Zealand, *J. Geophys. Res.*, 96, 21,503-21,516, 1991.
- Karnassopoulou, A., Joint investigation of source parameters and seismic anisotropy using microearthquakes in Greece, Arkansas and Northeast Brazil, 1996, unpublished Ph.D. thesis. University of Edinburgh.
- Lee, W. H. K., and J. C. Lahr, *HYP071 (revised): a computer program for determining hypocenter and magnitude and first motion pattern of local earthquakes. Open File Rep. 75-311*, U. S. Geol. Surv., 1975.
- Lima, C. E. Nascimento, and M. Assumpção, Stress orientation in Brazilian sedimentary basins from breakout analysis for force models in the south American plate, *Geophys. J. Int.*, 130, 112-124, 1997.
- Menke, W., B. Brandsdottir, S. Jakobsdottir, and R. Stefansson, Seismic anisotropy in the crust at the mid-atlantic plate boundary in the south-west Iceland, *Geophys. J. Int.*, 119, 783-790, 1994.
- Mueller, B., J. Reinecker, and K. Fuchs, The 2000 release of the world stress map, Available online at <http://www-wsm.physik.uni-karlsruhe.de/>, 2000.
- Sophia, C. M., A reativação sísmica de João Câmara, RN, de janeiro-fevereiro de 1987, 1989, unpublished Master's thesis. University of São Paulo. In Portuguese.
- Takeya, M., J. M. Ferreira, R. G. Pearce, M. Assumpção, J. M. Costa, and C. M. Sophia, The 1986-1989 intraplate earthquake sequence near João Câmara, northeast Brazil - evolution of seismicity, *Tectonophysics*, 167, 117-131, 1989.
- Takeya, M. K., High precision studies of an intraplate earthquake sequence in Northeast Brazil, 1992, unpublished Ph.D. thesis. University of Edinburgh.
- Vaucher, A., S. Neves, R. Cabuy, M. Corsini, M. Egydio-Silva, M. Arthaud, and V. Amaro, The Borborema shear zone system, NE Brazil, *J. S. Am. Earth Sci.*, 8, 247-266, 1995.
- Wessel, P., and W. H. F. Smith, New, improved version of Generic Mapping Tools released, *EOS Trans. Am. Geophys. U.*, 79, 579, 1998.
- Zhang, Z., and S. Y. Schwartz, Seismic anisotropy in the shallow crust of the Loma Prieta segment of the San Andreas fault system, *J. Geophys. Res.*, 99, 9651-9661, 1994.
- Aderson F. do Nascimento (corresponding author), Departamento de Física Teórica e Experimental, Campus Universitário Lagoa Nova, Natal, RN, 59072-970, Brazil. (aderson@dfte.ufrn.br)
- Robert G. Pearce, Department of Geology and Geophysics, The University of Edinburgh, West Mains Road, EH9 3JW, Edinburgh, UK. (bob.pearce@glg.ed.ac.uk)
- Mario K. Takeya, Departamento de Física Teórica e Experimental, Campus Universitário Lagoa Nova, Natal, RN, 59072-970, Brazil.

(Received _____)